ABSTRACT

Title of Dissertation:	EVALUATING THE STRATOSPHERIC LOADING OF HALOGENS: BROMINATED VERY SHORT-LIVED SUBSTANCES AND LOWER STRATOSPHERIC INORGANIC CHLORINE
	Pamela Adelaide Wales, Doctor of Philosophy, 2019
Dissertation directed by:	Dr. Ross J. Salawitch, Department of Chemistry and Biochemistry, Department of Atmospheric and Oceanic Science, Earth System Science Interdisciplinary Center

Bromine and chlorine compounds catalyze the removal of stratospheric ozone. The Montreal Protocol and subsequent regulations have decreased the atmospheric abundance of anthropogenic, long-lived halogen sources. This dissertation quantifies the stratospheric supply of halogens from very short-lived substances (VSLS), which are important drivers of ozone loss in the lower stratosphere. First, the contribution of natural, biogenic VSLS to stratospheric bromine (Br_y^{VSLS}) is calculated using the first comprehensive sampling of organic and inorganic bromine gases in the Tropical Western Pacific (TWP), obtained by two aircraft campaigns in winter 2014. Measurements of BrO and organic bromine compounds, including VSLS, were used to determine that the value of Br_y^{VSLS} is 5.0 ± 2.1 ppt, about 25% of total stratospheric bromine. This analysis indicates that 60% of Br_y^{VSLS} enters the stratosphere as organic

compounds, higher than previous estimates. Second, the representation of brominated VSLS within 14 global models used to project the recovery of the ozone layer is examined. Bromine within global models that explicitly simulate VSLS compare better with TWP observations than bromine within models that utilize longer-lived chemicals as a surrogate for VSLS. Both methods for incorporating VSLS are significant improvements over previous simulations that only included long-lived bromine sources. Third, ground and satellite-based measurements of column BrO collected over Fairbanks, Alaska during spring 2011 are examined. Ground-based retrievals support the central, 5 ppt value of our TWP estimate of Br_y^{VSLS}. Satellite measurements of BrO are consistently higher than reported by the ground-based instrument. Satellite observations indicate either the upper, 7 ppt limit of Br_y^{VSLS} or, if we consider 5 ppt of Br_y^{VSLS}, the presence of 1.2 ppt of tropospheric BrO uniformly mixed between 2 km and the tropopause. Finally, inorganic chlorine in the midlatitude lower stratosphere is evaluated. Ground and satellite-based measurements of HCl and $ClONO_2$ support a stratospheric contribution of anthropogenic chlorinated VSLS as well as recently proposed updates to parameterizations of the stratospheric decomposition of long-lived halocarbons. Simulations including chlorinated VSLS and the updated parameterization project a slower recovery of the ozone layer than previously expected.

EVALUATING THE STRATOSPHERIC LOADING OF HALOGENS: BROMINATED VERY SHORT-LIVED SUBSTANCES AND LOWER STRATOSPHERIC INORGANIC CHLORINE

by

Pamela Adelaide Wales

Dissertation submitted to the Faculty of the Graduate School of the
University of Maryland, College Park, in partial fulfillment
of the requirements for the degree of
Doctor of Philosophy
2019

Advisory Committee:
Professor Ross J. Salawitch, Chair
Professor Akua Asa-Awuku, Dean's Representative
Professor Neil V. Blough
Professor Timothy Canty
Professor Alice Mignerey

Dedication

To my parents, for all their love and support along the way.

Acknowledgements

I would first like to thank my advisor, Ross Salawitch. Without his insightful guidance and support, this dissertation would not have been possible. Thanks to Tim Canty and Russ Dickerson for continuously asking challenging questions and pushing me to think critically about the direction of my research. I would also like to thank the atmospheric chemistry group as a whole for being an all-around pleasant group of people that humored me as I talked about bromine for over 5 years. A special thanks to Sandra Roberts, Maggie Marvin, Laura McBride, and Dolly Hall for their emotional support and intellectual comradery. An additional thanks to my family and friends for being understanding and supportive when I chose to go back to school. Finally, I would like to thank my husband, Brett Arnold, for not only agreeing to move to Maryland but sticking with me as I worked through graduate school. Thank you for reading over my work even when you didn't understand the science. Your love and friendship mean the world to me.

Table of Contents

List of Tables

List of Figures

List of Abbreviations

ACE-FTS	Atmospheric Chemistry Experiment-Fourier Transform Spectrometer (satellite instrument)
AMAX-DOAS	Airborne MultiAxis Differential Optical Absorption Spectroscopy
AMF	Air Mass Factor
ATMOS	Atmospheric Trace Molecule Spectroscopy (space-based instrument)
ATTREX	Airborne Tropical Tropopause Experiment (aircraft campaign)
AWAS	Advanced Whole Air Sampler
Br_y	Inorganic bromine
Br_y^{VSLS}	The contribution of very short-lived substances to stratospheric bromine
Br_y^{SGI}	The amount of stratospheric bromine from source gas injection
BrO^{VC}	Vertical Column of BrO
CAM-chem-SD	Community Atmosphere Model version 4 with interactive chemistry and Specified Dynamics
CAST	Coordinated Airborne Studies in the Tropics (aircraft campaign)
CBr_y	Organic bromine
CCM	Chemistry-Climate Model
CCMI	Chemistry-Climate Modeling Initiative
CIMS	Chemical Ionization Mass Spectrometry
Cl_y	Inorganic chlorine
CONTRAST	CONvective TRansport of Active Species in the Tropics (aircraft campaign)
CTM	Chemical Transport Model
DOAS	Differential Optical Absorption Spectroscopy
dSCD	differential Slant Column Density
EESC	Equivalent Effective Stratospheric Chlorine
FRF	Fractional Release Factors
FTIR	Fourier Transform Infrared Spectroscopy
F_y	Fluorine product gases (HF, COClF, COF_2)
GH	Global Hawk (NASA airplane, used during ATTREX)

GOME	Global Ozone Monitoring Experiment (satellite instrument)
GMI	Global Modeling Initiative (NASA chemical transport model)
GV	Gulfstream V (NCAR airplane, used during CONTRAST)
GWAS	Global Hawk Whole Air Sampler
HARP	HIAPER Airborne Radiation Package
HATS	Halocarbon and other Atmospheric Trace Species (NOAA monitoring network)
HIAPER	High-performance Instrument Airborne Platform for Environmental Research
IUPAC	International Union of Pure and Applied Chemistry
JPL 2015	Kinetic recommendations from the NASA Jet Propulsion Laboratory (Burkholder et al., 2015)
LMS	Lowermost stratosphere
MFDOAS	Multifunction Differential Optical Absorption Spectroscopy
NCEP-FNL	National Center for Environmental Prediction – Final operational global analysis
NDACC	Network for the Detection of Atmospheric Composition Change
NO_y	Total nitrogen oxides
OMI	Ozone Monitoring Instrument (satellite instrument)
PGI	Product Gas Injection
RF	Research Flight
SAD	Surface Area Density
SCD	Slant Column Density
SD	Specified Dynamics
SGI	Source Gas Injection
SGI^{VSLS}	Source Gas Injection of Very Short-Lived Substances
SZA	Solar Zenith Angle
TTL	Tropical Tropopause Layer
TWP	Tropical Western Pacific
UHSAS	Ultra-High Sensitivity Aerosol Spectrometer
VCD	Vertical Column Density
VSLS	Very Short-Lived Substances

WAS	Whole Air Sampler
WMO	World Meteorological Organization
WMO 2014	WMO Ozone Assessment 2014

Chapter 1: Introduction

1-1. Background

Stratospheric ozone is an important absorber of incoming solar radiation and regulator of the thermal structure of the atmosphere. The ozone hole was first reported over Antarctica in 1985 (Farman et al., 1985). This discovery was followed by decreasing trends in stratospheric ozone in the midlatitudes and tropics, and anthropogenic emissions of chlorofluorocarbons (CFC) were identified as the main driver of the observed ozone depletion. Following photolysis in the stratosphere, CFCs release chlorine atoms that provide pathways for catalytic destruction of ozone (Molina and Rowland, 1974). Even though the atmospheric abundance of anthropogenic bromine compounds is much lower than CFCs, these compounds are an important contributors to ozone depletion, owing to the high catalytic efficiency of bromine-driven ozone loss (Wofsy et al., 1975; McElroy et al., 1986; Salawitch et al., 2005).

The World Meteorological Organization (WMO) produces Ozone Assessment reports every four years. These reports summarize important updates to ozone layer research, projections of the recovery of the ozone layer, as well as recommendations for policy makers. Projections for the recovery of the ozone layer rely on global model simulations, and historically the only sources of stratospheric halogens considered in these models had been long-lived source gases (e.g., Douglass et al., 2011). The long-lived source gases have atmospheric lifetimes that are long with respect to tropospheric mixing. The chlorine and bromine content of long-lived compounds are shown in Figure 1-1. In this figure, solid lines represent mean global observations and dashed lines are projections recommended by the 2014 WMO Ozone Assessment. In both

panels the black lines are the total chlorine and bromine content of the long-lived substances.

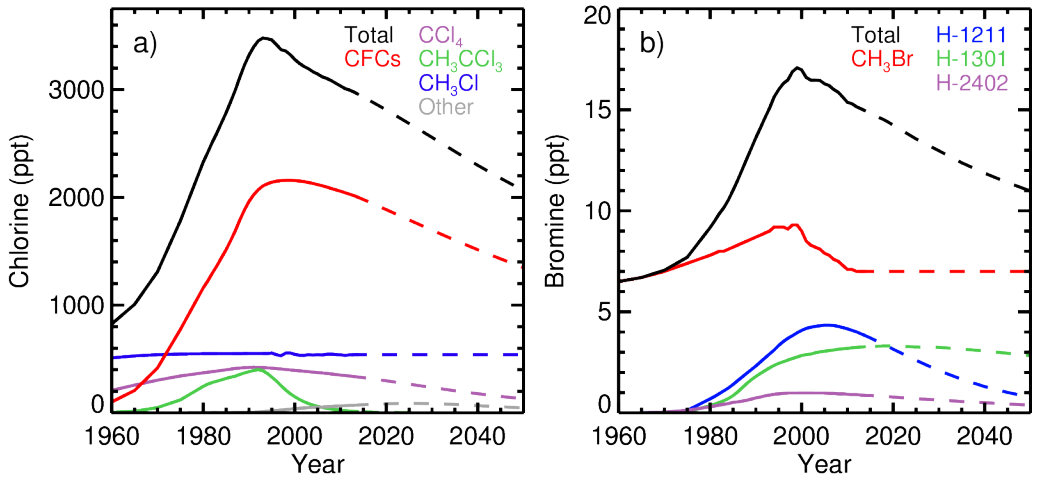

Figure 1-1. Time series for the (a) chlorine and (b) bromine content of long-lived halocarbons at the surface, as given by the 2014 WMO Ozone Assessment (Harris and Wuebbles et al., 2014). Organic chlorine is shown in panel (a), where the surface mixing ratio of each compound is multiplied by its chlorine atomicity. The chlorine content of CFC-11, CFC-12, CFC-113, CFC-114, and CFC-115 is shown in red. The chlorine content of HCFC-141b, HCFC-142b, and Halon-1211 is shown in grey. Organic bromine is shown in panel (b), where the surface mixing ratio of each compound is multiplied by its bromine atomicity. In both panels, the solid lines represent the mean global surface observation, and the dashed lines represent projections.

All compounds in Figure 1-1, except CH_3Cl, are now regulated by the Montreal Protocol or subsequent amendments. The sources of CH_3Cl are natural, and following regulations, mixing ratios of CH_3Br have returned to their natural background. The total chlorine abundance of long-lived source gases peaked at 3500 parts per trillion by volume (ppt) in 1993, while total bromine peaked at 17 ppt in 1999. The tropospheric lifetimes of these compounds are long with respect to time need for large-scale tropospheric transport, about 6 months (Ko et al., 2003; Law et al., 2006). As a result, long-lived source gases are well mixed within the troposphere and the proximity of emissions to strong convection is unimportant for determining the amount of bromine

or chlorine that reaches the stratosphere. Following transport to the stratosphere, inorganic chlorine and bromine compounds are formed after the photodissociation of the organic source gases. This occurs most readily in the tropics and upper stratosphere where source gases are exposed to high levels of radiation. The formation of inorganic halogen species can be parameterized as a function of the time air has spent in the stratosphere (i.e., mean age of air), and the amount of inorganic halogen in parcel of air will increase as the air ages (Newman et al., 2007; Engel et al., 2018).

Chapters 2 through 4 of this dissertation evaluate the contribution of natural, very short-lived substances (VSLS) to stratospheric bromine. These compounds are expected to contribute an additional 5 ± 3 ppt of bromine to the stratosphere (Carpenter et al., 2014). Since long-lived compounds currently supply ~15 ppt of bromine to the stratosphere (Figure 1-1), VSLS are a source of ~25% of total stratospheric bromine. Due to their short atmospheric lifetimes, VSLS readily inject inorganic bromine to the lowest portions of the stratosphere, amplifying their influence on the ozone layer (Salawitch et al., 2005). As discussed in Section 1-1.3 and 2-1, because VSLS partially dissociate in the troposphere, models must include a more detailed representation of tropospheric processes to estimate the stratospheric injection of VSLS than is required for long-lived sources. Lastly, Chapter 5 will assess the potential stratospheric contribution of anthropogenic, chlorinated VSLS as well as different formulations for the stratospheric release of inorganic chlorine from long-lived compounds.

1-1.1. Stratospheric Halogen Chemistry

Following photolysis or reaction with a hydroxyl radical (OH), organic halogen compounds form inorganic species in the stratosphere. For bromine, the family of

inorganic bromine (Br_y) compounds includes Br, BrO, $BrONO_2$, HOBr, HBr, Br_2, BrCl, and $BrNO_2$. Inorganic halogens cycle between active radicals (i.e., Br and BrO) and more stable reservoir species (i.e., HBr, HOBr, and $BrONO_2$). The seasonality and extent of ozone depletion depends on the partitioning of inorganic halogens between the active radicals and reservoir compounds.

Halogen atoms (X) react with ozone, forming a halogen oxide (XO) and molecular oxygen:

$$X + O_3 \rightarrow XO + O_2 \qquad (1\text{-}1)$$

Halogen oxides and atomic halogens rapidly cycle between each other. Catalytic loss of ozone occurs when XO reforms X without also forming ozone or a precursor to ozone formation (i.e., O, NO_2, HO_2, ClO, and BrO). For instance, halogen oxides catalyze ozone loss by reacting with atomic oxygen to form atomic halogens and molecular oxygen:

$$XO + O \rightarrow X + O_2 \qquad (1\text{-}2)$$

Catalytic cycles with reaction (1-2) are most important in the middle and upper stratosphere, above ~30 km in altitude, due to the higher abundance of atomic oxygen (Osterman et al., 1997).

The contribution of bromine to ozone loss is most significant in the lower stratosphere, below ~25 km (Salawitch et al., 2005). Since the concentration of ozone is largest in the lower stratosphere, perturbations to the levels of ozone in this region have a strong impact on the total column of ozone. Reactions on particle surfaces, such as polar stratospheric clouds and sulfate aerosols, enhances the influence of halogen chemistry at lower altitudes. These heterogeneous reactions increase the abundance of

active halogen radicals relative to the stable reservoirs (McCormick et al., 1982; McElroy et al., 1992; Fahey et al., 1993).

Bromine-catalyzed ozone loss in the lower stratosphere largely occurs through the reaction between hydroperoxyl radical (HO_2) and the products of reaction (1-1) (Poulet et al., 1992; Garcia and Solomon, 1994):

$$BrO + HO_2 \rightarrow HOBr + O_2 \qquad (1\text{-}3)$$

Stratospheric bromine also enhances the efficiency of chlorine-mediated ozone loss by providing an additional reaction partner for ClO, via:

$$\begin{aligned} ClO + BrO &\rightarrow BrCl + O_2 && (1\text{-}4a)\\ &\rightarrow Br + ClOO && (1\text{-}4b)\\ &\rightarrow Br + OClO && (1\text{-}4c) \end{aligned}$$

Ozone loss occurs through reactions (1-4a) and (1-4b), since these two pathways ultimately lead to the formation of $Br + Cl + O_2$. However, OClO formed by reaction (1-4c) photolyzes and forms ozone precursors, atomic O and ClO, leading to a null catalytic cycle (Yung et al., 1980; Canty et al., 2005). The catalytic pathways in reaction (1-4) are crucial for the formation of the Antarctic ozone hole as well as loss of ozone in the midlatitudes following major volcanic eruptions (McElroy et al., 1986; Salawitch et al., 2005).

Chlorine and bromine chemistry are the key drivers of halogen-catalyzed ozone destruction. Fluorine atoms from CFCs do not significantly contribute to ozone loss, due to the strong bond strength of HF and the resulting negligible mixing ratios of active fluorine radicals (Kaye et al., 1991). Ozone loss occurs very efficiently via iodine reactions, and evidence of iodine-catalyzed ozone loss has been detected in the troposphere (Saiz-Lopez et al., 2014). However, iodine-containing source gases have

even shorter tropospheric lifetimes than brominated VSLS (Carpenter et al., 2014). Based on column measurements of iodine monoxide (IO), the stratospheric loading of inorganic iodine (I_y) is below 0.2 ppt, while balloon measurements of IO and OIO support upper limits of 0.1 ppt for I_y. As a result, iodine chemistry is thought to be a negligible catalytic pathway for stratospheric ozone loss (Wennberg et al., 1997; Bösch, 2003; Butz et al., 2009)

The reservoirs for bromine radicals are less stable than chlorine reservoirs. Consequently, a higher fraction of Br_y than inorganic chlorine (Cl_y) is available as active species in the lower stratosphere where the molecular density of ozone is high. Throughout much of the daytime stratosphere about half of Br_y is partitioned into bromine monoxide (BrO), a reactive radical compound (Lary, 1996; Lary et al., 1996). Conversely, the majority of stratospheric Cl_y is in the form of HCl (Zander et al., 1996; Nassar et al., 2006). The higher partitioning of Cl_y into HCl than Br_y into HBr occurs because the reaction between atomic Cl and CH_4 is exothermic, while the reaction between atomic Br and CH_4 is endothermic and does not proceed at stratospheric temperatures (Wofsy et al., 1975; Watson et al., 1976; Spencer and Rowland, 1978). As a result, bromine-catalyzed ozone loss is approximately 60 times more efficient than chlorine (Daniel et al., 2006). Even though stratospheric mixing ratios of bromine are over 100 times smaller than chlorine (Figure 1-1), bromine chemistry is need to account for up to half of the observed ozone loss in the midlatitudes (Sinnhuber et al., 2009).

1-1.2. Bromine Monoxide Observations

Measurements of BrO are commonly used to infer the stratospheric loading of Br_y. Bromine monoxide is the most frequently measured Br_y compound, and about half

of daytime Br_y is in the form of BrO throughout much of the stratosphere. Photochemical models are used to calculate the BrO/Br_y ratio, and stratospheric loading of bromine is found using this ratio and observed BrO. These models rely on laboratory measurements of the rate constants and the photolysis cross sections that govern the ratio of BrO to total Br_y (e.g., Pfeilsticker et al., 2000; Dorf et al., 2008; Salawitch et al., 2010; Wales et al., 2018).

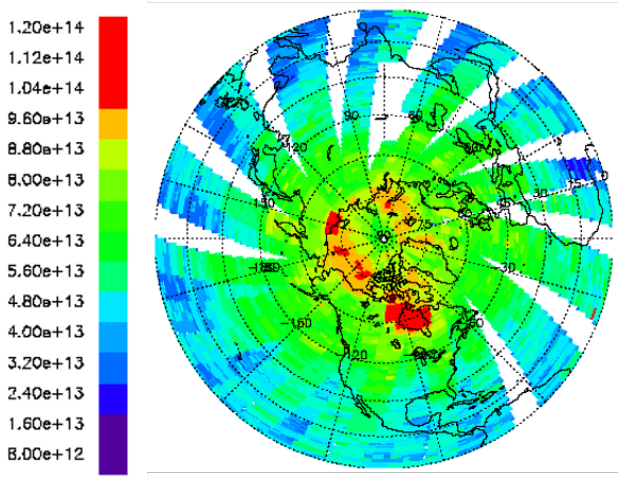

Figure 1-2. Northern Hemisphere measurements of vertical column BrO, in unit of molecules cm^{-2} from GOME for 30 April through 02 May, 1997. Adapted from Chance (1998).

Satellite measurements of BrO have been collected since 1995 (Chance, 1998; Hegels et al., 1998). The satellite observations are usually reported as vertical column amounts of BrO (BrO^{VC}), from the top of the atmosphere to the surface. An early satellite observation of BrO^{VC}, reported in Chance (1998), is shown in Figure 1-2. The measurements in Figure 1-2 were acquired by the Global Ozone Monitoring Experiment (GOME) instrument and are reported in units of molecules/cm^2. The GOME instrument was onboard the ERS-2 satellite, which had a near polar, sun-synchronous orbit and an equatorial local crossing time of 10:30 am. Complete coverage of the equatorial region was obtained in three days. The GOME instrument

measured back-scattered and reflected ultraviolet-visible (UV-Vis) radiation. Spectra of BrO were retrieved using Differential Optical Absorption Spectroscopy (DOAS) at wavelengths between 346 to 359 nm (Hegels et al., 1998; Wagner and Platt, 1998). A similar method for measuring BrO^{VC} is used by the Ozone Monitoring Instrument (OMI), discussed in Chapter 4.

Early satellite studies assumed that stratospheric BrO was evenly distributed within latitude bands (i.e., zonally symmetric). This assumption lead to the conclusion that periods of elevated BrO^{VC} , such as over the Hudson Bay and the Arctic in Figure 1-2, were due to high mixing ratios of BrO in the troposphere (Richter et al., 1998; Wagner and Platt, 1998). Elevated mixing ratios of BrO in the boundary layer have been detected during Arctic spring using ground-based in situ techniques, and these periods of elevated BrO have been connected to near complete removal of surface ozone (Barrie et al., 1988). However, stratospheric BrO is not zonally symmetric. Enhancements of BrO in the stratosphere can be misattributed to the troposphere, particularly when dynamical conditions lead to a low altitude (high-pressure) tropopause (Salawitch et al., 2010; Theys et al., 2011). Consequently, a detailed representation of stratospheric chemistry and the amount of bromine in the stratosphere is required to properly quantify both tropospheric and stratospheric bromine using satellite observations.

Numerous studies have indicated that marine biogenic emissions of brominated VSLS could be an important source of stratospheric bromine, in addition to the compounds shown in Figure 1-1 (Dvortsov et al., 1999; Pfeilsticker et al., 2000; Dorf et al., 2008). Long-lived source gases decay slowly as air photochemically ages and

rises through the Brewer Dobson circulation, releasing Br_y months to years after entering the stratosphere. However, as demonstrated in Chapter 2, VSLS dissociate and produce Br_y compounds either before or soon after entering the stratosphere, supplying Br_y to lowermost stratosphere. Since the density of air is greater at lower altitudes, simulations of BrO^{VC} are sensitive to the assumed distribution of BrO (and Br_y) in the lower stratosphere. As a result, an accurate representation of the contribution of VSLS to stratospheric bromine (Br_y^{VSLS}) is required to properly model the stratospheric component of measurements of BrO^{VC} (Salawitch et al., 2005, 2010; Dorf et al., 2006; Hendrick et al., 2007). Furthermore, the Br_y supplied by VSLS in the lower stratosphere is required to properly interpret long-term trends of column ozone over the midlatitudes (Salawitch et al., 2005; Sinnhuber et al., 2009).

1-1.3. Very Short-Lived Substances

Very short-lived substances are compounds that have tropospheric lifetimes comparable to or less than 6 months, the transport time needed to attain close to uniform mixing in the troposphere (Ko et al., 2003). Processes controlling the fate of the halogen atoms contained within organic VSLS are depicted in Figure 1-3. Following photolysis or reaction with OH, VSLS quickly produce inorganic halogen compounds in the troposphere (Hossaini et al., 2010). The resulting inorganic product gases include soluble species, which can be taken up by aerosols and washed out of the atmosphere. Heterogeneous reactions occurring on the surface of tropospheric aerosols can release labile bromine back to the atmosphere (Iraci et al., 2005; Sinnhuber and Folkins, 2006). If the VSLS reach the stratosphere before being oxidized, this is referred to as source gas injection (SGI). Product gas injection (PGI) is the amount of halogens that enters

the stratosphere through inorganic product gases. The total supply of halogen atoms from VSLS to the stratosphere is the sum of SGI and PGI. The contribution of VSLS to the stratospheric halogen loading is sensitive to the geographic distribution of emissions of VSLS relative to regions of active convection as well as the tropospheric chemical and physical processing of VSLS and their decomposition by-products. The numerous processes affecting the transport of bromine from VSLS to the stratosphere complicates the reliability of model representation of VSLS (Sinnhuber and Folkins, 2006; Hossaini et al., 2010; Liang et al., 2010; Aschmann et al., 2011; Schofield et al., 2011; Tegtmeier et al., 2012; Fernandez et al., 2014; Liang et al., 2014).

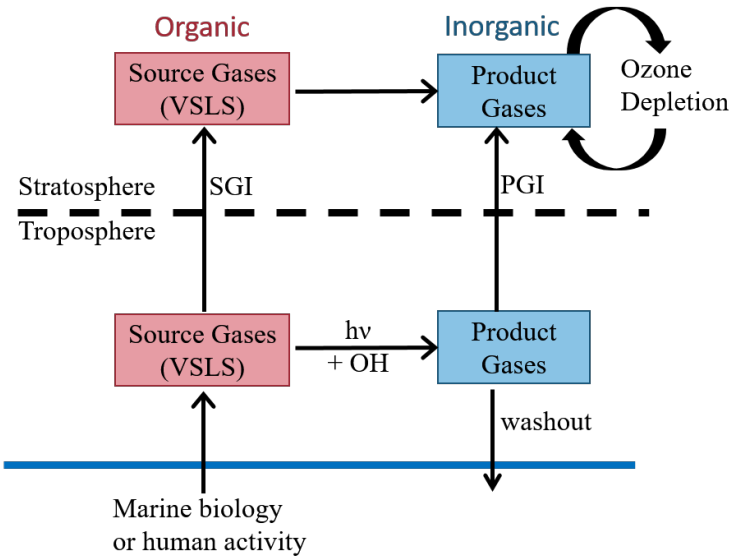

Figure 1-3. Schematic representation of processes affecting the stratospheric supply of halogens from VSLS. The source gases are organic VSLS emitted by either marine biology or human activity. VSLS form inorganic product gases either through photolysis or reaction with a hydroxyl radical. These inorganic product gases can be taken up by aerosols and washed out of the atmosphere. Halogens from VSLS are either supplied to the stratosphere through organic source gas injection (SGI) or inorganic product gas injection (PGI). The species that participate in ozone depletion are inorganic halogen compounds.

Chlorinated VSLS will be discussed in Chapter 5. Currently, chlorinated VSLS constitute a small fraction of the stratospheric chlorine loading, about 100 ppt, relative

to the contribution of long-lived compounds shown in Figure 1-1a (Carpenter et al., 2014). However, unregulated anthropogenic emissions of chlorinated VSLS have increased within the past decade (Hossaini et al., 2015a). If these emissions continue to increase at observed rates, the chlorinated VSLS could significantly contribute to a delay in the recovery of the ozone layer (Hossaini et al., 2017). A detailed understanding of transport and chemical processing of VSLS is required to accurately assess the impact of future halogenated anthropogenic emissions of VSLS on the ozone layer. Studies of naturally produced VSLS, such as those presented in Chapters 2 through 4, provide a basis for evaluating the impact of anthropogenic VSLS.

This dissertation will primarily focus on brominated VSLS that are produced by marine biology. Unless otherwise noted, the term VSLS will be used to refer to five brominated VSLS, which are $CHBr_3$, CH_2Br_2, CH_2BrCl, $CHBr_2Cl$, and $CHBrCl_2$. These five VSLS are produced by phytoplankton and seaweed and have lifetimes ranging from 17 days to 6 months in the tropical upper troposphere (Carpenter et al., 2014). Recent studies estimate that VSLS supply ~25% of stratospheric bromine (Navarro et al., 2015; Chen et al., 2016; Koenig et al., 2017; Werner et al., 2017; Wales et al., 2018), and their relative contribution will increase as mixing ratios of regulated long-lived bromocarbons decrease to the natural background mixing ratio of methyl bromide (CH_3Br, red dashed line in Figure 1-1b).

Incorporating VSLS into models improves agreement between simulated and measured columns of ozone (Salawitch et al., 2005; Feng et al., 2007; Sinnhuber et al., 2009). Due to their short lifetimes relative to CH_3Br and halons, VSLS increase the supply of Br_y at lower altitudes where ozone loss is most sensitive to bromine

chemistry. Consequently, the influence of VSLS on modeled O_3 is greatest in the lowermost stratosphere (LMS) and in polar spring (Sinnhuber and Meul, 2015; Oman et al., 2016). In the LMS, the inclusion of 6 ppt of Br_y^{VSLS} results in a 5 to 10% reduction in O_3 mixing ratios in the midlatitudes, reaching up to 20% in the Antarctic ozone hole (Sinnhuber and Meul, 2015). Stratospheric aerosols provide surfaces for the heterogeneous processing of reservoir Br_y compounds into active bromine radicals. As a result, the influence of VSLS on stratospheric ozone is more pronounced following volcanic eruptions that deposit sulfate aerosols into the stratosphere (Salawitch et al., 2005).

The inclusion of VSLS also influences modeled projections for the future of the ozone layer. Stratospheric injection of VSLS alters the modeled sensitivity of the ozone layer to both future volcanic eruptions (Klobas et al., 2017) and proposed geoengineering of climate via injection of stratospheric sulfate (Tilmes et al., 2008, 2012). Recent modeling studies have also demonstrated that Br_y^{VSLS} affects the depth, seasonality, and area of simulations of the Antarctic ozone hole (Sinnhuber and Meul, 2015; Oman et al., 2016; Fernandez et al., 2017) as well as the seasonal loss of Arctic ozone (Frieler et al., 2006). However, there is currently disagreement if Br_y^{VSLS} delays the recovery of the ozone layer. One study reports that 5 ppt of Br_y^{VSLS} has the potential to delay the recovery of the ozone layer by a decade (Oman et al., 2016), while another estimates that the same amount of Br_y^{VSLS} does not have a significant impact on the recovery of the ozone layer since VSLS also influenced the natural levels of stratospheric ozone before the formation of the ozone hole (Fernandez et al., 2017).

Finally, accurate calculations of tropospheric abundance of BrO based on satellite measurements of BrO^{VC} require proper representation of the stratospheric injection of brominated VSLS (Salawitch et al., 2010; Theys et al., 2011; Choi et al., 2012). In the troposphere, active bromine compounds alter the tropospheric oxidative capacity. Active bromine compounds decrease tropospheric mixing ratios of ozone, nitrogen oxides, and hydrogen oxides as well as speed up the bioavailability of atmospheric mercury (Simpson et al., 2015). Because satellite records of total column BrO are available for over two decades and cover the entire sunlight portion of the planet, they are vitally useful for studying the sources and distribution of tropospheric BrO (Choi et al., 2018). Furthermore, two satellite retrievals with improved sensitivity to tropospheric BrO are currently being developed, one for a satellite instrument that was launched in 2017 and another for an instrument that is scheduled to launch in 2019 (Veefkind et al., 2012; Zoogman et al., 2017).

1-2. Outline

In Chapter 2, the stratospheric injection of brominated VSLS based on aircraft observations acquired in winter 2014 above the convectively active Tropical Western Pacific is quantified. Overall, Br_y^{VSLS} is determined to be 5.0 ± 2.1 ppt, in excellent agreement with the 5 ± 3 ppt estimate provided in the 2014 WMO Ozone Assessment report, but with lower uncertainty. Measurements of organic bromine compounds, including VSLS, are analyzed using CFC-11 as a reference stratospheric tracer. From this analysis, 2.9 ± 0.6 ppt of bromine enters the stratosphere via organic source gas injection of VSLS. This value is two times the mean bromine content of VSLS measured at the tropical tropopause in regions outside of the Tropical Western Pacific

(Carpenter et al., 2014). A photochemical box model, constrained to aircraft observations, is used to estimate Br_y in air entering the stratosphere from measurements of BrO collected by two instruments. This analysis indicates that 2.1 ± 2.1 ppt of bromine enters the stratosphere via inorganic product gas injection. The work presented in Chapter 2 was published in Wales et al. (2018), and the results will be included in the upcoming 2018 WMO Ozone Assessment report.

In Chapter 3, the representation of brominated VSLS within 14 global models that participated in the Chemistry-Climate Model Initiative is examined. The Chemistry-Climate Model Initiative is a collection of models that have been developed to study ozone depletion, climate change, and tropospheric chemistry as well as the interactions between these three fields. The representation of stratospheric bromine in these models generally lies within the range of our empirical estimate, presented in Chapter 2. Models that include explicit representations of VSLS compare better with bromine observations in the lower stratosphere than models that use scaled mixing ratios of longer-lived CH_3Br as a proxy for VSLS. The work presented in Chapter 3 was published in part in Wales et al. (2018), along with the results of Chapter 2.

Historically, estimates of Br_y^{VSLS} derived from observations of stratospheric BrO are higher than estimates based on aircraft and ship measurements of VSLS (Montzka et al., 2011b). In Chapter 4, the results of Chapter 2 are reconciled with observations of BrO^{VC} collected by satellite and ground-based instruments over Fairbanks, Alaska. The ground-based measurements of BrO^{VC}, collected during spring 2011, are consistently lower than satellite observations. We estimate upper limits for the value of Br_y^{VSLS} by modeling the ratio of BrO to Br_y and assuming the column

measurements of BrO are purely stratospheric. If BrO^{VC} is simulated using parameters recommended by the 2015 Jet Propulsion Laboratory kinetic evaluation (Burkholder et al., 2015), we estimate that VSLS contribute 7.8 ± 2.5 ppt of bromine to the stratosphere based on satellite measurements of BrO^{VC}. This estimate drops to 5.2 ± 1.1 ppt if ground-based measurements of BrO from Fairbanks are used. However, if the model uses alternative kinetic recommendations (Atkinson et al., 2007) for the formation and photolysis of bromine nitrate, the estimate for Br_y^{VSLS} decreases by ~1.5 ppt.

The Western Pacific observations from Chapter 2 suggests that the value of Br_y^{VSLS} is 5.0 ± 2.1 ppt. The ground-based measurements support the central and lower limit of the Western Pacific observations, while the satellite-based observations provide evidence for either the upper limit of the tropical observations or a greater tropospheric loading of BrO. Calculations of the fraction of BrO^{VC} present in the troposphere are most sensitive to the estimated range in the stratospheric loading of VSLS, while the difference between satellite and ground-based retrievals of BrO^{VC} is the second most important source of uncertainty for inferring the tropospheric burden of BrO from measurements of BrO^{VC}.

In Chapter 5, the stratospheric loading of Cl_y over the midlatitudes is evaluated. The results presented in this chapter are preliminary and were prepared in support of ozone regression conducted in collaboration with campus colleagues. Equivalent effective stratospheric chlorine (EESC) is the weighted sum of Cl_y and Br_y, calculated as a function of the mean time a parcel of air has been in the stratosphere (i.e., mean age of air). EESC is commonly used to estimate the propagation of organic ozone depleting substances into the stratosphere and assess the long-term impacts of

halocarbon regulations. Many EESC formulations used in past studies did not consider the stratospheric sources of chlorine and bromine from VSLS (Daniel et al., 2011; Harris et al., 2014). Over midlatitudes the mean age of air is about 3 years and the organic source gases are not fully dissociated. A recent study has proposed an updated method for representing the dissociation of organic source gases using fractional release factors (FRFs) (Engel et al., 2018).

In Chapter 5, we isolate air with a mean age of 3 years using measurements of N_2O. Based on ground and space-based measurements of HCl and $ClONO_2$, the proposed updates to the FRFs (Engel et al., 2018) are shown to improve the representation of Cl_y over the midlatitudes. Additionally, including the source of stratospheric chlorine from VSLS in the EESC calculations leads to an improved simulation of the observed magnitude of HCl and $ClONO_2$ as well as the slow decline of stratospheric Cl_y in recent years. While the new FRFs (Engel et al., 2018) and the inclusion of chlorinated VSLS results in a better simulation of stratospheric chlorine than the old FRFs (Newman et al., 2007) and the neglect of chlorinated VSLS, we cannot definitely rule out the latter combination. Furthermore, as shown by colleagues (manuscript in preparation), trends of total column ozone at midlatitudes collected over the past four decades are simulated more accurately using new FRFs and chlorinated VSLS, which implies a 12 year delay in column ozone returning to 1980 levels compared to the combination of old FRFs and no chlorinated VSLS.

Chapter 2: Stratospheric Injection of Brominated Very Short-Lived Substances Inferred from Aircraft Observations over Western Pacific

2-1. Introduction

Very short-lived substances are compounds that have lifetimes of six months or less due to photochemical loss in the global troposphere. Since compounds with lifetimes less than six months cannot be assumed to be well mixed within the troposphere (Ko and Poulet et al., 2003), the stratospheric input of VSLS is more sensitive to the geographic location of their atmospheric sources than the input of CH_3Br and halons, which have atmospheric lifetimes ranging from 0.8 to 65 years. Thus, emissions of VSLS in regions of active, vigorous convection (such as the Tropical Western Pacific, TWP) have a much larger probability of reaching the tropical tropopause layer (TTL) without being chemically altered than compounds released in other areas (e.g., Aschmann et al., 2009; Hossaini et al., 2013; Fernandez et al., 2014).

In this chapter, the abbreviation VSLS refers solely to brominated very short-lived substances. The VSLS relevant to this study (i.e., $CHBr_3$, CH_2Br_2, CH_2BrCl, $CHBr_2Cl$, and $CHBrCl_2$) are produced by phytoplankton or algae in the upper ocean (e.g., Tokarczyk and Moore, 1994; Carpenter and Liss, 2000; Quack and Wallace, 2003). The bromine contained in VSLS can reach the stratosphere either via source gas injection (SGI) or product gas injection (PGI). If the VSLS reach the stratosphere in the original organic form (termed CBr_y), this is considered SGI. Alternatively, if the VSLS are oxidized in the troposphere, the constituent bromine atoms rapidly produce inorganic bromine compounds (termed Br_y). If the tropospheric Br_y product gases reach the stratosphere, this is termed PGI. Consequently, SGI and PGI are sensitive to the

strength of convection relative to the lifetime of the VSLS as well as the partitioning of product gases into soluble compounds that are susceptible to both washout and heterogeneous recycling (Sinnhuber and Folkins, 2006; Hossaini et al., 2010; Liang et al., 2010, 2014; Aschmann et al., 2011; Schofield et al., 2011; Tegtmeier et al., 2012; Fernandez et al., 2014).

Prior estimates of the contribution of VSLS to stratospheric bromine are summarized in the most recent World Meteorological Organization Ozone Assessment (WMO 2014; Carpenter and Reimann et al., 2014). The total contribution of VSLS to stratospheric bromine (i.e., SGI + PGI, denoted Br_y^{VSLS}) was assessed to be 5 ± 3 parts per trillion by volume (ppt). The best estimate for SGI of VSLS (SGI^{VSLS}) presented in WMO 2014 is 1.4 ppt, with a range of 0.7 to 3.4 ppt, based on measurements of VSLS at the average tropical tropopause height of 17 km (e.g., Schauffler et al., 1999; Laube et al., 2008; Brinckmann et al., 2012). Observations of Br_y compounds at the tropical tropopause are sparse (Dorf et al., 2008; Werner et al., 2017). As a result, PGI has previously been estimated to be 1.1 to 4.3 ppt based on a range of global model simulations considering the chemical processing of VSLS released by oceanic emissions (Liang et al., 2010, 2014; Hossaini et al., 2012b; Aschmann and Sinnhuber, 2013). The WMO 2014 estimate for PGI is consistent with the abundance of Br_y reported around 17 km in the tropics by Dorf et al. (2008) as well as the range of Br_y mixing ratios at the base of the TTL and above the cold point tropopause reported by Werner et al. (2017). The combined observed SGI^{VSLS} and modeled PGI value generally agrees with estimates of Br_y^{VSLS} that are based on analysis of slant column measurements of BrO in the middle to upper stratosphere (e.g., Dorf et al., 2008;

Parrella et al., 2013; Schofield et al., 2004). However, there are significant uncertainties concerning the modeled estimates of PGI (e.g., Liang et al., 2014; Sinnhuber & Folkins, 2006; Tegtmeier et al., 2012) as well as the inference of Br_y from measurements of BrO for photochemically aged stratospheric air (Sioris et al., 2006; Kreycy et al., 2013).

In this study we use measurements of organic source gases and BrO, collected in the TTL and lower stratosphere of the TWP, to quantify both SGI^{VSLS} and PGI. The TWP, particularly during boreal winter, is a region of active convection and one of the most important pathways for compounds with short tropospheric lifetimes to reach the stratosphere (Levine et al., 2007; Aschmann et al., 2009; Schofield et al., 2011; Bergman et al., 2012). Consequently, the TWP and nearby Southeast Asia have been regions where a number of ground and ship-based campaigns have been conducted to study oceanic emissions of VSLS (Brinckmann et al., 2012; Mohd Nadzir et al., 2014; Robinson et al., 2014). Additionally, aircraft campaigns observed mixing ratios of VSLS in Southeast Asia that were slightly elevated with respect to measurements collected in the rest of the tropics (Sala et al., 2014; Wisher et al., 2014). However, past campaigns in the TWP did not sample the TTL or the lower stratosphere. Strong convection and potentially suppressed mixing ratios of OH (Rex et al., 2014) could enable efficient transport of VSLS to the TTL. Due to uncertainties in the removal of product gases (Sinnhuber and Folkins, 2006; Tegtmeier et al., 2012; Liang et al., 2014) as well as the transport of source gases within the TTL, direct observations of VSLS and their product gases within air entering the stratosphere are required to better constrain SGI^{VSLS} and PGI.

In the winter of 2014, three aircraft campaigns based in Guam (13.5°N, 144.8°E) extensively sampled the TWP at different heights, including the TTL and lower stratosphere. Our study is based on analysis of data collected during the National Aeronautics and Space Administration (NASA) Airborne Tropical TRopopause EXperiment (ATTREX; Jensen et al., 2017) and the National Science Foundation (NSF) CONvective TRansport of Active Species in the Tropics (CONTRAST; Pan et al., 2017) campaigns. The ATTREX campaign sampled air masses up to 20 km, while CONTRAST included measurements up to 15 km. A third campaign, Coordinated Airborne Studies in the Tropics (CAST; Harris et al., 2017), provided measurements of VSLS (Andrews et al., 2016) and BrO (Le Breton et al., 2017) from the marine boundary layer up to 8 km over the TWP. Since our emphasis is on analysis of observations within and above the TTL, including the lower stratosphere, data from CAST are not shown.

We rely on measurements of CH_3Br, halons, and a suite of organic VSLS provided by the Whole Air Sampler (WAS) instruments (Navarro et al., 2015) during both ATTREX and CONTRAST. We also utilize measurements of BrO obtained by two instruments during CONTRAST: in situ observations from a Chemical Ionization Mass Spectrometer (CIMS; Chen et al., 2016) and remote observations from an Airborne Multi AXis Differential Optical Absorption Spectroscopy (AMAX-DOAS) instrument (Koenig et al., 2017). A limb-scanning mini-Differential Optical Absorption Spectroscopy (mini-DOAS) instrument measured BrO during ATTREX (Stutz et al., 2017; Werner et al., 2017). However, at the time of writing, observations of BrO from the mini-DOAS for the winter 2014 phase of ATTREX are not available.

Our study builds upon prior analyses of ATTREX and CONTRAST data. Navarro et al. (2015) presented an estimate of SGI^{VSLS} based on WAS observations of CBr_y compounds acquired during ATTREX and PGI based solely on a model estimate of gas phase Br_y. Both Chen et al. (2016) and Koenig et al. (2017) estimated PGI using observations of BrO at the base of the stratosphere acquired during CONTRAST, but did not incorporate measurements of CBr_y. In this study, we use empirical bromocarbon-tracer relations to combine all three sets of measurements (i.e., WAS organics plus CIMS and AMAX-DOAS BrO) to develop comprehensive, observation-based estimates of SGI^{VSLS}, PGI, and overall Br_y^{VSLS}. Since our study examines measurements obtained within the lower stratosphere and includes a method for quantifying the contribution to BrO from the stratospheric decomposition of CBr_y source gases, our value of PGI is likely more robust than prior estimates because a larger ensemble of air masses is represented. We have made no attempt to quantify the amount of PGI that results from the oxidation of VSLS versus other sources, such as sea-salt aerosol. We refer the interested reader to Koenig et al. (2017) for analysis concerning the possible contributions of sea-salt aerosol as well as stratospheric injection of brominated particles to PGI.

2-2. Observation and Model Descriptions

2-2.1. CONTRAST and ATTREX Campaigns

Observations from the CONTRAST and ATTREX campaigns provide a comprehensive suite of chemical and physical measurements of air entering the stratosphere from the TWP. During the CONTRAST campaign, the Gulfstream V (GV) High-performance Instrument Airborne Platform for Environmental Research

(HIAPER) payload collected measurements from the marine boundary layer up to 15 km (Pan et al., 2017), and during the ATTREX campaign the NASA Global Hawk (GH) sampled air masses primarily between 14 and 20 km (Jensen et al., 2017). The Guam-based flights of CONTRAST occurred between 17 January 2014 and 24 February 2014, whereas the Guam-based phase of ATTREX took place between 12 February 2014 and 12 March 2014.

Only two CONTRAST research flights (RF), RF06 (24 January 2014) and RF15 (24 February 2014), reached the stratosphere. Consequently, data collected during RF06 and RF15 are the primary focus of this study. The GV flew north of Guam into the extratropical lowermost stratosphere (LMS) on both flights, as shown in Figure 2-1. Figures 2-1b and 2-1c also include a cross section of potential temperature, the pressure of the thermal tropopause (black dashed lines), as well as the 2 potential vorticity unit (PVU = 10^{-6} K m^{-2} kg^{-1} s^{-1}) surface (green dashed lines), for the respective flight dates. These meteorological fields are from the National Center for Environmental Prediction's final (NCEP-FNL) Operational Global Analysis, which is provided every 6 hours, at 1° × 1° (latitude, longitude) resolution. The NCEP-FNL data were interpolated bilinearly in latitude and longitude, and linearly in time and pressure, to the GV flight track. Throughout most of this study, the GV is considered to have entered the stratosphere where it crossed the thermal tropopause, as defined by WMO (World Meteorological Organization, 1957). The sensitivity of major results to the tropopause definition is quantified in section 2.3.3 by also using the 2 PVU surface (i.e., the dynamical tropopause). Data collected on CONTRAST research flights other

than RF06 and RF15 are also used to describe the profile of bromocarbons throughout the TWP troposphere. Tracks of these other flights are shown in Pan et al. (2017).

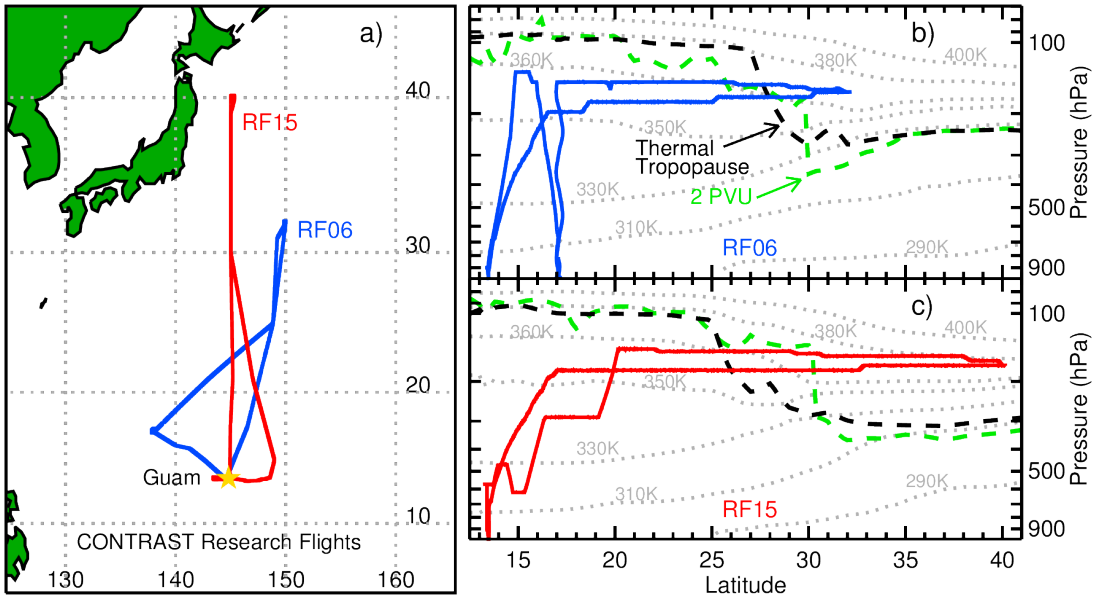

Figure 2-1. (a) Flight paths for the only two CONTRAST research flights that reached the stratosphere, RF06 and RF15. These flights were based out of Guam, indicated with a yellow star. (b) Average of the profiles of potential temperature, the 2 PVU surface, and tropopause pressure from NCEP-FNL sampled along the RF06 (24 January 2014) flight track. (c) Same as panel (b), for RF15 (24 February 2014).

Measurements from the seven ATTREX flights (transit to Guam, RF01 to RF06) that sampled the stratosphere above the TWP are used. Flight tracks are shown in Figure 2-2. Here we only use ATTREX measurements of the nine organic compounds described in section 2.1.1 that were acquired within the TWP. We define the TWP as between latitudes of 20°S to 20°N and longitudes of 120°E to 165°E. Flight segments within the TWP are shown using blue. Figure 2b shows the GH track along with cross sections of NCEP-FNL meteorological fields for a typical ATTREX flight, RF04, which took place on 6 March 2014. In all flights, the GH provided extensive sampling within the tropical stratosphere by traveling vertically in the tropics to collect measurements above the tropical tropopause. Conversely, during CONTRAST the GV

sampled the extratropical stratosphere by flying horizontally across the subtropical jet (Figure 2-1).

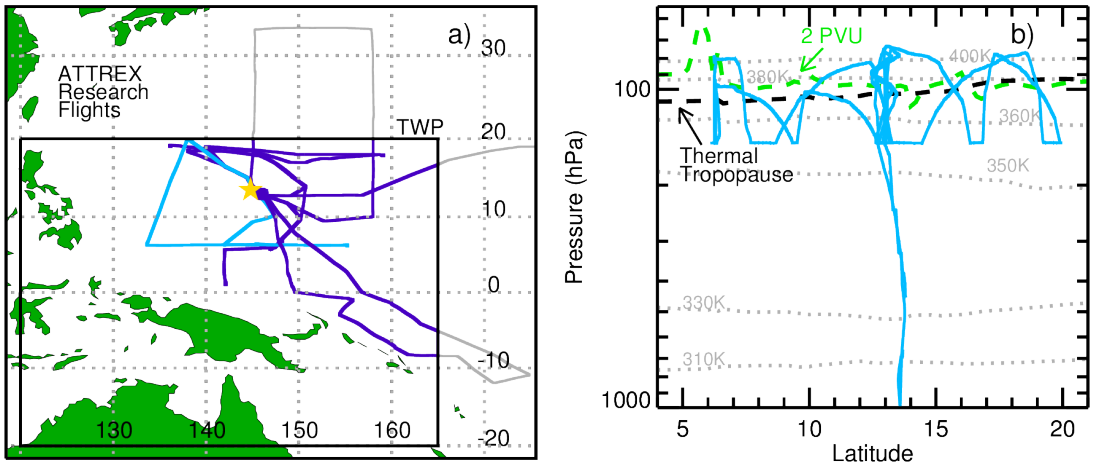

Figure 2-2. (a) Flight paths of ATTREX 2014 research flights based out of Guam (yellow star). Flight tracks within the TWP (black box) are shown as blue and outside of the TWP as grey. A specific ATTREX flight, RF04, is highlighted in light blue. (b) Average of the profiles of potential temperature, the 2 PVU surface, and tropopause pressure from NCEP-FNL sampled along the RF04 (06 March 2014) flight track.

2-2.2. Aircraft Observations

The University of Miami Whole Air Sampler (WAS) instruments collected measurements of trace gases, including CFC-11 (CCl_3F) and bromocarbons during both ATTREX and CONTRAST (Navarro et al., 2015; Andrews et al., 2016). During the CONTRAST campaign the WAS configuration is referred to as the Advanced WAS (AWAS), while during the ATTREX campaign the WAS configuration is the GH WAS (GWAS). The WAS instruments collected air samples in canisters that were later analyzed using gas chromatography/mass spectrometry (GC/MS). Differences between inlet and canister systems onboard the two aircrafts are described in Andrews et al. (2016). Both sets of measurements were calibrated using the method described by Schauffler et al. (1999) and analyzed using the same GC/MS system. Our study focuses on WAS measurements of five VSLS ($CHBr_3$, CH_2Br_2, CH_2BrCl, $CHBr_2Cl$, and

$CHBrCl_2$), three longer-lived bromocarbons [CH_3Br, halon-1211 ($CBrClF_2$), and halon-2402 ($C_2Br_2F_4$)], and CFC-11. The WAS uncertainty and limit of detection for these nine compounds is given in Table A2-1 of the supporting information. Overall, measurements and calibrations of VSLS collected by AWAS agree well with other instruments during CONTRAST and CAST (Andrews et al., 2016).

Halon-1301 ($CBrF_3$) was not measured during CONTRAST and ATTREX by any instrument. Therefore, computed values of halon-1301 as a function of CFC-11 from the CAM-chem-SD global model (described in section 2.2.1.2) are used to provide complete representation of all important organic bromine sources. Uncertainty in WAS measurements of these compounds (plus the use of modeled halon-1301 from CAM-chem-SD) are minor factors in the overall uncertainty of our scientific conclusions. Additionally, since halon-1301 is stable within the troposphere, we expect mixing ratios at the base of the stratosphere to be similar to surface observations (Prinn et al., 2000), and there is close agreement between surface WMO measurements and CAM-chem-SD simulations (see section 2.3.1.2).

Measurements of CFC-11 acquired by the AWAS instrument aboard the CONTRAST GV are shown in Figure 2-3, for the segments of RF06 and RF15 that sampled the stratosphere. The dashed vertical lines denote crossings of the thermal tropopause. During RF06, the aircraft sampled stratospheric air only where potential temperature was below 380 K (Figure 2-1b), which means air masses could have entered the stratosphere through recent, isentropic transport from the tropical troposphere (Holton et al., 1995). Observed CFC-11 reached a minimum of 227 ppt, only slightly lower than the mean value of 233 ppt observed between 16.5 and 17.5 km

in the TWP. During RF15, the aircraft reached air parcels with a potential temperature just above 380 K, indicative of the stratospheric overworld. Minimum CFC-11 was 188 ppt, demonstrating much deeper penetration of the stratosphere and a more photochemically aged chemical composition than sampled during RF06.

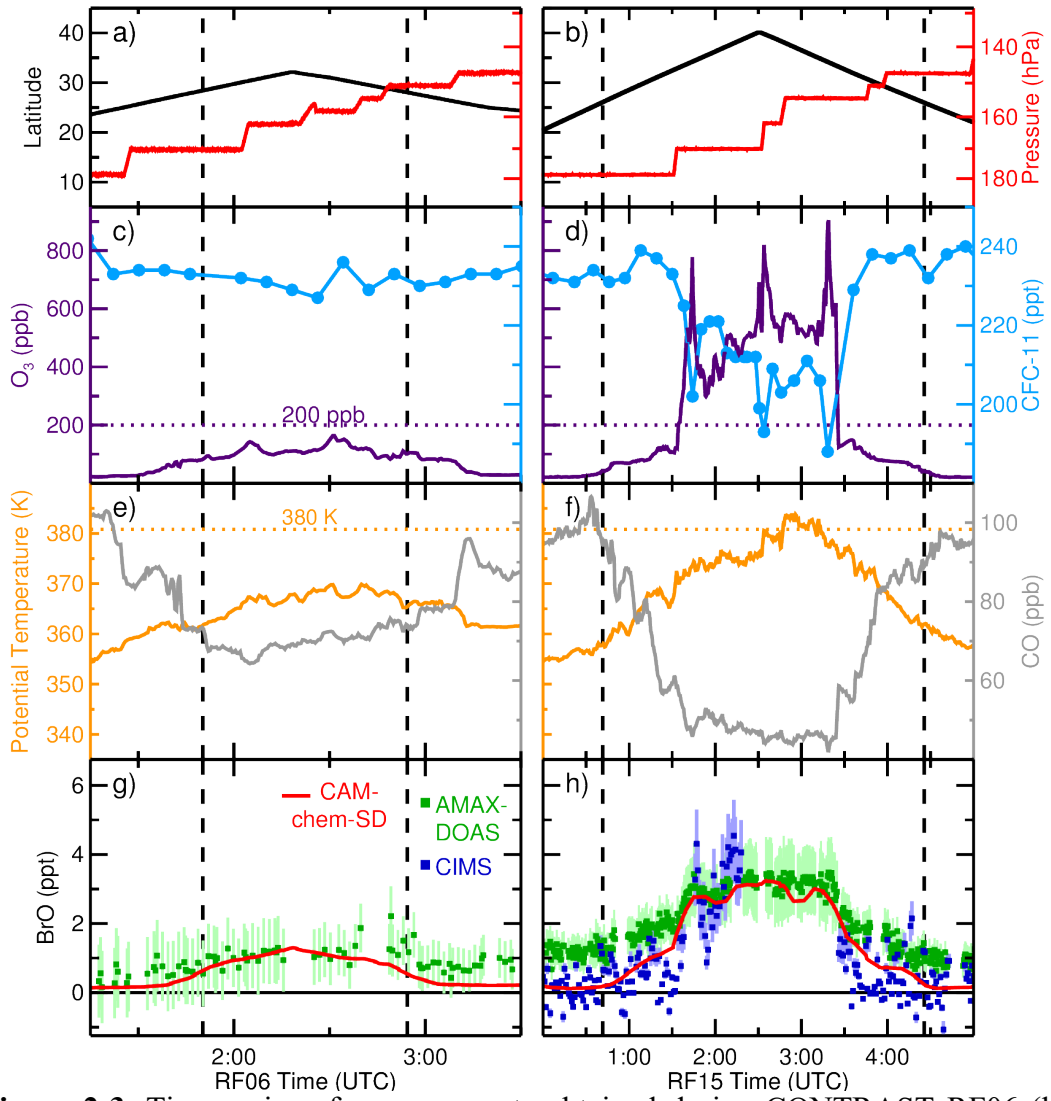

Figure 2-3. Time series of measurements obtained during CONTRAST RF06 (left panels) and RF15 (right panels). The black dashed vertical lines indicate when the plane crossed the NCEP-FNL thermal tropopause. (a and b) The Gulfstream V (GV) aircraft latitude (black) and pressure (red), (c and d) chemiluminescence O_3 (purple) and AWAS CFC-11 (blue), (e and f) potential temperature (orange) and observed CO (grey), and (g and h) AMAX-DOAS (green) and CIMS (blue) observed BrO and CAM-chem-SD (red) modeled BrO are shown. Light green and blue bars indicate the reported

1σ total uncertainty in AMAX-DOAS and CIMS BrO, respectively. CIMS BrO is only available for RF15 when mixing ratios of O_3 are below 480 ppb.

While many other chemical and physical measurements acquired by the GV HIAPER payload during RF06 and RF15 are used in our study, the time series central to our analysis are shown in Figure 2-3. Previous CONTRAST bromine studies (Chen et al., 2016; Koenig et al., 2017) have used the relation between mixing ratios of O_3, CO, and H_2O collected during RF15 to chemically define both the stratosphere as well as a transition layer, where there is a mixture of tropospheric and stratospheric air. While our study primarily uses the thermal tropopause, we also make use of a chemical tropopause (described below) to facilitate comparison to these two studies.

Measurements of O_3 and CO are shown in Figure 2-3. During RF06, chemiluminescence measurements of O_3 (Ridley and Grahek, 1990) peaked at 164 ppb, consistent with the indication that the plane was in the LMS based on potential temperature. For the portion of RF06 where the GV was above the thermal tropopause (between black dashed lines in Figure 2-3e), observations of CO, provided by an AeroLaser vacuum ultraviolet fluorescence instrument (Gerbig et al., 1999), were considerably lower than observed in the troposphere. Conversely, O_3 peaked at 904 ppb on RF15, which was the deepest penetration of the stratosphere for the Guam-based flights of CONTRAST. The extremely low levels of CO observed in the middle portion of RF15 are again consistent with deep penetration of the stratosphere. During both flights, minimum mixing ratios of H_2O (not shown) measured using an open-path laser hygrometer (Zondlo et al., 2010) were around 3 ppm, characteristic of dry stratospheric air.

Koenig et al. (2017) distinguish air for which O_3 is greater than 200 ppb along RF15 as the chemical stratosphere, which provides a comparable view of RF15 to the discussion in Chen et al. (2016). We also use a 200 ppb boundary because this threshold marks a sharp rise in O_3 and a leveling off of the mixing ratio of CO. The two distinct relations between CO and O_3 that occur on RF15, above and below where O_3 is about 200 ppb, are indicative of the chemically-defined stratosphere and extratropical transition layer (i.e., Pan et al., 2004, 2007; Gettelman et al., 2011).

A key component of our study is the measurement of BrO by two instruments aboard the GV during CONTRAST. The Georgia Institute of Technology CIMS instrument (Huey, 2007; Liao et al., 2011) measured BrO during CONTRAST, as described by Chen et al. (2016). For RF01 through RF08, the use of a Br_2 calibration gas interfered with these measurements, while for RF09 to RF16, a Cl_2 calibration gas that posed no interference was used. As a result, CIMS observations of BrO were reported for RF15 but not RF06. Additionally, CIMS BrO was not reported where O_3 is greater than 480 ppb, due to a possible instrumental interference. Our study uses CIMS 1 min measurements of BrO acquired during RF15, which have a 1σ total measurement uncertainty of 11.5% (blue points with error bars, Figure 2-3h). For stratospheric air masses where O_3 is below 200 ppb, CIMS BrO was frequently near or below the 0.6 ppt limit of detection (Chen et al., 2016). The CIMS instrument also reported a measurement of HOBr + Br_2, but we do not consider the observation of HOBr + Br_2 in our estimates of PGI, because data for this quantity are not available where O_3 mixing ratios are above 200 ppb.

The University of Colorado AMAX-DOAS instrument (Baidar et al., 2013; Volkamer et al., 2015; Dix et al., 2016) measured the differential slant column density (dSCD) of BrO and NO_2 horizontally, ahead of the GV. The retrieval of dSCD and the conversion to mixing ratio for BrO and NO_2 are described by Koenig et al. (2017). The AMAX-DOAS measurements of BrO and NO_2 mixing ratios are reported every 30 s, as shown in Figure 2-3 for BrO. The total measurement uncertainty for BrO and NO_2 is the root sum of square combination of the dSCD fitting error and the 30% uncertainty in the volume mixing ratio conversion (Dix et al., 2016). The total error for AMAX-DOAS BrO is shown by the green errors bars in Figure 3. Throughout the stratospheric portions of RF06 and RF15, the AMAX-DOAS measurement of BrO is well above the 0.4 ppt limit of detection.

Since the AMAX-DOAS instrument measures ahead of the plane, the measurements of BrO and NO_2 must be shifted in time to properly relate to the in situ observations. In theory, this shift depends on mean scattering distance, wind speed, and wind direction (Koenig et al., 2017). In practice, the sharp gradients in the mixing ratios of O_3 and NO_2 encountered at the boundaries of the chemical stratosphere during RF15 provide another means to temporally align the remote and in situ observations (Figure 2-4). We have applied a 1.8 min delay to the AMAX-DOAS observations shown in Figure 2-3g and 2-3h based on these gradients. To determine this delay, correlation coefficients between in situ chemiluminescence O_3 and AMAX-DOAS NO_2 were calculated between 1:00 and 2:00 UTC as well as between 3:00 and 4:00 UTC when the GV was entering and leaving the stratosphere, respectively. In these two time periods, sharp increases in O_3 were observed. Correlation coefficients between O_3 and

NO_2 were calculated with a delay between 0 and 6 min applied to AMAX-DOAS NO_2 (Figure 2-4). In general, shorter delays provided the best correlations between 3:00 and 4:00 UTC while longer delays provide the best correlations between 1:00 and 2:00 UTC. A 1.8 min delay was determined to provide the highest overall correlation between the time periods (i.e. where the calculated correlations between the two time periods intersected).

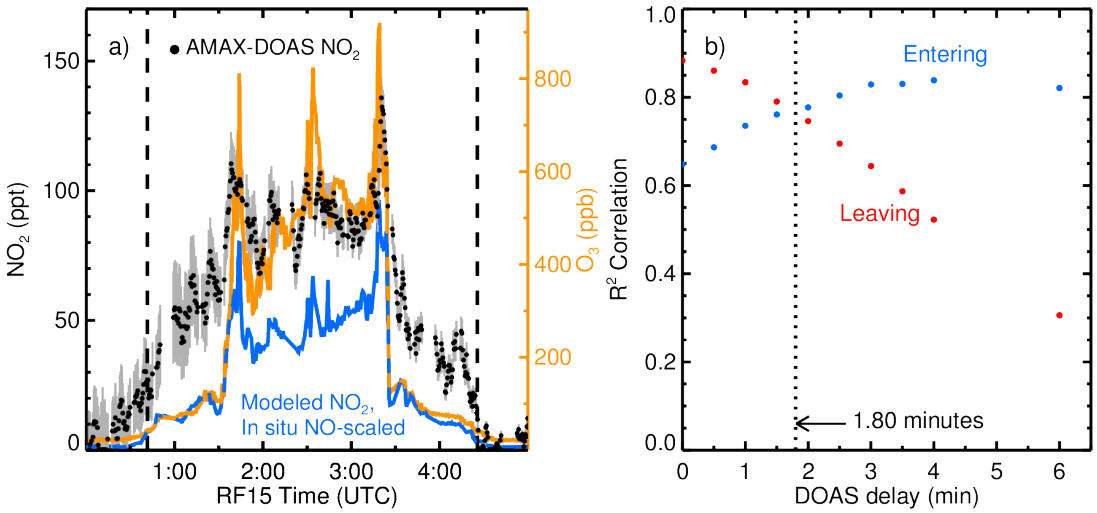

Figure 2-4. Time series and correlations of remote AMAX-DOAS NO_2 and in situ chemiluminescence O_3 measurements during RF15. (a) AMAX-DOAS NO_2, with a 1.8 minute delay applied, are shown as points in black. Grey bars are the 1σ reported total measurement uncertainty. Modeled NO_2, where NO_y has been scaled to match chemiluminescence NO, is shown in blue. Chemiluminescence O_3 is shown in orange. (b) Blue points are the correlation (R^2) between AMAX-DOAS NO_2 and chemiluminescence O_3 between 1:00 and 2:00 UTC, as the GV is entering the stratosphere, with increasing time delays applied to the AMAX-DOAS data. Red points are the correlation between 3:00 and 4:00 UTC, as the GV is leaving the stratosphere. The black dotted line in panel (b) represents the 1.8 minute delay applied to all AMAX-DOAS data.

The measurements of BrO from AMAX-DOAS exhibit a broad peak value of about 1 ppt for RF06 (Figure 2-3g). Measurements of BrO from AMAX-DOAS and CIMS peak around 3.5 and 4.5 ppt, respectively, for RF15 (Figure 2-3h). The largest consistent offsets between the two observations of BrO for RF15 occur on the approach

and exit from the stratosphere (i.e., in the upper troposphere) and in the region of the LMS where O_3 is below 200 ppb.

2-2.3. CAM-chem-SD

Simulations of the Community Atmosphere Model version 4 with interactive chemistry and specified dynamics (CAM-chem-SD; Tilmes et al., 2015) were prepared in support of the CONTRAST (Pan et al., 2017) and ATTREX (Jensen et al., 2017) campaigns. Dynamics were specified based on meteorological fields from the NASA Goddard Earth Observing System Model, version 5 (GEOS-5; Molod et al., 2012). Model output was prepared on a 0.94° latitude by 1.25° longitude resolution with 56 vertical levels and a 30 s temporal resolution. CAM-chem-SD simulations have been used for flight planning of both campaigns as well as post-mission data analysis (Navarro et al., 2015; Anderson et al., 2016; Nicely et al., 2016; Koenig et al., 2017; Navarro et al., 2017).

We use output from CAM-chem-SD from a simulation that includes a detailed representation of the chemistry of bromine (Fernandez et al., 2014) and iodine (Saiz-Lopez et al., 2014) compounds, including VSLS and longer-lived bromine and chlorine sources. All five brominated VSLS measured by the WAS instruments were included in the model. Geographically-resolved time-dependent marine emissions were prescribed based on a parameterization involving satellite measurements of chlorophyll-*a* (Ordóñez et al., 2012). Additional sources of inorganic bromine and chlorine through sea-salt dehalogenation as well as heterogeneous recycling reactions occurring on upper tropospheric aerosols were also considered (Fernandez et al., 2014).

Figure 2-3 includes time series of BrO found using CAM-chem-SD, interpolated in time and location to the GV flight tracks during CONTRAST RF06 and RF15. The BrO mixing ratios from CAM-chem-SD exhibit close agreement with the AMAX-DOAS retrieval when the GV is above the thermal tropopause during RF06 and within the chemical stratosphere (O_3 > 200 ppb) during RF15. The agreement with CIMS BrO for the chemical stratosphere portion of RF15 is also very good, although there is more variability in the CIMS measurement of BrO than the AMAX-DOAS data. Sharp gradients within the chemical stratosphere are also present in the in situ measurements of O_3 and CFC-11 (Figure 2-3d). Since AMAX-DOAS is a remote sensing instrument that measures ahead as well as in a narrow band vertically above and below the aircraft, it is possible that AMAX-DOAS observations are not able to capture the gradients in BrO observed by CIMS. However, the AMAX-DOAS observations of NO_2 do reflect the sharp gradients indicated by observations of O_3 (Figure 2-4a), and the CIMS measurements have known interferences at high mixing ratios of O_3 (Chen et al., 2016)**.** As a result, in lieu of a third observation of BrO, we use measurements from both instruments in a statistical fashion to arrive at a best estimate for Br_y^{VSLS} and PGI.

For the region of the LMS where O_3 < 200 ppb, the mixing ratio of BrO from CAM-chem-SD falls between the AMAX-DOAS and CIMS observations. Within this region, the CIMS observations are close or below the 0.6 ppt lower limit of detection, causing significant variability in the measurements of BrO. Additionally, Koenig et al. (2017) discuss potential reasons for the BrO difference between CAM-chem-SD and AMAX-DOAS where O_3 < 200 ppb, including uncertainties in heterogeneous

reaction chemistry and an additional source of Br_y from sea-salt aerosols. Difference in the two observations of BrO for this region of the LMS as well as possible shortcomings in modeled BrO supports our use of both measurements of BrO for our baseline determination of Br_y^{VSLS} and PGI in section 2.3.2.

2-2.4. Box Model

A photochemical steady state box model (Salawitch et al., 2005, 2010; Sioris et al., 2006; Choi et al., 2012) was used to infer gas phase Br_y from observed BrO during RF06 and RF15. The box model includes 37 chemical species and uses rate constants and absorption cross sections from the NASA Jet Propulsion Laboratory 2015 (JPL 2015) kinetic compendium (Burkholder et al., 2015) for a complete set of gas phase and heterogeneous chemical reactions known to affect stratospheric BrO. Photolysis frequencies and rate constants were calculated at the location of each AMAX-DOAS and CIMS measurement of BrO for a full diel cycle (at the latitude and pressure of the observation) in 15 min intervals. The partitioning of all species within the Br_y family was found assuming photochemical steady state over the diel cycle. The modeled BrO/Br_y ratio for the local solar time of each measurement of BrO was then used to infer Br_y along the tracks of RF06 and RF15. Our analysis of Br_y inferred from BrO is restricted to measurements obtained in the stratosphere, as defined by either the thermal or dynamical tropopause.

Table 2-1. The GV HIAPER measurements, collected during CONTRAST RF06 and RF15, used to constrain the steady-state box model.

Instrument	Measurement	Reference
Airborne Multiaxis DOAS (AMAX-DOAS)	NO_2 (NO_y)	Koenig et al. (2017)
Advanced Whole Air Sampler (AWAS)	CFC-11 (Cl_y)	Schauffler et al. (2003)
Chemiluminescence	O_3	Ridley & Grahek (1990)
HIAPER Airborne Radiation Package (HARP)	$J(NO_2)$ and $J(O_3 \rightarrow O(^1D))$	Shetter & Müller (1999)
Picarro	CH_4	Crosson (2008)
Open Path Hygrometer	H_2O	Zondlo et al. (2010)
Ultra-High Sensitivity Aerosol Spectrometer (UHSAS)	Aerosol surface area density	Cai et al. (2008)
AeroLaser vacuum ultraviolet (VUV)	CO	Gerbig et al. (1999)

The box model was constrained to a wide range of GV HIAPER observations, listed in Table 2-1. One minute averages of GV HIAPER measurements of temperature, pressure, O_3, CO, CH_4, and H_2O were used to constrain the box model. Additionally, surface reflectivity in the model was scaled so that the modeled photolysis frequency of NO_2 (J_{NO_2}) matched the observation of J_{NO_2} from the HARP instrument. Similarly, total column O_3 was scaled to force agreement between modeled and measured photolysis frequency of O_3, producing $O(^1D)$, $J_{O_3 \rightarrow O(^1D)}$. All other photolysis frequencies were calculated using the HARP-based estimates of surface reflectivity and total column O_3. The number distribution of particles with diameters between 0.06 and 1 μm was measured using an Ultra-High Sensitivity Aerosol Spectrometer (UHSAS; Cai et al., 2008). Aerosol surface area density (SAD) was calculated from UHSAS

measurements assuming spherical sulfate particles. Due to variability in the aerosol SAD calculated from UHSAS measurements, the box model was constrained to the 5 min running mean of aerosol SAD. We treat all aerosols as sulfate, since the temperature was well above the frost point during all stratospheric observations. We have also specified inorganic chlorine (Cl_y) along the GV tracks of RF06 and RF15 using AWAS measurements of CFC-11, by computing the relation between CFC-11 and Cl_y within CAM-chem-SD for the latitudes and longitudes of both flights. Based on our analysis, presented in section 2.3.2, this estimate introduces only a minor uncertainty in inferred Br_y.

Chemiluminescence measurements of both NO and NO_2 were acquired during CONTRAST. However, this measurement of NO_2 is believed to have been influenced by an unknown amount of thermally decomposed nitrogen compounds, which leads to an overestimate in the upper troposphere and stratosphere due to the cold conditions of ambient air. Since the modeled BrO/Br_y ratio is sensitive to the termolecular reaction between BrO and NO_2 (see section 2.3.2), total nitrogen oxides (NO_y) in the box model have been scaled to match the mixing ratio of NO_2 reported by the AMAX-DOAS instrument. However, the use of chemiluminescence NO rather than AMAX-DOAS NO_2 as a model constraint indicates a lower abundance of NO_2 (Figure 2-4), thereby lowering the amount of Br_y inferred from the observed BrO. As a result, we examine uncertainty in modeled Br_y by also constraining the model to the observed mixing ratio of NO, since the chemiluminescence measurement of NO is unaffected by thermally labile nitrogen compounds due to the design of the instrument. Because NO_2 provides

a more direct constraint for the BrO/Br_y ratio, we use AMAX-DOAS NO_2 in our baseline simulations.

The value of Br_y consistent with each observation of BrO along RF06 and RF15 was found in an iterative fashion. The box model was initialized with Br_y from CAM-chem-SD. Box-modeled Br_y was then adjusted so that box-modeled BrO matched either AMAX-DOAS or CIMS BrO, to within 2%. Analysis of Br_y found in this manner is limited to the stratosphere (i.e., region between the black vertical dashed lines of Figure 2-3). The effects on computed Br_y of kinetic and measurement uncertainties are considered in section 2.3.2 by applying a 1σ displacement in the JPL 2015 uncertainty for the rates of the eight most important chemical reactions that govern the BrO/Br_y ratio and by adjusting model inputs according to their 1σ uncertainty (Table A2-2).

2-3. Results and Discussion

2-3.1. Organic Bromine

2-3.1.1. Organic Bromine Tracer Relations

Stratospheric tracer-tracer relations were developed using simultaneous WAS measurements of bromocarbons and CFC-11. The use of a stratospheric tracer, such as CFC-11, allows bromocarbons to be analyzed as a function of photochemical aging in the stratosphere (Wamsley et al., 1998) and provides a convenient means for comparing field measurements with the output of global models (e.g., Salawitch et al., 2005, 2010; Kovalenko et al., 2007). Our study uses measurements of CFC-11 and eight bromocarbons to estimate how much Br_y should have formed as a result of the stratospheric decay of both VSLS and longer-lived bromocarbons.

Our procedure for calculating the tracer-tracer relations follows Wamsley et al. (1998). The decay of a long-lived bromocarbon, denoted as (X), in relation to decay of CFC-11 can be represented as

$$(X) = (X)_o \left[\frac{(CFC\text{-}11)}{(CFC\text{-}11)_o}\right]^{\frac{1}{d}} \quad (2\text{-}1)$$

where $(X)_o$ and $(CFC\text{-}11)_o$ represent the tropical tropopause mixing ratios. For long-lived compounds, such as halons, the decay parameter d in equation (1) is equal to the ratio of the lifetimes (τ) of the bromocarbon relative to CFC-11 (i.e., $d = \tau_X/\tau_{CFC\text{-}11}$; Plumb & Ko, 1992). However, discrepancies between the observed decay parameter d and the ratio of the lifetimes have been observed for shorter-lived compounds, including CH_3Br (Avallone and Prather, 1997; SPARC, 2013).

Table 2-2 contains fitting parameters used to define tracer-tracer relations central to our analysis. For our primary analysis of aircraft data, we have taken the logarithm of equation (1), which leads to:

$$\ln(X) = \frac{1}{d}\ln\left[\frac{(CFC\text{-}11)}{(CFC\text{-}11)_o}\right] + \ln(X)_o \quad (2\text{-}2)$$

and solved for d and $(X)_o$ using linear least squares analysis of simultaneous measurements of each bromocarbon and CFC-11. The value for $(CFC\text{-}11)_o$ was set to 233 ppt throughout our study, based on the mean of all ATTREX observations of CFC-11 obtained at 17 km altitude (i.e., between 16.5 and 17.5 km) by the GWAS instrument in the TWP. The use of data collected at 17 km to define the abundance of CFC-11 at the base of the stratosphere is also consistent with the approach used in WMO 2014 (Carpenter and Reimann et al., 2014) and other estimates of SGI (i.e., Navarro et al., 2015) because the cold-point tropopause, used to denote the top of the TTL, lies close to 17 km in the tropics. Since many of the bromocarbon compounds have short

tropospheric lifetimes, resulting in large seasonal and geographic gradients, solving for $(X)_o$ using equation (2) is more representative of entry into the global stratosphere than values of $(X)_o$ based on ATTREX measurements at 17 km within the TWP. Comparison of $(X)_o$ from these two methods is given in section 2.3.1.2. For Table 2-2 and throughout, we report values of $(X)_o$ as the mixing ratio multiplied by the bromine atomicity in each compound, since the sum of bromine atoms is used to define SGI. The lifetime of each VSLS at 10 km altitude in the tropics, from Tables 1 to 5 of WMO 2014, is also given for each VSLS.

Table 2-2. Fitting parameters for the stratospheric tracer-tracer relation between bromocarbons and CFC-11 (equation 2-1).

	CBr_y	WMO lifetime[a]	$(X)_o$ (ppt)	d	Source
Long-lived	CH_3Br	26.3 years	7.20 ± 0.21	0.77 ± 0.09	CONTRAST
	$CBrClF_2$ (halon-1211)	41	3.72 ± 0.09	0.66 ± 0.06	CONTRAST
	$CBrF_3$ (halon-1301)	73.5	3.24 ± 0.06	1.265 ± 0.001	CAM-chem-SD
	$C_2Br_2F_4$ (halon-2402)	41	0.81 ± 0.03	0.73 ± 0.08	CONTRAST
	SGI^{LL}		15.0 ± 0.2		
VSLS	CH_2Br_2	150 days	1.36 ± 0.42	0.10 ± 0.03	CONTRAST
	$CHBr_3$	17	1.01 ± 0.47	0.05 ± 0.01	ATTREX
	$CHBrCl_2$	48	0.24 ± 0.07	0.06 ± 0.01	ATTREX[b]
	$CHBr_2Cl$	28	0.20 ± 0.08	0.06 ± 0.01	ATTREX
	CH_2BrCl	174	0.11 ± 0.03	0.12 ± 0.03	CONTRAST
	SGI^{VSLS}		2.9 ± 0.6		

Note: All mixing ratios are multiplied by the bromine atomicity. The value for $(CFC\text{-}11)_o$ is 233 ppt and is calculated from the mean of ATTREX observations at 17 km in the TWP. The stratospheric lifetime of CFC-11 is 52 years.

[a]The WMO 2014 lifetimes for long-lived compounds are the stratospheric partial lifetimes and for VSLS are the 10 km tropical lifetimes.

[b]For $CHBrCl_2$, $(X)_o$ is the ATTREX TWP mean at 17 km, and d is estimated from observations of $CHBr_2Cl$.

The relations between the two major VSLS (CH_2Br_2 and $CHBr_3$) and CFC-11, observed during CONTRAST and ATTREX, are shown in Figure 2-5. Similar plots for

the minor VSLS (CH_2BrCl, $CHBr_2Cl$, and $CHBrCl_2$) are shown in Figure A2-1, and all fitting parameters calculated using ATTREX observations are given in Table A2-3. Figures 2-5a and 2-5b show data collected in the extratropical stratosphere during RF06 and RF15 of CONTRAST, whereas the Figures 2-5c and 2-5d show observations in the tropical stratosphere during ATTREX. In all cases, data are shown only if the airplane was in the stratosphere, as defined by the thermal tropopause (section 2-2.2).

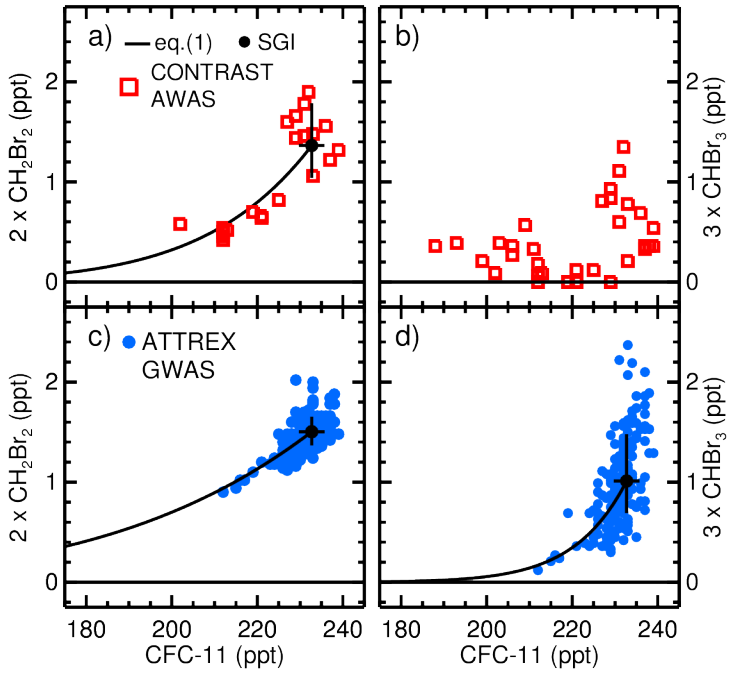

Figure 2-5. Stratospheric observations of VSLS as function of CFC-11. The solid lines are linear fits to the observations found using equation (2-2). The black points are SGI of each compound, also calculated using equation (2-2). The horizontal error bars are the standard deviation the ATTREX measurements of CFC-11 between 16.5 and 17.5 km. The vertical error bars are the uncertainty in the fit where CFC-11 is 233 ppt. (a) CONTRAST AWAS measurements of CH_2Br_2 and CFC-11 collected in the extratropical stratosphere. (b) CONTRAST AWAS measurements of $CHBr_3$ and CFC-11; the short lifetime of $CHBr_3$ combined with presumably rapid horizontal transport of the LMS air masses, sampled during CONTRAST, prevents the calculation of a meaningful fit. (c) ATTREX GWAS observations of CH_2Br_2 and CFC-11 in the TWP; (d) ATTREX GWAS observations of $CHBr_3$ and CFC-11 in the TWP.

The solid lines in Figure 2-5 show the fit to the respective data using equation (1). The black points show the values of $(X)_o$ for the various compounds,

along with the 1σ fitting uncertainty (numerical values in Table 2-2). Observations of CH_2Br_2 and $CHBr_3$ versus CFC-11 during ATTREX in the tropical stratosphere (Figures 4c and 4d) can be represented well using equation (1). The same is true for CONTRAST observations of CH_2Br_2 versus CFC-11 in the extratropical stratosphere (Figure 2-5a). Conversely, CONTRAST observations of $CHBr_3$ versus CFC-11 exhibit considerable scatter, and are not amenable to being fit using equation (2). The difference between the tropical tropospheric lifetimes for CH_2Br_2 and $CHBr_3$, respectively, 150 and 17 days (Table 2-2), provides a likely explanation for this dichotomy.

Compact relations for equation (1) will exist only if the photochemical removal lifetime is long relative to the time scale of mixing (Plumb and Ko, 1992). The ATTREX observations were obtained in a region of the tropical stratosphere characterized by slow ascent ($\theta > 385$ K) and likely isolated from other chemical regimes (e.g., Volk et al., 1996). The CONTRAST measurements, on the other hand, were acquired in the extratropical LMS at potential temperatures between 360 and 385 K, a region that allows for the possibility of rapid horizontal mixing of air parcels with different chemical histories, resulting in a wide range of possible transit times. As discussed above, the decay parameters for CH_3Br and VSLS will not be a direct function of their lifetime (Avallone and Prather, 1997; SPARC, 2013). For CH_3Br and the two VSLS with longer lifetimes (CH_2Br_2 and CH_2BrCl), the observed decline relative to CFC-11 in the extratropical stratosphere can be adequately described using equation (1). As expected, these compounds exhibit more scatter versus CFC-11 than observed for longer-lived halons (Figure A2-2), but a reasonable fit can be achieved.

Since the three shortest-lived VSLS ($CHBr_3$, $CHBr_2Cl$, and $CHBrCl_2$) are more sensitive to local chemical environments, meaningful fits could not be determined for CONTRAST observations of these VSLS in the LMS (Figures 2-5b and A2-1).

Consequently, Table 2-2 contains entries for fitting parameters of five VSLS from a mixture of CONTRAST and ATTREX observations. Together, minor VSLS supply 0.6 ppt to the stratosphere in comparison to $CHBr_3$ and CH_2Br_2, which supply a combined 2.4 ppt. Careful consideration for $CHBrCl_2$ was necessary, because WAS observations were sparse at low mixing ratios of CFC-11 during both CONTRAST and ATTREX. For this species, we used the mean value of $CHBrCl_2$ observed at 17 km (i.e., between 16.5 and 17.5 km) in the TWP during ATTREX to define $(X)_o$. Since the lifetime of $CHBrCl_2$ is closest to the lifetime of $CHBr_2Cl$, the decay parameter from the $CHBr_2Cl$ fit was used.

Finally, Table 2-2 also shows fitting parameters for the four long-lived bromocarbons (Figure A2-2) that have traditionally been considered in studies of stratospheric ozone depletion and recovery. For reference, Table 2-2 also lists the stratospheric lifetimes of these compounds, obtained from Table 1-3 of WMO 2014, originally reported in SPARC (2013). Data acquired in the stratosphere on CONTRAST RF06 and RF15 are used, except for halon-1301, which was not measured during either CONTRAST, ATTREX, or CAST. The fit parameters for halon-1301 are based on analysis of output from CAM-chem-SD along RF06 and RF15 of CONTRAST. The fits conform to prior expectation (Wamsley et al., 1998) and yield a value of 15.0 ± 0.2 ppt for the sum of the four values of $(X)_o$, which means 15.0 ppt of bromine was delivered to the stratosphere by long lived sources in winter 2014. This

estimate is in agreement with the WMO 2014 time series for the delivery of bromine to the stratosphere by these four compounds (Figure 1-1). Finally, the product of the decay parameter for the various halons and the WMO 2014 estimate of 52 years for the stratospheric lifetime for CFC-11 results in computed lifetimes of 34, 66, and 38 years, respectively, for halon-1211, -1301, and -2404. These values are slightly lower than but consistent with the stratospheric partial lifetimes reported by WMO 2014, given in Table 2-2.

2-3.1.2. Source Gas Injection from VSLS (SGI^{VSLS})

An important focus of CONTRAST and ATTREX was the quantification of the stratospheric supply of bromine via both SGI and PGI. Here we used the fits of VSLS as functions of CFC-11 (Table 2-2) to arrive at an estimate for SGI^{VSLS} of 2.9 ± 0.6 ppt. The value of 2.9 ppt is the sum of the five values of $(X)_o$ for VSLS, and the uncertainty of 0.6 ppt is a root sum of squares combination of the fitting uncertainties for the five VSLS. This estimate combines data acquired at the top of the TTL and within the photochemically aged stratosphere in the context of a physically plausible model for the decay of the bromocarbons and mimics the approach of Wamsley et al. (1998). An alternate method to estimate SGI^{VSLS} is to tabulate the bromine content of the five VSLS compounds near 17 km in the tropics, which we quantify below.

Figure 2-6 shows vertical profiles of VSLS in the TWP, and compares these two approaches for estimating SGI^{VSLS}. The square and circle symbols represent the organic bromine content of various VSLS measured during CONTRAST and ATTREX, respectively. The WAS measurements have been averaged within 1 km altitude bins, and the error bars represent the standard deviation about the mean within

each bin. CONTRAST data shown in Figure 2-6 were acquired during 12 flights in the TWP, including portions of RF06 and RF15. The lines show calculations of profiles for these VSLS, averaged for February over the TWP, from CAM-chem-SD (Fernandez et al., 2014; Navarro et al., 2015; section 2.2.1.2). Note that the three minor VSLS have been summed together, for both measured and modeled profiles. Comparatively, the red diamond represents the tracer-based estimate for SGI^{VSLS} of 2.9 ± 0.6 ppt, described above.

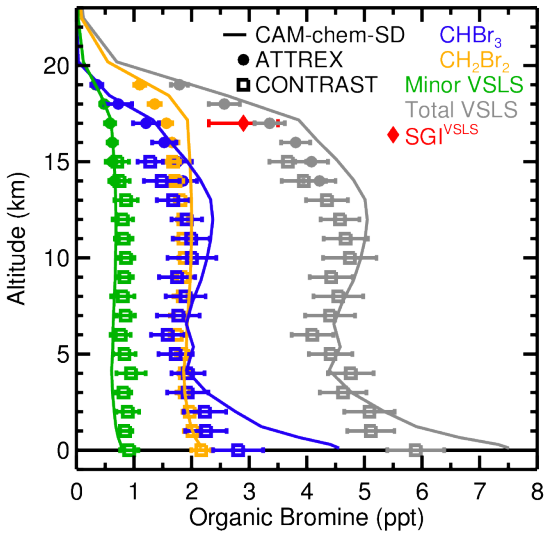

Figure 2-6. Profiles of VSLS in the TWP during winter 2014. Observations have been sorted into 1 km altitude bins, and all quantities represent mixing ratios multiplied by bromine atomicity. Square points are CONTRAST AWAS means, circle points are ATTREX GWAS means, and error bars are the standard deviation of data within each bin (various colors as indicated). The solid lines are average CAM-chem-SD profiles in the TWP. Minor VSLS (green) is the sum of CH_2BrCl, $CHBr_2Cl$, and $CHBrCl_2$, and total VSLS (grey) is the sum of minor VSLS, $CHBr_3$, and CH_2Br_2. The red diamond is SGI^{VSLS} calculated from CFC-11 tracer relations, 2.9 ± 0.6 ppt (Table 2-2).

Overall the observed vertical profiles of VSLS from CONTRAST and ATTREX compare well to modeled profiles from CAM-chem-SD in the TTL. Navarro et al. (2015) showed similarly good comparisons, based on ATTREX observations in the Western and Eastern Pacific. The CAM-chem-SD profile is slightly higher than

observed for CH_2Br_2 above 15 km and for $CHBr_3$ between 11 and 14 km, leading to slightly larger modeled values for CBr_y than observed in TTL (~13 to 17 km). Below 2 km, $CHBr_3$ mixing ratios are higher in CAM-chem-SD than the mean values observed during CONTRAST (Figure 2-6). A similar discrepancy exists between CAM-chem-SD $CHBr_3$ and measurements obtained during CAST (not shown), which sampled altitudes below 8 km in the TWP during winter 2014 (Andrews et al., 2016). Previous evaluations of the Ordóñez et al. (2012) climatology, used by CAM-chem-SD for emissions of VSLS, have identified the potential to overestimate the actual emissions of $CHBr_3$ based on a comparison of model output to ground-based and Southeast Asian aircraft observations (Hossaini et al., 2013, 2016). However, CAM-chem-SD shows very good agreement with ATTREX measurements of $CHBr_3$ sampled at higher altitudes. Vertical profiles of all individual VSLS and longer-lived compounds are shown in Figure A2-3. In this figure, WMO 2014 surface mixing ratios of CH_3Br, halons, and CFC-11 are included (Harris and Weubbles et al., 2014), demonstrating good agreement between CAM-chem-SD tropospheric and WMO 2014 surface values for all compounds.

As noted above, some prior estimates of SGI^{VSLS} have been based on observations near 17 km. For this altitude in the TWP, the bromine content of the five VSLS observed during ATTREX is 3.4 ± 0.3 ppt (Table 2-3). This estimate differs slightly from the value of 3.27 ± 0.47 ppt reported by Navarro et al. (2015), because we have restricted our analysis to GWAS measurements collected within 20°S to 20°N. A comparison to the prior estimates of VSLS at 17 km in the tropics, given in Chapter 1 of WMO 2014, shows that ATTREX observations of CH_2Br_2, CH_2BrCl, and

$CHBr_2Cl$ all lie within the WMO 2014 range (0.7 to 3.4 ppt), albeit on the upper end (Table 3). The ATTREX determination of SGI^{VSLS} in the TWP of 3.4 ± 0.3 ppt is, however, more than a factor of 2 greater than the WMO 2014 best estimate of 1.4 ppt. Furthermore, the ATTREX 17 km mean observations of $CHBr_3$ and $CHBrCl_2$ exceed the upper range from WMO 2014. This difference could be due to our sampling of the biologically and convectively active TWP, since the WMO 2014 average values are based on measurements throughout the tropics. Additionally, the mean and standard deviation of AWAS measurements of VSLS between 10 and 12 km is 4.7 ± 0.6 ppt. This value is slightly higher than but within one standard deviation of previously reported upper tropospheric VSLS of 4.4 ± 0.4 ppt (Sala et al., 2014) and 4.2 ± 0.6 ppt (Wisher et al., 2014) that are based on aircraft observations collected above Southeast Asia. Recently, Fiehn et al. (2018) have emphasized that considerable seasonal and inter-annual variability in SGI^{VSLS} could be expected.

Table 2-3. Mean mixing ratios between 16.5 and 17.5 km from ATTREX and WMO 2014.

VSLS	ATTREX TWP 17 km mean (ppt)	WMO 2014 Tropical 17 km mean (ppt)
CH_2Br_2	1.56 ± 0.10	1.06 (0.6 – 1.72)
$CHBr_3$	1.21 ± 0.23	0.24 (0.00 – 0.93)
$CHBrCl_2$	0.24 ± 0.07	0.06 (0.03 – 0.12)
$CHBr_2Cl$	0.22 ± 0.05	0.04 (0.00 – 0.28)
CH_2BrCl	0.12 ± 0.02	0.07 (0.05 – 0.11)
SGI^{VSLS}	3.4 ± 0.3	1.4 (0.7 – 3.4)

Note: All mixing ratios are multiplied by the bromine atomicity.

The upper limit for the uncertainty in our 2.9 ± 0.6 ppt tracer-based estimate for SGI^{VSLS} (red diamond in Figure 2-6) encompasses the value of SGI^{VSLS} measured at 17 km during ATTREX (3.4 ± 0.3 ppt, grey circle at 17 km in Figure 2-6). Despite the coverage of observations provided by seven flights of the GH during ATTREX, it is

unclear how representative the measurements acquired at 17 km are of the conditions for the entire winter in the TWP. Furthermore, SGI^{VSLS} sampled over the TWP during the biologically and convectively active boreal winter may be high with respect to the tropical average. Due to their short lifetimes, the transport of VSLS is expected to be highly variable in both time and space. For instance, the CONTRAST campaign sampled the TTL in the TWP earlier in the winter season compared to ATTREX (Jensen et al., 2017; Pan et al., 2017). For the overlapping altitude region of these two data sets (i.e., between 14 and 15 km), the CONTRAST observations of the bromine content of VSLS in the TWP are 0.3 ppt lower than measured during ATTREX. This offset is largely due to lower $CHBr_3$ mixing ratios measured during CONTRAST than ATTREX (Figures 5 and S8). Since AWAS and GWAS measurements use the same calibration and GC/MS systems (Andrews et al., 2016), this difference probably indicates that for the conditions sampled during CONTRAST, there was either slightly smaller emissions or less efficient vertical transport of $CHBr_3$ than occurred for the air masses sampled later in winter at 17 km during ATTREX.

We use the tracer-based value for SGI^{VSLS} of 2.9 ± 0.6 ppt in the analysis below. Given the short lifetimes of many VSLS, we place greater emphasis on this estimate of SGI^{VSLS}, since this method inherently includes air parcels with a much greater diversity of convective history than estimates based only on observations near 17 km in the TWP. For instance, the tracer-based estimates of SGI from $CHBr_3$ and CH_2Br_2 (Table 2-2) are both about 0.2 ppt lower than their 17 km means (Table 2-3). The tracer analysis for $CHBr_3$ is based on all stratospheric ATTREX measurements in the TWP, which includes measurements around 17 km as well as more convectively aged air

parcels at higher altitudes. Additionally, the tracer-based estimate for SGI of CH_2Br_2 makes use of data that span a large range of latitudes and provides a more direct representation of the conditions sampled by the instruments that measured BrO, which is used to calculate PGI.

2-3.1.3. Inorganic Bromine from SGI (Br_y^{SGI})

The bromocarbon versus CFC-11 tracer relations, defined in section 2.3.1.1 are used to calculate the expected formation of Br_y following stratospheric decay of VSLS, CH_3Br and halons, which we term Br_y^{SGI}. Figure 2-7 illustrates our approach for estimating the expected rise of Br_y^{SGI} as a function of decay of CFC-11. This estimate of Br_y^{SGI} is an essential component for a comprehensive analysis of the bromine budget for the TWP. Here we combine the estimate of Br_y^{SGI} with a box model analysis of measured BrO to infer PGI from VSLS (section 2.3.2).

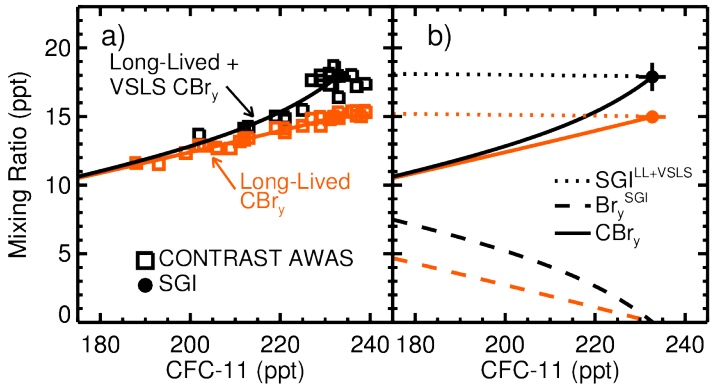

Figure 2-7. Stratospheric tracer relations between bromine and CFC-11 in winter 2014. In both panels, orange is the sum of bromine supplied by only long-lived compounds (CH_3Br and halons), and black is the sum of bromine supplied by long-lived compounds and VSLS. Circle points and error bars are the mean and standard deviation of CBr_y and CFC-11 at the base of the stratosphere (i.e., CFC-11 = 233 ppt). (a) The solid lines are the calculated relation between CBr_y and CFC-11 from CONTRAST and ATTREX observations (Table 2-2). Squares represent the sum of CONTRAST measurements of bromocarbons collected during RF06 and RF15. (b) Br_y^{SGI} (dashed lines) calculated from the difference between CBr_y (solid lines) and $SGI^{LL+VSLS}$ (dotted lines) using equation (4).

Figure 2-7a shows the relation between stratospheric CBr_y (i.e., carbon-bonded bromine) and CFC-11, calculated according to:

$$CBr_y = \sum (X_i)_o \left[\frac{(\text{CFC-11})}{(\text{CFC-11})_o} \right]^{\frac{1}{d_i}} \quad (2\text{-}3)$$

where the summation is performed over all bromocarbons, indicated by *i*. The two lines in Figure 2-7a make use of values of $(X_i)_o$ and d_i given in Table 2-2. Here and throughout, orange is used to represent the stratospheric supply of bromine from only CH_3Br and halons, while black is used to represent the supply from both VSLS and long-lived compounds. The solid lines show the slow decay of the bromocarbons in the LMS, as CFC-11 decreases, represented by equation (2-3). The squares indicate the total organic bromine content as measured by AWAS during CONTRAST, plus the CAM-chem-SD value for halon-1301. In some instances, the measurements from AWAS are incomplete (i.e., the mixing ratio for one or more of the eight AWAS compounds in Table 2-2 is not available). If values for either $CHBrCl_2$ or halon-1211 are missing, we used the fit parameters to estimate the abundance. This allows for more data points on Figure 2-7.

Figure 2-7b illustrates our estimate for the appearance of inorganic bromine upon stratospheric oxidation of the organic sources, following the approach of Wamsley et al. (1998). Assuming that the total bromine content of the stratosphere is present either in organic or inorganic form in the gas phase (i.e., aerosol uptake and washout, within the stratosphere, are inconsequential), then the inorganic bromine (Br_y^{SGI}) provided by the oxidation of organics is represented by:

$$Br_y^{SGI} = SGI^{LL+VSLS} - CBr_y \quad (2\text{-}4)$$

where CBr_y is calculated according to equation (3). In equation (4), $SGI^{LL+VSLS}$ is the total bromine that entered the stratosphere in organic form; that is, $SGI^{LL+VSLS}$ equals the sum of SGI from long-lived compounds (SGI^{LL}) and SGI^{VSLS}.

We assume the value of SGI^{VSLS} measured during CONTRAST and ATTREX campaigns is constant over time. Conversely, it is known that SGI^{LL} varies over time, and the surface mixing ratios of CH_3Br and halons have decreased slightly over the past decade due to the success of the Montreal Protocol (Figure 1-1). In order to represent the slow decay of CH_3Br and halons in the global troposphere, an estimate for the age of stratospheric air is needed. Age of air is the mean time an air parcel takes to travel from the base of the stratosphere to the location of measurement (Hall and Plumb, 1994). Here the N_2O-based estimate for age of air given in Engel et al. (2002) is used, tied to the CFC-11 versus N_2O relation from CAM-chem-SD and AWAS observations of CFC-11. The mean age of air as a function of CFC-11 has been used to adjust SGI^{LL} in Figure 2-7b, such that the values correspond to the time series of CH_3Br and halon surface mixing ratios given in Chapter 5 of WMO 2014 (Harris and Wuebbles et al., 2014). The bromine content of SGI^{LL}, represented by the orange dotted line in Figure 2-7b, increases slightly from 15.0 ppt where CFC-11 is 233 to 15.2 ppt where CFC-11 is 175 ppt, which reflects the slow, gradual decline of long-lived bromocarbons.

Finally, the dashed lines in Figure 2-7b represent the rise in inorganic bromine due to the decay of long-lived bromocarbons as a function of CFC-11 (orange) and the rise in organic bromine due to the decay of all sources that enter the stratosphere with carbon intact (black; Br_y^{SGI}). The curve for Br_y^{SGI} was found using equation (4);

in simple graphical terms, Br_y^{SGI} is the difference between the black dotted and the black solid lines in Figure 2-7b. Similarly, the orange dashed line is the difference between the orange dotted and solid lines.

2-3.2. Product Gas Injection

Here we estimate the supply of bromine to the stratosphere by inorganic species that cross the tropopause. The estimate of PGI given below is unable to distinguish between inorganic bromine produced following the decomposition of VSLS and inorganic bromine from other sources, such as sea-salt aerosols. While theoretically sea-salt aerosols should be most important in the lower portions of the tropical troposphere, a number of recent studies have shown this source can be important at higher altitudes, mainly within regions of active convective such as the TWP (Yang et al., 2005; Fernandez et al., 2014; Long et al., 2014; Wang et al., 2015; Schmidt et al., 2016; Koenig et al., 2017).

Figures 2-8a and 2-8b show the partitioning of gas phase Br_y compounds within our constrained photochemical box model (section 2-2.4) along each of the CONTRAST flight tracks. Figures 2-8c and 2-8d display the time series of gas phase Br_y inferred from observations of BrO reported by AMAX-DOAS (green) and CIMS (blue) for CONTRAST RF06 and RF15. The error bars for Br_y in these panels were calculated by applying the box model BrO/Br_y partitioning to the upper and lower 1σ uncertainty limits of the BrO measurements reported by the two instruments teams. The value of Br_y within CAM-chem-SD, interpolated in space and time to the GV flight tracks, is shown by the red lines. As the GV entered the stratosphere (black vertical dashed lines), Br_y increases as expected. The value of Br_y inferred from AMAX-DOAS

BrO broadly peaked around 3 ppt for RF06, and Br_y inferred from both AMAX-DOAS and CIMS BrO peaks around 6 ppt for RF15. As noted in section 2-2.2, observations of BrO from CIMS are not available for RF06. The rise in Br_y is considerably more pronounced for RF15, reflecting deeper penetration into the stratosphere. The simulation of Br_y from CAM-chem-SD exhibits overall good agreement with Br_y inferred from BrO and related observations during the middle portion of RF15 where the aircraft sampled deeper in the stratosphere, and mixing ratios of O_3 are above 200 ppb.

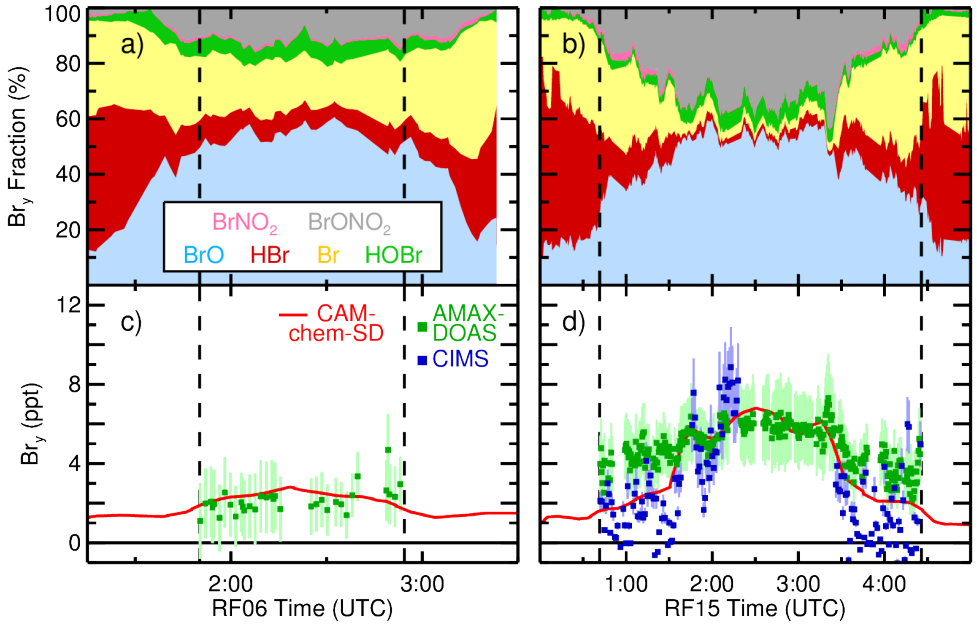

Figure 2-8. Model output and inferred Br_y for CONTRAST RF06 (left) and RF15 (right). In all panels, black vertical dashed lines indicate when the plane crossed the tropopause. (a and b) Br_y partitioning within the box model for the local solar time of aircraft observations. (c and d) Br_y inferred using the box modeled BrO/Br_y ratio as well as AMAX-DOAS (green) and CIMS (blue) BrO observations. Error bars represent BrO measurement uncertainties, multiplied by the modeled Br_y/BrO ratio. Red lines are CAM-chem-SD modeled Br_y interpolated to the respective flight tracks.

The largest difference between Br_y inferred from AMAX-DOAS and CIMS occurs near the edges of the stratosphere (Figure 2-8d). The CAM-chem-SD value for Br_y nearly splits the difference between the estimates based on AMAX-DOAS and

CIMS BrO, similar to the comparison of BrO shown in Figure 2-3h. We base our best estimate of PGI on a statistical analysis of both measurements, since we have no basis for assessing which observationally-based estimate of Br_y is more likely to be correct. Koenig et al. (2017) highlight large variations in the Br_y partitioning obtained with both box and global models in the upper troposphere, outside of the regions used here, particularly where aerosol SAD is below 1×10^{-8} cm^2 cm^{-3}. This suggests that further research regarding transport, recycling, and/or washout of inorganic bromine is still required.

Our estimate of PGI is based on inferred Br_y only within the stratosphere. As the GV aircraft travels deeper into the stratosphere, the BrO/Br_y ratio increases during both RF06 and RF15, due to the declines in atomic Br and HBr, driven by ambient O_3 and heterogeneous processing. This behavior is consistent with the explanation for bromine partitioning described by Fernandez et al. (2014) and Koenig et al. (2017). Within the stratosphere, the contribution of $BrONO_2$ to the Br_y budget increases as the mixing ratio of O_3 exceeds 200 ppb (grey shaded portion of Figure 2-8b) and NO_2 exceeds 50 ppt (Figure 2-4a). As discussed below, Br_y inferred for this flight segment is sensitive to the accuracy of the kinetic information used to define the rates of formation and loss of $BrONO_2$, which currently has considerable uncertainty (Sioris et al., 2006; Kreycy et al., 2013). Most importantly, our estimate of PGI is weighted toward flight segments for which BrO constitutes about half of Br_y.

The relationship between the inferred Br_y and AWAS CFC-11 was used to estimate PGI (Figure 2-9). Five-minute averages of stratospheric Br_y, inferred from BrO observations, were calculated, centered at the time of each AWAS CFC-11

measurement. PGI was calculated from the mean difference between Br_y^{SGI} (black line in Figure 2-9) and inferred Br_y. The PGI estimate using both AMAX-DOAS and CIMS measurements is 2.1 ± 2.1 ppt (Figure 2-9a). PGI estimated using only AMAX-DOAS measurements is 2.2 ± 2.1 ppt (Figure 2-9b) and using only CIMS measurements is 1.7 ± 2.0 ppt (Figure 2-9c).

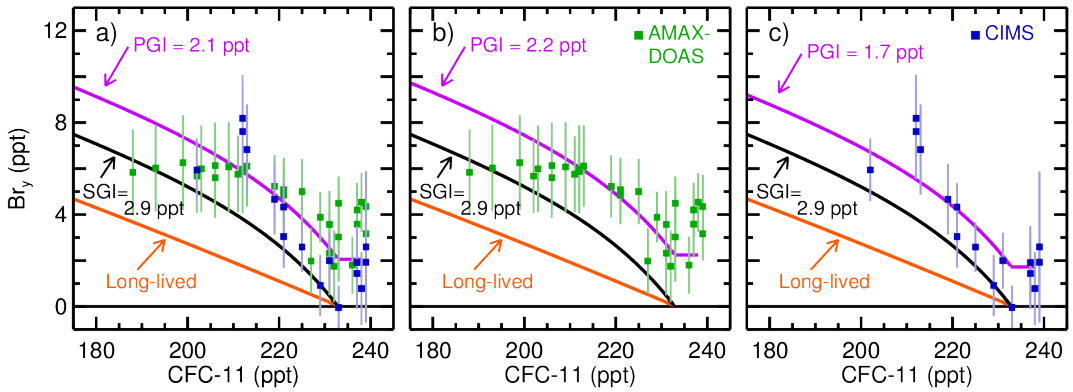

Figure 2-9. Stratospheric Br_y as a function of CFC-11 for winter 2014. In all panels, square points are Br_y inferred from AMAX-DOAS (green) and CIMS (blue) measurements of BrO, averaged for 5 minutes centered at the time of AWAS measurements of CFC-11. Orange lines are Br_y^{SGI} for long-lived compounds, and black lines show Br_y^{SGI} for the sum of long-lived and VSLS (dashed lines in Figure 2-7b). Purple lines are Br_y^{SGI} + PGI (a) The mean and uncertainty of PGI estimated using both AMAX-DOAS and CIMS-inferred Br_y is 2.1 ± 2.1 ppt. (b) PGI estimated using only AMAX-DOAS inferred Br_y is 2.2 ± 2.1 ppt. (c) PGI estimated using only CIMS-inferred Br_y is 1.7 ± 2.0 ppt.

The 2.1 ± 2.1 ppt PGI estimate presented here is in good agreement with previous ATTREX and CONTRAST studies. In the Navarro et al. (2015) analysis of ATTREX GWAS measurements, only CAM-chem-SD was used to estimate PGI. In their study, output from the CAM-chem-SD model at 17 km was used to estimate a value for PGI of 1.97 ± 0.21 ppt. Our observational based estimate is nearly identical, albeit with larger uncertainty, which most probably arises because we consider a wider age-spectrum of air masses within the lower stratosphere. The two previous studies that analyzed CONTRAST measurements of BrO restricted their estimates of PGI to

analysis of data collected in the upper troposphere and the bottom of the stratosphere (i.e., where O_3 < 200 ppb and the observed ratio of H_2O/O_3 < 0.1 ppm/ppb). The PGI estimate presented in Koenig et al. (2017) is 2.6 ± 0.6 ppt based on remotely sensed AMAX-DOAS measurements and is slightly higher than our estimate of 2.2 ± 2.1 ppt (Figure 2-9b) based on analysis of all AMAX-DOAS data collected for altitudes above the thermal tropopause. Chen et al. (2016) estimated a PGI of approximately 2 ppt based on Br_y inferred from in-situ CIMS observations of BrO acquired for air parcels where O_3 is between 100 and 200 ppb, which is in agreement with the 1.7 ± 2.0 ppt estimate (Figure 2-9c) presented here based on our analysis of all CIMS BrO acquired in the stratosphere. Our study is the first to present a single estimate for PGI by combining measurements of BrO obtained by both the AMAX-DOAS and CIMS instruments during CONTRAST.

2-3.2.1. Uncertainty Analysis

The overall PGI estimate was determined to be 2.1 ± 2.1 ppt. The total uncertainty is the root sum of square combination of four factors: (a) the standard deviation about the mean of the PGI estimate, (b) the 1σ measurement uncertainty in BrO, (c) the impact of JPL 2015 kinetic 1σ uncertainties on the BrO/Br_y ratio, and (d) 1σ uncertainties in observations other than BrO used to constrain the box model (Table A2-2). Of these factors, the largest contributions to the overall uncertainty in PGI (2.1 ppt) are the uncertainties in measured BrO (error bars in Figure 2-3g and 2-3h) and the standard deviation of the mean difference between inferred Br_y and Br_y^{SGI}, which both happen to be equal to 1.3 ppt.

The impact of chemical kinetics on our estimate of PGI is ~0.8 (− 0.67, + 0.98) ppt. To determine the effect of kinetic uncertainties on the PGI estimate, the rate constants for the reactions listed in the left column of Table 2-4 were each adjusted according to their 1σ uncertainty reported in JPL 2015 (Burkholder et al., 2015). The resulting total fractional difference in the BrO/Br_y ratio is 18.9% for all reactions, combined by root sum of squares. When this fractional difference is applied to the inferred Br_y, there is a − 0.67 to + 0.98 ppt uncertainty in the PGI estimate. The BrO/Br_y ratio is most sensitive to the rate constant controlling the formation of $BrONO_2$ ($BrO + NO_2 + M$). If the $BrONO_2$ reactions are adjusted according to the Kreycy et al. (2013) recommendations, this results in 0.50 ppt decrease in the PGI estimate, which is within the effect of the JPL 2015 uncertainties.

Table 2-4. Fractional difference in model BrO/Br due to the 1σ uncertainties in rate constants and instrumental measurements.

Kinetic		Instrumental	
Reaction	Fractional Difference	Observation	Fractional Difference
$BrO + NO_2 + M$	0.181	NO_2	0.038
$Br + O_3$	0.033	Aerosol SAD	0.015
$BrONO_2 + h\nu$	0.026	CO	0.009
$BrO + HO_2$	0.022	CH_4	0.009
$HOBr + h\nu$	0.016	H_2O	0.009
$Br + H_2CO$	0.010	O_3	0.008
$Br + HO_2$	0.009	Cl_y	0.001
BrO + NO	0.009		
Combined	0.189	Combined	0.048

The impact of non-BrO instrumental uncertainties on our estimate of PGI is −0.64 to +0.20 ppt. The upper limit was determined by adjusting the constrained variables, other than BrO, within the box model according to their reported 1σ measurement uncertainty (Table A2-2). Additionally, sulfate aerosol SAD was adjusted according to the 16 and 84 percentiles of the 5-minute running mean and Cl_y

was adjusted by ± 50 ppt. As summarized in the right column of Table 2-4, the modeled BrO/Br_y ratio was the most sensitive to uncertainties in AMAX-DOAS NO_2, followed by uncertainties in aerosol SAD. The combined fractional difference in the BrO/Br_y ratio is 4.78% due to uncertainties in model constraints, and contributes a ± 0.20 ppt uncertainty in the PGI estimate. In our base scenario, modeled NO_y is constrained by AMAX-DOAS measurements of NO_2 (section 2-2.4). If modeled NO_y is instead constrained to chemiluminescence measurements of NO, the PGI estimate decreases by 0.6 ppt due to the use of lower mixing ratios of NO_2 within the box model (blue line in Figure 2-4). Consequently, the lower limit of our PGI estimate includes the uncertainties introduced by constraining modeled NO_y to chemiluminescence NO.

Additionally, the analysis presented in this section and in section 2-3.1 was repeated using a dynamical definition of the tropopause (2 PVU, green lines in Figure 2-1) instead of the thermal tropopause. With the dynamical tropopause, the resulting SGI^{VSLS} increases to 3.0 ± 0.7 ppt and the PGI decreases to 1.7 ± 2.0 ppt, which is within the overall uncertainties calculated using the thermal tropopause.

Values of Br_y inferred from the AMAX-DOAS measurements of BrO level off, with respect to CFC-11, for mixing ratios of CFC-11 below about 210 ppt (green squares, Figure 2-9). This behavior is contrary to the theoretical expectation that Br_y should rise as CFC-11 declines. The lowest mixing ratios of CFC-11 are accompanied by sharp positive spikes in O_3 (Figure 2-3d). As discussed in section 2-2.2, since the AMAX-DOAS instrument collects differential slant column density measurements of BrO horizontally in front of the plane and in a narrow band above and below the aircraft, it is possible that the sharp gradients in atmospheric composition, as observed

by the in situ AWAS and chemiluminescence instruments, are not captured by the remote sensing AMAX-DOAS instrument. Conversely, since high levels of O_3 can interfere with the CIMS measurements, sharp atmospheric gradients can also affect the in situ observations. Furthermore, for locations where peak O_3 and NO_2 are observed, the impact of kinetic uncertainties on $BrONO_2$ kinetics increases. Consequently, we use the combination of the AMAX-DOAS and CIMS observations of BrO to calculate our reported values of Br_y^{VSLS} and PGI.

2-3.3. Stratospheric Bromine from VSLS (Br_y^{VSLS})

The total contribution of VSLS to stratospheric bromine is found by combining our SGI^{VSLS} (2.9 ± 0.6 ppt) and PGI (2.1 ± 2.1 ppt) estimates, yielding 5.0 ± 2.1 ppt of Br_y^{VSLS}. The uncertainties in the SGI^{VSLS} and PGI estimates are not additive, since our method implies that a decrease in SGI^{VSLS} would cause a corresponding increase in PGI. Overall uncertainty in Br_y^{VSLS} is dominated by the uncertainty in our estimate of PGI. The smaller range of values for PGI and Br_y^{VSLS} are true if (a) the lower limits of the uncertainties in measurements of BrO are more accurate, (b) the kinetics governing the formation of $BrONO_2$ are faster than the JPL 2015 recommendation, and/or (c) nitrogen oxide loading is better represented by chemiluminescence NO than by AMAX-DOAS NO_2. Conversely, the larger values of PGI and Br_y^{VSLS} are true if (a) the upper limits of the uncertainties in measurements of BrO are more accurate, (b) the kinetics governing the formation of $BrONO_2$ are slower than the JPL 2015 recommendation, and/or (c) nitrogen oxide loading is better represented by AMAX-DOAS NO_2 than by chemiluminescence NO.

Our best estimate of Br_y^{VSLS} of 5.0 ppt is in perfect agreement with the value given by WMO 2014. However, our ± 2.1 ppt uncertainty is smaller than the WMO 2014 uncertainty of ± 3 ppt. We also estimate that 58% of Br_y^{VSLS} enters the stratosphere as organic compounds (SGI^{VSLS} = 2.9 ± 0.6 ppt) and the remaining 42% enters as inorganic bromine (PGI = 2.1 ± 2.1 ppt). In WMO 2014, the best estimate for SGI^{VSLS} is 0.7 to 3.4 ppt based on observations of brominated VSLS at the tropical tropopause, and the best estimate for PGI is 1.1 to 4.3 ppt based on modeling studies (Table 1-9 of Carpenter and Reimann et al., 2014). In addition to observed SGI^{VSLS} and modeled PGI, estimates of Br_y^{VSLS} in WMO 2014 have been based on analysis of BrO profiles in the middle to upper stratosphere obtained by either ground-based (e.g., Schofield, 2004; Theys et al., 2007), balloon-borne (e.g., Dorf et al., 2008; Stachnik et al., 2013), or satellite instruments (e.g., Dorf et al., 2006; Sioris et al., 2006; Kovalenko et al., 2007; McLinden et al., 2010; Parrella et al., 2013). The mean value of the best estimate for Br_y^{VSLS} from these studies is 6 ppt, with a range of 3 to 8 ppt (Carpenter and Reimann et al., 2014). If the modification to the kinetics that govern the $BrONO_2$ to Br_y ratio put forth by Kreycy et al. (2013) based on atmospheric observations is adopted, these values fall to a best estimate of 5 ppt, with a range of 2 to 8 ppt. This proposed kinetic revision would decrease our Br_y^{VSLS} estimate by 0.5 ppt and is considered in our overall uncertainty (section 2-3.2.1).

Also, our estimate is in close agreement with the 5.2 ± 2.5 ppt value for Br_y^{VSLS} given by Dorf et al. (2008) based on analysis of balloon-borne observations acquired at Teresina, Brazil (5.1° S, 42.9° W) during June 2005. Dorf et al. (2008) estimated that a larger portion of the stratospheric transport of VSLS occurred as inorganic bromine

(PGI = 4.0 ± 2.5 ppt) than found in our study. They also ascribed the same uncertainty to both Br_y^{VSLS} and PGI (i.e., ± 2.5 ppt), since organic bromine species are able to be measured with much better accuracy and precision than can be achieved for BrO. The need to infer total inorganic bromine from measured BrO adds an additional, important source of uncertainty (e.g., Kreycy et al., 2013) to estimates of both PGI and Br_y^{VSLS}.

2-4. Conclusions

The combined organic and inorganic bromine measurements collected during the CONTRAST and ATTREX aircraft campaigns in the TWP during winter 2014 provide a unique opportunity to study the contribution of VSLS to stratospheric bromine. The TWP is a region of strong convection and is the dominant pathway for short-lived compounds to reach the stratosphere, particularly during boreal winter. The payloads onboard the CONTRAST and ATTREX aircrafts included instruments that measured BrO, a suite of long-lived bromocarbons, VSLS, many other chemical constituents critical to our analysis (i.e., O_3, NO, NO_2, CFC-11, H_2O, CO, and CH_4), as well as spectral actinic flux and aerosol surface area density. Data from the CONTRAST and ATTREX campaigns provide the first opportunity to quantify the gas phase bromine budget, across the tropical tropopause layer and extending into the lowermost stratosphere of the critically important TWP, in a comprehensive manner that includes direct observations of organic and inorganic bromine species.

Empirical relations between bromocarbons and CFC-11, a tracer of photochemical aging across the tropopause, were developed using whole air sampler measurements. These bromocarbon-tracer relations were used to quantify the stratospheric injection of long-lived substances and VSLS in organic form (source gas

injection, SGI). Based on this analysis, the contribution to stratospheric bromine from VSLS (SGI^{VSLS}) was determined to be 2.9 ± 0.6 ppt. This estimate is slightly lower than the 3.4 ± 0.3 ppt bromine content of organic VSLS observed at the average cold-point tropopause height (17 km) in the TWP during ATTREX. Estimates for SGI^{VSLS} found by both methods exceed the WMO 2014 best estimate of 1.4 ppt but lie within their upper uncertainty range (0.7 to 3.4 ppt), which was based on prior observations near the tropical tropopause (Carpenter and Reimann et al., 2014). The ATTREX value of 3.4 ± 0.3 ppt is likely influenced by vigorous convection during boreal winter in the TWP, and therefore could be biased high relative to the tropical average SGI^{VSLS}. We give 2.9 ± 0.6 ppt as our best estimate for SGI^{VSLS} because this value, found using the tracer-based approach, is based on analysis of data collected in the stratosphere that incorporates air-masses with a wide range of convective histories throughout the tropics. Further research is needed to define possible seasonal and inter-annual variability in SGI^{VSLS} (e.g., Fiehn et al., 2018; Hossaini et al., 2016).

Two flights during CONTRAST sampled the extratropical stratosphere by crossing the subtropical jet off the coast of Japan. Observations of BrO obtained during these flights by two instruments, AMAX-DOAS (Koenig et al., 2017) and CIMS (Chen et al., 2016), were combined with a photochemical box model to yield estimates of gas phase Br_y. This empirical estimate of Br_y was combined with observations of long-lived bromocarbons and VSLS to estimate the stratospheric injection of bromine that crosses the tropopause in inorganic form (product gas injection, PGI). Our best estimate of PGI is 2.1 ± 2.1 ppt. The use of empirical bromocarbon-tracer relations builds on previous CONTRAST and ATTREX studies by providing a method for estimating PGI

that considers the stratospheric decay of source gases and is applied to a large ensemble of stratospheric air masses. In the TWP, PGI represents both the decomposition products of brominated VSLS and the transport of labile inorganic species produced by brominated sea salt throughout the troposphere. Our value is within the 1.1 to 4.3 ppt range for PGI given by WMO 2014, which was largely based on model estimates of the whole tropical region. The largest contributor to the overall uncertainty in our estimate of PGI is the measurement uncertainty of BrO. Additionally, observations of BrO from both instruments exhibit considerable deviation about the respective means, which also contributes to the overall uncertainty in PGI. The chemical kinetics that drive the ratio of BrO to Br_y as well as ambient NO_2 and NO also contribute to the 2.1 ppt total uncertainty in PGI.

Our best estimate for the total contribution of VSLS to stratospheric bromine (Br_y^{VSLS}) is 5.0 ± 2.1 ppt. This estimate agrees with the 5 ± 3 ppt assessed value given in WMO 2014, albeit with lower uncertainty. Our overall uncertainty in Br_y^{VSLS} is dominated by the contribution of PGI, which in turn depends on the uncertainty in measured BrO. The value for Br_y^{VSLS} given in WMO 2014 is mainly based on model estimates of BrO near the tropical tropopause as well as stratospheric slant column measurements of BrO. There are large uncertainties in calculating BrO near the tropical tropopause due to: aerosol uptake and washout (e.g., Sinnhuber and Folkins, 2006), spatial distribution of biogenic emissions of VSLS (e.g., Hossaini et al., 2013), the strength of convection (e.g., Fernandez et al., 2014), the efficiency of removal of VSLS by OH (e.g., Rex et al., 2014), and the production of labile bromine from sea-salt aerosol (e.g., Schmidt et al., 2016). Given these uncertainties, an empirically based

estimate for PGI based on measured BrO in the Western Pacific constitutes a significant step forward in our understanding of the effect of oceanic biology on stratospheric composition.

Our best estimate of Br_y^{VSLS} of 5.0 ppt is the same as the WMO 2014 value. However, we apportion a larger fraction of the stratospheric transport of VSLS to source gases, 2.9 ppt versus the WMO 2014 value of 1.4 ppt based on prior observations at 17 km in the tropics. The consistency of our two estimates of SGI^{VSLS} further supports the notion that cross tropopause transport of brominated very short-lived source gases is higher than given in the WMO 2014 assessment. Prior estimates of SGI^{VSLS} have focused on analysis of data collected in the upper tropical troposphere at specific locations, outside of the TWP. Our best estimate is based on the use of tracer-based analysis of air masses sampled in the extratropical lower stratosphere, which reflects the influence of diverse convective histories throughout the tropics. Our estimate of SGI^{VSLS} emphasizes the importance of including measurements from convectively active regions in the recommended values of SGI^{VSLS} and PGI. Further research is required to quantify the temporal variability in Br_y^{VSLS}, as well as possible spatial and time-dependent variations in the relative contributions of SGI^{VSLS} and PGI (e.g., Fiehn et al., 2018; Hossaini et al., 2016).

Chapter 3: The Representation of Stratospheric Bromine in Models Participating in the Chemistry-Climate Modelling Initiative

3-1. Introduction

The Chemistry-Climate Modeling Initiative (CCMI) was established to study the interaction between ozone depletion, climate change, and tropospheric chemistry. CCMI is a continuation of the Chemistry-Climate Modeling Validation (CCMVal) program. Simulations prepared for CCMVal have been used by past studies and the World Meteorological Organization (WMO) Ozone Assessments to project the recovery of the ozone layer (Eyring et al., 2007, 2010; SPARC, 2010; Bekki et al., 2011). Models participating in CCMI are chemistry-climate models (CCMs), and simulations will feature in the upcoming 2018 WMO Ozone Assessment. CCMs are three-dimensional global models that internally calculate meteorological fields. The transport and dynamical fields within CCMs are responsive changes in radiative forcing due to simulated chemical processes. The purpose of CCMI, and previous CCMVal projects, is to evaluate the strengths and weaknesses of different CCMs and to assess how well processes that affect the ozone layer are represented in the CCMs (SPARC, 2010).

The main driver in the recovery of the ozone layer is expected to be the decline in stratospheric halogens. However, accurate projections of the ozone layer must also properly account for the influence of climate change and tropospheric chemistry on the ozone layer (Baldwin et al., 2007; Arblaster et al., 2014). Climate change can affect the recovery of the ozone layer by increasing the transport of air through the tropical tropopause and lowering stratospheric temperatures (Rosenfield and Douglass, 1998;

Shindell et al., 1998). Additionally, greenhouse gas emissions of N_2O and CH_4 influence stratospheric ozone chemistry by contributing to the abundances of NO_x (NO and NO_2) and HO_x (OH and HO_2) compounds (Randeniya et al., 2002; Ravishankara et al., 2009; Revell et al., 2012, 2015).

Tropospheric chemistry was added as a new component of CCMI (Eyring et al., 2013). Compounds such as CH_4 and very short-lived substances (VSLS) are partially lost in the troposphere via reaction with hydroxyl radicals (OH) before reaching the stratosphere. As a result, properly modeling the tropospheric oxidative capacity is important to understand the role of these compounds in stratospheric chemistry (Carpenter et al., 2014; Nicely et al., 2017). To evaluate the influence of climate change, stratospheric ozone, and tropospheric chemistry on each other, the CCMI simulations are conducted for historic (1960 – 2010) and forecast (1960 – 2100) time periods, using reference scenarios for ozone depleting substances and greenhouse gases (Eyring et al., 2013).

Eyring et al. (2013) recommended that CCMI models incorporate the stratospheric supply of bromine from VSLS in one of two manners. The first method we will refer to as an "explicit" representation of VSLS. Models that follow the recommended explicit representation of VSLS impose a 1.2 ppt surface mixing ratio for both CH_2Br_2 and $CHBr_3$ for a total of 6 ppt of bromine from VSLS at the surface. Since washout is expected to remove a fraction of the inorganic bromine (Br_y) gases produced by oxidation of VSLS in the troposphere, this method is designed to result in 4.5 to 5.0 ppt of stratospheric Br_y from VSLS (Br_y^{VSLS}), in agreement with the WMO best estimate (Montzka et al., 2011b). The second method we will refer to as the

"surrogate" representation of VSLS. Models that follow the surrogate representation of VSLS increase surface mixing ratios of methyl bromide (CH_3Br) by 5 ppt relative to the baseline to act as a surrogate for the additional bromine from VSLS. All of the CCMs already include CH_3Br as a regulated, longer-lived source of stratospheric bromine.

Recent studies have evaluated emission inventories for VSLS that utilize more detailed emission schemes than recommended for the first phase of CCMI (Hossaini et al., 2013, 2016; Lennartz et al., 2015). Previous CCMVal projects did not assess how well CCMs represented the troposphere, and some of the models involved in CCMI treat the troposphere in a simplified manner (Morgenstern et al., 2017). While other CCMI models do have sophisticated tropospheric modules and have run detailed simulations of VSLS in the troposphere (Hossaini et al., 2016), the simulations performed for those studies were not for the long (1960 – 2100) time periods required for the Ozone Assessment. Furthermore, there are remaining uncertainties in the representation of emissions, transport, and photochemical decomposition of VSLS as well as the deposition rates and heterogeneous reactions of the product gases (see Chapter 2 and references therein). Ultimately, the goal of including brominated VSLS is to accurately study ozone depletion and not to study the impact of VSLS on the troposphere. As a result, the methods for including VSLS presented by Eyring et al. (2013) are designed to assure proper Br_y^{VSLS} and not realistic tropospheric distributions.

In this chapter, we evaluate how well the CCMI models represent the stratospheric loading of bromine. In Chapter 2, we developed a tracer-tracer relation between CFC-11 and bromine based on aircraft measurements collected during the

CONvective TRansport of Active Species in the Tropics (CONTRAST) and Airborne Tropical Tropopause Experiment (ATTREX) campaigns (Jensen et al., 2017; Pan et al., 2017). This relation describes the decomposition of organic bromine compounds (CBr_y) and the formation of Br_y as air photochemically ages in the stratosphere. We will compare the combined CONTRAST and ATTREX-based estimate of Br_y^{VSLS} to the equivalent representation of this contribution within 14 global models that participated in CCMI. The results presented in this chapter and Chapter 2 were published in Wales et al. (2018).

3-2. Model Descriptions

Output from 14 global models involved in CCMI (Eyring et al., 2013; Morgenstern et al., 2017) was analyzed to assess the representation of the stratospheric supply of bromine from VSLS (Table 3-1). Thirteen of these models are CCMs that rely on internal, model generated transport fields, whereas TOMCAT is a chemical transport model (CTM) that uses meteorological fields from European Centre for Medium-Range Weather Forecasts reanalysis (ERA)-Interim meteorology (Dee et al., 2011). Three simulations of the EMAC CCM were considered. The EMAC-L47MA and EMAC-L90MA simulations use internally generated meteorological fields with 47 and 90 hybrid-pressure levels, respectively. The EMAC-L90MA-SD simulation, with 90 hybrid-pressure levels and nudged by Newtonian relaxation toward ERA-Interim meteorology (Dee et al., 2011), was examined to assess the effect of observed versus internally generated meteorology on the results of this study. The inclusion of EMAC in the multi-model mean analysis is based on the average of the three simulations before

combining with other models, so that EMAC does not have undue influence on the resulting multi-model mean.

Table 3-3-1. The bromine source gases included in the CCMI models considered by our study.

Model	Bromine sources	References
ACCESS-CCM	CH_3Br, $CHBr_3$, CH_2Br_2	Stone et al. (2016)
CCSRNIES	CH_3Br, halons, $CHBr_3$, CH_2Br_2	Akiyoshi et al. (2016)
CESM1 CAM4-Chem	CH_3Br, halons, $CHBr_3$, CH_2Br_2	Lamarque et al. (2012); Tilmes et al. (2016)
CESM1 WACCM	CH_3Br, halons, $CHBr_3$, CH_2Br_2	Garcia et al. (2017); Marsh et al. (2013); Solomon et al. (2015)
CMAM	CH_3Br, $CHBr_3$, CH_2Br_2	Scinocca et al. (2008)
EMAC	CH_3Br, halons, $CHBr_3$, CH_2Br_2, minor VSLS, sea	Jöckel et al. (2016); Kerkweg et al. (2008)
NIWA-UKCA	CH_3Br, $CHBr_3$, CH_2Br_2	Morgenstern et al. (2009)
SOCOL3	CH_3Br, halons, $CHBr_3$, CH_2Br_2	Stenke et al. (2013)
TOMCAT CTM	CH_3Br, halons, $CHBr_3$, CH_2Br_2	Chipperfield (2006)
CNRM-CM5.3	CH_3Br (+5ppt), halons	Michou et al. (2011); Voldoire et al. (2012)
GEOSCCM	CH_3Br (+5ppt), halons	Oman et al. (2013)
MRI-ESM1	CH_3Br (+5ppt), halons	Deushi & Shibata (2011); Yukimoto et al. (2012)
ULAQ-CCM	CH_3Br (+5ppt), halons	Pitari et al. (2014)
UMSLIMCAT	CH_3Br (+5ppt), halons	Tian & Chipperfield (2005)

For the CCMs considered in this study we have used monthly, zonal mean output of organic and inorganic bromine compounds as well as CFC-11 and tropopause pressure for January through March 2014 from the Ref-C2 scenario. These variables have been archived by the CCMI project and are maintained either by the National

Center for Atmospheric Research Earth System Grid (CESM1-CAM4Chem and WACCM) or the British Atmospheric Data Centre (all other CCMs). The EMAC-L90MA-SD and TOMCAT CTM variables are zonally resolved, monthly mean output. The Ref-C2 simulations utilize the surface mixing ratios of ozone depleting substances given by the A1 scenario from the 2010 WMO Ozone Assessment (Montzka and Reimann et al., 2010). Morgenstern et al. (2017) provides a high-level description of the global models involved in CCMI.

The CCMI models are grouped according to how they represent Br_y^{VSLS}. As listed in Table 3-1, nine models provide an explicit simulation of at least the two major VSLS ($CHBr_3$ and CH_2Br_2). The majority of the CCMs that explicitly represent VSLS impose a 1.2 ppt surface mixing ratio for both CH_2Br_2 and $CHBr_3$, as suggested by Eyring et al. (2013). The surface loading of VSLS from Eyring et al. (2013) is designed to result in 4.5 to 5.0 ppt of Br_y^{VSLS}, since washout is expected to remove a fraction of the inorganic gases produced by oxidation of VSLS in the troposphere. The EMAC models and TOMCAT CTM are exceptions among the explicit CCMI models for their treatment of Br_y^{VSLS}. In addition to CH_2Br_2 and $CHBr_3$, the EMAC simulations also include bromine sources from sea-salt aerosols and three minor VSLS (CH_2BrCl, $CHBr_2Cl$, and $CHBrCl_2$). Additionally, biogenic emissions of VSLS in EMAC emissions are parameterized according to Warwick et al. (2006). Within TOMCAT the surface mixing ratios of $CHBr_3$ and CH_2Br_2 are each 1 ppt. Finally, the implementation of sources of VSLS in the CESM1 CAM4-Chem version included in CCMI follows Eyring et al. (2013), while the CAM-chem-SD version used in section 2-2.3 to analyze

CONTRAST and ATTREX observations relied on the Ordóñez et al. (2012) emission scenario.

The last five CCMs listed in Table 3-1 utilize a simplified treatment for VSLS. Within these models, the surface mixing ratio of CH_3Br was increased by 5 ppt to represent the bromine loading from VSLS. This surrogate method was described by Eyring et al. (2013) as an option for modeling groups that did not have the resources to add explicit treatment of VSLS. The surface mixing ratio of CH_3Br was increased by 5 ppt since tropospheric loss of this compound, which is longer-lived than VSLS, is expected to be small.

We have included all CCMI models that have archived model output for CBr_y, Br_y, and CFC-11 for winter 2014. Except for the TOMCAT CTM and EMAC-L90MA-SD simulation, the model results are not based on observed transport fields and hence are not expected to match the actual meteorological conditions of 2014. However, due to changing anthropogenic emissions and regulation by the Montreal Protocol, the surface mixing ratios of CH_3Br and halons change over time. To assess the model representation of the bromine loading observed during the CONTRAST and ATTREX campaigns, output from all of the CCMI models is analyzed only for the time period January to March 2014.

3-3. Results and Discussion

3-3.1. Multi-Model Means

The goal of CCMI is to evaluate and improve the behavior of global models that have been designed to assess the interactions between climate change and atmospheric chemistry (Eyring et al., 2013; Morgenstern et al., 2017). Many scientific

studies that utilize CCMI models have focused on stratospheric ozone (e.g., Fernandez et al., 2017; Oman et al., 2016; Sinnhuber & Meul, 2015). Since realistic representation of bromine is necessary to properly simulate stratospheric ozone, we compare the bromine loading in 14 CCMI models (Table 3-1) to the empirical estimate based on CONTRAST and ATTREX observations. Each CCMI model is classified as either having "explicit" or "surrogate" treatment of VSLS, as discussed in Section 3-1.

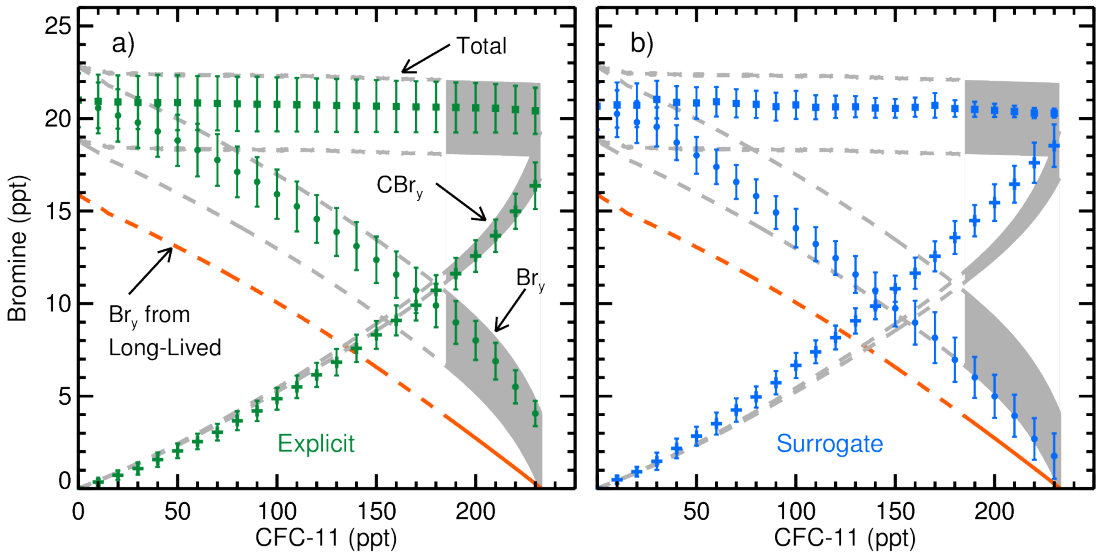

Figure 3-1. Observed and modeled relations of bromine as a function of CFC-11 for winter 2014. Observed relations of CBr_y, Br_y, and total bromine as a function of CFC-11 are shown in grey. Orange lines represent the expected rise of Br_y from the stratospheric supply of long-lived compounds only. Shaded grey regions represent the range of uncertainty in the observed relation, and dashed grey lines represent extrapolations of the upper and lower limits of the observed relations beyond the range of measured CFC-11. The observed CBr_y relation includes 2.9 ± 0.6 ppt from source gas injection of VSLS and the limits of this relation are defined according to the uncertainty in the linear fit of equation (2-2). The limits of both observed Br_y and total bromine relations are defined according to the 0.0 to 4.2 ppt range in observed PGI. Points and error bars are the multi-model mean and standard deviation of CCMI models with (a) explicit and (b) surrogate representations of VSLS. Model output is for January to March 2014, filtered for poleward of 30°N and binned for every 10 ppt of CFC-11.

Multi-model means of bromine as a function of CFC-11 from explicit and surrogate models are shown in Figure 3-1. The modeled CBr_y, Br_y, and total bromine (CBr_y + Br_y) have been averaged within 10 ppt bins of modeled CFC-11. Since the

variation of CBr_y compounds with CFC-11 is expected to be different in the tropics than in the extratropics (Volk et al., 1996), and the majority of the observations used in our study were obtained in the northern extratropics, model output was filtered to only include output poleward of 30°N and between the modeled tropopause pressure and 1 hPa. Similar figures for all individual explicit and surrogate models are discussed in Section 3-3.2.

Table 3-2. The mean mixing ratio of CFC-11 at the tropical tropopause in ATTREX and in CCMI models for winter 2014, and the surface mixing ratios from WMO 2010 and 2014.

Source	CFC-11 (ppt)
ATTREX TWP 17 km	232.7 ± 3.0
ACCESS-CCM	542.9 ± 2.4
CCSRNIES-MIROC3.2	226.2 ± 0.9
CESM1 CAM4-chem	227.9 ± 1.6
CESM1 WACCM	229.8 ± 1.2
CMAM	224.7 ± 1.3
CNRM-CM5.3	232.8 ± 1.8
EMAC-L47MA	223.8 ± 1.7
EMAC-L90MA	225.4 ± 1.0
EMAC-L90MA-SD	233.3 ± 2.6
GEOSCCM	229.1 ± 0.6
MRI-ESM1r1	276.8 ± 0.2
NIWA-UKCA	540.7 ± 1.7
SOCOL3	226.6 ± 1.5
TOMCAT CTM	231.5 ± 9.8
ULAQ-CCM	229.9 ± 1.6
UMSLIMCAT	559.1 ± 1.4
WMO 2010	230.4
WMO 2014	232.4

To properly compare observed and modeled bromine using CFC-11 in Figure 3-1, we have scaled model output for CFC-11 by the ratio of observed to modeled CFC-11 at the tropical tropopause. Table 3-2 lists the tropical tropopause mixing ratios of CFC-11 from the ATTREX campaign and within global models. Within the ACCESS-CCM, NIWA-UKCA, and UMSLIMCAT models, CFC-11 is scaled to represent

additional chlorinated source gases, and in MRI-ESM1r1 CFC-11 is scaled to represent minor CFCs. CCMI models, other than TOMCAT and EMAC-L90MA-SD, are constrained to the WMO 2010 time series of CFC-11, which had a slightly more aggressive decay of surface mixing ratios of CFC-11 than given by WMO 2014. The 2014 surface mixing ratios of CFC-11 reported in the 2010 and 2014 WMO Ozone Assessments are included in the bottom rows of Table 3-2.

The three observed bromine relations (total, organic decay, and inorganic rise) are shown in grey as functions of CFC-11 in Figure 3-1. The solid grey regions represent the observed range of CFC-11. The observed CBr_y relation is based on the solid black line shown in Figure 2-7b. The observed Br_y relation is inorganic bromine that forms upon stratospheric decay of all CBr_y compounds (equation 2-4, lower limit of grey shading) plus the amount of inorganic product gas that is transported across the tropopause (PGI = 2.1 ± 2.1 ppt, upper limit of grey shading). The lower and upper boundaries for Br_y and for total bromine, which is the sum of observed CBr_y and Br_y, are both defined according to the 0.0 to 4.2 ppt range estimated for PGI. For comparison, an additional orange line is shown in each panel to indicate the expected Br_y relation due to supply from only halons and CH_3Br (equation 2-4, orange dashed lines in Figure 2-7b). Since the lowest mixing ratio for CFC-11 observed during CONTRAST was 188 ppt, bromine relations at lower mixing ratios of CFC-11 are extrapolated and shown using dashed lines (only upper and lower limits are shown). These extrapolations are based on the values reported in Table 2-2 as well as equations (2-3) and (2-4), following an approach that is commonly used to relate aircraft observations to global model output (e.g., Wamsley et al., 1998).

Figure 3-1a shows results from the multi-model mean of CCMI models with explicit representation of VSLS. The values of CBr_y and Br_y in these models follow the observed curvature of the respective observed bromine versus CFC-11 relations quite well. However, the values of Br_y tend to lie either close to the central values of our empirical estimate or along the upper limit of the range for all levels of CFC-11. The good agreement between the modeled and observed relations implies that mean source gas injection (SGI) of VSLS and product gas injection (PGI) in explicit models are similar to that determined using CONTRAST and ATTREX data.

Table 3-3 compares the multi-model mean and standard deviation of SGI and PGI from the CCMI models to the same values inferred from the field observations. For this table, SGI of long-lived compounds (SGI^{LL}) and VSLS (SGI^{VSLS}) were calculated respectively from the sum of long-lived bromocarbons and VSLS at the tropopause pressures, reported by the global models, within the tropics (20°S to 20°N). Likewise, PGI and total bromine were calculated from the mixing ratios of modeled Br_y and the sum of modeled organic and inorganic bromine, respectively, at the tropical tropopause. Multi-model mean values are highlighted in bold and are calculated separately for explicit and surrogate models. Results for individual models are discussed in section 3-3.2.

Table 3-3. Stratospheric supply of bromine for winter 2014 from observations and CCMI models.

Source	SGI^{LL} (ppt)	SGI^{VSLS} (ppt)	PGI (ppt)	Total (ppt)
Observed	**15.0 ± 0.2**	**2.9 ± 0.6**	**2.1 ± 2.1**	**20.0 ± 2.1**
ACCESS-CCM	13.7 ± 0.2	2.0 ± 0.1	3.7 ± 0.3	19.4 ± 0.05
CCSRNIES-MIROC3.2	12.9 ± 0.05	2.0 ± 0.05	4.4 ± 0.2	19.3 ± 0.03
CESM1 CAM4-chem	14.2 ± 0.2	2.2 ± 0.07	3.0 ± 0.4	19.3 ± 0.06
CESM1 WACCM	14.4 ± 0.2	2.3 ± 0.08	2.9 ± 0.4	19.6 ± 0.1
CMAM	14.0 ± 0.1	2.8 ± 0.09	3.1 ± 0.3	19.9 ± 0.02
EMAC-L47MA	12.9 ± 0.2	5.0 ± 0.3	4.8 ± 0.8	22.7 ± 0.5
EMAC-L90MA	13.1 ± 0.1	5.1 ± 0.2	4.6 ± 0.5	22.8 ± 0.5
EMAC-L90MA-SD	13.5 ± 0.2	5.7 ± 2.3	3.7 ± 0.8	22.9 ± 0.8
NIWA-UKCA	13.5 ± 0.1	1.9 ± 0.1	3.8 ± 0.3	19.2 ± 0.07
SOCOL3	14.4 ± 0.1	3.0 ± 0.2	5.3 ± 0.5	22.7 ± 0.02
TOMCAT CTM	14.6 ± 0.8	3.4 ± 0.9	2.3 ± 1.6	20.4 ± 0.02
Explicit models	**13.9 ± 0.6**	**2.8 ± 1.1**	**3.6 ± 0.9**	**20.3 ± 1.5**
CNRM-CM5.3	19.6 ± 0.1		0.9 ± 0.2	20.5 ± 0.01
GEOSCCM	19.5 ± 0.06		1.2 ± 0.2	20.7 ± 0.1
MRI-ESM1r1	19.4 ± 0.01		0.7 ± 0.01	20.0 ± 0.07
ULAQ-CCM	17.0 ± 0.2		1.3 ± 0.3	18.4 ± 0.2
UMSLIMCAT	19.6 ± 0.08		0.7 ± 0.1	20.3 ± 0.1
Surrogate models	**19.0 ± 1.1**		**1.0 ± 0.3**	**20.0 ± 1.0**

Note: First row shows values based on observations. Other entries are based on model output at the tropical tropopause pressure for January to March 2014.

The mean value of SGI^{VSLS} for the explicit models is 2.8 ± 1.1 ppt, which is close to the observed value of 2.9 ± 0.6 ppt (Table 3-3). As described in Section 3-2, the Eyring et al. (2013) emission scheme for VSLS in CCMI models prescribes a sum of 6 ppt of bromine from VSLS at the surface. This value is consistent with the 5.9 ± 0.5 ppt of bromine from VSLS observed between altitudes of 0 and 0.5 km in the tropical Western Pacific (TWP) during CONTRAST (Figure 2-6). The mean value of SGI^{LL} is 13.9 ± 0.6 ppt for explicit models, which is lower than the observed value of 15.0 ± 0.2 ppt. All CCMI models assign surface mixing ratios of CH_3Br and halons according to the A1 scenario from the 2010 WMO Ozone Assessment, for a sum of 15.0 ppt of bromine. The WMO 2010 values for CH_3Br and halons are all within 0.1 ppt

of the mixing ratios given in the WMO 2014 scenario (dashed lines in Figure 1-1b) and within 0.2 ppt of surface CONTRAST observations in the TWP. Consequently, the lower value of SGI^{LL} within explicit models indicates a higher tropospheric loss of long-lived bromocarbons in CCMI models than observed.

Finally, the mean value of PGI for explicit models is 3.6 ± 0.9 ppt. This value is larger than the observed value of 2.1 ± 2.1 ppt but within the observed range of uncertainty. As shown in section 3-3.2, all nine models with explicit treatment of VSLS estimate higher PGI than observed. This reflects the tendency of the modeled Br_y to be along the upper range of observations in Figure 3-1a. The CCMI model representation of PGI depends on the rate of decomposition of organic bromocarbons in the tropical troposphere (e.g., Rex et al., 2014) and the subsequent efficiency of washout of inorganic product gases (e.g., Sinnhuber and Folkins, 2006). Additionally, the inclusion of both heterogeneous reactions of inorganic bromine species (e.g., Fernandez et al., 2014) and the sea-salt dehalogenation source (e.g., Schmidt et al., 2016; Wang et al., 2015) will also affect the representation of PGI within individual CCMI models. Finally, the faster decomposition of SGI^{LL} within explicit models compared to observations, discussed above, could be a contributing factor to the overestimate of PGI. Further research is required to understand the role of these factors in driving the differences of computed PGI shown in Table 3-3, as well as the tendency for all of the models to exceed our central empirical estimate of 2.1 ppt.

The bromine relations in CCMI models with surrogate VSLS are shown in Figure 3-1b. Since CH_3Br has a longer photochemical lifetime than VSLS in the lower stratosphere, the decay of CBr_y with decreasing mixing ratios of CFC-11 is slower in

these models compared to both observations (Figure 3-1b) and CBr_y from models that use an explicit treatment (Figure 3-1a). Consequently, Br_y in the surrogate CCMI models most commonly lies along the lower limit of the empirical range of the Br_y versus CFC-11 relation, particularly in the lower stratosphere (i.e., for the highest mixing ratios of CFC-11). As a result, these models could underestimate the role of bromine in photochemical loss of ozone in this region of the atmosphere. For older air parcels (i.e., low mixing ratios of CFC-11), Br_y in the surrogate models resembles the observed Br_y versus CFC-11 relation quite well, due to the release of bromine contained in CH_3Br.

Table 3-3 lists numerical values only for SGI^{LL}, PGI, and total bromine from the surrogate models. The entry for SGI^{LL} in Table 3-3 represents SGI by all organic compounds, since VSLS are not explicitly simulated. These surrogate models exhibit a PGI of 1.0 ± 0.3 ppt, which is lower than both the observed value of 2.1 ± 2.1 ppt as well as that found by the explicit models, 3.6 ± 0.9 ppt. This tendency is due to the relatively long tropospheric lifetime of CH_3Br compared to $CHBr_3$, and demonstrates a potential shortcoming in the surrogate treatment of VSLS.

The mean total bromine loading of 20.3 ± 1.5 ppt in the explicit models as well as the 20.0 ± 1.0 ppt in the surrogate models is both close to the 20.0 ± 2.1 ppt observed value (Table 3-2). Furthermore, for more photochemically aged air (i.e., CFC-11 less than ~120 ppt), the representation of Br_y in surrogate models is within the observed range (Figure 3-1b). Consequently, the representation of stratospheric bromine for studies of polar ozone should be reliable for both explicit and surrogate treatments of VSLS. All CCMI models that use either explicit or surrogate representations of VSLS

lie much closer to the empirical estimate of Br_y (grey) than to the estimate using only CH_3Br and halons (orange). As a result, both CCMI methods for including VSLS are able to more closely simulate observed stratospheric bromine than would be found if VSLS had been completely neglected.

Our estimates for stratospheric bromine injection in Table 3-2 are calculated using the tropopause values throughout the tropics from the CCMI models. Because the output from the majority of the CCMs are only available as zonal means, we are not able to separate the contribution of the TWP. The precise values for SGI and PGI within the CCMs can depend on details of the meteorological fields. However, a comparison between EMAC simulations that use internally generated transport fields and that relied on observed meteorology revealed no discernible difference in the resulting bromine relations in the middle and upper stratosphere and a small difference, well within the observational uncertainty, for the lower stratosphere (Section 3-3.2.1). Furthermore, values of SGI and PGI from the CCMI models calculated using the tracer-tracer relation approach are similar to those given in Table 3-3 (Table A3-1). The mean PGI for explicit models calculated using tracer-tracer relations is 0.6 ppt higher than the value given in Table 3-3. The difference between all other multi-model mean values in Tables 3-3 and A3-1 are between −0.2 and 0.3 ppt. Within individual models, there is no clear pattern to these offsets.

Previous modeling studies have evaluated the ability of different emission inventories of VSLS to represent stratospheric bromine injection. Our estimates for SGI^{VSLS} of 2.9 ± 0.6 ppt (observed) and 2.8 ± 1.1 ppt (explicit CCMI models; Table 3-3) are slightly higher than the SGI^{VSLS} value of 2.0 ppt (range 1.2 to 2.5 ppt) reported

by Hossaini et al. (2016). Additionally, the values of Br_y^{VSLS} calculated from the sum of PGI and SGI^{VSLS} are 5.0 ± 2.1 ppt based on observations and 6.4 ± 1.4 ppt in explicit models. Both values of Br_y^{VSLS} are well within the 4 to 8 ppt range reported by Hossaini et al. (2013). While the global models considered in the Hossaini et al. (2016) and Hossaini et al. (2013) studies use observation-based emission inventories for VSLS (Ordóñez et al., 2012; Ziska et al., 2013; Liang et al., 2014), the CCMI models (with the exception of EMAC) use a more simplified approach of prescribed surface mixing ratios of VSLS. It is therefore reassuring that this simplified approach is able to adequately represent stratospheric injection of VSLS. Explicit representation of oceanic emissions of VSLS provides an avenue for assessing the impact of climate change and oceanic biology on atmospheric bromine that is inaccessible upon use of prescribed mixing ratios (Lennartz et al., 2015; Falk et al., 2017). Our analysis of the aircraft observations in the TWP, developed in Chapter 2, provides a benchmark for evaluation of the simulated representation of stratospheric bromine within global models.

3-3.2. Individual Models

3-3.2.1. Explicit Models

Figure 3-2 shows bromine relations from all individual CCMI models with explicit treatment of VSLS. Each panel was prepared in the same manner as Figure 3-1, and the panel for EMAC uses the mean of the three simulations, discussed in Section 3-3.3. The total bromine in all models, except EMAC and SOCOL-3, lie within the observed range of uncertainty. The loading of inorganic bromine in EMAC and SOCOL-3 is above the observed range, contributing to the high total bromine in both

models. Three of the CCMI models with explicit representations of VSLS (ACCESS, CCSRNIES, and NIWA-UKCA) have CBr_y mixing ratios that lie a few ppt below the observed relation. However, for all three of these models, total bromine lies within the observed range of uncertainty.

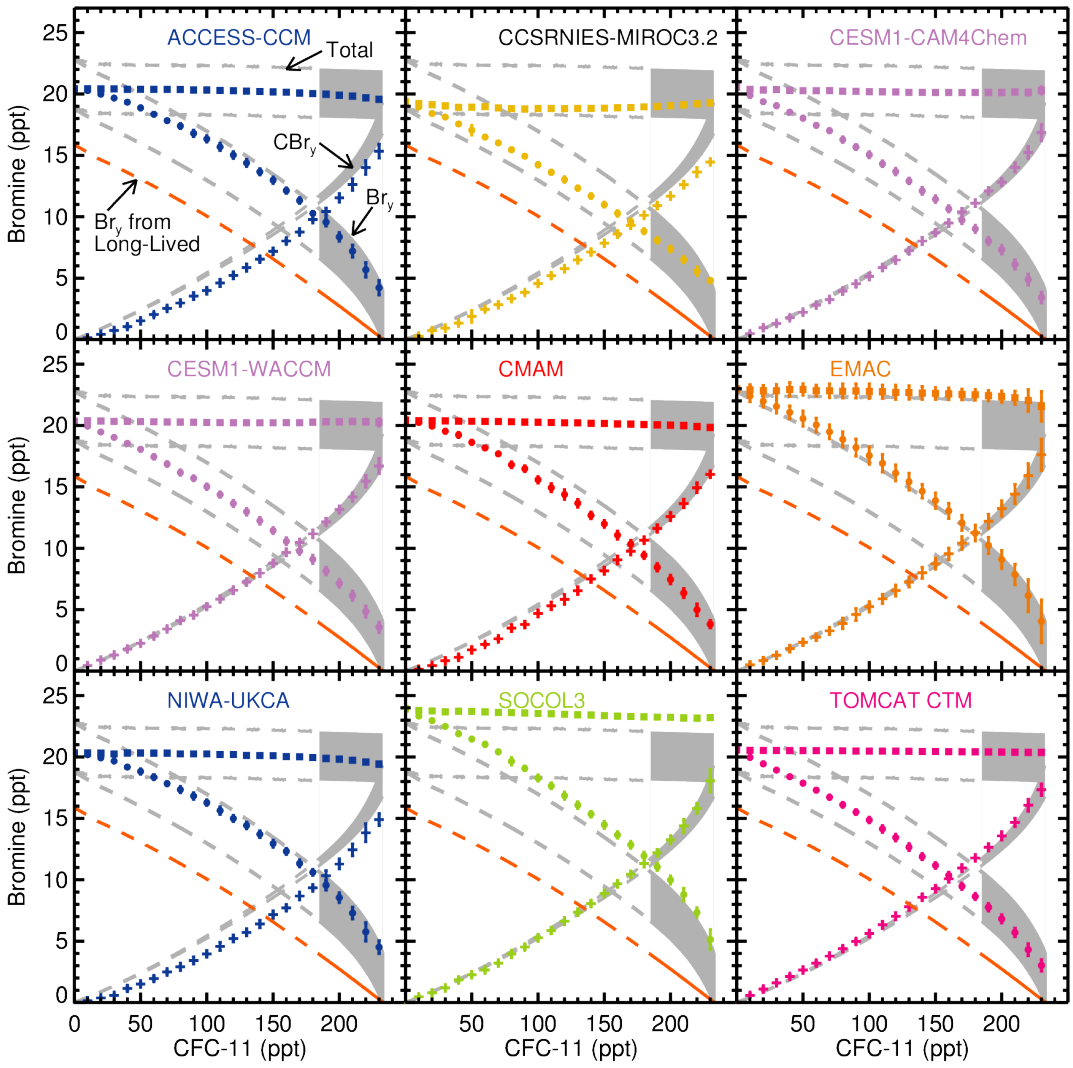

Figure 3-2. Same as Figure 3-1, but for individual CCMI models with explicit representations of VSLS (Table 3-1). The mean of three EMAC simulations is shown for EMAC.

Table 3-3 also includes SGI^{VSLS} values for each individual CCMI model. Of the CCMI models with explicit VSLS, values of SGI^{VSLS} in WACCM, CMAM, SOCOL3,

and TOMCAT are within the observed 2.9 ± 0.6 ppt range. Additionally, the values of SGI^{VSLS} in all three EMAC simulations are about 2 ppt above the observed central value. The tropical tropopause value of SGI^{VSLS} in the remaining four models with explicit treatment (ACCESS, CCSRNIES, CAM4Chem, NIWA-UKCA) are 0.7 ppt to 1 ppt below the observed central value. All explicit models, except EMAC and TOMCAT, follow the same boundary conditions for VSLS from the Eyring et al. (2013) emission scheme. Consequently, the differences in SGI^{VSLS} between these models are due to model variations in the convective lofting and chemical removal (i.e., reaction with OH and loss by photolysis) of these compounds in the tropical troposphere.

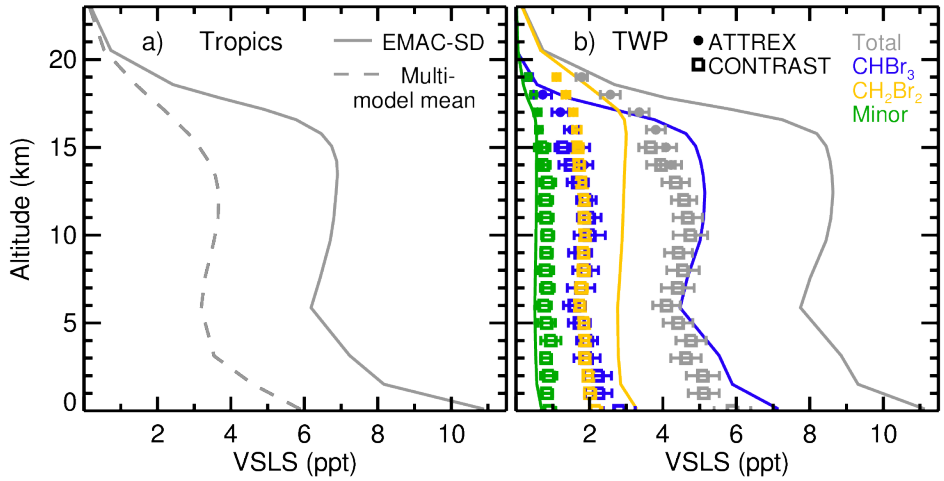

Figure 3-3. Mean profiles of VSLS in (a) the tropics and (b) the tropical Western Pacific (TWP) for winter 2014. (a) The sum of all VSLS is show as a solid line for EMAC-SD, dotted line for TOMCAT, and a dashed line for the multi-model mean of models that follow the Eyring et al. (2013) emission scheme. (b) Solid lines are the TWP mean profiles of VSLS in EMAC-SD, square points are CONTRAST observations, and circle points are ATTREX observations. Observations are sorted into 1 km bins and error bars are the standard deviation of each bin as described in Figure 2-6. All mixing ratios are multiplied by their bromine atomicity.

Mean profiles of VSLS are shown in Figure 3-3. In panel a, the tropical mean profile of the total VSLS is shown for EMAC-SD, TOMCAT, and the multi-model

mean of the remaining seven explicit models. For TOMCAT and the multi-model mean, the profiles are the sum of $CHBr_3$ and CH_2Br_2 mixing ratios, multiplied by the number of bromine atoms in each molecule while total bromine in EMAC-SD is the sum of all five VSLS. The TOMCAT model does not simulate tropospheric chemistry, so the mixing ratios of VSLS are constant throughout the troposphere.

Offsets between SGI^{VSLS} from the EMAC simulations and the other CCMI models are at least partially due to differences in how the tropospheric behaviors of the source gases are simulated. Eyring et al. (2013) prescribes a surface mixing ratio of 6 ppt of bromine from $CHBr_3$ and CH_2Br_2. The TOMCAT model prescribes a tropospheric value of 1 ppt for both $CHBr_3$ and CH_2Br_2, for a total of 5 ppt of bromine at the surface. The EMAC simulations rely on geographical oceanic emission fields for $CHBr_3$, CH_2Br_2, and minor VSLS from Warwick et al. (2006). For the whole tropics, the mean surface mixing ratio of bromine from VSLS in EMAC-SD is above 10 ppt.

In panel b of Figure 3-3, profiles of VSLS are constrained to the tropical Western Pacific (TWP) and are shown for EMAC-SD as well as ATTREX and CONTRAST observations. The total mean mixing ratios of VSLS in EMAC-SD are higher in the TWP than for the whole tropics and are nearly twice the observed mixing ratios from CONTRAST and ATTREX (shown in grey). The high values of total VSLS in EMAC-SD are largely due to high mixing ratios of $CHBr_3$ with respect to observations.

Mixing ratios of $CHBr_3$ modeled using the Warwick et al. (2006) emission scenario have also been shown to exceed observations in Southeast Asia (Pyle et al., 2011). Those observations prompted a downward revision to the local rate of emission

of $CHBr_3$. The location of the Pyle et al. (2011) study is near the area sampled during the CONTRAST and ATTREX campaigns. Therefore, the tendency for CBr_y from EMAC to lie above our observed value (Figure 3-2) will likely be resolved upon application of the downward revision in the emission of $CHBr_3$.

As discussed in section 3-3.1, the multi-model mean Br_y (Figure 3-1a) and PGI (Table 3-3) in explicit models are within the upper portion of the observed range. Similarly, in Figure 3-2 the values of Br_y from the explicit models tend to lie either close to the central values of our empirical estimate (CCSRNIES, CAM4Chem, WACCM, CMAM, and TOMCAT) or along the upper limit of the range (ACCESS, EMAC, NIWA-UKCA, and SOCOL3). CAM4Chem and WACCM both rely on the Community Earth System Model (CESM) framework, which we have also used to define the halon-1301 versus CFC-11 relation, because halon-1301 was not measured during CONTRAST and ATTREX. Since halon-1301 supplies 3.24 ppt to the bromine budget, this could contribute to the similarity between the results from these models and our estimated Br_y versus CFC-11 relation. Additionally, CH_3Br in ACCESS, CMAM, and NIWA-UKCA was scaled to represent halon loading (Stone et al., 2016). Since CH_3Br has a shorter photochemical lifetime than halons (Table 2-2), the use of CH_3Br to represent halons likely results in faster release of Br_y in these models, contributing to higher Br_y loading in the lower stratosphere.

The representations of PGI in CCSRNIES, SOCOL3, and all EMAC simulations are 0.4 to 1.3 ppt larger than the observed upper limit of 4 ppt (Table 3-3). As a result, the Br_y loadings in these models fall along the upper limit of the observed Br_y versus CFC-11 relation at the base of the stratosphere (i.e., where CFC-11 = 230 ppt

in Figure 3-2). However, because SGI^{LL} and SGI^{VSLS} are both low in CCSRNIES compared to other models as well as observations, inorganic bromine loading in CCSRNIES agrees well with observations. The higher value of PGI in EMAC is due to the use of emission fields from Warwick et al. (2006), which contributes to the formation of larger amounts of brominated product gases in the TTL. Finally, the SOCOL3 simulation has the largest value of PGI (5.3 ± 0.5 ppt), which lies above the observed upper limit of 4 ppt. For SOCOL3 and EMAC, the Br_y versus CFC-11 relations lie at or just above the upper range of our uncertainty.

3-3.2.2. Surrogate Models

The bromine relations in individual surrogate models are shown in Figure 3-4. Comparisons between these models and the observed bromine relations are consistent with the discussion provided in section 3-3.1. Furthermore, the total bromine loading in four of the surrogate models (CNRM-CM5.3, GEOSCCM, MRI, and UMSLIMCAT), given in the last column of Table 3-3, is close to the 20.0 ± 2.1 ppt estimate based on CONTRAST and ATTREX observations. For these four models, the representation of stratospheric bromine for studies of polar ozone should be reliable.

Based on the mean mixing ratio at the tropical tropopause, the total bromine loading in ULAQ is 18.4 ± 0.2 ppt. This value is at the lower limit of the range of uncertainty. However, within the stratosphere, total bromine loading in ULAQ exhibits scatter around 20 ppt (orange squares in Figure 3-4), which is much closer to the observed best estimate. Furthermore, PGI and total bromine loading in ULAQ calculated using the tracer-tracer relation method are about 2 ppt larger than found using model output at the tropical tropopause (Table A3-1). This discrepancy between

the two approaches for estimating stratospheric injection of bromine is unique to ULAQ and is presently not understood.

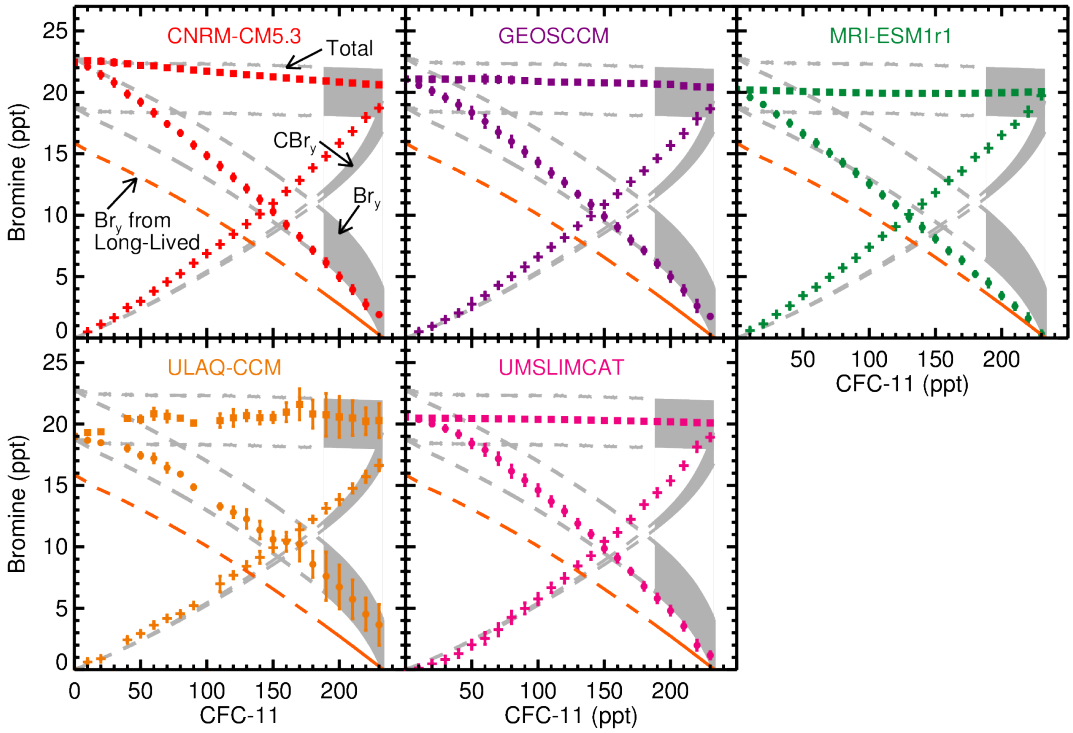

Figure 3-4. Same as Figure 3-1, but for individual CCMI models with surrogate representations of VSLS (Table 3-1).

3-3.3. Influence of Specified Dynamics

Three simulations of EMAC were considered in this study. The EMAC-L47MA and EMAC-L90MA simulations use internally generated meteorology and have 47 and 90 hybrid-pressure levels, respectively. The EMAC-L90MA-SD simulation uses specified dynamics and has 90 hybrid-pressure levels. The bromine loadings within these three EMAC simulations are shown in Figure 3-5 and Table 3-3.

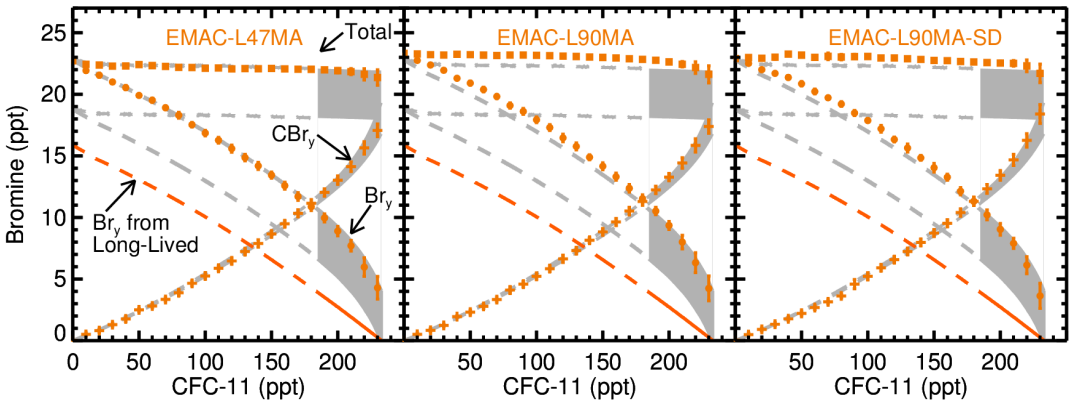

Figure 3-5. Same as Figure 3-1, but for three simulations of the EMAC model.

Comparisons between the EMAC-L90MA and EMAC-L90MA-SD simulations, which use the same number of levels, are examined to investigate whether the use of models with or without observed meteorology might affect the partitioning between modeled SGI and PGI. The use of observed meteorology increases SGI^{VSLS} by 0.6 ppt and SGI^{LL} by 0.4 ppt and decreases PGI by 0.9 ppt. However, the value for Br_y^{VSLS} decreases by only 0.3 ppt (from 9.7 ± 0.5 ppt to 9.4 ± 2.4 ppt) upon use of specified dynamics, which is well within the standard deviation of both values. Similarly, total bromine loading is consistent between all three simulations, ranging between 22.7 to 22.9 ppt, and in Figure 3-5 bromine at lower mixing ratios of CFC-11 (i.e. CFC-11 < 180 ppt) is nearly indistinguishable between the EMAC-L90MA and EMAC-L90MA-SD simulations.

Furthermore, Hossaini et al. (2016) reported that global model simulations with and without observed meteorology did not result in systematic differences in the transport of VSLS to the stratosphere. As a result, we conclude that the choice of meteorology could affect the precise values of SGI and PGI for individual models (Table 3-3) but does not have a significant impact on our overall assessment of stratospheric bromine loading within the CCMI models.

3-4. Conclusions

The Chemistry-Climate Modeling Initiative (CCMI) is a collection of models used to study the recovery of the ozone layer as well as the interactions between climate change, stratospheric ozone, and tropospheric chemistry. Unlike past groups of models that projected the recovery of the ozone layer (Eyring et al., 2010; Bekki et al., 2011), models participating in CCMI include a stratospheric supply of bromine from VSLS. Two methods were proposed to ensure that all participating models included enough stratospheric bromine (Eyring et al., 2013). In the first method the two major VSLS, $CHBr_3$ and CH_2Br_2, are added to the models with fixed surface mixing ratios. However, not all modeling groups had the resources needed to include $CHBr_3$ and CH_2Br_2 as well as the associated tropospheric chemistry. As a result, Eyring et al. (2013) recommended that mixing ratios of CH_3Br, a long-lived compound already included in the models, could be increased as a surrogate for the additional stratospheric bromine provided by VSLS.

We have assessed how accurately 14 CCMI models simulate the stratospheric supply of bromine from VSLS. We have compared organic, inorganic, and total bromine in the global models to observations using the CFC-11 tracer relation developed in Chapter 2. This relation describes, as a function of CFC-11, the decay of organic bromine and resulting formation of inorganic bromine as stratospheric air ages. The tracer relation was developed using aircraft observations of CFC-11, organic bromine compounds, and BrO collected above the convectively active tropical Western Pacific (TWP).

Overall, the CCMI models that have an explicit treatment of VSLS simulate the stratospheric injection of VSLS (SGI^{VSLS}) in a manner that is in agreement with

observations. Based on the TWP observations, 2.9 ± 0.6 ppt of SGI^{VSLS} is expected. All models that follow the Eyring et al. (2013) formation for including $CHBr_3$ and CH_2Br_2 are within the observed range of uncertainty or about 1 ppt below the central observed value. The values of SGI^{VSLS} in the EMAC simulations, which use the Warwick et al. (2006) emission scenario for VSLS, are 2 to 3 ppt higher than the observed value. A downward revision to emissions of $CHBr_3$ in the Warwick et al. (2006) emission scheme has been recommended by Pyle et al. (2011). Since the high SGI^{VSLS} in EMAC is driven by simulations of $CHBr_3$ that are much higher than our TWP observations, future EMAC simulations that follow the Pyle et al. (2011) modification are expected to be in agreement with our observed SGI^{VSLS}.

Additionally, the explicit CCMI models represent PGI either close to our best empirical estimate or near the upper range of the observed uncertainty. The CCSRNIES, EMAC, and SOCOL3 models simulate values of PGI that are above the observed 2.1 ± 2.1 ppt range of uncertainty. For the EMAC simulations, the high values of PGI are attributed to the tropospheric decay of high mixing ratios of $CHBr_3$. Future studies are required to evaluate the influence of tropospheric chemistry and transport of Br_y compounds as well as the tropospheric decay of longer-lived CH_3Br on high PGI in the remaining models.

Conversely, CCMI models that have surrogate treatment of VSLS (i.e., CH_3Br is used as a proxy for VSLS) simulate stratospheric injection of Br_y that is close to the lower range of our observationally-constrained estimate. The difference between the explicit and surrogate treatments of VSLS is driven by slower decay of CH_3Br relative to VSLS. However, in more stratospherically aged air, modeled mixing ratios of Br_y

are in agreement with the TWP observations. Additional research is need to assess the ability of these models to simulate ozone loss in the lower stratosphere where modeled Br_y is low with respect to observations.

The representation of total stratospheric bromine within CCMI models is significantly improved upon consideration of either treatment of VSLS. The multi-model mean of total bromine within explicit and surrogate models is 20.3 ± 1.5 ppt and 20.0 ± 1.0 ppt, respectively, in excellent agreement with the 20.0 ± 2.1 ppt expected based on our TWP observations. Methyl bromide and halons, long-lived sources, provided about 15 ppt of total bromine to the stratosphere in winter 2014. Therefore, both representations of VSLS provide a demonstrable, significant improvement over previous versions of these models that neglected the effect of VSLS on stratospheric bromine.

The current formations of bromine within the CCMI models should therefore provide more reliable simulations of the recovery of the Antarctic ozone hole (Oman et al., 2016; Fernandez et al., 2017) than the previous chemistry-climate models. Additionally, current CCMI models should be able to more accurately assess the effect of volcanic activity on midlatitude ozone (Salawitch et al., 2005; Feng et al., 2007; Klobas et al., 2017) as well as the impact of geoengineering of climate on ozone (Tilmes et al., 2008, 2012). However, CCMs with a surrogate representation of VSLS may not properly simulate stratospheric columns of BrO, due to low Br_y in the lower stratosphere (Hendrick et al., 2007). Lastly, the CFC-11 tracer relation developed in Chapter 2 effectively represents stratospheric loading of Br_y in chemistry-climate models that explicitly include VSLS. Consequently, the CFC-11 tracer relation is a

viable method for constraining stratospheric Br_y in box models that do not simulate transport of air parcels, as used in Chapter 4.

Chapter 4: Uncertainties in the Stratospheric Contribution of Brominated Very Short-Lived Substances and Tropospheric BrO Based on Measurements of Column BrO over Fairbanks, Alaska

4-1. Introduction

The role of bromine chemistry in stratospheric ozone depletion has been well established (Wofsy et al., 1975; McElroy et al., 1986). Long-lived compounds (halons and methyl bromine) as well as naturally produced very short-lived substances (VSLS) deliver bromine to the stratosphere. The contribution of halons and methyl bromide (CH_3Br) to stratospheric inorganic bromine (Br_y = BrO, Br, $BrONO_2$, HOBr, Br_2, HBr, BrCl, and $BrNO_2$) loading is also well characterized (Carpenter et al., 2014). However, the amount of stratospheric Br_y supplied by VSLS (Br_y^{VSLS}) is subject to a number of uncertainties. Brominated VSLS are organic compounds ($CHBr_3$, CH_2Br_2, CH_2BrCl, $CHBr_2Cl$, and $CHBrCl_2$) that are emitted by marine biology and have tropospheric lifetimes less than 6 months (Ko et al., 2003). Due to their short tropospheric lifetime, brominated VSLS partially decompose in the troposphere, forming inorganic product gases. Both VSLS and their inorganic product gases enter the stratosphere primarily through the tropical tropopause layer (TTL). Based on measurements of BrO and numerous observations of VSLS in the TTL, VSLS are expected to contribute 5 ± 2 ppt of bromine to the stratospheric (Dorf et al., 2008; Wales et al., 2018; World Meteorological Organization, 2018). Currently, VSLS supply about 25% of the bromine in the stratosphere, and their relative contribution to stratospheric bromine will increase as mixing ratios of regulated anthropogenic source gases decline (Carpenter et al., 2014).

Past studies have attempted to determine Br_y^{VSLS} as well as the total loading of stratospheric Br_y based on measurements of bromine monoxide (BrO) in stratospherically aged air. These studies made use of either ground-based (e.g., Schofield, 2004; Theys et al., 2007), balloon-borne (e.g., Dorf et al., 2008; Stachnik et al., 2013), or satellite instruments (e.g., Sinnhuber et al., 2005; Kovalenko et al., 2007; Salawitch et al., 2010) to measure stratospheric BrO. The stratospheric loading of Br_y was determined by modeling the BrO/Br_y ratio. These studies have produced a wide range of estimates for Br_y^{VSLS} (3 to 9 ppt) that are generally higher than the 5 ppt expected from measurements of VSLS in the tropics (Montzka et al., 2011b). However, estimates of Br_y^{VSLS} from stratospheric measurements of BrO are sensitive to uncertainties in the modeled kinetics that govern the BrO/Br_y ratio as well as instrumental uncertainties in the measurements of BrO (e.g., Sioris et al., 2006; McLinden et al., 2010; Salawitch et al., 2010; Parrella et al., 2013).

In the troposphere, bromine chemistry couples with chlorine and iodine catalytic cycles and alters the oxidative capacity most prominently in polar, marine and coastal regions (Saiz-Lopez and von Glasow, 2012; Simpson et al., 2015). Bromine chemistry reduces tropospheric ozone (O_3) directly through reactions with O_3 and indirectly by lowering mixing ratios of NO_x ($NO + NO_2$) (von Glasow et al., 2004; Yang et al., 2005; Parrella et al., 2012). Additionally, tropospheric bromine has been associated with the near-complete removal of surface ozone in the polar spring, referred to as ozone depletion events (Barrie et al., 1988). During ozone depletion events, halogens become the main tropospheric oxidant and have a strong influence on HO_x ($OH + HO_2$) and NO_x chemistry as well as the lifetimes of pollutants, transported to the

Arctic from northern industrial regions (Evans et al., 2003). However, there are significant uncertainties concerning the exact mechanism by which bromide (Br^-) from sea water is converted into gas phase Br_y prior to ozone depletion events (e.g, Simpson et al., 2007; Jones et al., 2009; Nghiem et al., 2012; Pratt et al., 2013; Choi et al., 2018).

Satellite measurements of BrO are a valuable resource for monitoring tropospheric bromine due to the large spatial and temporal coverage of the data (e.g., Wagner et al., 2001; Schmidt et al., 2016; Choi et al., 2018). Bromine monoxide is the dominant daytime Br_y species as well as the most frequently measured Br_y compound. In this study we utilize observations of vertical column BrO (BrO^{VC}) from the Ozone Monitoring Instrument (OMI) onboard the NASA Aura satellite (Veefkind et al., 2006). OMI measures BrO using the differential optical absorption spectroscopy (DOAS) technique (Stutz and Platt, 1996), which is also currently used by the GOME-2 and TROPOMI satellite instruments (Munro et al., 2006; Veefkind et al., 2012). The satellite measurements of BrO^{VC} are sensitive to a number of parameters involved in the DOAS retrieval, including the *a priori* profile shape, cross sections, and wavelength fitting window (Aliwell et al., 2002).

Tropospheric columns of BrO can be determined from satellite vertical column measurements through a residual technique (Wagner and Platt, 1998; Theys et al., 2011; Choi et al., 2012). Residual tropospheric BrO is calculated by removing the stratospheric component of BrO^{VC}. Thus, an accurate understanding of stratospheric BrO is first required to calculate tropospheric BrO from satellite measurements. Simulations of stratospheric BrO are dependent on the amount of Br_y in the stratosphere as well as the partitioning of stratospheric Br_y into BrO (Sioris et al., 2006; Salawitch

et al., 2010; Theys et al., 2011). Consequently, satellite-based estimates of active bromine in the troposphere are sensitive to the uncertainties in measurements of BrO^{VC}, the stratospheric loading of Br_y, and the kinetics regulating BrO/Br_y ratio.

The column BrO/Br_y ratio is largely governed by column NO_2 as well as the rates of formation and photolysis of $BrONO_2$ (Theys et al., 2011). In the lower stratosphere, the majority of daytime Br_y cycles between $BrONO_2$ and BrO via the formation of $BrONO_2$ through a three-body reaction, dependent on the density of air (M):

$$BrO + NO_2 + M \rightarrow BrONO_2 + M \quad (4\text{-}1)$$

as well as the photolysis of $BrONO_2$:

$$\begin{aligned} BrONO_2 + h\nu &\rightarrow BrO + NO_2 \\ &\rightarrow Br + NO_3 \\ &\rightarrow BrO + NO + O(^3P) \end{aligned} \quad (4\text{-}2)$$

All production pathways of reaction (4-2) rapidly feed into the BrO_x (Br + BrO) cycle.

Kreycy et al. (2013) suggested modifications to the photolysis frequency of $BrONO_2$ (J_2) relative to the rate constant of $BrONO_2$ (k_1). In their study, twilight observations of O_3, NO_2, and BrO were collected in the lower stratosphere using a balloon-borne DOAS instrument. These measurements focused on the lower stratosphere where the BrO/Br_y ratio is most sensitive to reactions (4-1) and (4-2). The observed BrO formed more quickly in the morning and decreased more slowly in the evening than predicted by model simulations. Consequently, Kreycy et al. (2013) proposed that the 2011 NASA Jet Propulsion Laboratory (JPL 2011) kinetic values (Sander et al., 2011) underestimate the ratio of J_2/k_1 at 220 ± 5 K. Their proposed modification to the kinetics that govern formation and loss of $BrONO_2$ is well within

the uncertainties of laboratory measurements, but has not been supported by twilight $BrONO_2$ measurements in the midlatitudes (Wetzel et al., 2017). The 2014 WMO Ozone Assessment (Carpenter et al., 2014) gave 5 ppt as the estimate for Br_y^{VSLS} compared to the prior estimate of 6 ppt given in the 2010 Assessment (Montzka et al., 2011b), based on the application of the kinetic parameters of Kreycy et al. (2013) to existing measurements of stratospheric BrO. The revised 5 ppt estimate brings estimates of Br_y^{VSLS} based on stratospheric BrO in agreement with observations and modeling studies based in the TTL (Carpenter et al., 2014).

Our study utilizes OMI and ground-based measurements of BrO^{VC} collected over Fairbanks, Alaska during March and April 2011. Using a stratospheric box model, we quantify the sensitivity Br_y^{VSLS} to a number of factors for both satellite and ground-based BrO^{VC}. Our box model, described in Section 3.3, uses rate constants and cross sections from the JPL 2015 kinetic compendium (Burkholder et al., 2015). For reactions (4-1) and (4-2), the International Union of Pure and Applied Chemistry (IUPAC) assessment considers the same laboratory studies as JPL but proposes higher $BrONO_2$ cross sections and a slower rate constant for reaction (4-1) at stratospheric temperatures (Atkinson et al., 2007). We assess the sensitivity of our simulations of BrO^{VC} by systematically switching kinetic parameters for $BrONO_2$ reactions to the IUPAC preferred values as well as applying the J_2/k_1 recommended scaling from Kreycy et al. (2013). The Fairbanks ground-based observations of BrO^{VC} use a different wavelength fitting window and are biased low with respect to the OMI retrieval. Consequently, we also evaluate the uncertainty in Br_y^{VSLS} due to the two datasets for

BrO^{VC}. Finally, we quantify the sensitivity of tropospheric residual BrO to uncertainties in the BrO^{VC} retrievals, the value of Br_y^{VSLS}, and $BrONO_2$ kinetics.

4-2. Bromine Nitrate ($BrONO_2$) Kinetics

Rate constants for $BrONO_2$ formation (reaction 1) recommended by JPL, IUPAC, and two laboratory studies are shown in Figure 4-1. The rate constant for three body reactions is a function of temperature and pressure and is parameterized using low and high-pressure limit rate constants, as described by IUPAC and JPL. For this figure rate constants have been calculated using [M] = 1.6×10^{18} molecules cm^{-3} to demonstrate conditions around 20 km, where the Br_y partitioning is most sensitive to $BrONO_2$ kinetics.

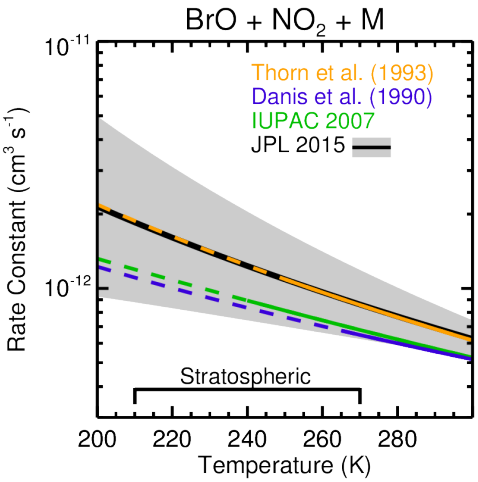

Figure 4-1. The reported rate constants of the BrO + NO_2 + M reaction as a function of temperature, evaluated for density of air equal to 1.8×10^{18} cm^{-3}. The solid black line is the JPL rate constant, and the grey shaded region is the associated uncertainty range. The green line is the rate constant recommended by IUPAC. The orange and blue lines are the rate constants reported by Thorn et al. (1993) and Danis et al. (1990), respectively. Dashed lines represent extrapolations beyond the measured temperature range of each study and the recommended range for IUPAC. The stratospheric temperatures relevant for this study are between 210 and 270 K, indicated along the bottom axis.

The Thorn et al. (1993) study measured the rate constant of reaction (4-1) at temperatures between 248 and 347 K. Sander et al. (1981), not shown in Figure 4-1,

measured the pressure dependence of $BrONO_2$ formation at 298 K, and the results of this study agree well with the Thorn et al. (1993) measurements. The Danis et al. (1990) study quantified the rate constant at low pressures for temperatures between 263 and 343 K. The low-pressure rate constant calculated from the Danis et al. (1990) study is slower than the extrapolation of the Thorn et al. (1993) measurements. However, the slower rate constants reported by Danis et al. (1990) could be due to heterogeneous loss of NO_2 in their reactor setup (Thorn et al., 1993).

The JPL rate constants for the formation of $BrONO_2$ is based on a least squares fit to data from the Thorn et al. (1993) and Sander et al. (1981) studies. As a result, the JPL rate constant closely follows the temperature dependence reported by Thorn et al. (1993). The IUPAC values are recommended for temperatures between 240 and 350 K. The low-pressure limit for IUPAC is based on all three studies, while the high-pressure limit is temperature independent and derived from measurements at 298 K from the Thorn et al. (1993) and Sander et al. (1981) studies.

At standard temperature and pressure, the IUPAC and JPL rate constants for reaction (4-1) are in agreement. However, since IUPAC includes the Danis et al. (1990) low-pressure measurements, the IUPAC rate constant is consistently slower than JPL at stratospheric pressures (Figure 4-1). Furthermore, the difference between the two rate constants are larger at the low temperatures found in the lower stratosphere, because the IUPAC high-pressure limit is temperature independent. At higher altitudes, the rate constant is less sensitive to the high-pressure limit, and the temperature dependence between IUPAC and JPL are nearly parallel.

Cross sections for $BrONO_2$ photolysis (reaction 4-2) are shown for 298 and 220 K in Figure 4-2. The cross sections measured by Burkholder et al. (1995) and Deters et al. (1998) are in close agreement at 298 K (Figure 4-2a). However, for wavelengths between 300 and 500 nm, the values reported by Burkholder et al. (1995) decrease at lower temperatures while the cross sections in Deters et al. (1998) increase (Figure 4-2b). The JPL cross sections are based on the values measured by Burkholder et al. (1995). Cross sections of $BrONO_2$ in IUPAC are an average of the two studies, and thus have a minimal temperature dependence. Consequently, photodissociation of $BrONO_2$ calculated using the JPL cross sections will be slower than IUPAC at stratospherically relevant temperatures.

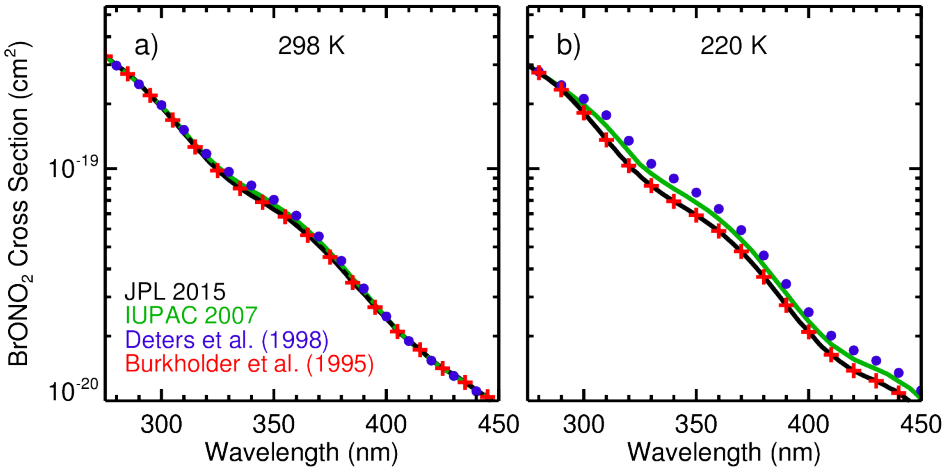

Figure 4-2. The reported cross sections for $BrONO_2$ photolysis at (a) 298 K and (b) 220 K. The black lines are JPL and the green lines are the IUPAC recommendation. Red points are cross sections reported by Burkholder et al. (1995) and blue points are cross sections from Deters et al. (1998).

The differences between the $BrONO_2$ kinetic recommendations in JPL 2011, used by Kreycy et al. (2013), and JPL, used in our study, are negligible. The reaction (4-2) cross sections are unchanged between the two versions. The JPL 2011 recommendation for reaction (4-1) was based entirely on the Thorn et al. (1993)

measurements (orange line in Figure 4-1). The updated recommendation (black line in Figure 4-1), based on Thorn et al. (1993) and Sander et al. (1981), results in a very slight modification to the rate constant.

4-3. Observations and Model Description

4-3.1. Fairbanks 2011 Campaign

The 2011 Fairbanks BrO campaign was based at the University of Alaska, Fairbanks (64.86°N, 212.15°E). During the campaign, ozonesondes were launched daily on 25 March through 8 April 2011. Daytime measurements of BrO^{VC} were collected by a multifunction DOAS (MFDOAS) instrument on 25 March through 5 April and on 8 April. A multi-axis DOAS (MAX-DOAS) instrument monitored BrO in the lower troposphere (Peterson et al., 2015; Simpson et al., 2017). Total column measurements of O_3 were collected by a Brewer spectrometer on 24 March through 4 April (Tzortziou et al., 2012).

Our model setup utilizes measurements of O_3 and temperature acquired by balloon-borne ozonesondes during the 2011 campaign. One balloon was launched each day between 25 March and 8 April around 11:00 am local solar time. On 1 April the balloon burst around 11 km, but for all other days of the campaign the balloon reached an altitude of ~30 km. Only observations collected below 20 km are used to constrain the box model and define tropopause pressure, as described in Section 4-3.3. We do not use measurements above 20 km due to potential errors in the ozonesonde pressure sensors that can contribute to uncertainties in the reported mixing ratios of O_3 (Stauffer et al., 2014).

During the campaign, BrO was below the MAX-DOAS lower limit of detection between the surface and 2 km over Fairbanks. Fairbanks is located in central Alaska and is isolated from marine sources of brominated sea-salt aerosols and VSLS (Sturges et al., 1992; Vogt et al., 1996; Quack and Wallace, 2003; Simpson et al., 2007b). Consequently, we treat the MFDOAS and OMI measurements of BrO^{VC} as purely stratospheric for our primary results. However, in Section 4-4.4 we discuss the sensitivity of tropospheric residual BrO to uncertainties in total column BrO and modeled stratospheric BrO.

During the 2011 campaign, an MFDOAS instrument measured BrO^{VC} above the University of Alaska, Fairbanks. This instrument has been used in the validation of OMI NO_2 and SO_2 (Herman et al., 2009; Spinei et al., 2010). The MFDOAS instrument has two separate telescopes to collect both direct sun and MAX-DOAS measurements. The wavelength fitting window used to retrieve BrO is 336 to 359 nm. The DOAS fitting technique considers BrO cross sections from Wilmouth et al. (1999) as well as cross sections for O_2, NO_2, OClO, H_2CO, and the O_2-O_2 collision complex. We apply a five-minute average to the MFDOAS measurements of BrO^{VC}, and the precision uncertainty in the MFDOAS observations is the combination in quadrature of the standard deviation about the 5 min mean and the 1σ fitting uncertainty.

Column measurements of O_3, NO_2, and BrO^{VC} were also collected over Fairbanks by a Pandora instrument on 29 March through 8 April 2011. The Pandora and Brewer measurements of O_3 over Fairbanks are reported in Tzortziou et al. (2012). However, the measurements of BrO^{VC} have not been finalized and, thus, are not the focus of this chapter. In general, the magnitude of the preliminary Pandora

measurements are in close agreement with the MFDOAS observations, and incorporation of Pandora BrO^{VC} would not affect the results of this chapter. For future reference, Figures 4-5 through 4-7, presented in Section 4-4 of the main body of this chapter are reproduced in the Appendix Figures A4-1 and A4-2.

4-3.2. The Ozone Monitoring Instrument

OMI is an ultraviolet-visible, nadir viewing instrument onboard the NASA Earth Orbiting System-Aura satellite. The Aura satellite is in a sun-synchronous, polar orbit with an equatorial crossing time of 13:45 in the ascending node. The OMI swath width is 2600 km with a 13×24 km^2 spatial resolution at the center of the swath (Levelt et al., 2006). Due to the high latitude location of Fairbanks, multiple OMI overpasses are available for most days during the campaign.

Measurements of BrO^{VC} from OMI are calculated using the DOAS method. The current OMI BrO retrieval (version 3.0) uses a wavelength fitting window of 319 to 347.5 nm and BrO cross sections from Wilmouth et al. (1999). The slant column density of BrO is calculated following spectral fitting of BrO, Ring scattering, O_3, NO_2, H_2CO, and SO_2. The final vertical columns are determined using a wavelength and albedo dependent air mass factor (Kurosu and Chance, 2011; Suleiman et al., 2018). For each orbit, we average level 2 data within 200 km of Fairbanks, weighted by the inverse of the distance to Fairbanks. The reported error in BrO^{VC} is the combination of 1σ uncertainties in the spectral fitting, cross sections, and the profile shape used by the air mass factor (Chance, 2002) as well as the standard deviation about the 200 km mean.

Additionally, OMI measurements are used to constrain the box model described in Section 4-3.3.Observations of total column O_3 and reflectivity from OMI are taken

from the level 3 DOAS product (Veefkind et al., 2006). Box modeled NO_2 is constrained to match the NASA level 2 gridded product of stratospheric column NO_2 (Bucsela et al., 2013; Krotkov et al., 2017). The OMI retrievals of NO_2 are scaled to noon using the box modeled diurnal variation of stratosphere column NO_2.

4-3.3. Box Model Setup

A stratospheric photochemical box model is used to calculate columns of BrO over Fairbanks for 25 March through 8 April 2011 (Salawitch et al., 2010; Wales et al., 2018). The box model includes 187 reactions as well as 37 chemical compounds. Rate constants and absorption cross sections are defined according to the JPL kinetic evaluation (Burkholder et al., 2015). The mechanism within the box model has been extensively tested and compared with global model simulations and observations (SPARC, 2010). Profiles of photolysis frequencies and rate constants are calculated over Fairbanks, Alaska (64.86°N, 212.15°E) in 15 min intervals for a full diel cycle. The partitioning of Br_y compounds were calculated assuming photochemical steady state over the diel cycle.

The box model is constrained to profiles of long-lived chemical and physical tracers from the NASA Global Modeling Initiative (GMI) chemical transport model (Strahan et al., 2007). The GMI model was constrained to reanalysis meteorological fields from Modern-Era Retrospective Analysis for Research and Application (MERRA; Rienecker et al., 2011). Daily GMI profiles of temperature, O_3, total nitrogen oxides (NO_y), CH_4, CO, H_2O, inorganic chlorine (Cl_y), N_2O, and CFC-11 were used to constrain long-lived tracers in the box model. The GMI variables are provided on a 2° latitude and 2.5° longitude grid with 72 vertical levels and are interpolated to the

latitude and longitude of the location of the University of Alaska, Fairbanks (64.86°N, 212.15°E).

Stratospheric aerosol surface area density in the box model is constrained to monthly, zonal mean profiles prepared for the Chemistry-Climate Model Initiative (CCMI). The CCMI aerosol dataset is based on 532 nm backscatter measurements from Cloud-Aerosol Lidar and Infrared Pathfinder Satellite Observations (CALIPSO) and is available on 1° latitude bins with 72 vertical levels (Eyring et al., 2013). Aerosol profiles are interpolated to the latitude of Fairbanks and the pressure levels of the GMI output.

Model constraints are further refined using OMI and ozonesonde observations. Photolysis frequencies are calculated using OMI total column O_3 and reflectivity. Below 20 km, the box model is constrained to ozonesonde profiles of temperature and ozone. Box model profiles of O_3 above 20 km, initially constrained to GMI output, are linearly scaled so that modeled column O_3 matches OMI observations. Additionally, profiles of NO_y in the box model, initially constrained to GMI output, are scaled so that box modeled stratospheric columns of NO_2 are within 1% of OMI observations of column NO_2.

Finally, profiles of Br_y are calculated using GMI CFC-11 and N_2O following the method described in Wales et al. (2018). In the stratosphere, VSLS and long-lived, organic bromine compounds (CH_3Br and halons) decompose forming Br_y. GMI CFC-11 is used as a stratospheric tracer to calculate the formation of Br_y, while N_2O is used to account for the long-term surface record of halons and CH_3Br. Since the total bromine mixing ratio of CH_3Br and halons at the surface has decreased by about 1 ppt

from 2005 to 2011, we do not expect uncertainties in GMI N_2O to have a strong effect on our calculations of Br_y.

The majority of inorganic bromine forms below 20 km. To represent observed dynamics, we adjust GMI profiles of CFC-11 using ozonesonde measurements of O_3. Mixing ratios of CFC-11 and O_3, simulated over Fairbanks for March and April 2011, are closely anti-correlated in GMI and are well represented using a quadratic fit (Figure 4-3). For each GMI pressure level, we calculate theoretical mixing ratios of CFC-11 from the quadratic fit for both ozonesonde and GMI O_3. Profiles of CFC-11 are adjusted based on the difference between the two calculated values of CFC-11, so that the final profile is consistent with the profile of O_3 reported by the ozonesonde. This adjustment to the profiles of CFC-11 has a minor impact on the scientific results of our study.

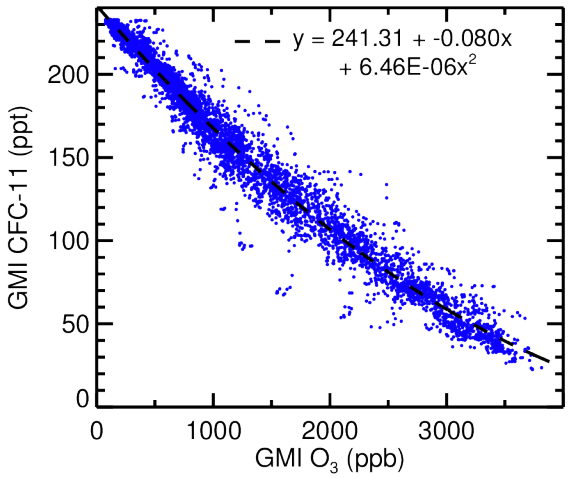

Figure 4-3. CFC-11 as a function of O_3, as output by the GMI model. Values of CFC-11 and O_3 have been filtered to only include output above the GMI thermal tropopause and below 20 km. The dashed line shows a quadratic fit to the output, where (CFC-11) = 241.31 – 0.08 (O_3) + 6.36 $\times 10^{-6}$ $(O_3)^2$ for O_3 in ppb and CFC-11 in ppt.

The model is constrained to profiles of Br_y for seven possible contributions of VSLS. For one scenario, we neglect the stratospheric contribution of VSLS and calculate Br_y using only long-lived source gases (Br_y^{VSLS} = 0 ppt). A second scenario

assumes only a stratospheric supply of Br_y from source gas injection (SGI) of long-lived bromocarbons and VSLS. Based on the aircraft observations described by Wales et al. (2018), the contribution of VSLS to stratospheric bromine via SGI is expected to be 2.9 ppt (which we take as Br_y^{VSLS} = 3 ppt for simplicity). The remaining five scenarios consider contributions of direct injection of Br_y (i.e., product gas injection, PGI) in 2 ppt increments (Br_y^{VSLS} = 5 to 13 ppt). To simulate PGI, we add constant amounts of Br_y (2 to 10 ppt) to the profiles calculated from the stratospheric CFC-11 tracer relation. The range of Br_y^{VSLS} extends to 13 ppt simulate BrO^{VC} above the upper limits of OMI BrO^{VC}

For our base kinetic scenario, profiles of BrO are simulated for each value of Br_y^{VSLS} using the kinetic recommendations given by JPL (Burkholder et al., 2015). We conduct four additional kinetic scenarios to test the sensitivity of our results to the different kinetic recommendations for $BrONO_2$ formation (reaction 4-1) and photolysis (reaction 4-2). To model the kinetic recommendations given in Kreycy et al. (2013), we decrease the JPL rate constant for reaction (4-1) by a factor of 0.75 and increase the photolysis frequency of reaction (4-2) by a factor of 1.27.

We also run three simulations with using $BrONO_2$ kinetics from IUPAC (Atkinson et al., 2007). With all other kinetic parameters defined by JPL, we use the IUPAC recommendation for $BrONO_2$ cross sections for one set of simulations. For a second run, the rate constants for reaction (4-1) are defined by IUPAC. A final run uses IUPAC kinetic parameters for both reactions (4-1) and (4-2). We refer to these three kinetic scenarios as IUPAC (J), IUPAC (k) and IUPAC (J & k), respectively.

Modeled profiles of BrO are integrated from the tropopause pressure to 0.1 hPa. Profiles of the thermal lapse rate are calculated from ozonesonde measured temperature profiles (red line in Figure 4-4). The tropopause pressure is calculated from the lapse rate according to the World Meteorological Organization (1957) definition. During the campaign, the observed tropopause is in close agreement with the tropopause pressure reported by GMI (black line in Figure 4-4) for all days except 6 April 2011 . On 6 April 2011, the observed lapse rate is close to 2 K km^{-1} between 400 and 210 hPa, resulting in an ambiguous tropopause pressure.

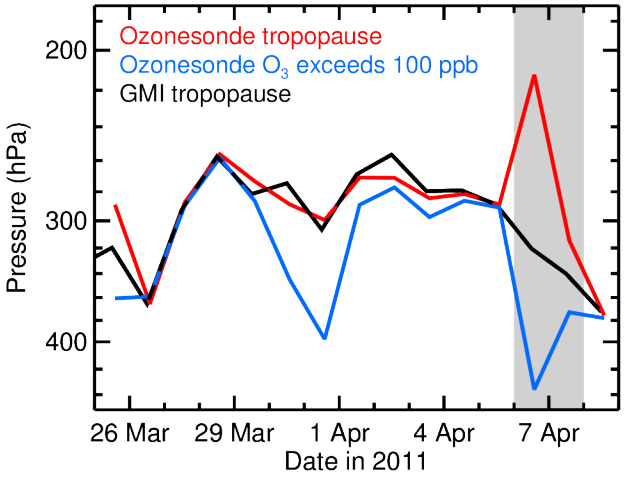

Figure 4-4. Tropopause pressure from ozonesonde measurements and GMI over Fairbanks, Alaska. The red line indicates the tropopause pressure defined using the thermal lapse rate calculated from ozonesonde temperature profiles. The blue line indicates the pressure level where ozonesonde measurements of O_3 first exceed 100 ppb. The black line is the tropopause pressure reported by GMI. The grey shaded region represents the two days where daytime MFDOAS observations were not collected during the spring 2011 campaign.

We also use ozonesonde measurements of O_3 to test the sensitivity of our results to BrO below the thermally-defined tropopause. High mixing ratios of O_3 are an indicator of stratospherically influenced air that may contain Br_y. The blue line in Figure 4-4 represents the pressure level where ozonesonde profiles of O_3 first exceed 100 ppb, characteristic of stratospheric values of ozone (Zahn and Brenninkmeijer,

2003). Since daytime observations of BrO were not collected by MFDOAS on 6 and 7 April and the tropopause pressures are not well defined for these two days (grey box in Figure 4-4), we do not include OMI observations of BrO on 6 and 7 April in our analysis.

4-3.4. Calculating Tropospheric Column Density

Tropospheric columns of BrO are calculated from measurements of BrO^{VC} using the tropospheric residual method (Wagner and Platt, 1998; Theys et al., 2011; Choi et al., 2012). The retrieval algorithm used for both OMI and MFDOAS first computes slant column densities (SCD) of BrO. The SCD is converted to vertical column density (VCD) using an air mass factor (AMF).

$$\mathrm{VCD} = \frac{\mathrm{SCD}}{\mathrm{AMF}} \tag{4-3}$$

The AMFs used in the OMI retrieval assume BrO resides entirely in the stratosphere (AMF_{Strat}). Since the sensitivity of the satellite instrument to the signal of BrO depends on the profile shape of the absorbing species, tropospheric AMFs (AMF_{Trop}) must be included to accurately calculate tropospheric VCD. We use AMF_{Trop} prepared using the Linearized Discrete Ordinate Radiative Transfer model (LIDORT; Spurr et al., 2001) following the procedure described by Choi et al. (2018). Under clear-sky conditions AMF_{Trop} is calculated as a function of solar zenith angle (SZA), the viewing zenith angle (VZA) of OMI, surface albedo, and tropopause height. Under cloudy-sky conditions AMF_{Trop} is calculated as function of SZA, VZA, cloud height, and tropopause height. Clear and cloudy-sky AMF_{Trop} calculations are averaged, weighted by the OMI cloud fraction. The resulting AMF_{Trop} is combined with

OMI total VCD, modeled stratospheric VCD, and OMI AMF_{Strat} to determine tropospheric VCD:

$$VCD_{Trop} = \frac{(VCD_{OMI} - VCD_{Strat}) \times AMF_{Strat}}{AMF_{Trop}} \quad (4\text{-}4)$$

4-4. Results and Discussion

4-4.1. MFDOAS and OMI Measurements of Vertical Column BrO

Measurements of BrO^{VC} from OMI and MFDOAS over Fairbanks, Alaska collected during spring 2011 are shown in Figure 4-5. In this figure, MFDOAS observations are 1 hour averages, centered at the time of each daytime OMI overpass. The error bars for MFDOAS are the combination in quadrature of the DOAS 1σ fitting uncertainty and the standard deviation about the 1 hour mean. The OMI error bars are the 1σ fitting uncertainty, described in Section 4-3.2.

Only observations collected at SZAs less than 70° and within 30 min of each other are shown in Figure 4-5. As noted above, daytime (SZA < 70°) MFDOAS measurements were not collected on 6 and 7 April. Since daytime measurements of OMI and MFDOAS BrO^{VC} on 5 April were not acquired within 30 min of each other, these observations are not shown in Figure 5. However, measurements of BrO^{VC} on 5 April are included in Sections 4-4.2 and 4-4.3. For all days except 26 March, the MFDOAS retrievals of BrO^{VC} are lower than reported by OMI. The mean and standard deviation of the OMI/MFDOAS BrO^{VC} ratio is 1.20 ± 0.14 (Figure 5b).

Both instruments use the DOAS technique to determine SCD of BrO. The DOAS method separates the signal of BrO from interfering absorbers through least-squares fitting of the multiple absorption spectra within a restricted wavelength range

(Stutz and Platt, 1996). The reported MFDOAS retrievals of BrO^{VC} are based on a 336 – 359 nm wavelength fitting window, while the OMI fitting window is 319 – 347.5 nm. The choice of fitting window must balance strong absorption by and unique spectral structure of BrO with minimal interference from other atmospheric absorbers (Platt and Stutz, 2008). Small changes in the chosen spectral window have been demonstrated to have a significant, systematic impact on retrievals of slant column BrO (Aliwell et al., 2002).

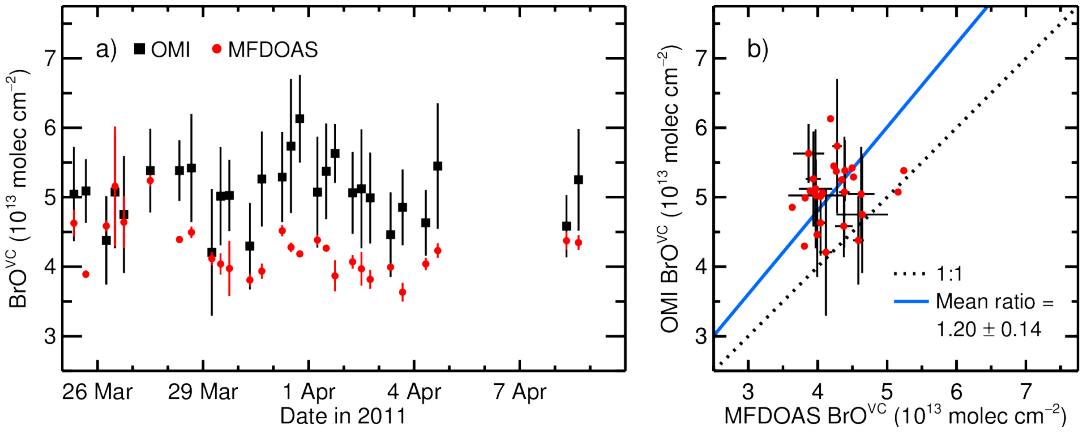

Figure 4-5. Simultaneous measurements of vertical column BrO over Fairbanks, Alaska obtained by OMI and MFDOAS. (a) Black squares are daytime OMI observations of BrO^{VC}, and error bars are the reported 1σ total measurement uncertainty. Red points are MFDOAS observations, averaged for 1 hour around each OMI retrieval. The error bars for MFDOAS are the root sum of squares combination of the DOAS fitting uncertainty and standard deviation of the measurements within 1 hour of each OMI observation. (b) The OMI observations of BrO^{VC} as a function of MFDOAS BrO^{VC}. Error bars are shown for every other measurement, for clarity. The mean and standard deviation of the OMI/MFDOAS BrO^{VC} ratio is 1.20 ± 0.14, represented by the blue line. The 1 to 1 line is shown for comparison.

The latest revision of the OMI retrieval algorithm (version 3) revised the wavelength window from 340.5 – 357.5 nm to 319 – 347.5 nm, in order to include more regions where the BrO signal has a well-defined structure (Suleiman et al., 2018). MFDOAS retrievals using the OMI fitting window produce values of BrO^{VC} similar in magnitude to OMI. However, the OMI fitting window produced non-physical

variability in MFDOAS measurements over the course of a day, indicating potential influence from other absorbing trace gases. Ultimately, the 336 – 359 nm window was chosen for the MFDOAS instrument to produce the most stable BrO^{VC} product that demonstrated expected daytime variation and least sensitivity to other DOAS fitting parameters.

Past studies have compared OMI measurements of BrO^{VC} over Harestua, Norway (60°N, 11°E) to ground-based DOAS observations for 2005 through 2011 (Choi et al., 2018; Suleiman et al., 2018). The DOAS measurements at Harestua employed the same cross sections for BrO and wavelength fitting window that was used by the MFDOAS instrument in the Fairbanks campaign (Hendrick et al., 2007). Choi et al. (2018) analyzed March and April twilight observations of BrO^{VC} from the ground-based instrument in the evening over Harestua. After converting the ground-based measurements to the OMI overpass time using a photochemical box model (Hendrick et al., 2007), the mean and standard deviation of the OMI to ground-based BrO^{VC} ratio was found to be 1.13 ± 0.12. Over Harestua, Suleiman et al. (2018) calculate a mean ratio of 1.03 ± 0.16, lower than the ratio found by the Choi et al. (2018) study. Unlike Choi et al. (2018), the comparison by Suleiman et al. (2018) uses daily mean observations for February through August from the ground-based instrument. The OMI/MFDOAS ratio calculated over Fairbanks is higher than both values but within standard deviation of the Choi et al. (2018) study.

4-4.2. The Contribution of VSLS to Stratospheric Bromine

For the entire spring 2011 campaign, vertical columns of stratospheric BrO are simulated using the box model described in Section 3.3 for five kinetic scenarios and

seven values of Br_y^{VSLS}. Figure 4-6 shows observed and modeled BrO^{VC} over Fairbanks on 1 April 2011. The lines in Figure 4-6 are simulations including 0 to 9 ppt of Br_y^{VSLS} using JPL (Figure 4-6a) and IUPAC (J & k) kinetics (Figure 4-6b). Similar figures for the remaining days with daytime MFDOAS measurements are shown in Figure 4-7. The solid lines in Figure 4-7 are simulated using JPL kinetics, and the dashed lines are simulated using IUPAC (J & k) kinetics.

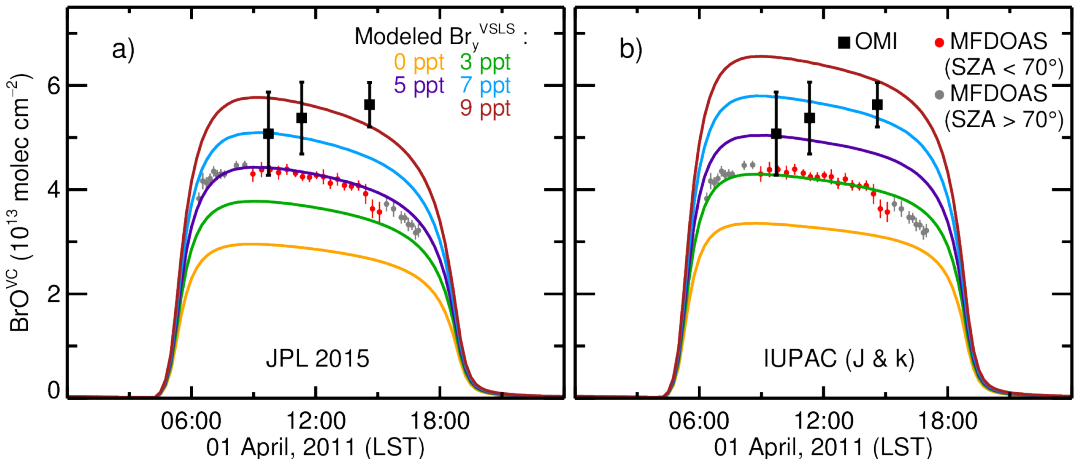

Figure 4-6. Vertical columns of BrO over Fairbanks, Alaska on 1 April, 2011. The time shown is local solar time (LST). Daytime observations of BrO^{VC} are shown for MFDOAS in red and OMI in black. MFDOAS measurements of BrO^{VC} collected at SZA > 70° are shown in grey. Error bars represent the 1σ total uncertainty in each measurement. Lines are modeled BrO^{VC} for the (a) JPL and (b) IUPAC (J & k) kinetic simulations. Modeled BrO^{VC} for both kinetic scenarios are shown for five different loadings of Br_y^{VSLS}.

Observations of BrO^{VC} collected at SZAs < 70° are shown in red in Figure 4-6 and Figure 4-7. During the day, modeled BrO^{VC} has a gradual, nearly linear decline with increasing time. At larger SZAs where BrO^{VC} changes rapidly with time, the diurnal variation is highly sensitive to kinetic uncertainties. Between SZAs of about 69° and 74°, the model begins to deviate from the daytime linear trend. The exact choice of the SZA threshold does not affect our interpretation of the MFDOAS data.

The correlation between modeled BrO^{VC} and MFDOAS observations at SZAs > 70° (show in grey) is discussed in Section 4-4.3.

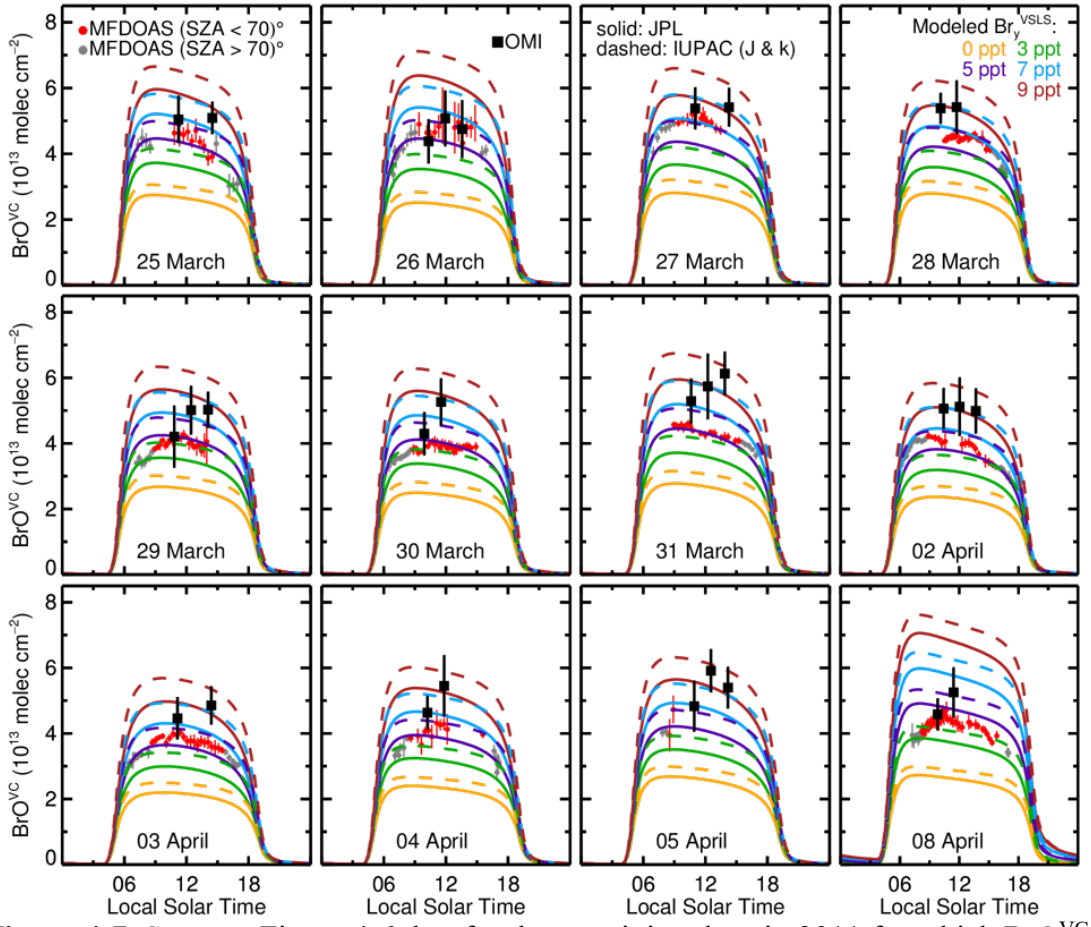

Figure 4-7. Same as Figure 4-6, but for the remaining days in 2011 for which BrO^{VC} was collected over Fairbanks, Alaska. Modeled BrO^{VC} for the JPL kinetic scenario is shown using solid lines. Modeled BrO^{VC} for the IUPAC (J & k) scenario is shown using dashed lines. Simulations and measurements of BrO^{VC} for 1 April are shown in Figure 4-6. Daytime MFDOAS measurements were not collected on 6 and 7 April.

As seen in Figure 4-6 and 4-7, higher quantities of Br_y^{VSLS} included in the box model result in higher daytime simulations of BrO^{VC}. The application of IUPAC parameters for $BrONO_2$ reactions increases the modeled BrO/Br_y ratio. On 1 April, the model captures the daytime diurnal variation of BrO^{VC} observed by MFDOAS, and for JPL simulations (Figure 4-6a) the box model is able to best represent MFDOAS observations with 5 ppt of Br_y^{VSLS}. For the IUPAC (J & k) simulations, only ~3 ppt of

Br_y^{VSLS} is needed to accurately model MFDOAS BrO^{VC}. On 1 April, BrO^{VC} is available from three daytime OMI overpasses within 200 km of Fairbanks, Alaska (black squares in Figure 4-6). These three measurements do not closely follow the modeled diurnal variation and are lie between the JPL simulations that include 7 and 11 ppt of Br_y^{VSLS} and the IUPAC (J & k) simulations that include 5 and 9 ppt of Br_y^{VSLS}.

For the remaining days, there are 2 or 3 OMI orbits over Fairbanks (Figures 4-7). To compare the range of OMI and MFDOAS observations to modeled BrO^{VC}, the observed and modeled BrO^{VC} for the whole campaign is shown at noon in Figure 8. MFDOAS and OMI daytime BrO^{VC} are scaled to noon using the modeled diurnal variation, shown for 1 April in Figure 6 and for all other days in Figure 4-7. The daily mean and standard deviation for each set of measurements is shown in Figure 4-8. Dotted lines are modeled BrO^{VC} at noon for the JPL and IUPAC (J & k) simulations with 0 to 9 ppt of Br_y^{VSLS} (in 2 ppt increments). Box model simulations for 11 to 13 ppt of Br_y^{VSLS} are not shown.

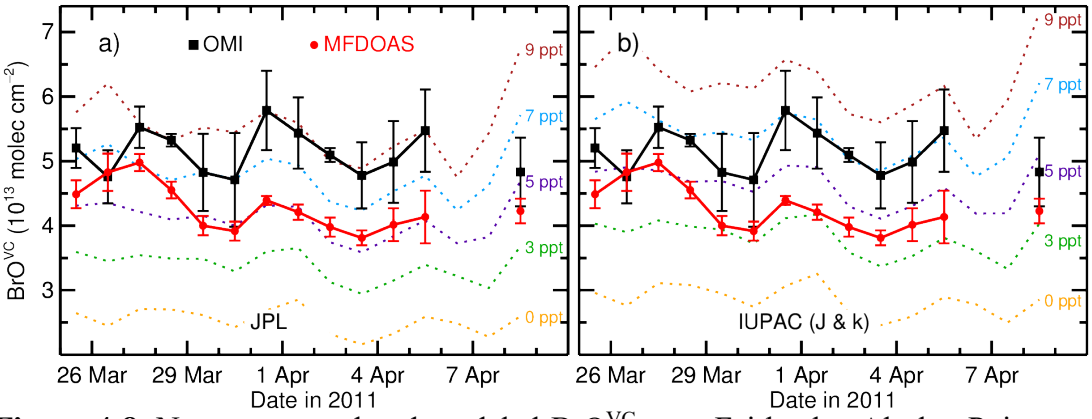

Figure 4-8. Noon measured and modeled BrO^{VC} over Fairbanks, Alaska. Points are daily mean measurements, scaled to noon using modeled diurnal variation, and error bars are the standard deviation about the mean. Dotted lines are modeled BrO^{VC} at noon using (a) JPL kinetics and (b) IUPAC (J & k) kinetics for various Br_y^{VSLS} loadings, ranging from 0 to 9 ppt.

In Figure 4-8a, BrO^{VC} is modeled using JPL kinetics. For these JPL simulations including 5 ppt of Br_y^{VSLS}, the model closely represents MFDOAS measurements on most days in March and April 2011. However, the 5 ppt loading of Br_y^{VSLS} underestimates MFDOAS observations on 26 through 28 March. The JPL simulations generally need to include between 7 and 9 ppt of Br_y^{VSLS} to accurately simulate OMI observations of BrO^{VC}. However, BrO^{VC} modeled with 7 ppt of Br_y^{VSLS} overestimates OMI measurements on 26 March and 8 April.

To determine the mean amount of Br_y^{VSLS} most consistent will all of the observations, we interpolate simulations of BrO^{VC} as a function of Br_y^{VSLS} to the value of each daytime OMI and MFDOAS measurement. The mean interpolated Br_y^{VSLS} is given in Table 4-1 for both OMI and MFDOAS as well as five kinetic scenarios. On average, when the model is constrained to only JPL kinetics, observations are best simulated with 7.8 ppt and 5.2 ppt of Br_y^{VSLS} for the OMI and MFDOAS records of BrO^{VC}, respectively. The uncertainty reported in Table 4-1 is the combination in quadrature of the standard deviation about the mean interpolated value of Br_y^{VSLS} as well as the uncertainty in Br_y^{VSLS} due to measurement uncertainties of BrO^{VC} and OMI stratospheric column NO_2. The uncertainty in our estimates of Br_y^{VSLS} is discussed in further detail in Section 4-4.2.1.

Table 4-1. Mean estimates of Br_y^{VSLS} based on OMI and MFDOAS observations of BrO^{VC} for five kinetic scenarios. The reported errors are the combination in quadrature of the standard deviation about the mean estimate as well as the uncertainties due to BrO^{VC} and OMI stratospheric column NO_2 measurements (see text).

Instrument	Br_y^{VSLS} (ppt)				
	JPL	IUPAC (J)	IUPAC (k)	IUPAC (J & k)	Kreycy et al. kinetics
OMI	7.8 ± 2.5	7.4 ± 2.4	6.4 ± 2.2	6.1 ± 2.1	6.0 ± 2.1
MFDOAS	5.2 ± 1.1	4.8 ± 1.1	4.0 ± 0.9	3.8 ± 0.9	3.7 ± 0.9

In Figure 4-8b, BrO^{VC} is modeled using the IUPAC kinetic parameters for $BrONO_2$ formation (reaction 4-1) and photolysis (reaction 4-2). At stratospheric temperatures, IUPAC recommends a slower rate constant for $BrONO_2$ formation (Figure 4-1) and a larger cross section for $BrONO_2$ photolysis (Figure 4-2). Consequently, the modeled BrO/Br_y ratio is larger for the IUPAC (J & k) simulation than for JPL, and lower amounts of Br_y^{VSLS} are needed to accurately simulate each BrO^{VC} dataset.

When IUPAC $BrONO_2$ kinetic recommendations are applied, our best estimate of Br_y^{VSLS} decreases relative to that found using the JPL kinetics. If the model is constrained to IUPAC parameters for both reactions (4-1) and (4-2), our estimates of Br_y^{VSLS} are 6.1 and 3.8 ppt for the OMI and MFDOAS datasets, respectively (Table 4-1). The IUPAC (J & k) simulations are in close agreement with model runs conducted with the kinetic adjustments suggested by Kreycy et al. (2013). The IUPAC (J) scenario uses only the $BrONO_2$ cross sections from IUPAC, and the IUPAC (k) scenario uses only the reaction (1) rate constant from IUPAC with all other kinetic parameters following JPL. More than half of the decrease between the estimates of Br_y^{VSLS} for the JPL and IUPAC (J & k) simulations is due to the different kinetic recommendations for reaction (4-1), as demonstrated by the IUPAC (k) scenario (Table 4-1).

Aircraft observations in the Western Pacific suggest that the value of Br_y^{VSLS} is 5 ± 2 ppt (Wales et al., 2018). If we assume the OMI observations of BrO^{VC} are purely stratospheric, our estimates of Br_y^{VSLS} are within the upper range of uncertainty of the tropical Western Pacific (TWP) study if the IUPAC rate constants for $BrONO_2$ formation (reaction 4-1) are applied in the box model. Improved agreement is achieved

with the TWP study if the IUPAC parameters for both $BrONO_2$ reactions or if the Kreycy et al. (2013) kinetic recommendations are used. All estimates of Br_y^{VSLS} based on the MFDOAS observations are within the uncertainty of the TWP observations. The MFDOAS-based estimates that use JPL kinetics or JPL kinetics with the IUPAC $BrONO_2$ cross sections (reaction 4-2) are in closest agreement with the central value for Br_y^{VSLS} reported by Wales et al. (2018) for the TWP.

4-4.2.1. Error Analysis

Here we assess the uncertainties that govern our estimate of Br_y^{VSLS}. The absolute error reported in Table 4-1 includes uncertainties due to the following factors: the standard deviation about the mean estimate, the measurement uncertainty in each retrieval of BrO^{VC}, and the measurement uncertainty in OMI stratospheric column NO_2. For MFDOAS-based estimates, the standard deviation is ~20% of the mean estimates for each kinetic scenario. For OMI-based estimates the standard deviation is 22% of the mean estimates, slightly higher than found for MFDOAS.

We also quantify the effect of measurement uncertainties of BrO^{VC} on our estimate of Br_y^{VSLS}. Modeled values of Br_y^{VSLS} are found for the upper and lower limits of each observation of BrO^{VC} shown in Figure 4-6 and Figure 4-7. For each set of observations and kinetic scenario, we calculate the difference between the mean value of Br_y^{VSLS} (given in Table 4-1) and value of Br_y^{VSLS} from the 1σ limit of measurement error. On average, measurement uncertainty contributes a relative error of 11% for MFDOAS and 26% for OMI-based estimates of Br_y^{VSLS}.

As discussed in Section 4-2, the modeled BrO/Br_y ratio is sensitive to the value of NO_2 used in the photochemical box model. The uncertainty in the stratosphere-

troposphere separation of OMI NO_2 is 2×10^{14} molecules cm^{-2} over the course of the campaign. Simulations of BrO^{VC} have been repeated, constrained to match stratospheric columns of NO_2 adjusted by $\pm 2 \times 10^{14}$ molecules cm^{-2} (Bucsela et al., 2013). The results are interpolated over Br_y^{VSLS} to MFDOAS and OMI observations. The uncertainty in OMI stratospheric column NO_2 leads to a minor, ~0.2 ppt, contribution to all uncertainties of Br_y^{VSLS} in Table 4-1.

As discussed in Section 4-3.3, our primary estimates of Br_y^{VSLS} in Table 4-1 are calculated assuming the observations of BrO^{VC} are purely stratospheric. However, stratospheric mixing can transport active Br_y compounds into the upper troposphere. We use ozone as a stratospheric tracer to estimate the vertical extent of stratospherically-influenced air below the tropopause (Gettelman et al., 2011).

Simulations of BrO^{VC} shown in Figures 4-6 and 4-7 are calculated by integrating profiles of BrO above the tropopause pressure (red line in Figure 4-4). If modeled BrO^{VC} is calculated above an ozone threshold instead of the thermally-defined tropopause, our estimates of Br_y^{VSLS} in Table 4-1 decrease by 0.1 to 0.4 ppt. The OMI-based estimates of Br_y^{VSLS} with JPL and IUPAC (J) kinetics include a higher contribution of direct stratospheric injection of Br_y through PGI. Consequently, simulations of BrO^{VC} for these scenarios are more sensitive to BrO below the tropopause and decrease by 0.4 ppt. The estimates of Br_y^{VSLS} based on MFDOAS BrO^{VC} only decrease by 0.1 ppt when BrO below the tropopause is considered. All other estimates of Br_y^{VSLS} in Table 4-1 decrease by 0.3 ppt.

4-4.3. Diurnal Variation

At high SZAs, simulations of BrO^{VC} are sensitive to the kinetic uncertainties regulating the conversion between BrO and the nighttime reservoirs of Br_y. At night, Br_y is mostly in the form of $BrONO_2$ in the lower stratosphere. The Kreycy et al. (2013) study reported that simulations of BrO with JPL kinetics underestimated observations in the morning (SZA < −75°) and evening (SZA > 86°) over Kiruna, Sweden (68°N). The Fairbanks data does not support the kinetic adjustments proposed by Kreycy et al. (2013). However, as discussed below, there are uncertainties in our comparison between modeled and MFDOAS data that have not been fully resolved. Additionally, the balloon-born observations used by Kreycy et al. (2013) focused directly on the lower stratosphere where the BrO/Br_y ratio is more sensitive to reactions (4-1) and (4-2), while our study evaluates the total column BrO/Br_y ratio.

The ratio of modeled to MFDOAS BrO^{VC} is shown in Figure 4-9 as a function of SZA. Our estimates of Br_y^{VSLS} are based on only observations of BrO^{VC} collected at SZA less than 70° (white background in Figure 4-9). Periods where the SZA is greater than 70° are shaded grey. The individual MFDOAS measurements at these higher SZAs are shown in grey in Figures 4-6 and 4-7. The largest SZA where MFDOAS observations are collected is 84.8° in the morning and 81.3° in the evening. In Figure 4-9, morning SZAs have been multiplied by −1 to differentiate between morning and evening results, and ratios of modeled to measured BrO^{VC} are placed into 5° SZA bins.

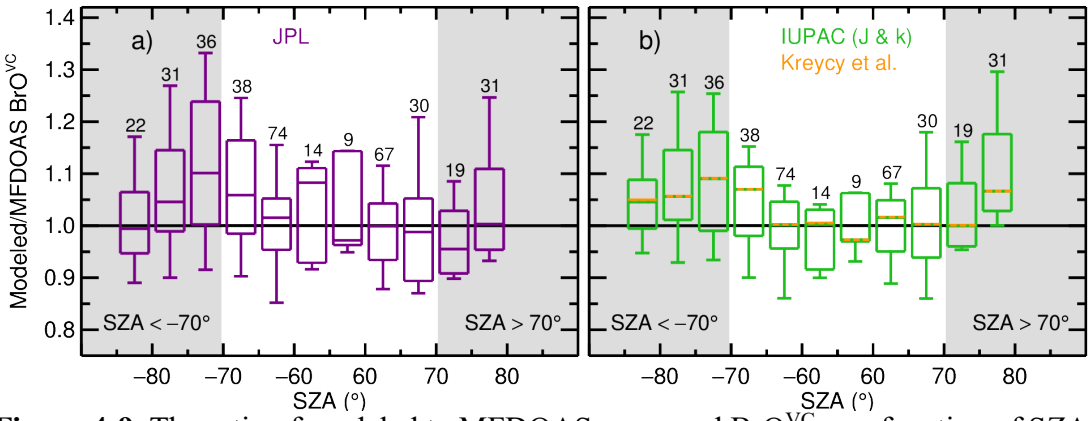

Figure 4-9. The ratio of modeled to MFDOAS measured BrO^{VC} as a function of SZA. Solar zenith angles before noon are shown as negative to differentiate between morning and evening results. Ratios are binned every 5° SZA. In each panel, the center lines for each bin are the median ratio, boxes are the 25 and 75 percentiles, and whiskers are the 5 and 95 percentiles. The number of measurements in each bin is given above the top whisker. The modeled to MFDOAS ratio of BrO^{VC} is shown for (a) JPL and (b) IUPAC (J & k) kinetic simulations. Orange lines in panel (b) represent the median modeled to MFDOAS ratio of BrO^{VC} for the simulations with reactions (4-1) and (4-2) scaled according to the recommendations of Kreycy et al. (2013). All modeled simulations use the respective mean estimates of Br_y^{VSLS}, given in the last row of Table 4-1.

For all kinetic simulations shown in Figure 4-9, the box model is initiated with the mean value of Br_y^{VSLS} found from daytime MFDOAS observations (Table 4-1). Simulations for the JPL kinetic scenario are shown in purple, while simulations using the IUPAC (J & k) scenario are shown in green. The whiskers are the 5 and 95 percentiles, boxes are the 25 and 75 percentiles, and center lines are the median ratio in each SZA bin. The orange lines in Figure 4-9b are the median ratios for the simulations scaled according to the Kreycy et al. (2013) recommendations. The median value for the IUPAC (J & k) and Kreycy et al. (2013) simulations are in near exact agreement with each other, as expected.

The photochemical simulation of BrO^{VC} is in agreement with MFDOAS observations (i.e., modeled/MFDOAS ratio is 1) for the 25 to 75 percentile of all SZA bins based on JPL kinetics. If BrO^{VC} is simulated using IUPAC (J & k) kinetics, the

modeled/MFDOAS ratio increases between SZAs of −85° and −80° in the morning and 70° and 80° in the evening. Modeled BrO^{VC} with IUPAC (J & k) kinetics better represents MFDOAS measurements in the evening 70° to 75° SZA bin. However, for the highest SZA bins the application of IUPAC kinetics results in worse agreement between modeled and measured BrO^{VC} compared to the JPL simulation. In particular, for the 75° to 80° SZA bin ~95% of modeled BrO^{VC} is higher than MFDOAS measurements upon application of IUPAC kinetics.

Based on the Kreycy et al. (2013) study, we would expect modeled BrO^{VC} to be low with respect to MFDOAS at high SZAs. However, the most notable feature in Figure 4-9 is the high model bias relative to MFDOAS BrO^{VC} in the morning twilight hours, seen for all three kinetic scenarios. The box model is constrained to GMI output at the OMI overpass time as well as OMI and ozonesonde measurements. During the campaign, the OMI overpass time is close to solar noon, while the ozonesondes were launched near 11:00 local solar time. In our box model simulations, we assume stratospheric Br_y, O_3, and NO_y are constant throughout the day. However, the effect of atmospheric transport could potentially mean that the ozone measurements and CFC-11 output from GMI, used to define stratospheric Br_y, may not be representative of the entire 24 hour period.

We use vertical column O_3 (O_3^{VC}) as an indicator for possible changes in atmospheric dynamics. Values of O_3^{VC} over Fairbanks, Alaska are shown in Figure 4-10 for 25 March through 8 April, 2011. In Figure 4-10, the black points are O_3^{VC} reported by OMI, while blue points are measurements collected by a ground-based Brewer spectrometer during the Fairbanks 2011 campaign. Brewer observations are

filtered to only include measurements where the reported error is less than 2 DU (Tzortziou et al., 2012). Output of O_3^{VC} reported by the National Center for Environmental Prediction (NCEP; doi: 10.5065/D6M043C6) is interpolated to 64.86°N and 212.15°E and is shown in red. Simulations of O_3^{VC} from the NCEP-final model are in excellent agreement with the Brewer and OMI measurements.

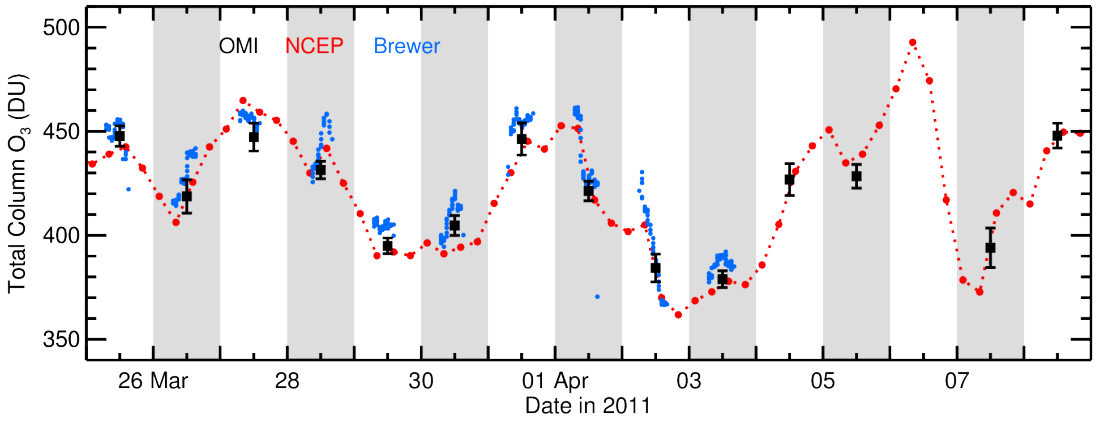

Figure 4-10. Total column O_3 over Fairbanks during the 2011 campaign. Measurements retrieved by OMI are shown in black. Ground-based measurements from a Brewer instrument are shown in blue. Total column ozone from the NCEP-FNL model are shown in red. The grey shaded regions are shown every other day.

For example, decreases in O_3^{VC} are observed during the day on 1 and 2 April, and a large increase in O_3^{VC} is simulated by the NCEP-final model on 4 April. Consequently, our assumption of constant stratospheric profile of Br_y throughout the day may not be valid on these three days. While the diurnal variation in MFDOAS BrO^{VC} is well captured by the model on 1 April (Figure 6), decreases and increases in MFDOAS BrO^{VC} on 2 April and 4 April, respectively, do not follow the modeled diurnal variation (Figure 7). Therefore, the standard deviation about our mean estimate of Br_y^{VSLS} (Table 1, Section 4.2.1) is likely influenced by changes in the stratospheric composition not accounted for by the box model.

However, we do not find evidence from O_3^{VC} that our high morning bias in modeled BrO^{VC} with respect to MFDOAS is due to atmospheric transport. On 1, 2, and 4 April the morning MFDOAS measurements are either close to or above modeled BrO^{VC} simulated using 5 ppt of Br_y^{VSLS} and JPL kinetics (solid, purple lines in Figures 4-6 and 4-7). In Figure 4-7, the morning MFDOAS measurements are most clearly lower than modeled BrO^{VC} on 29 and 30 March as well as 8 April. On 8 April, NCEP O_3^{VC} is lower in the morning than during the rest day, so atmospheric transport may be a contributing factor to the high modeled/MFDOAS BrO^{VC} on this day. However, O_3^{VC} is fairly constant on 29 and 30 March, so observations of O_3^{VC} on these days indicate that the modeled/MFDOAS ratio is likely not influenced by changes in stratospheric Br_y induced by atmospheric transport during the morning.

Overall, the ground-based MFDOAS observations of BrO^{VC} over Fairbanks obtained during spring 2011 do not support the findings of the Kreycy et al. (2013). The box model values of BrO^{VC} found using JPL kinetics do not consistently underestimate MFDOAS of BrO^{VC} observations at high SZA, as would be expected based on the conclusions of the Kreycy et al. (2013) study. Furthermore, the application of a slower rate constant for reaction (4-1) and higher cross sections for reaction (4-2) only improves agreement between modeled and measured BrO^{VC} within the evening 70° to 75° SZA bin. In the highest SZA bins (85° to 80° in the morning and 75° to 80° in the evening), the model simulations using the IUPAC recommendations for $BrONO_2$ reactions or the Kreycy et al. (2013) parameterization results in a modeled overestimate of MFDOAS BrO^{VC}.

4-4.4. Tropospheric Residual BrO

During the campaign, BrO in the lowest 2 km over Fairbanks was below the lower limit of detection of the MAX-DOAS instrument. However, Br_y compounds could be transported to the free troposphere from either non-local tropospheric sources or through stratosphere-troposphere exchange. Past studies have estimated that the tropospheric background BrO^{VC} can range from below 1×10^{13} molecules cm^{-2} (Schofield et al., 2004, 2006) to up to 3×10^{13} molecules cm^{-2} (Van Roozendael et al., 2002; Theys et al., 2011). Here, we assess the sensitivity of calculations for residual tropospheric BrO to the uncertainties in Br_y^{VSLS}, $BrONO_2$ kinetics, and the two different datasets of BrO^{VC}.

Table 4-2. Mean and standard deviation of calculated tropospheric BrO.

Instrument	Model Setup		Tropospheric BrO	
	Kinetics	Br_y^{VSLS} (ppt)	Column (10^{13} molec cm^{-2})	Mixing Ratio[a] (ppt)
OMI	JPL	7	0.3 ± 0.9	0.3 ± 0.9
OMI	JPL	5	1.3 ± 0.7	1.2 ± 0.7
OMI	JPL	3	2.3 ± 0.6	2.2 ± 0.6
OMI/1.20	JPL	5	0.2 ± 0.7	0.1 ± 0.7
OMI	IUPAC (J & k)	5	0.6 ± 0.7	0.5 ± 0.7

[a]Assuming BrO is well mixed between 2 km and the tropopause

In Table 4-2, tropospheric columns are calculated as described in Section 4-3.4. For each value of tropospheric BrO, the first column in Table 4-2 indicates the instrument used to measure total BrO^{VC}. To approximate the magnitude of MFDOAS retrievals of BrO^{VC}, we scale OMI measurements down by a factor of 1.20 (Figure 4-5). The second and third columns of Table 4-2 respectively indicate the kinetic scenario and value of Br_y^{VSLS} used to model stratospheric BrO^{VC}. The tropospheric mixing ratio of BrO is calculated from tropospheric BrO^{VC} assuming that BrO is vertically mixed

between 2 km and the tropopause height. The reported tropospheric BrO values are the mean and standard deviation during the Fairbanks campaign.

The first three rows in Table 4-2 utilize OMI measurements of BrO^{VC} and stratospheric simulations with JPL kinetics. If we assume OMI measurements of BrO^{VC} are purely stratospheric, 7.8 ± 2.5 ppt of Br_y^{VSLS} needs to be included in the box model to simulate the observations with JPL kinetics (Table 4-1). However, based on measurements in the TWP we expect 5 ± 2 ppt of bromine from VSLS reaches the stratosphere (Wales et al., 2018). When stratospheric BrO^{VC} is simulated using 5 ppt of Br_y^{VSLS} and JPL kinetics, we calculate a tropospheric residual of $1.3 \pm 0.4 \times 10^{13}$ molecules cm^{-2}. This value for tropospheric BrO^{VC} is close to the lower limit of previous studies (Van Roozendael et al., 2002; Hendrick et al., 2007; Theys et al., 2011).

If the true value of Br_y^{VSLS} is close to the 7 ppt upper limit of TTL-based estimates, tropospheric BrO^{VC} decreases to $0.3 \pm 0.9 \times 10^{13}$ molecules cm^{-2}. However, if the value of Br_y^{VSLS} is close to the 3 ppt lower limit, tropospheric BrO^{VC} would rise to $2.3 \pm 0.6 \times 10^{13}$ molecules cm^{-2}. Furthermore, if BrO is assumed to be vertically mixed between 2 km and the tropopause, the mixing ratio of BrO is between 0.3 and 2.2 ppt depending on the quantity of Br_y^{VSLS}. Consequently, the 3 to 7 ppt range in Br_y^{VSLS} is the largest source of uncertainty in our calculation of tropospheric residual BrO^{VC} over Fairbanks.

The second largest uncertainty in our calculation of tropospheric BrO^{VC} is due to the difference between OMI and MFDOAS retrievals of BrO^{VC}. If we assume MFDOAS measurements of BrO^{VC} are purely stratospheric, 5.4 ppt of Br_y^{VSLS} needs

to be included in the box model to simulate the observations with JPL kinetics (Table 4-1). If we reduce OMI BrO^{VC} by a factor of 1.20 to represent the magnitude of the MFDOAS observations, and we simulate stratospheric BrO^{VC} using JPL kinetics and the TWP-based best estimate of 5 ppt for Br_y^{VSLS}, our calculation of tropospheric BrO^{VC} is $0.2 \pm 0.7 \times 10^{13}$ molecules cm^{-2}. This value is 1.1×10^{13} molecules cm^{-2} lower than our estimate based on OMI measurements using the same stratospheric kinetics and estimate for Br_y^{VSLS}.

Finally, the IUPAC parameters for $BrONO_2$ kinetics increases the simulated ratio of BrO/Br_y. If we model stratospheric BrO^{VC} using IUPAC (J & k) kinetics and 5 ppt of Br_y^{VSLS}, we calculate tropospheric BrO^{VC} is $0.6 \pm 0.7 \times 10^{13}$ molecules cm^{-2} over Fairbanks based on OMI measurements. This value is 0.7×10^{13} molecules cm^{-2} lower than OMI-based calculations using JPL kinetics and lowers the free tropospheric mixing ratio of BrO by 0.7 ppt. As a result, depending on the parameters used to calculate tropospheric residual BrO, we find tropospheric BrO^{VC} between 0.2 and 2.3 $\times 10^{13}$ molecules cm^{-2}. Our estimates of BrO^{VC} are in agreement with the Schofield et al. (2004, 2006) ground-based studies conducted in New Zealand and Antarctica if either the upper limit of the TWP-based estimate of Br_y^{VSLS}, the MFDOAS retrievals of BrO^{VC}, or the IUPAC parameterization of $BrONO_2$ kinetics are supported by future studies. Only if the lower limit for Br_y^{VSLS} is applied do we find evidence for background tropospheric BrO^{VC} being close to the 3×10^{13} molecules cm^{-2} upper limit proposed by previous satellite-based studies (Van Roozendael et al., 2002; Theys et al., 2011).

4-5. Conclusions

In this chapter, we utilize satellite and ground-based measurements of vertical column BrO (BrO^{VC}) collected over Fairbanks, Alaska in March and April 2011. Fairbanks is located in central Alaska and is isolated from wind-blown sea salt and marine sources of active bromine. Consequently, we expect BrO in the lower troposphere (below ~2 km in altitude) to have a minimal contribution to the measurements of BrO^{VC}. We use a stratospheric box model to calculate upper limits for the contribution of VSLS to stratospheric Br_y (Br_y^{VSLS}) assuming the two measurements of BrO^{VC} are purely stratospheric.

The stratospheric box model uses kinetic parameters recommend in JPL (Burkholder et al., 2015). The model is constrained to ozonesonde measurements of temperature and O_3 in the lower stratosphere as well as long-lived tracers from the GMI chemical transport model. Stratospheric profiles of O_3 and nitrogen oxides within the box model are scaled to match the OMI observations of total column O_3 and stratospheric column NO_2. Profiles of inorganic bromine (Br_y) are defined using GMI CFC-11, according to the stratospheric tracer method described in Wales et al. (2018). Stratospheric BrO^{VC} is simulated over Fairbanks for spring 2011 for seven different values of Br_y^{VSLS}, ranging from 0 to 13 ppt. Additionally, stratospheric BrO^{VC} is calculated using JPL kinetics as well as kinetic recommendations for $BrONO_2$ formation and photolysis from IUPAC (Atkinson et al., 2007) and Kreycy et al. (2013).

The largest source of uncertainty in our estimate of Br_y^{VSLS} is due to the difference between the measurements of BrO^{VC} reported by the satellite-based OMI and ground-based MFDOAS instruments. Over Fairbanks, the satellite-based OMI (version 3) measurement of BrO^{VC} consistently higher than ground-based MFDOAS

observations, and the mean and standard deviation of the OMI/MFDOAS ratio of BrO^{VC} is 1.20 ± 0.14. The MFDOAS fitting retrieval uses a 336 to 359 nm wavelength window, while OMI uses 319 to 347.5 nm. The difference between the DOAS fitting windows could possibly be the cause of the systematic difference between the two retrievals. Further research is required to quantify the potential influence of interfering absorbers in both windows, and to assess which retrieval is more accurate. If we simulate BrO^{VC} using a stratospheric box model, 7.8 ± 2.5 ppt of Br_y^{VSLS} is needed to best represent OMI measurements of BrO^{VC}. Only 5.2 ± 1.1 ppt of Br_y^{VSLS} is needed to best represent MFDOAS BrO^{VC}. Consequently, the difference between the two datasets contributes a 2.6 ppt uncertainty in our estimate of Br_y^{VSLS}.

The modeled BrO/Br_y ratio is sensitive to kinetic uncertainties in the formation (reaction 4-1) and photolysis of $BrONO_2$ (reaction 4-2). The JPL (Burkholder et al., 2015) and IUPAC (Atkinson et al., 2007) kinetic evaluations review the same laboratory studies for reactions (4-1) and (4-2), but propose different rate constants and absorption cross sections. At stratospheric temperatures, the IUPAC parameters result in faster formation of $BrONO_2$ and slower $BrONO_2$ photolysis than the JPL recommendations. If the box model uses the IUPAC values for reactions (4-1) and (4-2), our value of Br_y^{VSLS} decreases to 6.1 ± 2.1 ppt and 3.8 ± 0.9 ppt, respectfully, for the OMI and MFDOAS measurements of BrO^{VC} over Fairbanks during spring 2011.

The different representations of the kinetics that govern formation and photolysis of $BrONO_2$ kinetics in JPL and IUPAC contribute a ~1.7 ppt uncertainty to our estimate of Br_y^{VSLS}. Only applying the IUPAC $BrONO_2$ cross sections results in a decrease of 0.4 ppt of Br_y^{VSLS}, while only applying the IUPAC rate constants for

reaction (4-1) decreases the value of Br_y^{VSLS} by ~1.3 ppt (both relative to a full JPL-based simulations). Modeled BrO^{VC} using kinetic adjustments proposed by Kreycy et al. (2013) is nearly identical to BrO^{VC} found by our IUPAC simulation. Based on the diurnal variation of the MFDOAS measurements of BrO^{VC}, we find better agreement with the JPL simulation than either IUPAC or the adjustment to $BrONO_2$ kinetics proposed by Kreycy et al. (2013). However, the BrO^{VC} measurements used by our study are not isolated to the lower stratosphere, and as a result, our analysis is not as sensitive to $BrONO_2$ chemistry as the Kreycy et al. (2013) balloon-borne study.

The current WMO estimate for Br_y^{VSLS} is 5 ± 2 ppt based on observations of VSLS and BrO entering the stratosphere through the TTL (World Meteorological Organization, 2018). Based on the OMI retrieval of BrO^{VC} and JPL kinetics, we have potential evidence for either the upper, 7 ppt limit of the Br_y^{VSLS} or up to 2.3×10^{13} molecules cm^{-2} of tropospheric BrO^{VC}. However, if stratospheric simulations of BrO are conducted using the IUPAC recommendations for $BrONO_2$ kinetics, our OMI-based estimate of Br_y^{VSLS} decreases to 6 ppt, closer to the WMO best estimate. The MFDOAS retrieval of BrO^{VC} does not support the 7 ppt upper limit of the WMO estimate of Br_y^{VSLS}. The calculated value of Br_y^{VSLS} based on MFDOAS measurements of BrO^{VC} and JPL kinetics is in near exact agreement with the WMO best estimate of 5 ppt with a minimal tropospheric contribution to column BrO over Fairbanks during spring 2011. If future laboratory studies support the IUPAC recommendation for $BrONO_2$ kinetics as well as the MFDOAS retrieval of BrO, the Fairbanks measurements are most consistent with the lower, 3 ppt limit for Br_y^{VSLS}.

Finally, we evaluate the sensitivity of tropospheric residual BrO to various factors. These calculations use OMI measurements of total BrO^{VC}, box model stratospheric BrO^{VC}, and tropospheric air mass factors calculated according to Choi et al. (2018). If the OMI measurements of BrO^{VC} are not assumed to be purely stratospheric, and the stratospheric box model is constrained to 5 ppt of Br_y^{VSLS} as well as JPL kinetics, the mean and standard deviation of tropospheric BrO^{VC} over Fairbanks is found to be $1.3 \pm 0.7 \times 10^{13}$ molecules cm^{-2}. In this case, the tropospheric BrO would result from long-range transport of surface emissions or stratosphere to troposphere exchange. This value is in close agreement with the lower limit of previous estimates for background tropospheric BrO (Van Roozendael et al., 2002; Theys et al., 2011). The 3 to 7 ppt range in Br_y^{VSLS} places an additional $\pm$ 1.0 $\times$ 10^{13} molecules cm^{-2} uncertainty on our estimate of tropospheric residual BrO, for OMI measurements of BrO^{VC} and JPL kinetics. Furthermore, when stratospheric BrO is simulated using IUPAC kinetics for $BrONO_2$, our central value for the tropospheric residual decreases to $0.6 \pm 0.7 \times 10^{13}$ molecules cm^{-2}, below the lower limit of past studies. If future research supports the accuracy of the MFDOAS retrieval of BrO^{VC} as well as JPL recommendations for the kinetics that govern $BrONO_2$ as well as the 5 ppt value for Br_y^{VSLS}, we do not find support for a global, ubiquitous background of tropospheric BrO extending over Fairbanks, Alaska during spring 2011. This finding is in agreement with the Schofield et al. (2004, 2006) studies conducted in the Southern Hemisphere.

Chapter 5: Representations of Equivalent Effective Stratospheric Chlorine and Observed Inorganic Chlorine in the Midlatitude Lower Stratosphere

5-1. Introduction

Regulations placed on ozone depleting substances have led to a steady decline in the surface mixing ratios of organic chlorine source gases since 1993 (Figure 1-1). Ozone depleting substances dissociate in the stratosphere, forming inorganic chlorine compounds ($Cl_y = HCl + ClONO_2 + ClO + HOCl + OClO + Cl + \ldots$). Throughout the stratosphere Cl_y is largely in the form of HCl, with modest partitioning into $ClONO_2$ as well as ClO in the upper stratosphere (Michelsen et al., 1996; Zander et al., 1996; Nassar et al., 2006; Santee et al., 2008). Numerous studies have monitored the growth and decline in stratospheric Cl_y using ground and satellite-based measurements of HCl (e.g., Rinsland et al., 2003; Froidevaux et al., 2006; Brown et al., 2011; Jones et al., 2011; Mahieu et al., 2014). In this chapter, various methods for calculating Equivalent Effective Stratospheric Chlorine (EESC) and their ability to accurately represent HCl and $ClONO_2$ in the midlatitude lower stratosphere will be evaluated.

Recovery of the ozone layer over Antarctica has recently been attributed to the decrease in halocarbons (Solomon et al., 2016; Strahan and Douglass, 2018). However, recovery of the ozone layer at midlatitudes has not been conclusively observed (Pawson et al., 2014; Ball et al., 2018). Interannual changes in the abundance of ozone in the lower stratosphere are sensitive to chemical processes as well as atmospheric transport and aerosol loading (Pawson et al., 2014). Since ozone abundances are higher in the lower stratosphere, interpretation of trends in total column ozone must properly account for the lower stratosphere. Numerous studies have focused on separating the influence

of halogens and atmospheric dynamics on the midlatitude ozone trend (e.g., Yang et al., 2006; Kiesewetter et al., 2010; Chipperfield et al., 2018). Furthermore, ozone in the midlatitude lower stratosphere is susceptible not only to the supply of halogens from VSLS but also variations in dynamics caused by climate change (Shepherd, 2008; Dhomse et al., 2018).

Stratospheric age of air is an important diagnostic that represents the mean time since a parcel of air entered the stratosphere. Halocarbon source gases, emitted in the troposphere, are transported to the stratosphere through the tropical tropopause. Within the stratosphere, air follows the Brewer Dobson circulation and travels from the tropics to higher latitudes before descending in polar regions. Consequently, the mean age of air in the lower stratosphere (~20 km in altitude) in polar regions is much older than air in the tropics and midlatitudes at the same altitude (Waugh and Hall, 2002). As air photochemically ages in the stratosphere, organic halocarbons dissociate, releasing halogen atoms. In stratospherically aged air found in the lower stratosphere over polar regions, halocarbons are nearly fully dissociated, releasing most of the contained Cl_y and Br_y (Newman et al., 2007; Engel et al., 2018). Under this circumstance, Cl_y and Br_y are nearly equal to total chlorine and bromine atomicity of long-lived organic source compounds that transit through the tropical tropopause, with a temporal delay of 5.5 to 6 years. In the midlatitude lower stratosphere, analysis of the inorganic halogen trends must properly estimate the fraction of chlorine and bromine still contained by the organic source gases.

EESC is a metric for relating the time series of the organic source gases at the surface to the stratospheric loading of inorganic halogens (Daniel et al., 1995). The

value of EESC represents the weighted quantity of Cl_y and Br_y at a given point in the stratosphere. EESC at a given time (t) is calculated using the stratospheric age of air (Γ) and the mixing ratio of each organic source gas (ρ^{entry}) at entry into the stratosphere. For EESC studies over the midlatitudes, a mean age of 3 years is typically used to represent air parcels around 20 km, while for air over polar regions the mean age is usually specified as 5.5 years (Daniel et al., 2011). Past studies have used estimates of EESC to evaluate the role of halocarbon regulations in the recovery of the ozone layer, the potential impact of halocarbon emissions on climate change, as well as the potential response of the ozone layer to climate geoengineering (e.g., Daniel et al., 1995; Yang et al., 2006; Tilmes et al., 2008).

A simple representation of EESC treats ρ^{entry} as a delay of the surface mixing ratios of halocarbons (Daniel et al., 1995):

$$\mathrm{EESC}(t, \Gamma) = \sum_{Cl} n_i f_i(\Gamma) \rho_i^{entry}(t - \Gamma) + \alpha \sum_{Br} n_i f_i(\Gamma) \rho_i^{entry}(t - \Gamma) \qquad (5\text{-}1)$$

Fractional release factors (FRF, f) describe the fraction of ρ^{entry} that has dissociated at a given altitude (z) and latitude (x) (Solomon et al., 1992):

$$f_i = \frac{\rho_i^{entry} - \rho_i(z, x)}{\rho_i^{entry}} \qquad (5\text{-}2)$$

Quantities in equation (5-1) are weighted by the number of chlorine or bromine atoms in each halocarbon (n). Since bromine atoms contribute to ozone loss with greater catalytic efficiency than chlorine, the bromine term is multiplied by a factor (α) that is typically 60 for midlatitude studies and 65 for analysis of polar ozone (Daniel et al., 2006).

However, a specific parcel of air is an irreversible mixture of numerous air masses with different transit histories. Consequently, a more accurate age of air calculation accounts for the statistical distribution of the stratospheric ages within the air parcel. Incorporating the width of the age spectrum in the calculation of ρ^{entry} causes a slight delay in the timing of the peak EESC loading and reduces the magnitude of the peak in EESC compared to the value of EESC found using equation 5-1 (Newman et al., 2007). The modification of equation (5-1) developed by Newman et al. (2007), which involves a function to represent the statistical distribution of age of air, has been used by the past two WMO Ozone Assessments to analyze the consequences for ozone of various halocarbon emission scenarios (Daniel et al., 2011; Harris et al., 2014).

A recent study by Engel et al. (2018) proposed updates to the method described by Newman et al. (2007). The statistical age distribution assumed by Newman et al. (2007) to calculate ρ^{entry} and FRFs is based upon an inert tracer that does not experience chemical loss. However, within a given parcel of air the organic component will, on average, originate from younger air, while the inorganic component will originate from older air (Plumb et al., 1999; Ostermöller et al., 2017). Throughout this chapter, we will refer to the method presented by Engel et al. (2018) as Engel FRFs and by Newman et al. (2007) as Newman FRFs.

In air with a mean age of 5.5 years, the majority of the chlorine from sources gases has dissociated and formed Cl_y (i.e., all FRFs are near 1). As a result, the difference between the Engel et al. (2018) and Newman et al. (2007) calculations of EESC is small for 5.5 year old air. Conversely, for air with a mean age of 3 years, EESC calculated using the Engel FRFs has a longer delay relative to the surface record

than is found using the Newman FRFs. As a result, the peak value of Cl_y over midlatitudes calculated using Engel FRFs occurs later than values based on Newman FRFs. An important metric for assessing the recovery of the stratospheric loading of halogens is when EESC values return to 1980 levels. With Engel FRFs, the quantity of EESC in 1980 is lower and recovery of midlatitude EESC is 10 years later than estimated by Newman FRFs (Engel et al., 2018).

Nearly all prior studies that make use of EESC have not included the additional stratospheric supply of bromine and chlorine from VSLS. While brominated VSLS are produced by marine biology, chlorinated VSLS (CH_2Cl_2, $CHCl_3$, C_2Cl_4, and $C_2H_4Cl_2$) mostly have anthropogenic sources. Currently, VSLS supply a small fraction of the total stratospheric loading of Cl_y. However, unregulated anthropogenic emissions of CH_2Cl_2 have increased since 2000 (Hossaini et al., 2015b, 2017). Recent studies have indicated that chlorinated VSLS, emitted in the industrial midlatitudes, reach tropical regions of the troposphere and are transported to the stratosphere (Hossaini et al., 2015a; Oram et al., 2017). Continued growth of CH_2Cl_2 could significantly delay the recovery of the ozone layer to 1980 levels (Hossaini et al., 2017). Since long-lived source gases have not fully dissociated, VSLS can supply a much larger fraction of Cl_y in the midlatitude lower stratosphere than for in stratospherically aged air of polar regions.

In this chapter, the chlorine component of EESC in air with a mean age of 3 years is analyzed. Midlatitude measurements of HCl, $ClONO_2$, and N_2O collected by ground-based instruments over Jungfraujoch, Switzerland (46.5°N, 8.0°E) (Zander et al., 2008) are utilized as well as space-based instruments from the Atmospheric Trace

Molecule Spectroscopy (ATMOS; Gunson et al., 1996) project and the Atmospheric Chemistry Experiment-Fourier Transform Spectrometer (ACE-FTS; Bernath et al., 2005; Boone et al., 2005). In the midlatitude lower stratosphere, Cl_y is almost entirely in the form of HCl and $ClONO_2$ (Zander et al., 1996; Nassar et al., 2006). The altitude of 3 year old air is isolated using observations of N_2O, while the sum of HCl and $ClONO_2$ serves as a proxy for total Cl_y. Finally, the time series of Cl_y with a mean age of 3 years is compared to various calculations for the chlorine term in EESC (equation 1) that consider the Newman and Engel FRFs as well as the potential contribution of VSLS.

The work presented in this chapter was prepared as part of ongoing research conducted by Walter Tribett and other members of the research group. The goal of our larger study is to quantify the effect of stratospheric halogens on the temporal evolution of the thickness of the ozone layer. We are analyzing trends in near global (55°S to 55°N) total column ozone using multiple linear regression with inorganic halogens (i.e. $Cl_y + \alpha Br_y$) defined through various possible formulations of EESC. This chapter quantifies observational support for the use of either the Newman or Engel FRFs as well as the possible role of stratospheric supply of chlorinated VSLS in the formation of EESC. The preliminary results of this larger study are that the time evolution of near global ozone is better simulated upon use of Engel FRFs and inclusion of chlorinated and brominated VSLS than by a model that makes use of Newman FRFs and neglects the contribution of VSLS. The former model (Engel FRFs + VSLS) indicates midlatitude ozone has recovered by about 27% relative to 1980 levels, whereas the later model (Newman FRFs, no VSLS) suggests ozone should have recovered by about 44%

relative to 1980 levels. In simulations that include Engel FRFs and VSLS, near global ozone recovers 50% relative to 1980 levels in year 2032, whereas this benchmark is reached in year 2021 for the simulations with Newman FRFs and no VSLS. At the time of submission, this larger study is under review for a possible 3 year program of support by NASA. This chapter focuses on the chlorine and age of air component of this study, which I have led.

5-2. Measurement Descriptions

5-2.1. Chlorinated VSLS

We account for the increase in chlorinated VSLS using aircraft measurements near the tropical tropopause. Measurements of chlorinated VSLS (CH_2Cl_2, $CHCl_3$, $C_2H_4Cl_2$, and C_2Cl_4,) were collected during six aircraft campaigns using the University of Miami Whole Air Sampler (WAS) instrument (Schauffler et al., 1999). The Pre-Aura Validation Experiment (Pre-AVE), Costa Rica-Aura Validation Experiment (CR-AVE), and Tropical Composition, Cloud and Climate Coupling (TC4) campaigns were conducted in 2004, 2006, and 2007, respectively. All three campaigns used the NASA WB-57 aircraft and were based in Central America (Toon et al., 2010). The three phases of the Airborne Tropical Tropopause Experiment (ATTREX) campaign were held in 2011, 2013, and 2014 and relied on the NASA Global Hawk aircraft (Jensen et al., 2013, 2017; Navarro et al., 2015). The 2014 phase of the ATTREX campaign took place in the tropical Western Pacific (see Chapter 2), while data shown for the 2011 and 2013 phases were collected in the tropical Eastern Pacific.

As discussed extensively in Chapter 2, the majority of air from the troposphere that reaches the stratosphere enters through the tropical tropopause. The average

tropopause height in the tropics is ~17 km. We calculate source gas injection from the chlorine content of VSLS between 16.5 and 17.5 km in the tropics (20°S to 20°N). The mean and standard deviation of the measurements of VSLS around the tropical tropopause is shown in Figure 5-1 for all six aircraft campaigns. All mixing ratios in this figure are multiplied by the chlorine atomicity of the respective VSLS. The total chlorine content of VSLS, shown as black points in Figure 5-1, is the sum of all four VSLS.

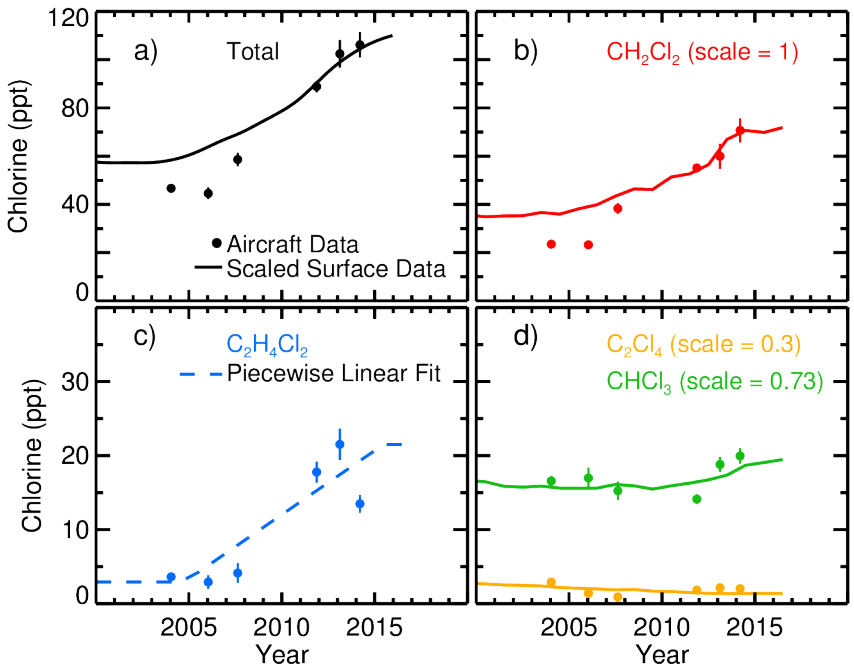

Figure 5-1. The chlorine content of VSLS in the upper tropical troposphere. The points and error bars are the mean and standard deviation of aircraft measurements VSLS between 16.5 and 17.5 km in the tropics. The solid lines are the surface mixing ratios, scaled by constant factor to represent tropospheric loss. (a) The sum of all chlorinated VSLS is shown in black. Points are the sum of aircraft measurements shown in panels (b), (c), and (d), and the line is the sum of scaled surface mixing ratios in panels (b) and (d) and the piecewise linear fit in panel (c). (b) Chlorine content of CH_2Cl_2 is shown, surface mixing ratios are not scaled to represent aircraft measurements in the tropical Pacific. (c) The dashed line is a piecewise linear fit to aircraft measurements. Surface measurements of $C_2H_4Cl_2$ are not published. (d) Chlorine content of C_2Cl_4 is shown in yellow, and the solid line is surface mixing ratios are scaled by 0.3. Chlorine content of $CHCl_3$ is shown in green, and surface mixing ratios are scaled by 0.73. All mixing ratios are multiplied by chlorine atomicity.

The solid line in Figure 5-1 is the total chlorine content of VSLS included in the EESC calculations that will be shown in Section 5-4. Global mean surface measurements of CH_2Cl_2, $CHCl_3$, and C_2Cl_4 are reported by the NOAA Halocarbon and other Atmospheric Trace Species (HATS) and Advanced Global Atmospheric Gases Experiment (AGAGE) networks (Prinn et al., 2000; Montzka et al., 2011a). To represent the stratospheric loading of chlorinated VSLS, the global mean surface measurements are reduced by a constant multiplicative factor to best fit the aircraft measurements. Physically, this represents tropospheric loss of the various source gases, prior to reaching the tropical tropopause. Of the chlorinated VSLS, $CHCl_3$ is the longest lived in the upper troposphere with a lifetime of 190 days at 10 km in the tropics, and $C_2H_4Cl_2$ is the shortest lived chlorinated VSLS with a 90 day lifetime in the upper tropical troposphere (Carpenter et al., 2014). Consequently, we assume Cl_y from SGI of VSLS is fully released from the organic compounds in 3 year old air.

Surface measurements of $CHCl_3$ and C_2Cl_4 are reduced by factors of 0.73 and 0.3, respectively. Atmospheric lifetimes in the upper tropical troposphere is 190 days for $CHCl_3$, 179 days for CH_2Cl_2, and 119 days for C_2Cl_4 (Carpenter et al., 2014). The surface measurements of CH_2Cl_2 are not scaled, resulting in a good fit to the ATTREX measurements obtained in the tropics between 16.5 and 17.5 km. However, the unscaled surface levels of CH_2Cl_2 are high with respect to measurements near 17 km from the earlier three campaigns. The gap between aircraft data collected before and after 2010 may reflect less vigorous convection over Central America or the closer proximity of the later campaigns to the predominant anthropogenic source region in Asia. Since the later three measurements of CH_2Cl_2 includes measurements from the

tropical Western Pacific, and air enters the stratosphere predominantly over the tropical Western Pacific, we have decided to not scale the surface data to represent stratospheric injection of CH_2Cl_2. Finally, the contribution of $C_2H_4Cl_2$ (blue in Figure 5-1) to stratospheric chlorine is included as a linear fit to the aircraft data, with an assumed constant mixing ratio before 2004 and after 2014. Surface measurements of $C_2H_4Cl_2$ are not available from either the HATS or AGAGE networks at the time of submission.

5-2.2. Ground-Based Records

We use global surface observations of N_2O and SF_6 from the HATS network. Mixing ratios of N_2O and SF_6 have been determined using gas chromatography from air samples collected at 13 stations in remote locations (Hall et al., 2007, 2011). Stations are located in both hemispheres and global averages are performed using a cosine weighting of latitude. Data are archived by the NOAA Earth System Research Laboratory at: https://www.esrl.noaa.gov/gmd/hats/.

We analyze the stratospheric loading of chlorine using measurements collected by Fourier Transform-Infrared Spectroscopy (FTIR) instruments over Jungfraujoch, Switzerland (46.5°N, 8.0°E). The surface to tropopause transport time is analyzed using FTIR measurements over Mauna Loa (20°N, 156°W). The Jungfraujoch and Mauna Loa FTIR stations are part of the Network for the Detection of Atmospheric Composition Change (NDACC) which includes 22 stations globally. A list of all stations collecting FTIR measurements is summarized in the Appendix in Table A5-1, and measurements are archived by NOAA at http://www.ndsc.ncep.noaa.gov/data/.

We use data from the Jungfraujoch station because profiles of Cl_y, F_y, and N_2O compounds are available for long periods of time, extending back before the expected

peak in stratospheric Cl_y (Zander et al., 2008; Duchatelet et al., 2009). The FTIR profiles are provided on a 1 km vertical grid in the lower stratosphere. We use profiles of HCl, $ClONO_2$, HF, COF_2, and N_2O from 1989 to 2016 over Jungfraujoch as well as profiles of N_2O from 1994 to 2017 over Mauna Loa. For both data sets, we calculate deseasonalized, monthly mean values of the FTIR data prior to the analysis presented in Sections 5-3 and 5-4. The 1σ error associated with each monthly mean is the combination in quadrature of the standard deviation and measurement uncertainties.

5-2.3. Space-Based Record

We analyze measurements of HCl, $ClONO_2$, and N_2O from the ATMOS project and the ACE-FTS instrument. Satellite observations of HCl are also available from the HALogen Occultation Experiment (HALOE; 1991 to 2005; Russell et al., 1994; Anderson et al., 2000) and Microwave Limb Sounder (MLS; 2004 to present; Livesey et al., 2018). However, HALOE did not monitor N_2O, and following failure of one MLS receiver, a measurement drift in the remaining, operating receiver was been detected for N_2O. The MLS drift in retrievals of N_2O begin in 2009 and affect pressure levels relevant to this study (Livesey et al., 2018). Consequently, we do not have a reliable method for isolating 3 year old air from the HALOE and MLS datasets.

The ATMOS instrument flew onboard the NASA space shuttle in 1985, 1992, 1993, and 1994. ATMOS measured sunrise and sunset solar occultation profiles of HCl, $ClONO_2$, and N_2O using infrared spectroscopy (Gunson et al., 1996). To compare the ATMOS observations to the Jungfraujoch record, we only use midlatitude measurements collected between latitudes of 25° and 55° in the northern and southern hemispheres. Measurements from the March 1992 and April 1993 shuttle flights are

only available for the southern hemisphere midlatitudes, while midlatitude observations were only collected in the northern hemisphere for the November 1994 shuttle flight. We calculate zonal means in 10° latitude bins for each flight. Measurements from the 1985 flight are not considered in our study due to missing $ClONO_2$ below 20 km.

The design of ACE-FTS is based on the ATMOS instrument. Occultation measurements from ACE-FTS, onboard the SCISAT-1 satellite, have been available since 2004. The ACE-FTS instrument retrieves sunrise and sunset profiles of HCl, $ClONO_2$, HF, COClF, COF_2, N_2O, and SF_6 on a 4 km vertical resolution in the lower stratosphere (Bernath et al., 2005; Boone et al., 2005). The profiles are provided on a 1 km vertical grid and are available at https://databace.scisat.ca/level2.

The ACE-FTS measurements obtained between latitudes of 25° and 55° in the northern and southern hemispheres are used to analyze Cl_y. Measurements of N_2O between 25°S and 25°N are used to assess the surface to tropopause transport time. The ACE satellite is in a high inclination (74°), low Earth circular orbit, and the latitudes that ACE-FTS samples roughly repeats every year. Consequently, we only include observations from full years (i.e., 2004 to 2017) to assure even global coverage. We deseasonalize the ACE-FTS measurements and sort data into monthly, zonal means in 10° latitude bins for the analysis in Sections 5-3 and 5-4. Following the procedure used by Froidevaux et al. (2015), we filter out ACE-FTS measurements that are outside of the 2.5σ standard deviation of the median of each bin and only include bins with at least 10 measurements.

5-3. Age of Air Calculations

5-3.1. N_2O Stratospheric Tracer

We use the N_2O age of air relation described in Engel et al. (2002) to sample the satellite and FTIR measurements for 3 year old air. The stratospheric age of air is the mean time a parcel of air has been in the stratosphere. Engel et al. (2002) calculated age of air using balloon-borne observations of SF_6 and CO_2. Both of these compounds have nearly linear tropospheric trends and negligible stratospheric sources and sinks. In general, the mean time since the sampled parcel of air was last in the troposphere is calculated using the tropospheric trend and a stratospheric measurement of a tracer. Further details for the calculating age of air from measurements of SF_6 are described in Section 5-3.2.

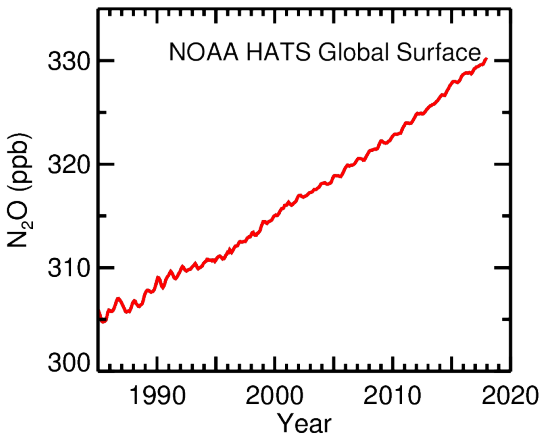

Figure 5-2. The global surface mixing ratio of N_2O as measured by the NOAA HATS network (Hall et al., 2007).

Mixing ratios of N_2O are well correlated with the stratospheric mean age of air (Plumb and Ko, 1992; Hall and Plumb, 1994; Volk et al., 1997). Current tropospheric mixing ratios of N_2O are ~330 ppb and have a nearly linear tropospheric trend. NOAA surface records from 1985 to 2018 are shown in Figure 5-2. In the stratosphere, N_2O breaks down following photolysis and reaction with $O(^1D)$. Engel et al. (2002)

determined a cubic relation between their calculated mean age of air (Γ, in years) and N_2O (in ppb):

$$\Gamma = 6.03 - 0.014(N_2O) + 8.59 \times (N_2O)^2 - 3.38 \times 10^{-7}(N_2O)^3 \quad (5\text{-}3)$$

Due to anthropogenic emissions of N_2O, the surface mixing ratio has increased over time (Figure 5-2). To analyze the FTIR and satellite measurements between 1988 and 2017, we use the NOAA HATS global surface record of N_2O to scale equation (5-3). Engel et al. (2002) measured SF_6, CO_2, and N_2O in four balloon flights, three in 1997 and one in 2000. The majority of their measurements collected in air that is ~3 years old and younger are from the 1997 flights. Consequently, we scale mixing ratios of N_2O in equation (5-3) using the ratio between the mean global surface mixing ratios of N_2O in 1997 and the same quantity for the time being analyzed.

The age of air calculations from Engel et al. (2002) do not account for the amount of time a parcel of air takes to transport from the surface to the tropical tropopause. We apply a 6 month delay to all calculations using equation (5-3) to account for the time needed for industrial emissions of N_2O and chlorinated source gases to mix into the tropics (Ko et al., 2003). For instance, to find the value of N_2O in a 3 year old parcel of air, we solve equation (5-3) for 3.5 years. This value is between transport times calculated from the ACE-FTS and FTIR measurements of N_2O (not shown), and within the range of tropospheric delays considered by past studies (Hall and Plumb, 1994; Boering et al., 1996; Volk et al., 1997). Since the magnitude of Cl_y rapidly increases as a function of altitude in the lower stratosphere, the uncertainty in our results due to this assumed 6 month delay will be considered.

To apply equation (5-3) to FTIR and satellite measurements of N_2O, we first solve equation (5-3) for 3.5 years. This resulting value of N_2O is shown as an × in Figure 5-3a, centered at 1997. The red line in Figure 5-3a is the 1997 mixing ratio of N_2O in 3 year old air (since entry into the stratosphere, equivalent to 3.5 year old air relative to global mean surface abundance), scaled to other years using the ratio of global surface mean N_2O in a given year to that measured in 1997.

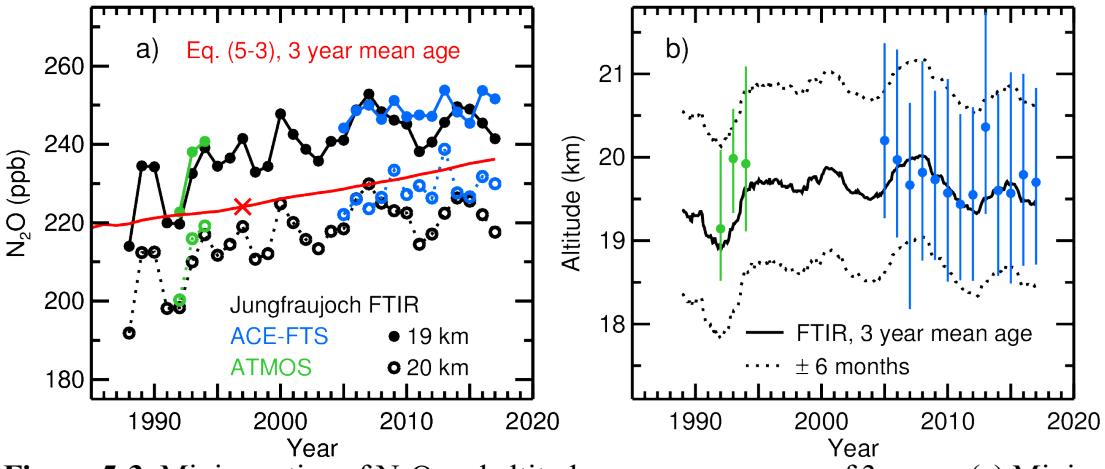

Figure 5-3. Mixing ratios of N_2O and altitudes near a mean age of 3 years. (a) Mixing ratios of N_2O in 3 year old air based on equation (5-3) are shown in red. The cross indicates the value in 1997, which is scaled to other years using the 1 year running mean of global surface values of N_2O. Solid circles are measured N_2O at 19 km and open circles are measured N_2O at 20 km from the FTIR (black), ATMOS (green), and ACE-FTS (blue) instruments. (b) The solid line and circles are the altitude for air that has a mean age of 3 years based on FITR, ATMOS, and ACE-FTS profiles of N_2O. Dotted lines and error bars are for mean ages of 3 years ± 6 months.

Yearly mean mixing ratios of N_2O at 19 and 20 km from the FTIR, ATMOS, and ACE-FTS instruments are shown in Figure 5-3a. Generally, values of N_2O associated with 3 year old air lie between the amounts observed at 19 and 20 km. Profiles of N_2O from the FTIR and satellite instruments are interpolated to find the altitude at which 3 year old air resides. The 1 year running mean for the resulting altitudes are shown in Figure 5-3b using a solid black line for the FTIR data and solid circles for ATMOS (green) and ACE-FTS (blue) measurements of N_2O. This process

is repeated for 2.5 and 3.5 year old air, with the results shown as dotted lines for the FTIR data and as error bars for ATMOS and ACE-FTS.

5-3.2. SF_6 Stratospheric Tracer

Here, we evaluate the consistency of our N_2O-based approach for isolating 3 year old air with a complementary analysis based on ACE-FTS measurements of SF_6. The abundance of SF_6 is a common tracer used calculate the mean age of air for stratospheric analyses (Waugh and Hall, 2002). In this section, we follow the approach of Volk et al. (1997) to calculate the mean age of air from ACE-FTS measurements.

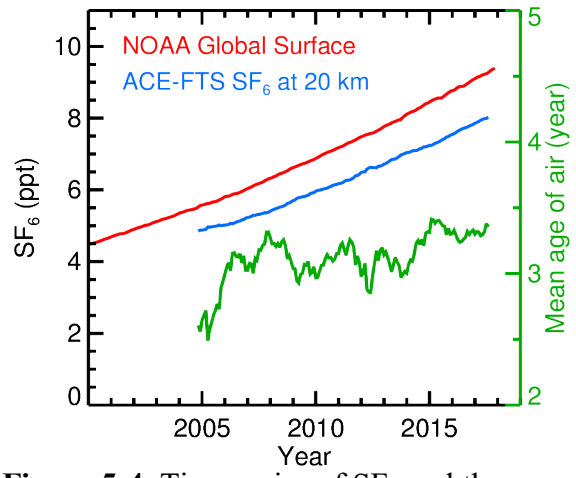

Figure 5-4. Time series of SF_6 and the mean age of air. The red line shows the global surface mixing ratio of SF_6 (Hall et al., 2011). The blue line depicts the 1 year running mean of the ACE-FTS measurements of SF_6 obtained at midlatitudes (55°S to 55°N), for 20 km in altitude. The green line is the 1 year running mean of the mean age of air at 20 km based upon analysis of midlatitude ACE-FTS at 20 and the surface record of SF_6 (red), using equation (5-5).

Surface mixing ratios of SF_6 from the HATS global stations are shown in red in Figure 5-4. The tropospheric mixing ratio of SF_6 has gradually increased over time with a nearly linear trend. Additionally, SF_6 does not have significant sources or sinks in the stratosphere. The yearly running mean of SF_6 measured by ACE-FTS at 20 km over midlatitudes (55°S to 55°N) is shown in blue. The mean age of air is estimated by

determining the last time the surface values of SF_6 were equal to the measured mixing ratio in a stratospheric parcel of air. However, age of air calculations in older parcels of air could be influenced by mesospheric loss of SF_6. Consequently, age of air calculations based on SF_6 are not recommended for air that is older than 5 years (Engel et al., 2002).

For compounds with purely linear tropospheric trends, the mean age of air can be calculated reliably from the time lag between measurement and tropospheric mixing ratios (Hall and Plumb, 1994). However, as discussed in Section 5-1, a stratospheric parcel of air is an irreversible mixture of air with different transit histories. Non-linearities in the tropospheric trend contribute to a systematic bias in mean age of air calculations using a time lag. A polynomial fit is applied to the NOAA HATS time series to define the surface mixing ratio of SF_6 (ρ^{surf}, in ppt) as a function of time (t, in years):

$$\rho^{surf}(t) = 4.48 + 0.19 \times (t - 2000) + 0.0046 \times (t - 2000)^2 \qquad (5\text{-}4)$$

The green line in Figure 5-4 is the 1 year running mean of the mean age of air at 20 km based on ACE-FTS measurements of SF_6. As in Section 5-3.1, we assume a 6 month delay for surface to tropopause transit time. Mean age of air is calculated from ACE-FTS midlatitude measurements of SF_6 at 20 km by solving equation (21) from Volk et al. (1997) for Γ:

$$SF_6(t) = \rho^{surf}(t - \Gamma - 0.5\ \text{yr}) + 2\Lambda \times 0.0046 \times (\Gamma + 0.5\ \text{yr}) \qquad (5\text{-}5)$$

The first term in equation (5-5) is ρ^{surf} from equation (5-4). The second term accounts for the width of the age spectrum (Δ). In the lower stratosphere, the ratio between Δ^2 and Γ are nearly constant with a value equal to Λ (Hall and Plumb, 1994):

$$\Lambda = \frac{\Delta^2}{\Gamma} \tag{5-6}$$

To compare our calculations from SF_6 to equation (5-3), we set $\Lambda = 0.7$ as used by Engel et al. (2002).

In Figure 5-5a we show age of air, calculated from 2017 ACE-FTS midlatitude measurements of SF_6, as a function of N_2O. The blue points represent monthly, zonal mean ACE-FTS at latitudes between 25° and 55° in both hemispheres. As air ages in the stratosphere, mixing ratios of N_2O decrease. For each year, we apply a cubic fit to the monthly, zonal mean data, shown by the solid line for 2017 in Figure 5-5a. The solid blue circles in Figure 5-5b are the value of N_2O in 3 year old air, based on these cubic fits. Generally, mixing ratios of N_2O in 3 year old air based on ACE-FTS SF_6 are slightly lower than values calculated using the Engel et al. (2002) relation in equation (5-3). As a result, mean altitudes for 3 year old air based on equation (5-5) will be slightly higher than the values shown in Figure 5-3b.

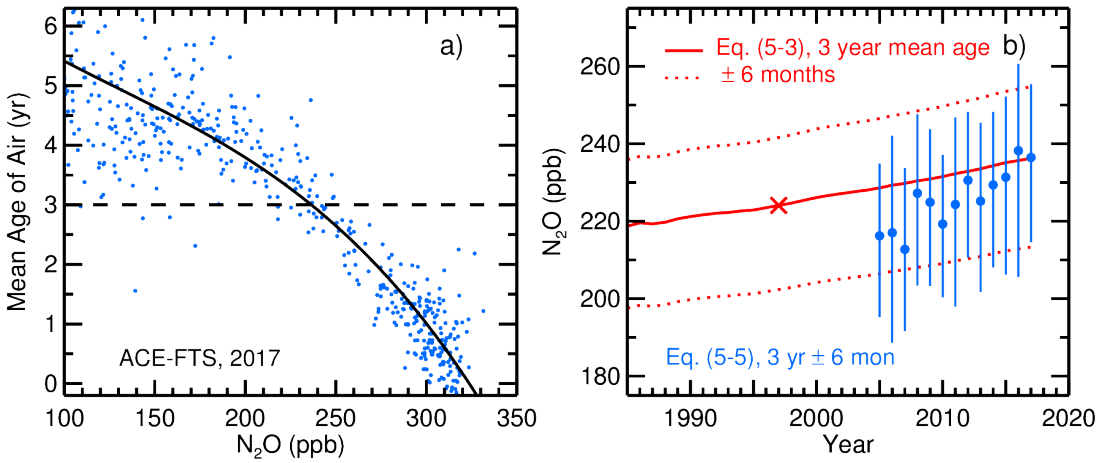

Figure 5-5. Age of air as a function of ACE-FTS N_2O in 2017 and values of N_2O associated with 3 ± 0.5 year old air. (a) Mean age of air found using ACE-FTS measurements of SF_6 colleced at midlatitudes in 2017, plotted as a function of ACE-FTS N_2O. Blue points are monthly, zonal means. The black line is a cubic fit to the data. The dashed line indicates a mean age of 3 years. (b) Mixing ratios of N_2O associated with 3 year old air based on equation (5-3) scaled to account for the temporal

rise in N_2O are shown as a solid red line, and mixing ratios of N_2O inferred from ACE-FTS measruements of SF_6, found using equation (5-5) to first infer age and then the cubic fit to the data in panel (a) are shown as blue circles. The dotted lines and error bars indicate mixing ratios of N_2O in 3 ± 0.5 year old air respectively based on equation (5-3) and equation (5-5).

5-4. Results and Discussion

We use the N_2O-defined altitude of 3 year old air (Section 5-3.1, Figure 5-3b) for our analysis. As discussed in Section 5-2.2, the FTIR instrument measures profiles of HCl, $ClONO_2$, HF, and COF_2 over Jungfraujoch (46.5°N). Past observations indicate that the majority of Cl_y in the lower stratospheric is in the form of HCl and $ClONO_2$ (Zander et al., 1996; Nassar et al., 2006). Based on CCMI archived zonal mean output from CAM4Chem and GEOSCCM (described in Chapter 3), HCl and $ClONO_2$ together represent about 99% of total Cl_y at 19.5 km and 46.5°N (Figure 5-6a). The modeled $(HCl + ClONO_2)/Cl_y$ fraction decreases to 98% between 1990 and 1995, coinciding with elevated levels of stratospheric aerosols following the eruption of Mount Pinatubo in June 1991.

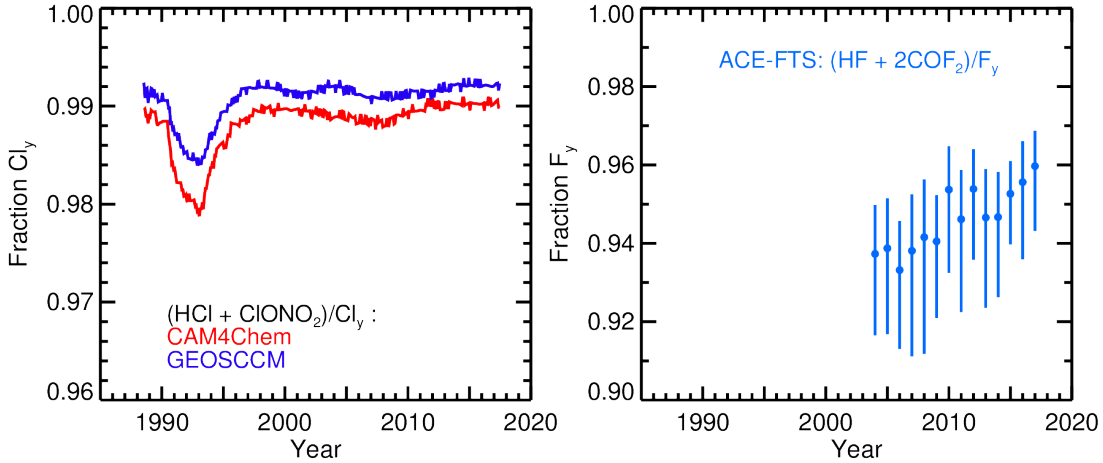

Figure 5-6. Fraction of observed Cl_y to total Cl_y and FTIR-observed F_y to total F_y at 19.5 km over Jungfraujoch. (a) CCMI monthly, zonal mean output of HCl, $ClONO_2$, and Cl_y at 46.5°N is interpolated in altitude to 19.5 km. The 3 year running mean of the fraction of HCl + $ClONO_2$ to total Cl_y is shown for CAM4Chem (red) and GEOSCCM (blue) CCMI model output. (b) ACE-FTS measurements of HF, COClF, and COF_2 between 41° and 51°N are interpolated to 19.5 km. The fraction of the sum of HF +

$2\times COF_2$ to total F_y is shown. Points are yearly means, and error bars are the standard deviation about the mean.

Additionally, the total fluorine product gases are HF, COF_2, and COClF. However, only HF and COF_2 are measured by the FTIR instrument. Based on ACE-FTS midlatitude observations at 19.5 km between 41° and 51°N, COClF is expected to contribute an additional 30 ppt to F_y. During the time period measured by the ACE-FTS instrument, the sum of FTIR-observed F_y compounds ($HF + 2 \times COF_2$) is between 93 and 96% of total F_y (Figure 5-6b).

FTIR profiles are interpolated to the altitude of 3 year old air, based on N_2O. The sum of observed fluorine product gases (observed $F_y = HF + 2 \times COF_2$) and observed Cl_y compounds ($HCl + ClONO_2$) over Jungfraujoch are shown in Figures 5-7a and 5-7b, respectively. Potential contributions of COClF to F_y are discussed below. In Figure 5-7, the grey points represent monthly mean FITR-observed F_y and Cl_y compounds, while the solid black line is the 3 year running mean of the monthly data. The blue lines represent F_y and Cl_y calculated using Newman FRFs, while the red lines are calculated using Engel FRFs. In Figures 5-7b and 5-7d, the solid blue and red lines include the stratospheric contribution of chlorinated VSLS while the dashed lines only consider stratospheric Cl_y from long-lived sources.

The measured Cl_y record over Jungfraujoch is smoothed using the time series of F_y. Any measured variability of F_y is expected to be due to dynamics, since this quantity is chemically stable. In Figure 5-7c, ΔCl_y is the difference between monthly Cl_y and the 3 year running mean (i.e., monthly – running mean), and ΔF_y is the difference between monthly F_y and the 3 year running mean. We expect that when ΔCl_y is well correlated with ΔF_y, the deviation of Cl_y from the long term trend is due to local

dynamics and not chemistry. The linear fit to ΔCl_y as a function of ΔF_y is shown as the dashed line in Figure 5-7c. The anomalies of measured Cl_y (ΔCl_y) exhibit an R^2 value of 0.63 with respect to the anomalies of measured F_y (ΔF_y), indicating the majority of the variations of measured Cl_y are indeed due to dynamical variability. The Cl_y time series shown in Figure 5-7d has been smoothed, based on the deviations in measured F_y from the long-term trend, to obtain a time series for Cl_y that has been corrected for dynamical variability.

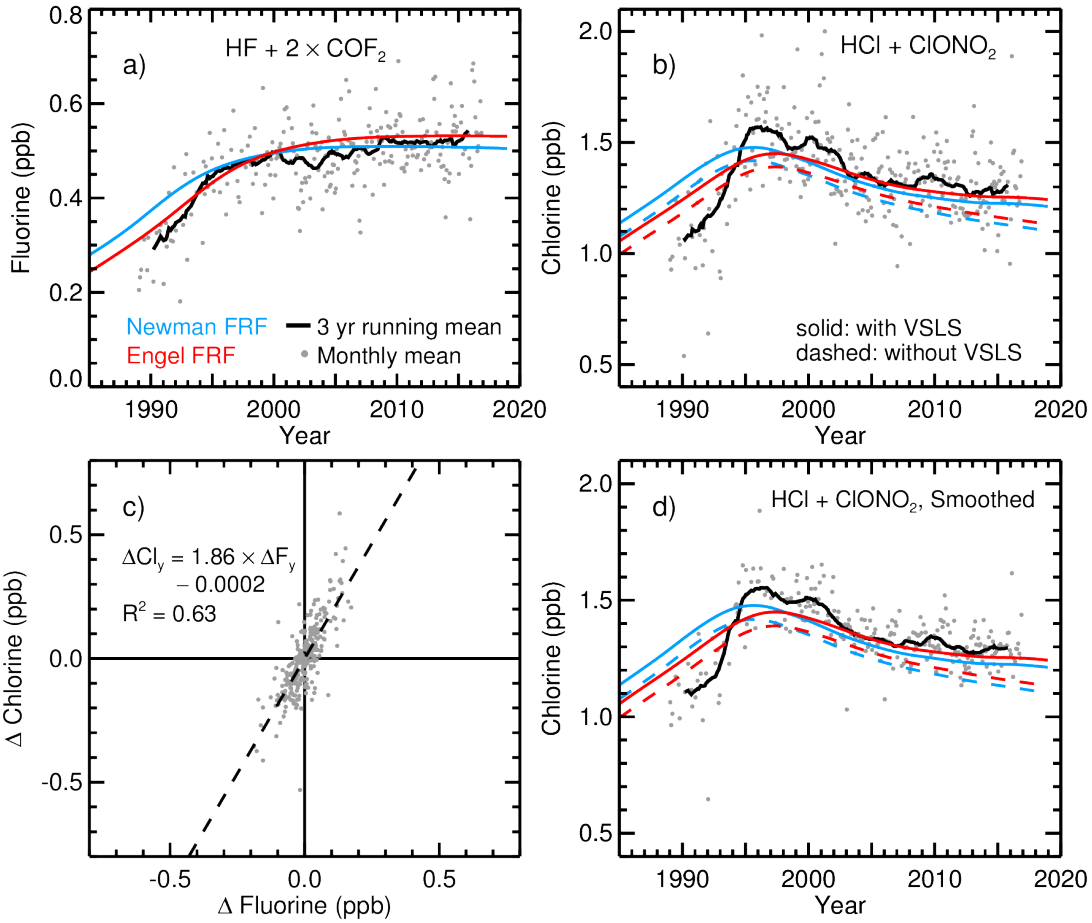

Figure 5-7. Inorganic fluorine and chlorine in air with a mean age of 3 years as measured by FTIR over Jungfraujoch and as calculated using various FRFs. In all panels, the grey points are monthly mean values. Inorganic fluorine is shown in panel (a). Inorganic chlorine is shown in panel (b). The difference between monthly mean inorganic fluorine and chlorine from the respective running means are shown in panel (c). In this panel, the dashed line is the linear fit to the differences, and the R^2 value of the linear fit is 0.63. In panel (d), the inorganic chlorine time series from panel (b) has

been smoothed using the linear fit shown in panel (c). The solid black lines in panels (a), (b), and (d) are the 3 year running means of the monthly data. Blue lines show the chlorine contribution to EESC calculated using Newman FRFs, and red lines show the same quantity found using Engel FRFs. In panels (b) and (d) the solid blue and red lines also include chlorinated VSLS while the dashed lines neglect the contribution of VSLS.

The series of simulated F_y and Cl_y are shown in Figures 5-7a, 5-7b, and 5-7c using either FRFs reported by Newman et al. (2007) (blue lines) and Engel et al. (2018) (red lines) based on surface values of halocarbons recommended by the 2014 WMO Ozone Assessment (Harris et al., 2014; see Figure 1-1a). In Figures 5-7b and 5-7d, the dashed lines are used for estimates that do not include the stratospheric contribution of chlorinated VSLS. The solid lines in these panels include VSLS, found by applying a 3 year delay to the time series of total VSLS Cl_y shown as the black line in Figure 5-1a.

In Table 5-1, reduced χ^2 values for the fit of each FRF time series to the observed 3 year running means are given. The error used to calculate χ^2 is dominated by the standard deviation about the 3 year running mean. In general, the Engel FRFs more accurately represent observed F_y and Cl_y records in 3 year old air (i.e., lower values of reduced χ^2). Before 1994, the observed levels of F_y and Cl_y are both lower than simulated with either formulation for the FRFs. After 1995, the observed values of Cl_y are on average slightly higher than but in close agreement with Cl_y calculated with a stratospheric contribution of VSLS. Similarly, including chlorinated VSLS lowers the reduced χ^2 values for time series of Cl_y calculated with either FRF. Smoothing the measured Cl_y record to account for dynamical variability further reduces the values of reduced χ^2, and calculations using Engel FRFs with VSLS result in closest agreement with the observed record of Cl_y in the midlatitude, lower stratosphere.

Table 5-1. Reduced χ^2 goodness of fit to 3 year running mean of FTIR F_y (HF + $2\times COF_2$) and Cl_y ($HCl + ClONO_2$) in air with a mean age of 3 years. The 1σ standard deviation about the 3 year running mean was used at the uncertainty in the goodness of fit test.

	Reduced χ^2		
	F_y (HF + $2\times COF_2$)	Cl_y ($HCl + ClONO_2$)	Smoothed Cl_y
Newman FRF, no VSLS	0.22	0.82	0.79
Engel FRF, no VSLS	0.16	0.58	0.53
Newman FRF, VSLS	N/A	0.34	0.28
Engel FRF, VSLS	N/A	0.19	0.14

Our assumption of a 6 month surface to tropopause transport time results in close agreement between the observed and calculated records of F_y. Neglecting this 6 month delay in the age of air calculations results in the observed quantities of F_y being consistently lower than expected (not shown). Without the 6 month delay, the χ^2 values reported in Table 1 increase to 4.8 and 5.5 based on the Newman and Engel FRFs, respectively. Including an additional 0.03 ppb from COClF in the observed F_y values, shown in Figure 7a, adjusts the χ^2 values to 0.32 and 0.13, slightly improving the agreement with the Engel FRFs calculation. As a result, our assumption of a 6 month surface to tropopause transit time results excellent agreement with the observed photochemical aging of fluorine source gases that is found for stratospheric air with a mean age of 3 years since entry from the tropopause.

In Figure 5-8, we compare the FTIR record of Cl_y in 3 ± 0.5 year old air to data from ATMOS and ACE-FTS. In this figure, yearly means are shown for the ATMOS and ACE-FTS measurements, and a 3 year running mean is shown for FTIR observations. The grey shaded region and error bars represent the range of observed Cl_y in air that is 2.5 to 3.5 years old. The ATMOS measurements are in near exact agreement with the rise of Cl_y in 3 ± 0.5 year old air calculated over Jungfraujoch.

Additionally, the ACE-FTS record is close to, but generally slightly higher than, the FTIR measurements of Cl_y.

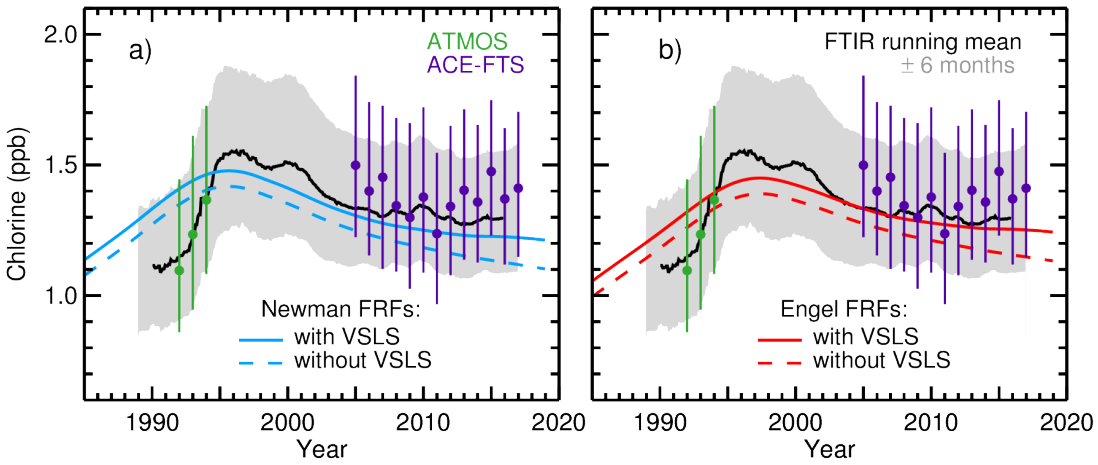

Figure 5-8. Inorganic chlorine in air with a mean age of 3 ± 0.5 years. The black line is FTIR Cl_y in 3 year old air, and the grey shaded region is the range of FTIR Cl_y in 3 ± 0.5 year old air. The solid green and purple points are the yearly mean of ATMOS and ACE-FTS measurements of HCl + $ClONO_2$ in 3 year old air, respectively. Error bars represent the yearly mean of ATMOS and ACE-FTS measurements in 3 ± 0.5 year old air. (a) The blue lines are Cl_y calculated using the Newman FRFs. (b) The red lines are Cl_y calculated using the Engel FRFs. In both panels, solid lines are FRF calculations that include a stratospheric source of chlorine from VSLS, while dashed lines do not consider VSLS.

The values of Cl_y with a mean age of 3 years is shown for Newman FRFs in Figure 5-8a and Engel FRFs in Figure 5-8b. The solid lines include the stratospheric contribution of chlorinated VSLS while the dashed lines only consider long-lived chlorine source gases. In both figures, the calculations with VSLS closely resemble FTIR measurements in 3 year old air for years after ~2003. After the peak in Cl_y, the calculations without VSLS are between measurements with a mean age of 3 to 2.5 years. Since we assume a 6 month delay in our calculations of stratospheric age of air, as discussed in Section 5-3, we cannot discount the Cl_y calculations that do not include VSLS. However, both the FTIR and ACE-FTS records indicate a more gradual decline in stratospheric Cl_y than is predicted by the model estimates of Cl_y that neglect VSLS.

For the years before ~1994, the FTIR and ATMOS measurements are consistently lower than all Cl_y calculations. As shown in Figure 5-6a, the modeled partitioning of Cl_y into HCl and $ClONO_2$ decreases following the eruption of Mount Pinatubo in June 1991. However, the lowest fraction of $(HCl + ClONO_2)/Cl_y$ is 0.98, which is too large to account for the difference between observed and calculated Cl_y. Between 1991 and 1993, the mean altitude calculated for 3 year old air exhibits a slight decrease (Figure 5-3b). Consequently, changes in atmospheric dynamics or the correlation between N_2O and mean age of air following this volcanic eruption could possibly contribute to the low measurements of Cl_y in the early 1990s. Finally, since FTIR measurements around 1990 more closely agree with the Engel FRFs calculation without VSLS (dashed line in Figure 5-8b), there might also be lower amounts of CH_2Cl_2 reaching the stratosphere than assumed in Figure 5-1. However, the dashed red line in Figure 5-8b assumes the stratospheric contribution of VSLS to Cl_y is 0, so this suggestion does not entirely account for the discrepancy between theory and observations of the early part of the record.

5-5. Conclusions

Previous assessments of the recovery of the ozone layer used EESC formulations defined by Newman et al. (2007) and neglected the contribution of VSLS to stratospheric halogens (Daniel et al., 2011; Harris et al., 2014). For the midlatitude lower stratosphere, an update to the method for calculating EESC delays the propagation of surface halocarbons into inorganic halogen compounds in the stratosphere (Engel et al., 2018). Additionally, there has been an observed rise in anthropogenic emissions of CH_2Cl_2, an anthropogenic VSLS not regulated by the

Montreal Protocol. Both the updated formulation of EESC and persistent growth of CH_2Cl_2 and other chlorinated VSLS would delay the recovery of the ozone layer, relative to a projection based on the old formulation of EESC that neglects chlorinated VSLS (Hossaini et al., 2017; Engel et al., 2018). Ground and space-based measurements of HCl and $ClONO_2$, collected between 1989 and 2017, are used to assess the ability of different EESC formulations to represent Cl_y in the midlatitude lower stratosphere. Properly representing inorganic halogens in the lower stratosphere is necessary to understand the relative contributions of halocarbon emissions, atmospheric dynamics, and stratospheric aerosol loading to changes in the ozone layer (Ball et al., 2018; Chipperfield et al., 2018).

Parcels of air with a 3 year mean age are isolated using a N_2O tracer relation calculated by Engel et al. (2002), updated to reflect temporal growth of N_2O. Measurements of N_2O, HCl, and $ClONO_2$ are available in the lower stratosphere over Jungfraujoch, Switzerland (46.5°N, 8.0°E) as well as from the space-based instruments, ATMOS and ACE-FTS, from 1989 to present. The observed profiles of N_2O are analyzed to determine the location of 3 year old air. For comparison, we also calculate the mean age of air from ACE-FTS measurements of SF_6. Calculations of the stratospheric age of air from SF_6 are similar to our N_2O calculations, but indicate that air with a 3 year mean age is generally at slightly higher altitudes (and hence has larger values of Cl_y) than our primary age of air calculations.

The FRF formulas describe the stratospheric decay of halogen source gases as a function of the mean time since air entered the stratosphere. We also assume a 6 month transit time for global abundances to reach the tropopause. We evaluate Cl_y in

air with a mean age of 3 ± 0.5 years to account for the range of tropopause transit times calculated from measurements of N_2O between 16.5 and 17.5 km in the tropics. Profiles of HF and COF_2 measured by FTIR over Jungfraujoch are interpolated to the estimated altitude of 3 ± 0.5 year old air. Based on our 6 month delay, the magnitude of observed F_y compounds (i.e., HF + 2 × COF_2) in air with a mean age of 3 years is represented extremely well by F_y calculated using both Newman et al. (2007) and Engel et al. (2018) FRFs. Additionally, calculated F_y is consistently higher than observed F_y for 2.5 year old air and lower than measurements for 3.5 year old, representing global mean surface to tropopause transit times of 0 to 12 months, respectively.

We analyze observed Cl_y (HCl + $ClONO_2$) at a mean age of 3 ± 0.5 years from FTIR, ATMOS, and ACE-FTS measurements. The Engel et al. (2018) formulations of EESC provide a better representation of the FTIR-observed F_y and Cl_y records over Jungfraujoch than the FRFs from Newman et al. (2007). Stratospheric chlorine from VSLS is included in the calculations of Cl_y using surface measurements from the NOAA HATS and multinational AGAGE networks, scaled to represent aircraft measurements near the tropical tropopause. For years after 2000, calculations of Cl_y that include VSLS provide the best representation of FTIR and ACE-FTS observations at a mean age of 3 years. Representations of Cl_y without VSLS are within the lower limit of measured uncertainty after 2000 and in close agreement with FTIR at ATMOS measurements in the early 1990s.

The results presented in this chapter were prepared in support of ozone regression analysis research. In this study, a multiple linear regression model is used to simulate column ozone as a function of total solar irradiance, EESC, aerosol optical

depth, and zonal winds. Simulations are conducted for two EESC scenarios. One scenario uses the FRFs defined by Newman et al. (2007) and does not include VSLS. The other scenario uses the Engel et al. (2018) FRFs and includes sources of stratospheric chlorine and bromine from VSLS. Brominated VSLS are assumed to contribute a constant 5 ppt to stratospheric bromine based on results presented in Chapter 2. Since bromine is more efficient than chlorine in depleting ozone, bromine content is scaled up by a factor of 60 (α in equation 1), and brominated VSLS contribute 0.03 ppb to EESC. The contribution of chlorinated VSLS to EESC follows the description presented in Section 5-2.1.

Simulations using Newman et al. (2007) FRFs and no VSLS indicate that near-global (55°S and 55°N) total column ozone has currently recovered by 44 ± 6% relative to a minimum in November 1996. Total column ozone modeled with Engel et al. (2018) FRFs and VSLS predicts a recovery of 27 ± 4% relative to a minimum in October 1998. Both simulations have been compared to a dataset of total column ozone collected between 55°S and 55°N from multiple satellite instruments (McPeters et al., 2013; Frith et al., 2014). The inclusion of Engel et al. (2018) FRFs and VSLS improves the ability of the model to represent the measured total column ozone record, especially during the past decade.

Future research will assess how well chemistry-climate models represent stratospheric Cl_y over the midlatitudes. This research will make use of models participating in the Chemistry Climate Modeling Initiative (CCMI, see Chapter 3). The CCMI models are all initiated with the same surface mixing ratios of long-lived halocarbons (Daniel et al., 2011) and do not include chlorinated VSLS (Eyring et al.,

2013). Dhomse et al. (2018) and Morgenstern et al. (2018) recently evaluated the simulated ozone recovery in CCMI models. A comparison of modeled Cl_y in these models is shown only for polar regions by Dhomse et al. (2018). As a result, previous evaluations of CCMI models do not provide insight into how well these models represent the stratospheric formation of Cl_y in the midlatitude lower stratosphere.

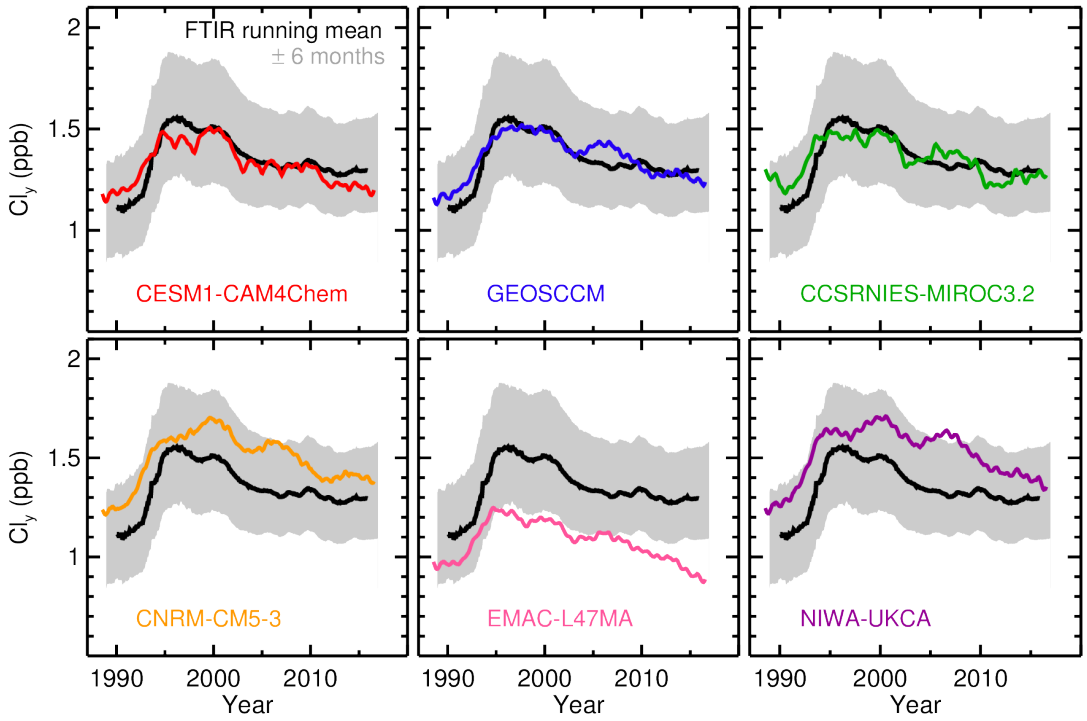

Figure 5-9. Modeled and observed inorganic chlorine in air with a mean age of 3 years. The black line is FTIR-observed Cl_y in 3 year old air, and the grey shaded region is the range of FTIR Cl_y in 3 ± 0.5 year old air as shown in Figure 5-8. The colored lines are Cl_y from various CCMI models at 46.5°N, interpolated to the altitude of 3 year old air, as indicated in Figure 5-3b. A description of the CCMI models is given in Chapter 3.

Stratospheric Cl_y from six models participating in CCMI is shown in Figure 5-9. All of the models used for Figure 5-9 are described in Chapter 3. In each panel the black line and grey shaded region is observed Cl_y ($HCl + ClONO_2$) in 3 ± 0.5 year old air over Jungfraujoch, as shown in Figure 5-8. The additional lines are CCMI model output of total Cl_y at 46.5°N, interpolated to altitudes with a mean age of 3 years as

defined using FTIR measurements of N_2O (Section 5-3.1, Figure 5-3b). With the exception of the EMAC model, simulated Cl_y is largely within the observed range of uncertainty even though these models do not include chlorinated VSLS. Both EMAC and CCSRNIES were identified by Dhomse et al. (2018) as having significantly low representations of Cl_y over polar regions that could not be explained only by differences in modeled dynamics. Over the midlatitudes, Cl_y in CCSRNIES is in close agreement with the Jungfraujoch observations, while Cl_y from EMAC is below the range of observations.

Previous studies have demonstrated that the distribution of Cl_y in global models is highly sensitive to transport and mixing within the models. The lifetimes of the organic source gases are determined by the rate of transport through the tropics (Douglass et al., 2008; Chipperfield et al., 2014). Levels of Cl_y in the lower stratosphere also depend on both the mean age of air as well as the fraction of air that is transported from the upper stratosphere (Waugh et al., 2007). As a result, additional research is required to determine how accurately these models represent the mean age of air in the midlatitude lower stratosphere. To achieve this task, long-term records of N_2O are available from numerous FTIR stations, listed in Table A5-1. Additionally, the model lifetimes of long-lived chlorine source gases can be evaluated using ACE-FTS measurements of N_2O, CFC-11, CFC-12, CCl_4, and CH_3Cl (Brown et al., 2011, 2013).

Chapter 6: Conclusions

6-1. Summary

Aircraft observations have been used to develop a comprehensive estimate of the contribution of very short-lived substances (VSLS) to the loading of stratospheric bromine. Measurements of VSLS, long-lived bromocarbons, and bromine monoxide (BrO) were collected during the Airborne Tropical TRopopause EXperiment (ATTREX; Jensen et al., 2017) and CONvective TRansport of Active Species in the Tropics (CONTRAST; Pan et al., 2017) aircraft campaigns in the winter of 2014 over the tropical Western Pacific (TWP). The bromine from VSLS can enter the stratosphere through organic (SGI, source gas injection) or inorganic bromine species (PGI, product gas injection). The TWP is a convectively active region that is expected to be the primary pathway for the transport of VSLS and their product gases from the troposphere to the stratosphere (Levine et al., 2007; Aschmann et al., 2009; Schofield et al., 2011; Bergman et al., 2012). Data collected during the CONTRAST and ATTREX campaigns provide the first opportunity to quantify the total gas phase bromine budget using measurements of organic and inorganic bromine species in the tropical tropopause layer and lower stratosphere.

Our best estimate for the total contribution of VSLS to stratospheric bromine (Br_y^{VSLS}) is 5.0 ± 2.1 ppt. Previous estimates of SGI were based on areas of the tropics outside of the TWP, as summarized by Carpenter et al. (2014). Additionally, only a few studies have reported tropical measurements of BrO in air entering the stratosphere (Dorf et al., 2008; Werner et al., 2017). Most studies of PGI have been based on model simulations of the chemical processing of VSLS released by oceanic emissions as well

as the washout rates and heterogeneous chemistry of the inorganic bromine (Br_y) product gases (Liang et al., 2010; Hossaini et al., 2012b; Aschmann and Sinnhuber, 2013; Liang et al., 2014). We have developed a stratospheric tracer relation that describes, as a function of CFC-11, the decay of organic bromine and resulting formation of inorganic bromine as air photochemically ages. Our tracer relation averages air parcels with different transit histories and accounts for the contribution of decomposition of organic source gases to BrO. As a result, our values for SGI, PGI, and Br_y^{VSLS} are likely more robust than previous estimates

The representation of stratospheric bromine within models participating in the Chemistry-Climate Modeling Initiative (CCMI) has been evaluated. These models are being used to project the recovery of the ozone layer and estimate the potential impact of climate change as well as air quality on stratospheric chemistry (Dhomse et al., 2018). The CCMI models either explicitly represent the major VSLS ($CHBr_3$ and CH_2Br_2) or increase the mixing ratio of methyl bromide (CH_3Br) to act as a surrogate for Br_y^{VSLS}. We compared organic, inorganic, and total bromine in the global models to our TWP observations using the stratospheric tracer relation developed in Chapter 2. Overall, the CCMI models that explicitly simulate VSLS are within the range of uncertainty of our TWP observations. Since CH_3Br has a longer atmospheric lifetime than VSLS, models that use a surrogate representation of VSLS underestimate inorganic bromine in photochemically young air. However, in more stratospherically aged air both methods for representing VSLS are in good agreement with the TWP observations, and provide an improvement over previous versions of these models that neglected Br_y^{VSLS}.

Our TWP estimate of Br_y^{VSLS} has been reconciled with satellite and ground-based measurements of vertical column BrO (BrO^{VC}) collected over Fairbanks, Alaska. A stratospheric box model was used to calculate the ratio of BrO/Br_y and estimate the amount of Br_y^{VSLS} needed to represent each retrieval of BrO^{VC}. Retrievals of BrO^{VC} reported by the satellite-based Ozone Monitoring Instrument (OMI) are biased high with respect to the ground-based MFDOAS instrument. The difference between the DOAS fitting windows used by each retrieval likely contributes to this systematic difference. Furthermore, the modeled BrO/Br_y ratio is highly sensitive to the kinetics regulating the formation and photolysis of $BrONO_2$. The largest source of uncertainty in our estimate of Br_y^{VSLS} is due to the difference between the measurements of BrO^{VC} from OMI and MFDOAS. If measurements of BrO^{VC} are assumed to be purely stratospheric, the calculation of Br_y^{VSLS} based on MFDOAS observations is in excellent agreement with our TWP estimate. OMI-based estimates of Br_y^{VSLS} are in agreement with the TWP observations only if the ratio of BrO/Br_y is modeled using slower formation and faster photolysis of $BrONO_2$ than recommended by Burkholder et al. (2015).

Additionally, the sensitivity of calculated tropospheric residual BrO to uncertainties in the value of Br_y^{VSLS}, measurements of BrO^{VC}, and stratospheric $BrONO_2$ kinetics is quantified. Satellite measurements of BrO^{VC} are a valuable resource for monitoring the tropospheric levels of BrO. The tropospheric fraction of BrO^{VC} is calculated using OMI measurements of BrO^{VC} and modeled stratospheric BrO. Calculations of tropospheric BrO^{VC} are most sensitive to the 5 ± 2 ppt range in Br_y^{VSLS}. The difference between the OMI and MFDOAS retrievals are the second most

important source of uncertainty for inferring the tropospheric loading of BrO from measurements of BrO^{VC}. If stratospheric BrO is modeled using 5 ppt of Br_y^{VSLS}, OMI measurements support values for tropospheric columns of BrO that are close to the 1×10^{13} molecules cm^{-2} lower limit proposed by past studies that combined global satellite and ground-based measurements (Van Roozendael et al., 2002; Theys et al., 2011). However, if the OMI measurements are scaled down to reflect MFDOAS observations, we do not find evidence for any significant background of tropospheric BrO over Fairbanks, in agreement with ground-based studies conducted in the Southern Hemisphere (Schofield et al., 2004, 2006).

Parameterizations of inorganic chlorine (Cl_y) in the midlatitude lower stratosphere have been evaluated. A valuable metric for studies of the ozone layer recovery is equivalent effective stratospheric chlorine (EESC), which simulates the weighted sum of inorganic chlorine (Cl_y) and Br_y as a function of the mean time since air entered the stratosphere. Ground and space-based measurements of N_2O, HCl and $ClONO_2$, collected between 1989 and 2017, are used to assess how well different methods for calculating EESC simulate Cl_y in the midlatitude lower stratosphere. Overall, the Engel et al. (2018) formulation of EESC better represents the observed Cl_y record over Jungfraujoch, Switzerland than the EESC method from Newman et al. (2007). Including the stratospheric contribution of chlorinated VSLS further improves the ability of EESC calculations to capture both Jungfraujoch and space-based observations of Cl_y. Simulations that include the Engel et al. (2018) calculation of EESC as well as the stratospheric chlorine and bromine from VSLS better represent

the midlatitude ozone and project a slower recovery of the ozone layer record than simulations with the Newman et al. (2007) formulation that neglect VSLS.

6-2. Coauthored Publications

Here, contributions to coauthored papers published in the peer-reviewed literature are summarized. Chen et al. (2016) presented the chemical ionization mass spectrometry (CIMS) measurements of BrO, as well as the sum of HOBr and Br_2, during the CONTAST aircraft campaign. Generally, the CIMS instrument detected low levels of BrO and HOBr + Br_2 in the tropical free troposphere and tropical tropopause layer (TTL). Periods of elevated mixing ratios of Br_y species were associated with biomass burning tracers, and analysis using a photochemical model indicated that HBr is the most prevalent Br_y compound in the tropical free troposphere. Within the free troposphere and TTL, the partitioning of Br_y into HBr is highly sensitive to heterogeneous reactions (Fernandez et al., 2014). For this paper, I analyzed HBr/Br_y partitioning and aerosol surface area density within the CAM-chem-SD model (Section 2-2.1) to validate the box model results presented in earlier drafts of the manuscript.

Koenig et al. (2017) presented the CONTRAST AMAX-DOAS measurements of BrO. Generally, the AMAX-DOAS BrO measurements were higher than reported by the CIMS instrument, as shown for research flight (RF) 15 in Figure 2-3. This paper evaluated the vertical distribution of BrO and Br_y in the TWP and proposed that sea salt aerosols are a potential source of Br_y in the upper free troposphere and TTL. I worked with the AMAX-DOAS team to maintain a consistent analysis of RF15 between our two papers, including interpretation of aerosol data, chemiluminescence NO, and modeled Br_y partitioning. As shown in Figure 2-4 and discussed in Section 2-

2.2, the chemiluminescence measurements suggest a lower mixing ratio of NO_2 than measured by the AMAX-DOAS instrument. This finding was initially unexpected and modeled ratios of NO_2/NO prepared by the AMAX-DOAS team's model and our box model were compared to verify our analysis of the chemiluminescence data.

Choi et al. (2018) explored the connection between proposed Arctic tropospheric bromine sources and OMI-observed large tropospheric enhancements of bromine. Satellite observations have previously identified quickly forming, large enhancements in tropospheric bromine (Richter et al., 1998; Wagner and Platt, 1998). Past studies have proposed multiple potential sources for elevated levels of bromine, including: first year sea ice, ice leads, frost flowers, snowpack, and blowing snow (Simpson et al., 2007b). This study evaluated blowing snow and first year sea ice as possible mechanisms for converting aqueous bromine (Br^-) from sea water into gas phase active bromine.

Arctic tropospheric BrO was calculated for March and April from 2005 to 2011 using OMI measurements of BrO^{VC} and BrO from a stratospheric climatology. This climatology defines profiles of Br_y and the BrO/Br_y ratio based on OMI total column O_3 and stratospheric NO_2, respectively (Theys et al., 2011). Profiles of Br_y within the climatology include 5 ppt of bromine from CH_2Br_2 source gas injection and 1 ppt of bromine from product gas injection for a total of 6 ppt of Br_y^{VSLS}. Choi et al. (2018) determined that there is a high correlation between the temporal and spatial distribution of tropospheric column BrO with sea salt aerosols generated by wind-blown snow. Minimal correlation was found between OMI-observed tropospheric BrO and the area of first year sea ice. I conducted box-modeling work for the early drafts of this paper

to evaluate the effect of different treatments of Br_y^{VSLS}, and I assisted in preparing responses to the reviews of this paper.

The sensitivity of the magnitude of tropospheric residual BrO to uncertainties in Br_y^{VSLS} and $BrONO_2$ kinetics is presented in Chapter 4, was conducted in collaborations with the lead author of Choi et al. (2018). She provided the tropospheric air mass factors essential for our analysis of these uncertainty in tropospheric residual BrO, which had not been considered in Choi et al. (2018) . Further research is still required to determine the impact of Br_y^{VSLS} on the simulated seasonality of tropospheric BrO as well as the spatial distribution of enhanced tropospheric bromine.

6-3. Future Directions

The results presented in Chapter 2 quantify Br_y^{VSLS} over the TWP in winter 2014. Our tracer relation approach represents air parcels with various transit histories, and the resulting value of Br_y^{VSLS} is representative of the entire tropical stratosphere, rather than air entering the stratosphere in the TWP. However, further research is needed to define possible temporal variability in Br_y^{VSLS}, as well as spatial and time-dependent variations in the relative amounts of bromine that enter through organic or inorganic compounds (e.g., Fiehn et al., 2018; Hossaini et al., 2016). Additionally, climate-induced increases in sea surface temperatures and convection rates could affect the emission and transport rates of VSLS. Further quantification of the geographic and seasonal distribution of emissions of VSLS would assist research into how climate change may alter Br_y^{VSLS} (Hossaini et al., 2012a; Falk et al., 2017; Ziska et al., 2017).

Improved retrievals of tropospheric column BrO from satellite measurements would facilitate research into the effect of halogen chemistry on the tropospheric

oxidative capacity. Additional measurements of BrO are planned for the recently launched TROPOMI and upcoming TEMPO satellite instruments (Veefkind et al., 2012; Zoogman et al., 2017). These new instruments will have much higher spatial resolution than existing instruments, which may assist in the separation of the stratospheric and tropospheric contributions to total column BrO. Reduced uncertainty in satellite measurements of total column BrO as well as the simulations of stratospheric BrO that reflect our best understanding of Br_y^{VSLS} will allow for a more accurate quantification of tropospheric bromine (as demonstrated in Chapter 4). Accurate calculations of residual tropospheric BrO from satellite data could be used to monitor the frequency, duration, and extent of large scale enhancements in active bromine as well as study their impact on Arctic ozone depletion events (e.g., Hollwedel et al., 2004). Resolving the mechanisms that activate bromine is required to predict the effect of climate change and loss of sea ice coverage on ozone depletion events as well as Arctic springtime chemistry (e.g., Simpson et al., 2007a; Hughes et al., 2012; Burd et al., 2017; Choi et al., 2018). Furthermore, ozone in the tropical free troposphere has a strong radiative effect. Consequently, accurate quantification of active bromine (and iodine) compounds in the free troposphere is required to estimate the cooling impact of tropospheric halogens via reduction of ozone (von Glasow et al., 2004; Saiz-Lopez et al., 2012; Hossaini et al., 2015b).

Further research is required to assess how well chemistry-climate models represent stratospheric Br_y and Cl_y over the midlatitudes. Models participating in CCMI currently do not include chlorinated VSLS, which are not regulated under the Montreal Protocol. Chlorinated VSLS are a minor contribution to Cl_y in stratospherically aged

air in regions such as the polar vortices. However, as shown in Chapter 5, VSLS supply a significant fraction of Cl_y in the midlatitude lower stratosphere. Additionally, models that use CH_3Br as a surrogate for VSLS generally underestimate Br_y in stratospherically young air (Figure 3-4). Consequently, the models that rely on this surrogate representation of brominated VSLS may also underestimate halogen-driven ozone loss over midlatitudes.

As discussed in Section 5-5, the modeled distributions of Cl_y and Br_y are dependent on the simulated rates and pathways of atmospheric transport within global models (Waugh et al., 2007; Douglass et al., 2008; Chipperfield et al., 2014). As a result, future research could assess the accuracy of CCMI model representation of both stratospheric age of air as well as the loading of Cl_y and Br_y for the midlatitude lower stratosphere. The modeled stratospheric age of air can be assessed using long-term measurements of N_2O that are available from multiple FTIR stations within the NDACC global network. Additionally, chlorinated VSLS were measured during the CONTRAST and ATTREX aircraft campaigns. Using the same methods detailed in Chapters 2 and 3, stratospheric CFC-11 tracer relations could be defined for chlorinated VSLS and long-lived compounds and used to evaluate Cl_y within CCMI models.

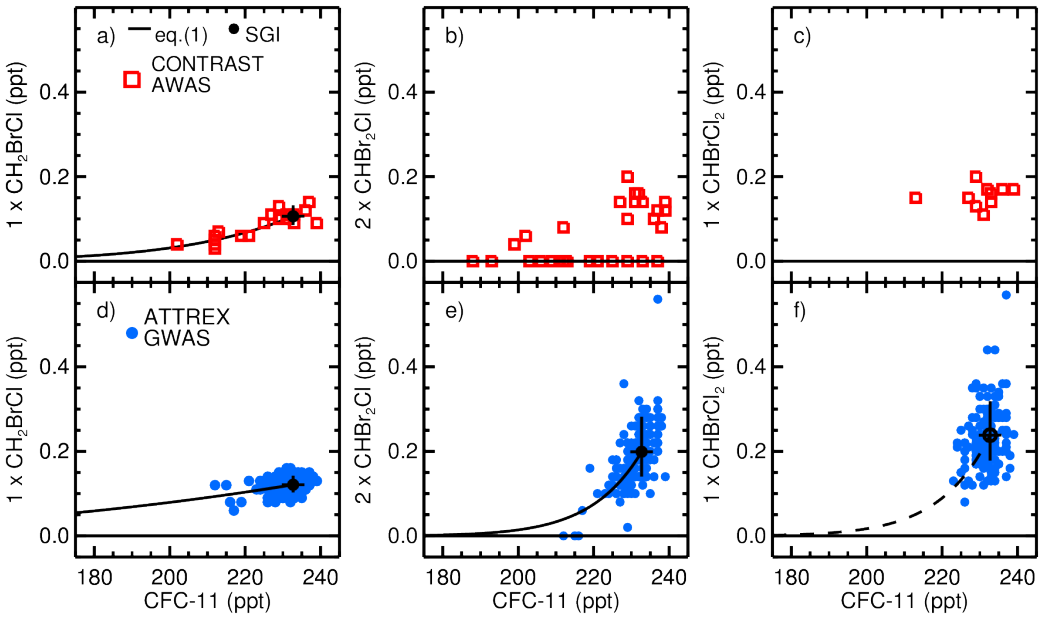

Figure A2-1. Simultaneous stratospheric observations of bromocarbons and CFC-11 for VSLS not shown in Figure 2-5. Red points are extratropical measurements collected during CONTRAST. Blue points are TWP measurements collected during ATTREX. Black lines and points are fitting parameters listed in Table 2-3 for CONTRAST and Table A2-3 for ATTREX observations. Meaningful fits could not be achieved for the relation of CFC-11 with CONTRAST observations of (b) $CHBr_2Cl$ and (c) $CHBrCl_2$ for reasons explained in section 2-3.1. (f) The dashed line for the relation between ATTREX $CHBrCl_2$ and CFC-11 is the decay constant calculated using ATTREX $CHBr_2Cl$ measurements applied to the 17 km mean observations of $CHBrCl_2$.

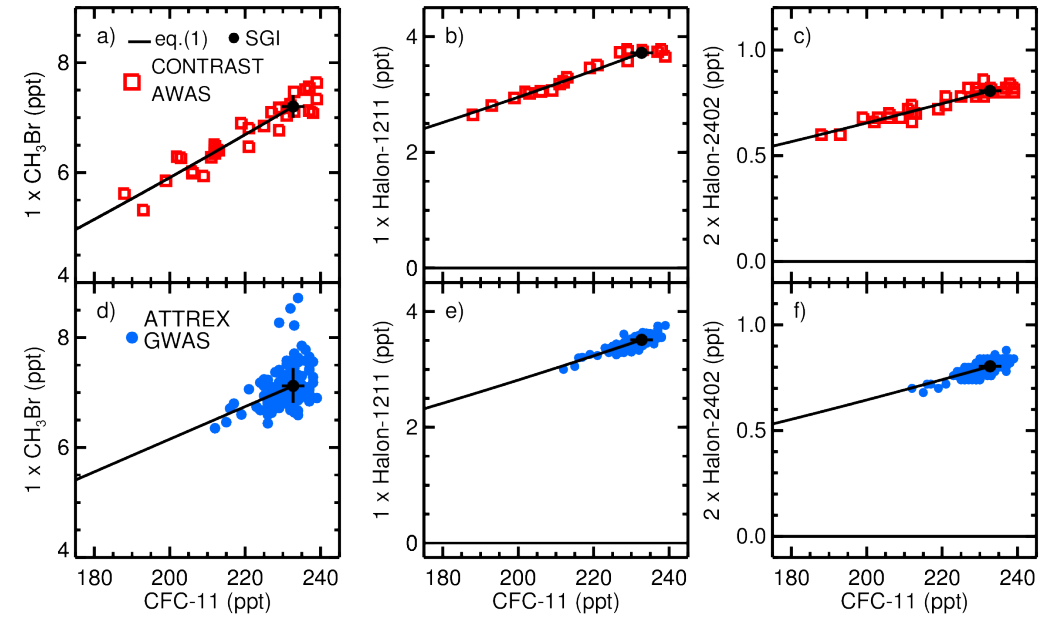

Figure A2-2. Same as Figure A2-1, but for longer-lived bromocarbons.

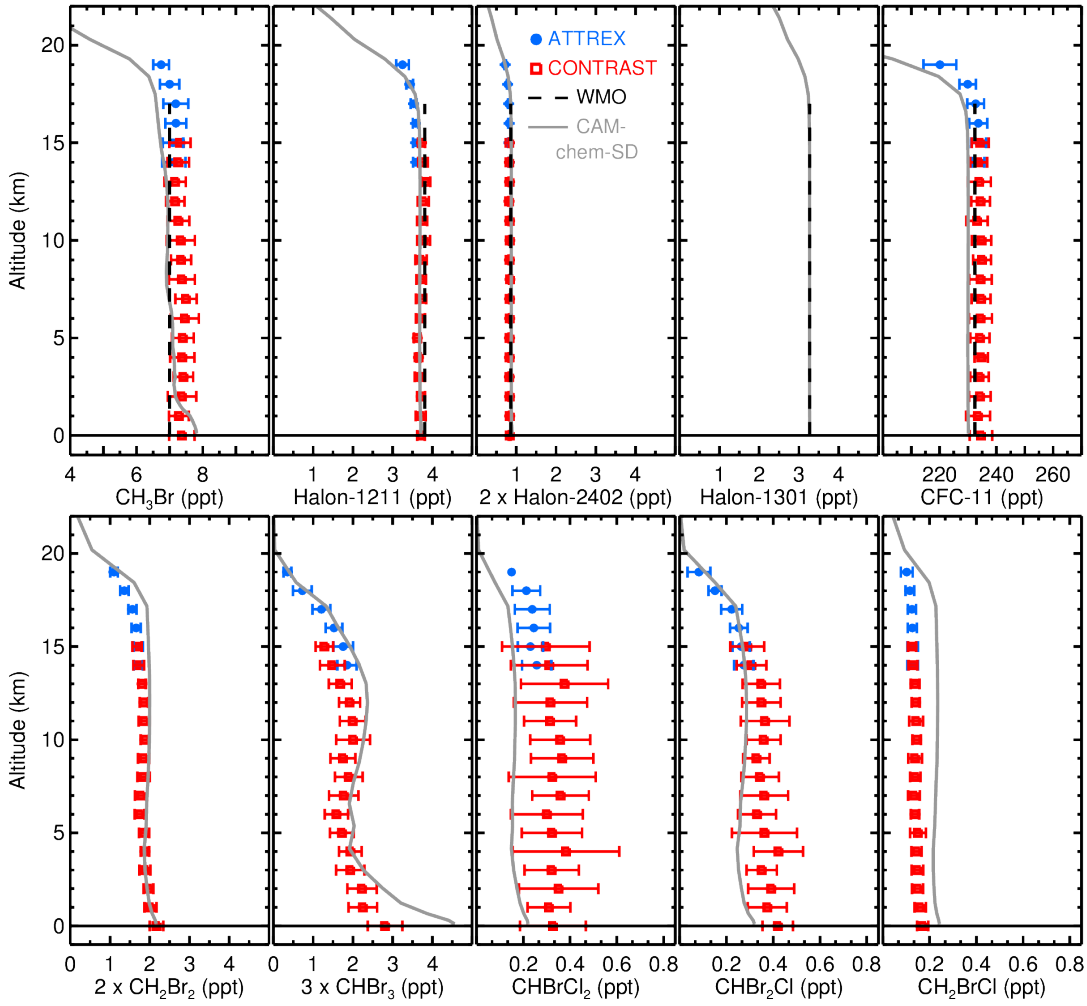

Figure A2-3. Profiles of CFC-11 and bromocarbons in the TWP. Mean profiles of ATTREX GWAS (blue) and CONTRAST AWAS (red) measurements, collected within the TWP box (shown in Figure 2-2), binned for each 1 km, are shown. Error bars represent the standard deviation of data within each altitude bin. Dashed black lines are the 2014 surface mixing ratios reported in WMO 2014 (Harris and Wuebbles et al., 2014) extended up to 17 km for long-lived compounds. Solid grey lines are the mean CAM-chem-SD profiles in the TWP.

Table A2-1. AWAS 1σ measurement uncertainties and limit of detection as reported in Schauffler et al. (2003) for CFC-11 and Schauffler et al. (1999) for bromine compounds.

Observation	Uncertainty (%)	Limit of Detection (ppt)
CFC-11	3.2	0.03
CH_3Br	3.5	< 0.1
Halon-1211	4.2	0.05
Halon-2402	7.0	< 0.05
$CHBr_3$	15.0	< 0.05
CH_2Br_2	11.0	< 0.04
CH_2BrCl	20.0	< 0.01
$CHBr_2Cl$	15.0	< 0.04
$CHBrCl_2$	20.0	< 0.01

Table A2-2. The 1σ uncertainties in the GV measurements used to constrain the box model described in section 2-2.4. The effect of these uncertainties on inferred Br_y is discussed in section 2-3.2.1.

Observation	Uncertainty (1σ)
Chemiluminescence O_3	0.1 to 0.7 ppb ± 5 %
Picarro CH_4	3 ppb
Hygrometer H_2O	1.5 %
VUV CO	1.5 ppb ± 1.5 %

Table A3-1. Stratospheric supply of bromine for winter 2014 from CCMI models, calculated using stratospheric tracer relations. The numerical quantities in parentheses are values in this table minus those in Table 3-3. Total bromine loading was calculated using a linear fit to the modeled total bromine loading as a function of CFC-11, and PGI was estimated from the difference between SGI and the total bromine where the mixing ratio of CFC-11 is 233 ppt.

Source	SGI^{LL} (ppt)	SGI^{VSLS} (ppt)	PGI (ppt)	Total (ppt)
ACCESS-CCM	13.0 ± 0.6 (−0.7)	1.9 ± 0.3 (−0.1)	4.8 ± 1.1 (+1.1)	19.7 ± 0.1 (+0.3)
CCSRNIES-MIROC3.2	12.9 ± 0.3 (+0.02)	2.0 ± 0.1 (+0.01)	4.1 ± 0.5 (−0.3)	19.1 ± 0.1 (−0.2)
CESM1 CAM4-chem	14.3 ± 0.4 (+0.1)	2.4 ± 0.4 (+0.2)	3.4 ± 1.0 (+0.4)	20.1 ± 0.1 (+0.8)
CESM1 WACCM	14.5 ± 0.3 (+0.1)	2.2 ± 0.3 (−0.08)	3.6 ± 0.8 (+0.7)	20.3 ± 0.1 (+0.7)
CMAM	13.9 ± 0.6 (−0.1)	2.5 ± 0.2 (−0.3)	3.6 ± 1.0 (+0.5)	19.9 ± 0.06 (+0.06)
EMAC-L47MA	13.1 ± 0.2 (+0.2)	4.0 ± 0.2 (−1.0)	4.7 ± 0.7 (−0.1)	21.7 ± 0.2 (−1.0)
EMAC-L90MA	13.3 ± 0.3 (+0.2)	4.0 ± 0.4 (−1.1)	5.0 ± 0.9 (+0.4)	22.3 ± 0.4 (−0.5)
EMAC-L90MA-SD	13.6 ± 0.3 (+0.1)	4.4 ± 0.5 (−1.3)	4.3 ± 0.7 (+0.6)	22.2 ± 0.4 (−0.7)
NIWA-UKCA	12.9 ± 0.8 (−0.6)	1.7 ± 0.3 (−0.2)	5.0 ± 1.3 (+1.2)	19.6 ± 0.1 (+0.4)
SOCOL3	14.4 ± 0.4 (0.0)	3.4 ± 0.7 (+0.4)	5.3 ± 1.3 (0.0)	23.1 ± 0.07 (+0.4)
TOMCAT CTM	14.5 ± 0.6 (−0.1)	2.9 ± 0.4 (−0.5)	3.0 ± 0.8 (+0.7)	20.4 ± 0.02 (+0.01)
Explicit models	**13.8 ± 0.7 (−0.1)**	**2.6 ± 0.8 (−0.2)**	**4.1 ± 0.8 (+0.6)**	**20.5 ± 1.3 (+0.2)**
CNRM-CM5.3	19.1 ± 0.5 (−0.5)		1.4 ± 0.8 (+0.5)	20.5 ± 0.07 (+0.02)
GEOSCCM	19.4 ± 1.6 (−0.06)		1.1 ± 1.6) (−0.1)	20.5 ± 0.1 (−0.2)
MRI-ESM1r1	19.9 ± 0.6 (+0.5)		0.1 ± 0.6 (−0.6)	20.0 ± 0.07 (−0.03)
ULAQ-CCM	16.8 ± 0.7 (−0.2)		3.7 ± 2.1 (+2.4)	20.4 ± 1.2 (+2.0)
UMSLIMCAT	19.9 ± 2.3 (+0.3)		0.2 ± 2.3 (−0.5)	20.1 ± 0.03 (−0.2)
Surrogate models	**19.0 ± 1.3 (+0.0)**		**1.3 ± 1.4 (+0.3)**	**20.3 ± 0.2 (+0.3)**

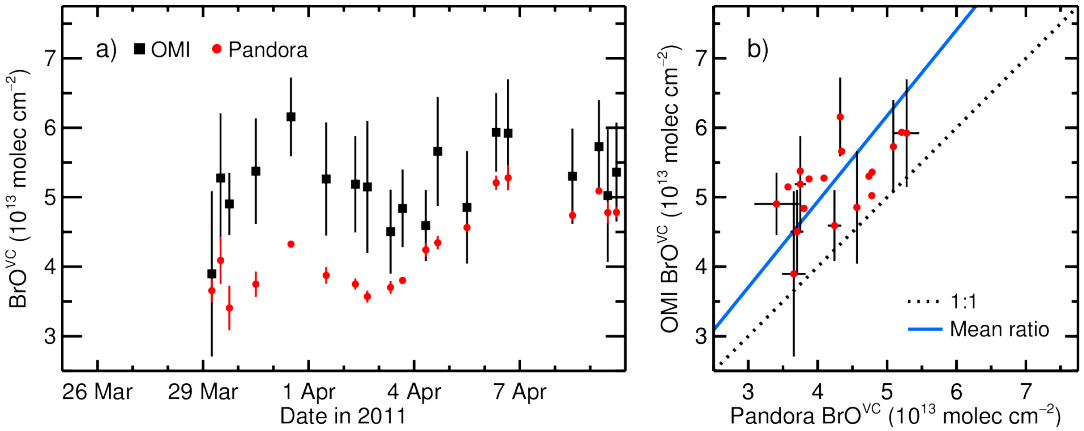

Figure A4-1. Same as Figure 4-5 in the main text but with Pandora ground-based observations of BrO^{VC}. The mean and standard deviation of the ratio of OMI/Pandora BrO^{VC} is 1.23 ± 0.15, consistent with the 1.20 ± 0.14 OMI/MFDOAS ratio.

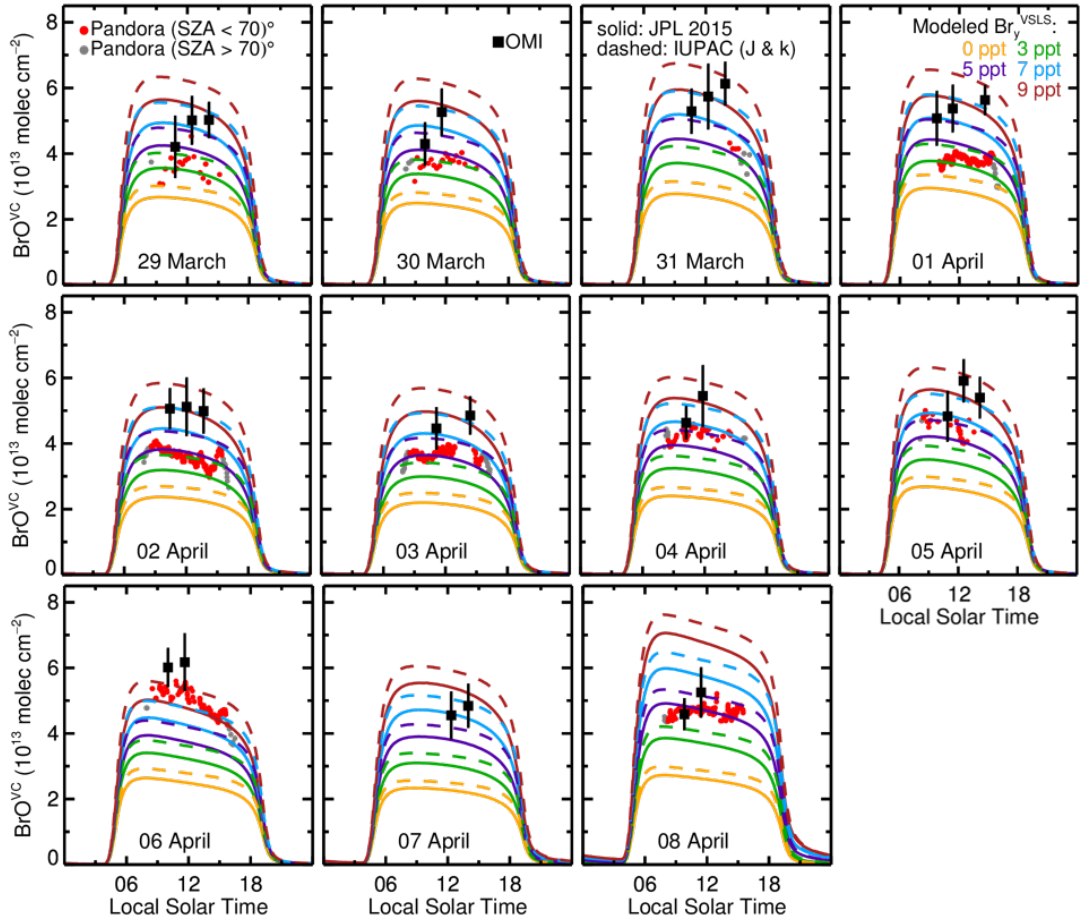

Figure A4- 2. Same as Figure 4-7 of the main text, but with Pandora ground-based measurements of BrO^{VC}. The ozonesonde tropopause pressure on 06 and 07 April is poorly defined.

Table A5- 1. List of stations with archived column and profile FITR data.

Location	Column		Profile	
	Compounds	Years	Compounds	Years
Eureka (80°N)	HCl, $ClONO_2$, HF, COF_2	1996 – 2006	HCl, $ClONO_2$, HF, N_2O	2006 – 2016
Ny Alesund (79°N)	HCl, N_2O, HF $ClONO_2$ COF_2	1992 – 2017 1992 – 2013 1992 – 2008	HCl, HF N_2O $ClONO_2$	1993 – 2017 1996 – 2017 1993 – 2013
Thule (77°N)	HCl, $ClONO_2$, N_2O, HF, COF_2	1999 – 2007	HCl, $ClONO_2$, N_2O, HF	1999 – 2007
Kiruna (68°N)	HCl, $ClONO_2$, N_2O, HF COF_2	1996 – 2016 1996 – 2007	HCl, $ClONO_2$, N_2O, HF	1996 – 2016
Harestua (60°N)	HCl, $ClONO_2$, N_2O, HF, COF_2	1994 – 2015		
St. Petersburg (60°N)	HCl, N_2O, HF	2009 – 2017	HCl, N_2O, HF	2009 – 2017
Bremen (53°N)	HCl, $ClONO_2$, N_2O, HF, COF_2, SF_6	2002 – 2017	HCl, $ClONO_2$, N_2O, HF, COF_2, SF_6	2002 – 2017
Zugspitze (47°N)	HCl, $ClONO_2$, N_2O, HF	1995 – 2017	HCl, $ClONO_2$, N_2O, HF	1995 – 2017
Jungfraujoch (46°N)[a]	HCl, $ClONO_2$, N_2O, HF, COF_2	1989 – 2017	HCl, $ClONO_2$, N_2O, HF, COF_2	1989 – 2017
Moshiri (44°N)	HCl, HF $ClONO_2$	1996 – 2007 1996 – 2004	HCl, HF	1996 – 2007
Toronto (44°N)	HCl, N_2O, HF	2002 – 2017	HCl, N_2O, HF	2002 – 2017
Rikubetsi (44°N)	HCl, N_2O, HF $ClONO_2$	1995 – 2018 1996 – 2010	HCl, N_2O, HF $ClONO_2$	1995 – 2018 1996 – 2010
Kitt Peak (32°N)	HCl, $ClONO_2$, HF	1978 – 2005		
Izana (28°N)	HCl, N_2O, HF $ClONO_2$	1999 – 2018 1999 – 2015	HCl, N_2O, HF $ClONO_2$	1999 – 2018 1999 – 2015
Mauna Loa (20°N)	HCl, N_2O, HF	1991 – 2007	HCl, N_2O, HF	1995 – 2017
Altzomoni (19°N)	HCl, N_2O HF	2012 – 2016 2013 – 2016	HCl, N_2O HF	2012 – 2016 2013 – 2016
Paramaribo (6°N)	HCl, N_2O	2004 – 2017	HCl, N_2O	2004 – 2017
Reunion, St Denis (22°S)	HCl, HF N_2O	2004 – 2013 2004 – 2011	HCl, HF N_2O	2004 – 2013 2004 – 2011
Reunion, Maido (22°S)	HCl HF, N_2O	2013 2013 – 2017	HCl HF, N_2O	2013 2013 – 2017
Wollongong (34°S)	HCl, N_2O $ClONO_2$, HF, COF_2	1995 – 2013 1995 – 2008	HCl, N_2O	2007 – 2013
Lauder (45°S)	HCl, $ClONO_2$ N_2O, HF	1990 – 2017 1994 – 2017	HCl, $ClONO_2$ N_2O, HF	1990 – 2017 1994 – 2017
Arrival Heights (78°S)	HCl, $ClONO_2$, N_2O, HF	1997 – 2017	HCl, $ClONO_2$, N_2O, HF	1997 – 2017

[a]Profile measurements of $ClONO_2$ and N_2O before 1995 and 2000, respectively, were shared privately by Emmanuel Mahieu (emmanuel.mahieu@uliege.be).

Bibliography

Akiyoshi, H., Nakamura, T., Miyasaka, T., Shiotani, M., and Suzuki, M. (2016). A nudged chemistry-climate model simulation of chemical constituent distribution at northern high-latitude stratosphere observed by SMILES and MLS during the 2009/2010 stratospheric sudden warming. *Journal of Geophysical Research: Atmospheres*, *121*(3), 1361–1380. https://doi.org/10.1002/2015JD023334

Aliwell, S. R., Van Roozendael, M., Johnston, P. V., Richter, A., Wagner, T., Arlander, D. W., et al. (2002). Analysis for BrO in zenith-sky spectra: An intercomparison exercise for analysis improvement. *Journal of Geophysical Research Atmospheres*, *107*(14), 1–20. https://doi.org/10.1029/2001JD000329

Anderson, D. C., Nicely, J. M., Salawitch, R. J., Canty, T. P., Dickerson, R. R., Hanisco, T. F., et al. (2016). A pervasive role for biomass burning in tropical high ozone/low water structures. *Nature Communications*, *7*(10267). https://doi.org/10.1038/ncomms10267

Anderson, J., Russell, J. M., Solomon, S., and Deaver, L. E. (2000). Halogen Occultation Experiment confirmation of stratospheric chlorine decrease in accordance with the Montreal Protocol. *Journal of Geophysical Research*, *105*(D4), 4483–4490.

Andrews, S. J., Carpenter, L. J., Apel, E. C., Atlas, E., Donets, V., Hopkins, J. R., et al. (2016). A comparison of very short lived halocarbon (VSLS) and DMS aircraft measurements in the tropical west Pacific from CAST, ATTREX and CONTRAST. *Atmospheric Measurement Techniques*, *9*(10), 5213–5225. https://doi.org/10.5194/amt-9-5213-2016

Arblaster, J. M., Gillett, N. P., Calvo, N., Forster, P. M., Polvani, L. M., Son, S.-W., et al. (2014). Stratospheric ozone changes and climate, Chapter 4. In *Scientific Assessment of Ozone Depletion: 2014, Global Ozone Research and Monitoring Project – Report No. 55*. Geneva, Switzerland: World Meteorological Organization.

Aschmann, J., and Sinnhuber, B. M. (2013). Contribution of very short-lived substances to stratospheric bromine loading: Uncertainties and constraints. *Atmospheric Chemistry and Physics*, *13*(3), 1203–1219. https://doi.org/10.5194/acp-13-1203-2013

Aschmann, J., Sinnhuber, B. M., Atlas, E. L., and Schauffler, S. M. (2009). Modeling the transport of very short-lived substances into the tropical upper troposphere and lower stratosphere. *Atmospheric Chemistry and Physics*, *9*(23), 9237–9247. https://doi.org/10.5194/acp-9-9237-2009

Aschmann, J., Sinnhuber, B. M., Chipperfield, M. P., and Hossaini, R. (2011). Impact of deep convection and dehydration on bromine loading in the upper troposphere and lower stratosphere. *Atmospheric Chemistry and Physics*, *11*(6), 2671–2687. https://doi.org/10.5194/acp-11-2671-2011

Atkinson, R., Baulch, D. L., Cox, R. a., Crowley, J. N., Hampson, R. F., Hynes, R. G., et al. (2007). Evaluated kinetic and photochemical data for atmospheric chemistry: Volume III -- gas phase reactions of inorganic halogens. *Atmospheric Chemistry and Physics*, *7*, 981–1191. https://doi.org/10.5194/acp-6-3625-2006

Avallone, L. M., and Prather, M. J. (1997). Tracer-tracer correlations: Three-dimensional model simulations and comparisons to observations. *Journal of*

Geophysical Research: Atmospheres, *102*(D15), 19233–19246. https://doi.org/10.1029/97JD01123

Baidar, S., Oetjen, H., Coburn, S., Dix, B., Ortega, I., Sinreich, R., and Volkamer, R. (2013). The CU Airborne MAX-DOAS instrument: vertical profiling of aerosol extinction and trace gases. *Atmospheric Measurement Techniques*, *6*(3), 719–739. https://doi.org/10.5194/amt-6-719-2013

Baldwin, M., Dameris, M., Austin, J., Bekki, S., Bregman, B., Butchart, N., et al. (2007). Climate-Ozone Connections, Chapter 5. In *Scientific Assessment of Ozone Depletion: 2006, Global Ozone Research and Monitoring Project – Report No. 50*. Geneva, Switzerland: World Meteorological Organization.

Ball, W. T., Alsing, J., Mortlock, D. J., Staehelin, J., Haigh, J. D., Peter, T., et al. (2018). Evidence for a continuous decline in lower stratospheric ozone offsetting ozone layer recovery. *Atmospheric Chemistry and Physics*, *18*(2), 1379–1394. https://doi.org/10.5194/acp-18-1379-2018

Barrie, L. A., Bottenheim, J. W., Schnell, R. C., Crutzen, P. J., and Rasmussen, R. A. (1988). Ozone destruction and photochemical reactions at polar sunrise in the lower Arctic atmosphere. *Nature*, *334*(6178), 138–141. https://doi.org/10.1038/334138a0

Bekki, S., Bodeker, G. E., Bais, A. F., Butchart, N., Eyring, V., Fahey, D. W., et al. (2011). Future Ozone and Its Impact on Surface UV, Chapter 3. In *Scientific Assessment of Ozone Depletion: 2010, Global Ozone Research and Monitoring Project – Report No. 52* (52nd ed., p. 64). Geneva, Switzerland. Retrieved from http://ozone.unep.org/new_site/en/scientific_assessment_2010.php

Bergman, J. W., Jensen, E. J., Pfister, L., and Yang, Q. (2012). Seasonal differences of vertical-transport efficiency in the tropical tropopause layer: On the interplay between tropical deep convection, large-scale vertical ascent, and horizontal circulations. *Journal of Geophysical Research Atmospheres*, *117*(D05302), 1–20. https://doi.org/10.1029/2011JD016992

Bernath, P. F., McElroy, C. T., Abrams, M. C., Boone, C. D., Butler, M., Camy-Peyret, C., et al. (2005). Atmospheric chemistry experiment (ACE): Mission overview. *Geophysical Research Letters*, *32*(15), 1–5. https://doi.org/10.1029/2005GL022386

Boering, K. A., Wofsy, S. C., Daube, B. C., Schneider, H. R., Loewenstein, M., Podolske, J. R., and Conway, T. J. (1996). Stratospheric Mean Ages and Transport Rates from Observations of Carbon Dioxide and Nitrous Oxide. *Science*, *274*(5291), 1340–1343. https://doi.org/10.1126/science.274.5291.1340

Boone, C. D., Nassar, R., Walker, K. A., Rochon, Y., McLeod, S. D., Rinsland, C. P., and Bernath, P. F. (2005). Retrievals for the atmospheric chemistry experiment Fourier-transform spectrometer. *Applied Optics*, *44*, 7218–7231. https://doi.org/10.1364/AO.44.007218

Bösch, H. (2003). Upper limits of stratospheric IO and OIO inferred from center-to-limb-darkening-corrected balloon-borne solar occultation visible spectra: Implications for total gaseous iodine and stratospheric ozone. *Journal of Geophysical Research*, *108*(D15), 4455. https://doi.org/10.1029/2002JD003078

Brinckmann, S., Engel, A., Bönisch, H., Quack, B., and Atlas, E. (2012). Short-lived brominated hydrocarbons - Observations in the source regions and the tropical

tropopause layer. *Atmospheric Chemistry and Physics*, *12*(3), 1213–1228. https://doi.org/10.5194/acp-12-1213-2012

Brown, A. T., Chipperfield, M. P., Boone, C., Wilson, C., Walker, K. A., and Bernath, P. F. (2011). Trends in atmospheric halogen containing gases since 2004. *Journal of Quantitative Spectroscopy and Radiative Transfer*, *112*(16), 2552–2566. https://doi.org/10.1016/j.jqsrt.2011.07.005

Brown, A. T., Volk, C. M., Schoeberl, M. R., Boone, C. D., and Bernath, P. F. (2013). Stratospheric lifetimes of CFC-12, CCl4, CH4, CH3Cl and N2O from measurements made by the Atmospheric Chemistry Experiment-Fourier Transform Spectrometer (ACE-FTS). *Atmospheric Chemistry and Physics*, *13*(14), 6921–6950. https://doi.org/10.5194/acp-13-6921-2013

Bucsela, E. J., Krotkov, N. A., Celarier, E. A., Lamsal, L. N., Swartz, W. H., Bhartia, P. K., et al. (2013). A new stratospheric and tropospheric NO2 retrieval algorithm for nadir-viewing satellite instruments: applications to OMI. *Atmospheric Measurement Techniques*, *6*(10), 2607–2626. https://doi.org/10.5194/amt-6-2607-2013

Burd, J. A., Peterson, P. K., Nghiem, S. V., Perovich, D. K., and Simpson, W. R. (2017). Snow Melt Onset Hinders Bromine Monoxide Heterogeneous Recycling in the Arctic. *Submitted to J. Geophys. Res.* https://doi.org/10.1002/2017JD026906

Burkholder, J. B., Ravishankara, A. R., and Solomon, S. (1995). UV/visible and IR absorption cross sections of BrONO2. *Journal of Geophysical Research*, *100*(D8), 16793. https://doi.org/10.1029/95JD01223

Burkholder, J. B., Sander, S. P., Abbatt, J., Barker, J. R., Huie, R. E., Kolb, C. E., et al. (2015). *Chemical Kinetics and Photochemical Data for Use in Atmospheric Studies, Evaluation Number 18*. *JPL Publication 15-10*. Jet Propulsion Laboratory, Pasadena. Retrieved from http://jpldataeval.jpl.nasa.gov/

Butz, A., Bösch, H., Camy-Peyret, C., Chipperfield, M. P., Dorf, M., Kreycy, S., et al. (2009). Constraints on inorganic gaseous iodine in the tropical upper troposphere and stratosphere inferred from balloon-borne solar occultation observations. *Atmospheric Chemistry and Physics*, *9*(18), 7229–7242. https://doi.org/10.5194/acp-9-7229-2009

Cai, Y., Montague, D. C., Mooiweer-Bryan, W., and Deshler, T. (2008). Performance characteristics of the ultra high sensitivity aerosol spectrometer for particles between 55 and 800 nm: Laboratory and field studies. *Journal of Aerosol Science*, *39*(9), 759–769. https://doi.org/10.1016/j.jaerosci.2008.04.007

Canty, T., Riviere, E. D., Salawitch, R. J., Berthet, G., Renard, J.-B., Pfeilsticker, K., et al. (2005). Nighttime OClO in the winter Arctic vortex. *Journal of Geophysical Research*, *110*(D1), D01301. https://doi.org/10.1029/2004JD005035

Carpenter, L. J., and Liss, P. S. (2000). On temperate sources of bromoform and other reactive organic bromine gases. *Journal of Geophysical Research*, *105*(D16), 20539–20547. https://doi.org/10.1029/2000JD900242

Carpenter, L. J., Reimann, S., Burkholder, J. B., Clerbaux, C., Hall, B. D., Hossaini, R., et al. (2014). Ozone-depleting substances (ODSs) and other gases of interest to the Montreal Protocol, Chapter 1. In *Scientific Assessment of Ozone*

Depletion: 2014, Global Ozone Research and Monitoring Project – Report No. 55. Geneva, Switzerland: World Meteorological Organization.
Chance, K. (1998). Analysis of BrO measurements from the Global Ozone Monitoring Experiment. *Geophysical Research Letters*, *25*(17), 3335–3338. https://doi.org/10.1029/98GL52359
Chance, K. V. (2002). *OMI Algorithm Theoretical Basis Document Volume IV: OMI Trace Gas Algorithms* (Vol. IV). Cambridge, MA. Retrieved from http://ozoneaq.gsfc.nasa.gov/media/docs/ATBD-OMI-04.pdf
Chen, D., Huey, L. G., Tanner, D. J., Salawitch, R. J., Anderson, D. C., Wales, P. A., et al. (2016). Airborne measurements of BrO and the sum of HOBr and Br_2 over the Tropical West Pacific from 1 to 15 km during the CONvective TRansport of Active Species in the Tropics (CONTRAST) experiment. *Journal of Geophysical Research: Atmospheres*, *121*(20), 12,560-12,578. https://doi.org/10.1002/2016JD025561
Chipperfield, M. P. (2006). New version of the TOMCAT/SLIMCAT off-line chemical transport model: Intercomparison of stratospheric tracer experiments. *Quarterly Journal of the Royal Meteorological Society*, *132*(617), 1179–1203. https://doi.org/10.1256/qj.05.51
Chipperfield, M. P., Dhomse, S., Hossaini, R., Feng, W., Santee, M. L., Weber, M., et al. (2018). On the Cause of Recent Variations in Lower Stratospheric Ozone. *Geophysical Research Letters*, *45*(11), 5718–5726. https://doi.org/10.1029/2018GL078071
Chipperfield, M. P., Liang, Q., Strahan, S. E., Morgenstern, O., Dhomse, S. S., Abraham, N. L., et al. (2014). Multimodel estimates of atmospheric lifetimes of long-lived ozone-depleting substances: Present and future. *Journal of Geophysical Research: Atmospheres*, *119*(5), 2555–2573. https://doi.org/10.1002/2013JD021097
Choi, S., Theys, N., Salawitch, R. J., Wales, P. A., Joiner, J., Canty, T. P., et al. (2018). Link Between Arctic Tropospheric BrO Explosion Observed From Space and Sea-Salt Aerosols From Blowing Snow Investigated Using Ozone Monitoring Instrument BrO Data and GEOS-5 Data Assimilation System. *Journal of Geophysical Research: Atmospheres*, *123*(13), 6954–6983. https://doi.org/10.1029/2017JD026889
Choi, S., Wang, Y., Salawitch, R. J., Canty, T., Joiner, J., Zeng, T., et al. (2012). Analysis of satellite-derived Arctic tropospheric BrO columns in conjunction with aircraft measurements during ARCTAS and ARCPAC. *Atmospheric Chemistry and Physics*, *12*(3), 1255–1285. https://doi.org/10.5194/acp-12-1255-2012
Crosson, E. R. (2008). A cavity ring-down analyzer for measuring atmospheric levels of methane, carbon dioxide, and water vapor. *Applied Physics B*, *92*(3), 403–408. https://doi.org/10.1007/s00340-008-3135-y
Daniel, J. S., Solomon, S., and Albritton, D. L. (1995). On the evaluation of halocarbon radiative forcing and global warming potentials. *Journal of Geophysical Research: Atmospheres*, *100*(D1), 1271–1285. https://doi.org/10.1029/94JD02516
Daniel, J. S., Velders, G. J. M., Morgenstern, O., Toohey, D. W., Wallington, T. J.,

Wuebbles, D. J., et al. (2011). A focus on information and options for policymakers, Chapter 5. In *Scientific Assessment of Ozone Depletion* (52nd ed.). Geneva, Switzerland: World Meteorological Organization.

Daniel, J., Velders, G., Douglass, A. R., Forster, P. M. D., Hauglustaine, D. A., Isaksen, I. S. A., et al. (2006). Halocarbon Scenarios, Ozone Depletion Potentials, and Global Warming Potentials, Chapter 8. In *Scientific Assessment of Ozone Depletion: 2006*. Geneva, Switzerland.

Danis, F., Caralp, F., Masanet, J., and Lesclaux, R. (1990). Kinetics of the Reaction $BrO + NO_2 + M \rightarrow BrONO_2 + M$ in the Temperature Range 263-343 K. *Chemical Physics Letters*, *167*(5), 450–456.

Dee, D. P., Uppala, S. M., Simmons, A. J., Berrisford, P., Poli, P., Kobayashi, S., et al. (2011). The ERA-Interim reanalysis: Configuration and performance of the data assimilation system. *Quarterly Journal of the Royal Meteorological Society*, *137*(656), 553–597. https://doi.org/10.1002/qj.828

Deters, B., Burrows, J. P., and Orphal, J. (1998). UV-visible absorption cross sections of bromine nitrate determined by photolysis of $BrONO_2$/Br2 mixtures. *Journal of Geophysical Research-Atmospheres*, *103*(D3), 3563–3570.

Deushi, M., and Shibata, K. (2011). Development of a Meteorological Research Institute chemistry-climate model version 2 for the study of tropospheric and stratospheric chemistry. *Papers in Meteorology and Geophysics*, *62*(May), 1–46. https://doi.org/10.2467/mripapers.62.1

Dhomse, S., Kinnison, D., Chipperfield, M. P., Cionni, I., Hegglin, M., Abraham, N. L., et al. (2018). Estimates of Ozone Return Dates from Chemistry-Climate Model Initiative Simulations. *Atmospheric Chemistry and Physics Discussions*, 1–40. https://doi.org/10.5194/acp-2018-87

Dix, B., Koenig, T. K., and Volkamer, R. (2016). Parameterization retrieval of trace gas volume mixing ratios from Airborne MAX-DOAS. *Atmospheric Measurement Techniques*, *9*(11), 5655–5675. https://doi.org/10.5194/amt-9-5655-2016

Dorf, M., Butler, J. H., Butz, A., Camy-Peyret, C., Chipperfield, M. P., Kritten, L., et al. (2006). Long-term observations of stratospheric bromine reveal slow down in growth. *Geophysical Research Letters*, *33*(24), L24803. https://doi.org/10.1029/2006GL027714

Dorf, M., Butz, A., Camy-Peyret, C., Chipperfield, M. P., Kritten, L., and Pfeilsticker, K. (2008). Bromine in the tropical troposphere and stratosphere as derived from balloon-borne BrO observations. *Atmospheric Chemistry and Physics*, *8*(23), 7265–7271. https://doi.org/10.5194/acp-8-7265-2008

Douglass, A., Fioletov, V., Godin-Beekmann, S., Müller, R., Stolarski, R. S., and Webb, A. (2011). Stratospheric ozone and surface ultraviolet radiation, Chapter 2. In *Scientific Assessment of Ozone Depletion: 2010, Global Ozone Research and Monitoring Project – Report No. 52*. Geneva, Switzerland: World Meteorological Organization.

Douglass, A. R., Stolarski, R. S., Schoeberl, M. R., Jackman, C. H., Gupta, M. L., Newman, P. A., et al. (2008). Relationship of loss, mean age of air and the distribution of CFCs to stratospheric circulation and implications for atmospheric lifetimes. *Journal of Geophysical Research Atmospheres*, *113*(14),

1–14. https://doi.org/10.1029/2007JD009575
Duchatelet, P., Mahieu, E., Ruhnke, R., Feng, W., Chipperfield, M., Demoulin, P., et al. (2009). An approach to retrieve information on the carbonyl fluoride (COF2) vertical distributions above Jungfraujoch by FTIR multi-spectrum multi-window fitting. *Atmospheric Chemistry and Physics*, *9*(22), 9027–9042. https://doi.org/10.5194/acp-9-9027-2009
Dvortsov, V. L., Geller, M. A., Solomon, S., Schauffler, S. M., Atlas, E. L., and Blake, D. R. (1999). Rethinking reactive halogen budgets in the midlatitude lower stratosphere. *Geophysical Research Letters*, *26*(12), 1699–1702. https://doi.org/10.1029/1999GL900309
Engel, A., Bönisch, H., Ostermöller, J., Chipperfield, M. P., Dhomse, S., and Jöckel, P. (2018). A refined method for calculating equivalent effective stratospheric chlorine. *Atmospheric Chemistry and Physics*, *18*(2), 601–619. https://doi.org/10.5194/acp-18-601-2018
Engel, A., Strunk, M., Müller, M., Haase, H.-P., Poss, C., Levin, I., and Schmidt, U. (2002). Temporal development of total chlorine in the high-latitude stratosphere based on reference distributions of mean age derived from CO2 and SF6. *J. Geophys. Res*, *107*(12), ACH 1-1-ACH 1-11. https://doi.org/10.1029/2001JD000584
Evans, M. J., Jacob, D. J., Atlas, E., Cantrell, C. A., Eisele, F., Flocke, F., et al. (2003). Coupled evolution of BrO_x -ClO_x -HO_x -NO_x chemistry during bromine-catalyzed ozone depletion events in the arctic boundary layer. *Journal of Geophysical Research*, *108*(D4), 8368. https://doi.org/10.1029/2002JD002732
Eyring, V., Cionni, I., Bodeker, G. E., Charlton-Perez, A. J., Kinnison, D. E., Scinocca, J. F., et al. (2010). Multi-model assessment of stratospheric ozone return dates and ozone recovery in CCMVal-2 models. *Atmospheric Chemistry and Physics*, *10*(19), 9451–9472. https://doi.org/10.5194/acp-10-9451-2010
Eyring, V., Lamarque, J.-F., Hess, P., Arfeuille, F., Bowman, K., Chipperfield, M. P., et al. (2013). Overview of IGAC/SPARC Chemistry-Climate Model Initiative (CCMI) community simulations in support of upcoming ozone and climate assessments. *SPARC Newsletter*, *40*, 48–66. Retrieved from http://www.sparc-climate.org/fileadmin/customer/6_Publications/Newsletter_PDF/40_SPARCnewsletter_Jan2013_web.pdf
Eyring, V., Waugh, D. W., Bodeker, G. E., Cordero, E., Akiyoshi, H., Austin, J., et al. (2007). Multimodel projections of stratospheric ozone in the 21st century. *Journal of Geophysical Research Atmospheres*, *112*(16). https://doi.org/10.1029/2006JD008332
Fahey, D. W., Kawa, S. R., Woodbridge, E. L., Tin, P., Wilson, J. C., Jonsson, H. H., et al. (1993). In situ measurements constraining the role of sulphate aerosols in mid-latitude ozone depletion. *Nature*, *363*(6429), 509–514. https://doi.org/10.1038/363509a0
Falk, S., Sinnhuber, B.-M., Krysztofiak, G., Jöckel, P., Graf, P., and Lennartz, S. T. (2017). Brominated VSLS and their influence on ozone under a changing climate. *Atmospheric Chemistry and Physics*, *17*(18), 11313–11329. https://doi.org/10.5194/acp-17-11313-2017
Farman, J. C., Gardiner, B. G., and Shanklin, J. D. (1985). Large losses of total ozone

in Antarctica reveal seasonal ClO_x/NO_x interaction. *Nature*, *315*(6016), 207–210. https://doi.org/10.1038/315207a0

Feng, W., Chipperfield, M. P., Dorf, M., Pfeilsticker, K., and Ricaud, P. (2007). Mid-latitude ozone changes: studies with a 3-D CTM forced by ERA-40 analyses. *Atmospheric Chemistry and Physics*, *7*(9), 2357–2369. https://doi.org/10.5194/acp-7-2357-2007

Fernandez, R. P., Kinnison, D. E., Lamarque, J.-F., Tilmes, S., and Saiz-Lopez, A. (2017). Impact of biogenic very short-lived bromine on the Antarctic ozone hole during the 21st century. *Atmospheric Chemistry and Physics*, *17*(3), 1673–1688. https://doi.org/10.5194/acp-17-1673-2017

Fernandez, R. P., Salawitch, R. J., Kinnison, D. E., Lamarque, J. F., and Saiz-Lopez, A. (2014). Bromine partitioning in the tropical tropopause layer: Implications for stratospheric injection. *Atmospheric Chemistry and Physics*, *14*(24), 13391–13410. https://doi.org/10.5194/acp-14-13391-2014

Fiehn, A., Quack, B., Stemmler, I., Ziska, F., and Krüger, K. (2018). Importance of seasonally resolved oceanic emissions for bromoform delivery from the tropical Indian Ocean and west Pacific to the stratosphere. *Atmospheric Chemistry and Physics*, *18*(16), 11973–11990. https://doi.org/10.5194/acp-18-11973-2018

Frieler, K., Rex, M., Salawitch, R. J., Canty, T., Streibel, M., Stimpfle, R. M., et al. (2006). Toward a better quantitative understanding of polar stratospheric ozone loss. *Geophysical Research Letters*, *33*(10), n/a-n/a. https://doi.org/10.1029/2005GL025466

Frith, S. M., Kramarova, N. A., Stolarski, R. S., McPeters, R. D., Bhartia, P. K., and Labow, G. J. (2014). Recent changes in total column ozone based on the SBUV Version 8.6 Merged Ozone Data Set. *Journal of Geophysical Research: Atmospheres*, *119*(16), 9735–9751. https://doi.org/10.1002/2014JD021889

Froidevaux, L., Anderson, J., Wang, H. J., Fuller, R. A., Schwartz, M. J., Santee, M. L., et al. (2015). Global OZone Chemistry and Related trace gas Data records for the Stratosphere (GOZCARDS): Methodology and sample results with a focus on HCl, H2O, and O3. *Atmospheric Chemistry and Physics*, *15*(18), 10471–10507. https://doi.org/10.5194/acp-15-10471-2015

Froidevaux, L., Livesey, N. J., Read, W. G., Salawitch, R. J., Waters, J. W., Drouin, B., et al. (2006). Temporal decrease in upper atmospheric chlorine. *Geophysical Research Letters*, *33*(23), 8–12. https://doi.org/10.1029/2006GL027600

Garcia, R. R., Smith, A. K., Kinnison, D. E., De La Cámara, Á., and Murphy, D. J. (2017). Modification of the gravity wave parameterization in the Whole Atmosphere Community Climate Model: motivation and results. *Journal of the Atmospheric Sciences*, *74*(1), 275–291. https://doi.org/10.1175/JAS-D-16-0104.1

Garcia, R. R., and Solomon, S. (1994). A new numerical model of the middle atmosphere: 2. Ozone and related species. *Journal of Geophysical Research*, *99*(D6), 12937. https://doi.org/10.1029/94JD00725

Gerbig, C., Schmitgen, S., Kley, D., Volz-Thomas, A., Dewey, K., and Haaks, D. (1999). An improved fast-response vacuum-UV resonance fluorescence CO instrument. *Journal of Geophysical Research: Atmospheres*, *104*(D1), 1699–1704. https://doi.org/10.1029/1998JD100031

Gettelman, A., Hoor, P., Pan, L. L., Randel, W. J., Hegglin, M. I., and Birner, T.

(2011). The extratropical upper troposphere and lower stratosphere. *Reviews of Geophysics*, *49*(3). https://doi.org/10.1029/2011RG000355

Gunson, M. R., Abbas, M. M., Abrams, M. C., Allen, M., Brown, L. R., Brown, T. L., et al. (1996). The Atmospheric Trace Molecule Spectroscopy (ATMOS) Experiment: Deployment on the ATLAS space shuttle missions. *Geophysical Research Letters*, *23*(17), 2333–2336. https://doi.org/10.1029/96GL01569

Hall, B. D., Dutton, G. S., and Elkins, J. W. (2007). The NOAA nitrous oxide standard scale for atmospheric observations. *Journal of Geophysical Research Atmospheres*, *112*(9), 1–9. https://doi.org/10.1029/2006JD007954

Hall, B. D., Dutton, G. S., Mondeel, D. J., Nance, J. D., Rigby, M., Butler, J. H., et al. (2011). Improving measurements of SF6 for the study of atmospheric transport and emissions. *Atmospheric Measurement Techniques*, *4*(11), 2441–2451. https://doi.org/10.5194/amt-4-2441-2011

Hall, T. M., and Plumb, R. A. (1994). Age as a diagnostic of stratospheric transport. *Journal of Geophysical Research*, *99*(D1), 1059–1070. https://doi.org/10.1029/93JD03192

Harris, N. R. P., Carpenter, L. J., Lee, J. D., Vaughan, G., Filus, M. T., Jones, R. L., et al. (2017). Coordinated Airborne Studies in the Tropics (CAST). *Bulletin of the American Meteorological Society*, *98*(1), 145–162. https://doi.org/10.1175/BAMS-D-14-00290.1

Harris, N. R. P., Wuebbles, D. J., Daniel, J. S., Hu, J., Kuijpers, L. J. M., Law, K. S., et al. (2014). Scenarios and information for policymakers, Chapter 5. In *Scientific Assessment of Ozone Depletion: 2014, Global Ozone Research and Monitoring Project – Report No. 55,*. Geneva, Switzerland: World Meteorological Organization.

Hegels, E., Crutzen, P. J., Klüpfel, T., Perner, D., and Burrows, J. P. (1998). Global distribution of atmospheric bromine-monoxide from GOME on Earth Observing Satellite ERS-2. *Geophysical Research Letters*, *25*(16), 3127–3130. https://doi.org/10.1029/98GL02417

Hendrick, F., Van Roozendael, M., Chipperfield, M. P., Dorf, M., Goutail, F., Yang, X., et al. (2007). Retrieval of stratospheric and tropospheric BrO profiles and columns using ground-based zenith-sky DOAS observations at Harestua, 60°N. *Atmospheric Chemistry and Physics Discussions*, *7*(3), 8663–8708. https://doi.org/10.5194/acpd-7-8663-2007

Herman, J., Cede, A., Spinei, E., Mount, G., Tzortziou, M., and Abuhassan, N. (2009). NO_2 column amounts from ground-based Pandora and MFDOAS spectrometers using the direct-sun DOAS technique: Intercomparisons and application to OMI validation. *Journal of Geophysical Research Atmospheres*, *114*(13), 1–20. https://doi.org/10.1029Z2009JD011848

Hollwedel, J., Wenig, M., Beirle, S., Kraus, S., Kuhl, S., Wilms-Grabe, W., et al. (2004). Year-to-year variations of spring time polar tropospheric BrO as seen by GOME. *Advances in Space Research*, *34*, 804–808. https://doi.org/https://doi.org/10.1016/j.asr.2003.08.060

Holton, J. R., Haynes, P. H., McIntyre, M. E., Douglass, A. R., Rood, R. B., and Pfister, L. (1995). Stratosphere-troposphere exchange. *Reviews of Geophysics*, *33*(4), 403–439. https://doi.org/10.1029/95RG02097

Hossaini, R., Chipperfield, M. P., Dhomse, S., Ordóñez, C., Saiz-Lopez, A., Abraham, N. L., et al. (2012a). Modelling future changes to the stratospheric source gas injection of biogenic bromocarbons. *Geophysical Research Letters*, *39*(20), 2–5. https://doi.org/10.1029/2012GL053401

Hossaini, R., Chipperfield, M. P., Feng, W., Breider, T. J., Atlas, E., Montzka, S. A., et al. (2012b). The contribution of natural and anthropogenic very short-lived species to stratospheric bromine. *Atmospheric Chemistry and Physics*, *12*(1), 371–380. https://doi.org/10.5194/acp-12-371-2012

Hossaini, R., Chipperfield, M. P., Harrison, J. J., Glasow, R., Sommariva, R., Atlas, E., et al. (2015a). Growth in stratospheric chlorine from short-lived chemicals. *Geophysical Research Letters*, *42*, 1–8. https://doi.org/10.1002/2015GL063783.Received

Hossaini, R., Chipperfield, M. P., Monge-Sanz, B. M., Richards, N. a. D., Atlas, E., and Blake, D. R. (2010). Bromoform and dibromomethane in the tropics: a 3-D model study of chemistry and transport. *Atmospheric Chemistry and Physics*, *10*(2), 719–735. https://doi.org/10.5194/acp-10-719-2010

Hossaini, R., Chipperfield, M. P., Montzka, S. A., Leeson, A. A., Dhomse, S. S., and Pyle, J. A. (2017). The increasing threat to stratospheric ozone from dichloromethane. *Nature Communications*, *8*(May), 15962. https://doi.org/10.1038/ncomms15962

Hossaini, R., Chipperfield, M. P., Montzka, S. A., Rap, A., Dhomse, S., and Feng, W. (2015b). Efficiency of short-lived halogens at influencing climate through depletion of stratospheric ozone. *Nature Geoscience*, *8*, 186–190. https://doi.org/10.1038/ngeo2363

Hossaini, R., Mantle, H., Chipperfield, M. P., Montzka, S. A., Hamer, P., Ziska, F., et al. (2013). Evaluating global emission inventories of biogenic bromocarbons. *Atmospheric Chemistry and Physics*, *13*(23), 11819–11838. https://doi.org/10.5194/acp-13-11819-2013

Hossaini, R., Patra, P. K., Leeson, A. A., Krysztofiak, G., Abraham, N. L., Andrews, S. J., et al. (2016). A multi-model intercomparison of halogenated very short-lived substances (TransCom-VSLS): Linking oceanic emissions and tropospheric transport for a reconciled estimate of the stratospheric source gas injection of bromine. *Atmospheric Chemistry and Physics*, *16*(14), 9163–9187. https://doi.org/10.5194/acp-16-9163-2016

Huey, L. G. (2007). Measurement of trace atmospheric species by chemical ionization mass spectrometry: Speciation of reactive nitrogen and future directions. *Mass Spectrometry Reviews*, *26*(2), 166–184. https://doi.org/10.1002/mas.20118

Hughes, C., Johnson, M., Glasow, R. Von, Chance, R., Atkinson, H., Souster, T., et al. (2012). Climate-induced change in biogenic bromine emissions from the Antarctic marine biosphere. *Global Biogeochemical Cycles*, *26*(BG3019), 1–9. https://doi.org/10.1029/2012GB004295

Iraci, L. T., Michelsen, R. R., Ashbourn, S. F. M., Rammer, T. a., and Golden, D. M. (2005). Uptake of hypobromous acid (HOBr) by aqueous sulfuric acid solutions: low-temperature solubility and reaction. *Atmospheric Chemistry and Physics Discussions*, *5*(2), 1213–1239. https://doi.org/10.5194/acpd-5-1213-2005

Jensen, E. J., Pfister, L., Jordan, D. E., Bui, T. V., Ueyama, R., Singh, H. B., et al. (2017). The NASA Airborne Tropical Tropopause Experiment: High-altitude aircraft measurements in the Tropical Western Pacific. *Bulletin of the American Meteorological Society*, *98*(1), 129–143. https://doi.org/10.1175/BAMS-D-14-00263.1

Jensen, E. J., Pister, L., Jordan, D. E., Fahey, D. W., Newman, P. A., Thornberry, T., et al. (2013). The NASA Airborne Tropical TRopopause EXperiment (ATTREX). *SPARC Newsletter*, (41), 129–144. https://doi.org/10.1029/2009GL038587.Eyring

Jöckel, P., Tost, H., Pozzer, A., Kunze, M., Kirner, O., Brenninkmeijer, C. A. M., et al. (2016). Earth System Chemistry integrated Modelling (ESCiMo) with the Modular Earth Submodel System (MESSy) version 2.51. *Geoscientific Model Development*, *9*(3), 1153–1200. https://doi.org/10.5194/gmd-9-1153-2016

Jones, A. E., Anderson, P. S., Begoin, M., Brough, N., Hutterli, M. A., Marshall, G. J., et al. (2009). BrO, blizzards, and drivers of polar tropospheric ozone depletion events. *Atmospheric Chemistry and Physics*, *9*(14), 4639–4652. https://doi.org/10.5194/acp-9-4639-2009

Jones, A., Urban, J., Murtagh, D. P., Sanchez, C., Walker, K. A., Livesey, N. J., et al. (2011). Analysis of HCl and ClO time series in the upper stratosphere using satellite data sets. *Atmospheric Chemistry and Physics*, *11*(11), 5321–5333. https://doi.org/10.5194/acp-11-5321-2011

Kaye, J. A., Douglass, A. R., Jackman, C. H., Stolarski, R. S., Zander, R., and Roland, G. (1991). Two-dimensional model calculation of fluorine-containing reservoir species in the stratosphere. *Journal of Geophysical Research*, *96*(D7), 12865. https://doi.org/10.1029/91JD01178

Kerkweg, A., Jöckel, P., Warwick, N., Gebhardt, S., Brenninkmeijer, C. A. M., and Lelieveld, J. (2008). Consistent simulation of bromine chemistry from the marine boundary layer to the stratosphere – Part 2: Bromocarbons. *Atmospheric Chemistry and Physics*, *8*(19), 5919–5939. https://doi.org/10.5194/acp-8-5919-2008

Kiesewetter, G., Sinnhuber, B.-M., Weber, M., and Burrows, J. P. (2010). Attribution of stratospheric ozone trends to chemistry and transport: a modelling study. *Atmospheric Chemistry and Physics*, *10*(24), 12073–12089. https://doi.org/10.5194/acp-10-12073-2010

Klobas, J. E., Wilmouth, D. M., Weisenstein, D. K., Anderson, J. G., and Salawitch, R. J. (2017). Ozone depletion following future volcanic eruptions. *Geophysical Research Letters*. https://doi.org/10.1002/2017GL073972

Ko, M. K. W., Poulet, G., Blake, D. R., Boucher, O., Burkholder, J. H., Chin, M., et al. (2003). Very short-lived halogen and sulfur substances, Chapter 2. In *Scientific Assessment of Ozone Depletion: 2002, Global Ozone Research and Monitoring Project – Report No. 47*. Geneva, Switzerland: World Meteorological Organization.

Koenig, T. K., Volkamer, R., Baidar, S., Dix, B., Wang, S., Anderson, D. C., et al. (2017). BrO and inferred Bry profiles over the western Pacific: relevance of inorganic bromine sources and a Bry minimum in the aged tropical tropopause layer. *Atmospheric Chemistry and Physics*, *17*(24), 15245–15270.

https://doi.org/10.5194/acp-17-15245-2017
Kovalenko, L. J., Livesey, N. L., Salawitch, R. J., Camy-Peyret, C., Chipperfield, M. P., Cofield, R. E., et al. (2007). Validation of Aura Microwave Limb Sounder BrO observations in the stratosphere. *Journal of Geophysical Research Atmospheres*, *112*(24), 1–17. https://doi.org/10.1029/2007JD008817
Kreycy, S., Camy-Peyret, C., Chipperfield, M. P., Dorf, M., Feng, W., Hossaini, R., et al. (2013). Atmospheric test of the $J(BrONO_2)/k_{BrO+NO2}$ ratio: Implications for total stratospheric Br_y and bromine-mediated ozone loss. *Atmospheric Chemistry and Physics*, *13*(13), 6263–6274. https://doi.org/10.5194/acp-13-6263-2013
Krotkov, N. A., Lamsal, L. N., Celarier, E. A., Swartz, W. H., Marchenko, S. V., Bucsela, E. J., et al. (2017). The version 3 OMI NO_2 standard product. *Atmospheric Measurement Techniques Discussions*, (2), 1–42. https://doi.org/10.5194/amt-2017-44
Kurosu, T. P., and Chance, K. (2011). *OMBRO Readme File v003*. Retrieved from https://disc.gsfc.nasa.gov/datasets/OMBRO_V003/summary
Lamarque, J.-F., Emmons, L. K., Hess, P. G., Kinnison, D. E., Tilmes, S., Vitt, F., et al. (2012). CAM-chem: description and evaluation of interactive atmospheric chemistry in the Community Earth System Model. *Geoscientific Model Development*, *5*(2), 369–411. https://doi.org/10.5194/gmd-5-369-2012
Lary, D. J. (1996). Gas phase atmospheric bromine photochemistry. *Journal of Geophysical Research: Atmospheres*, *101*(D1), 1505–1516. https://doi.org/10.1029/95JD02463
Lary, D. J., Chipperfield, M. P., Toumi, R., and Lenton, T. (1996). Heterogeneous atmospheric bromine chemistry. *Journal of Geophysical Research: Atmospheres*, *101*(D1), 1489–1504. https://doi.org/10.1029/95JD02839
Laube, J. C., Engel, A., Bönisch, H., Möbius, T., Worton, D. R., Sturges, W. T., et al. (2008). Contribution of very short-lived organic substances to stratospheric chlorine and bromine in the tropics – a case study. *Atmospheric Chemistry and Physics*, *8*(23), 7325–7334. https://doi.org/10.5194/acp-8-7325-2008
Law, K. S., Sturges, W. T., Blake, D. R. B. N. J., Cox, R. A., Burkholder, J. B., Butler, J. H., et al. (2006). Halogenated Very Short-Lived Substances, Chapter 2. In *Scientific Assessment of Ozone Depletion: 2006, Global Ozone Research and Monitoring Project*. Geneva, Switzerland.
Le Breton, M., Bannan, T. J., Shallcross, D. E., Khan, M. A., Evans, M. J., Lee, J., et al. (2017). Enhanced ozone loss by active inorganic bromine chemistry in the tropical troposphere. *Atmospheric Environment*, *155*, 21–28. https://doi.org/10.1016/j.atmosenv.2017.02.003
Lennartz, S. T., Krysztofiak, G., Marandino, C. A., Sinnhuber, B. M., Tegtmeier, S., Ziska, F., et al. (2015). Modelling marine emissions and atmospheric distributions of halocarbons and dimethyl sulfide: The influence of prescribed water concentration vs. prescribed emissions. *Atmospheric Chemistry and Physics*, *15*(20), 11753–11772. https://doi.org/10.5194/acp-15-11753-2015
Levelt, P. F., Van den Oord, G. H. J., Dobber, M. R., Malkki, A., Visser, H., de Vries, J., et al. (2006). The Ozone Monitoring Instrument. *IEEE Transactions On Geoscience And Remote Sensing*, *44*(5), 1093–1101. https://doi.org/Urn:nbn:nl:ui:25-648485

Levine, J. G., Braesicke, P., Harris, N. R. P., Savage, N. H., and Pyle, J. A. (2007). Pathways and timescales for troposphere-to-stratosphere transport via the tropical tropopause layer and their relevance for very short lived substances. *Journal of Geophysical Research Atmospheres*, *112*(4), 1–15. https://doi.org/10.1029/2005JD006940

Liang, Q., Atlas, E., Blake, D., Dorf, M., Pfeilsticker, K., and Schauffler, S. (2014). Convective transport of very short lived bromocarbons to the stratosphere. *Atmospheric Chemistry and Physics*, *14*(11), 5781–5792. https://doi.org/10.5194/acp-14-5781-2014

Liang, Q., Stolarski, R. S., Kawa, S. R., Nielsen, J. E., Douglass, A. R., Rodriguez, J. M., et al. (2010). Finding the missing stratospheric Br_y: a global modeling study of $CHBr_3$ and CH_2Br_2. *Atmospheric Chemistry and Physics*, *10*(5), 2269–2286. https://doi.org/10.5194/acp-10-2269-2010

Liao, J., Sihler, H., Huey, L. G., Neuman, J. A., Tanner, D. J., Friess, U., et al. (2011). A comparison of Arctic BrO measurements by chemical ionization mass spectrometry and long path-differential optical absorption spectroscopy. *Journal of Geophysical Research Atmospheres*, *116*(1), 1–14. https://doi.org/10.1029/2010JD014788

Livesey, N. J., Read, W. G., Wagner, P. A., Froidevaux, L., Lambert, A., Manney, G. L., et al. (2018). *Earth Observing System (EOS) Aura Microwave Limb Sounder (MLS) version 4.2x level 2 data quality and description document*. *JPL D-33509 Rev D*.

Long, M. S., Keene, W. C., Easter, R. C., Sander, R., Liu, X., Kerkweg, A., and Erickson, D. (2014). Sensitivity of tropospheric chemical composition to halogen-radical chemistry using a fully coupled size-resolved multiphase chemistry-global climate system: Halogen distributions, aerosol composition, and sensitivity of climate-relevant gases. *Atmospheric Chemistry and Physics*, *14*(7), 3397–3425. https://doi.org/10.5194/acp-14-3397-2014

Mahieu, E., Chipperfield, M. P., Notholt, J., Reddmann, T., Anderson, J., Bernath, P. F., et al. (2014). Recent Northern Hemisphere stratospheric HCl increase due to atmospheric circulation changes. *Nature*, *515*(7525), 104–107. https://doi.org/10.1038/nature13857

Marsh, D. R., Mills, M. J., Kinnison, D. E., Lamarque, J. F., Calvo, N., and Polvani, L. M. (2013). Climate change from 1850 to 2005 simulated in CESM1(WACCM). *Journal of Climate*, *26*(19), 7372–7391. https://doi.org/10.1175/JCLI-D-12-00558.1

McCormick, M. P., Steele, H. M., Hamill, P., Chu, W. P., and Swissler, T. J. (1982). Polar Stratospheric Cloud Sightings by SAM II. *Journal of the Atmospheric Sciences*, *39*(6), 1387–1397. https://doi.org/10.1175/1520-0469(1982)039<1387:PSCSBS>2.0.CO;2

McElroy, M. B., Salawitch, R. J., and Minschwaner, K. (1992). The changing stratosphere. *Planetary and Space Science*, *40*(2–3), 373–401. https://doi.org/10.1016/0032-0633(92)90070-5

McElroy, M. B., Salawitch, R. J., Wofsy, S. C., and Logan, J. A. (1986). Reductions of Antarctic ozone due to synergistic interactions of chlorine and bromine. *Nature*, *321*(6072), 759–762. https://doi.org/10.1038/321759a0

McLinden, C. A., Haley, C. S., Lloyd, N. D., Hendrick, F., Rozanov, A., Sinnhuber, B. M., et al. (2010). Odin/OSIRIS observations of stratospheric BrO: Retrieval methodology, climatology, and inferred Br_y. *Journal of Geophysical Research Atmospheres*, *115*(15), 1–19. https://doi.org/10.1029/2009JD012488

McPeters, R. D., Bhartia, P. K., Haffner, D., Labow, G. J., and Flynn, L. (2013). The version 8.6 SBUV ozone data record: An overview. *Journal of Geophysical Research Atmospheres*, *118*(14), 8032–8039. https://doi.org/10.1002/jgrd.50597

Michelsen, H. A., Salawitch, R. J., Gunson, M. R., Aellig, C., Kämpfer, N., Abbas, M. M., et al. (1996). Stratospheric chlorine partitioning: Constraints from shuttle-borne measurements of [HCl], [ClNO 3], and [ClO]. *Geophysical Research Letters*, *23*(17), 2361–2364. https://doi.org/10.1029/96GL00787

Michou, M., Saint-Martin, D., Teyssèdre, H., Alias, A., Karcher, F., Olivié, D., et al. (2011). A new version of the CNRM Chemistry-Climate Model, CNRM-CCM: description and improvements from the CCMVal-2 simulations. *Geoscientific Model Development*, *4*(4), 873–900. https://doi.org/10.5194/gmd-4-873-2011

Mohd Nadzir, M. S., Phang, S. M., Abas, M. R., Abdul Rahman, N., Abu Samah, A., Sturges, W. T., et al. (2014). Bromocarbons in the tropical coastal and open ocean atmosphere during the 2009 Prime Expedition Scientific Cruise (PESC-09). *Atmospheric Chemistry and Physics*, *14*(15), 8137–8148. https://doi.org/10.5194/acp-14-8137-2014

Molina, M. J., and Rowland, F. S. (1974). Stratospheric sink for chlorofluoromethanes: chlorine atom-catalysed destruction of ozone. *Nature*, *249*(5460), 810–812. https://doi.org/10.1038/249810a0

Molod, A., Takacs, L., Suarez, M., Bacmeister, J., Song, I., and Eichmann, A. (2012). The GEOS-5 Atmospheric General Circulation Model: Mean Climate and Development from MERRA to Fortuna. *Technical Report Series on Global Modeling and Data Assimilation*, *27*.

Montzka, S. A., Krol, M., Dlugokencky, E., Hall, B., Jockel, P., and Lelieveld, J. (2011a). Small Interannual Variability of Global Atmospheric Hydroxyl. *Science*, *331*(6013), 67–69. https://doi.org/10.1126/science.1197640

Montzka, S. A., Reimann, S., Engel, A., Krüger, K., Sturges, W. T., and O'Doherty, S. (2011b). Ozone-depleting substances (ODSs) and related chemicals, Chapter 1. In *Scientific Assessment of Ozone Depletion: 2010, Global Ozone Research and Monitoring Project – Report No. 52* (52nd ed.). Geneva, Switzerland: World Meteorological Organization.

Morgenstern, O., Braesicke, P., O'Connor, F. M., Bushell, A. C., Johnson, C. E., Osprey, S. M., and Pyle, J. A. (2009). Evaluation of the new UKCA climate-composition model – Part 1: The stratosphere. *Geoscientific Model Development*, *2*(1), 43–57. https://doi.org/10.5194/gmd-2-43-2009

Morgenstern, O., Hegglin, M. I., Rozanov, E., O'Connor, F. M., Abraham, N. L., Akiyoshi, H., et al. (2017). Review of the global models used within phase 1 of the Chemistry–Climate Model Initiative (CCMI). *Geoscientific Model Development*, *10*(2), 639–671. https://doi.org/10.5194/gmd-10-639-2017

Morgenstern, O., Stone, K. A., Schofield, R., Akiyoshi, H., Yamashita, Y., Kinnison, D. E., et al. (2018). Ozone sensitivity to varying greenhouse gases and ozone-depleting substances in CCMI-1 simulations. *Atmospheric Chemistry and*

Physics, *18*(2), 1091–1114. https://doi.org/10.5194/acp-18-1091-2018
Munro, R., Eisinger, M., Anderson, C., Callies, J., Corpaccioli, E., Lang, R., et al. (2006). GOME-2 on MetOp. In *Proc. of The 2006 EUMETSAT Meteorological Satellite Conference* (p. 48). Helsinki, Finland.
Nassar, R., Bernath, P. F., Boone, C. D., Clerbaux, C., Coheur, P. F., Dufour, G., et al. (2006). A global inventory of stratospheric chlorine in 2004. *Journal of Geophysical Research Atmospheres*, *111*(22), 1–13. https://doi.org/10.1029/2006JD007073
Navarro, M. A., Atlas, E. L., Saiz-Lopez, A., Rodriguez-Lloveras, X., Kinnison, D. E., Lamarque, J., et al. (2015). Airborne measurements of organic bromine compounds in the Pacific tropical tropopause layer. *Proceedings of the National Academy of Sciences*, *112*(45), 13789–13793. https://doi.org/10.1073/pnas.1511463112
Navarro, M. A., Saiz-Lopez, A., Cuevas, C. A., Fernandez, R. P., Atlas, E., Rodriguez-Lloveras, X., et al. (2017). Modeling the inorganic bromine partitioning in the tropical tropopause layer over the eastern and western Pacific Ocean. *Atmospheric Chemistry and Physics*, *17*(16), 9917–9930. https://doi.org/10.5194/acp-17-9917-2017
Newman, P. A., Daniel, J. S., Waugh, D. W., and Nash, E. R. (2007). A new formulation of equivalent effective stratospheric chlorine (EESC). *Atmospheric Chemistry and Physics*, *7*(17), 4537–4552. https://doi.org/10.5194/acp-7-4537-2007
Nghiem, S. V., Rigor, I. G., Richter, A., Burrows, J. P., Shepson, P. B., Bottenheim, J., et al. (2012). Field and satellite observations of the formation and distribution of Arctic atmospheric bromine above a rejuvenated sea ice cover. *Journal of Geophysical Research: Atmospheres*, *117*(D17), n/a-n/a. https://doi.org/10.1029/2011JD016268
Nicely, J. M., Anderson, D. C., Canty, T. P., Salawitch, R. J., Wolfe, G. M., Apel, E. C., et al. (2016). An observationally constrained evaluation of the oxidative capacity in the tropical western Pacific troposphere. *Journal of Geophysical Research: Atmospheres*, *121*(12), 7461–7488. https://doi.org/10.1002/2016JD025067
Nicely, J. M., Salawitch, R. J., Canty, T., Anderson, D. C., Arnold, S. R., Chipperfield, M. P., et al. (2017). Quantifying the causes of differences in tropospheric OH within global models. *Journal of Geophysical Research: Atmospheres*, *122*(3), 1983–2007. https://doi.org/10.1002/2016JD026239
Oman, L. D., Douglass, A. R., Salawitch, R. J., Canty, T. P., Ziemke, J. R., and Manyin, M. (2016). The effect of representing bromine from VSLS on the simulation and evolution of Antarctic ozone. *Geophysical Research Letters*, *43*, 9869–9876. https://doi.org/10.1002/2016GL070471
Oman, L. D., Douglass, A. R., Ziemke, J. R., Rodriguez, J. M., Waugh, D. W., and Nielsen, J. E. (2013). The ozone response to ENSO in Aura satellite measurements and a chemistry-climate simulation. *Journal of Geophysical Research: Atmospheres*, *118*(2), 965–976. https://doi.org/10.1029/2012JD018546
Oram, D. E., Ashfold, M. J., Laube, J. C., Gooch, L. J., Humphrey, S., Sturges, W. T.,

et al. (2017). A growing threat to the ozone layer from short-lived anthropogenic chlorocarbons. *Atmospheric Chemistry and Physics*, *17*(19), 11929–11941. https://doi.org/10.5194/acp-17-11929-2017

Ordóñez, C., Lamarque, J. F., Tilmes, S., Kinnison, D. E., Atlas, E. L., Blake, D. R., et al. (2012). Bromine and iodine chemistry in a global chemistry-climate model: Description and evaluation of very short-lived oceanic sources. *Atmospheric Chemistry and Physics*, *12*(3), 1423–1447. https://doi.org/10.5194/acp-12-1423-2012

Osterman, G. B., Salawitch, R. J., Sen, B., Toon, G. C., Stachnik, R. A., Pickett, H. M., et al. (1997). Balloon-borne measurements of stratospheric radicals and their precursors: Implications for the production and loss of ozone. *Geophysical Research Letters*, *24*(9), 1107–1110. https://doi.org/10.1029/97GL00921

Ostermöller, J., Bönisch, H., Jöckel, P., and Engel, A. (2017). A new time-independent formulation of fractional release. *Atmospheric Chemistry and Physics*, *17*(6), 3785–3797. https://doi.org/10.5194/acp-17-3785-2017

Pan, L. L., Atlas, E. L., Salawitch, R. J., Honomichl, S. B., Bresch, J. F., Randel, W. J., et al. (2017). The Convective Transport of Active Species in the Tropics (CONTRAST) Experiment. *Bulletin of the American Meteorological Society*, *98*(1), 106–128. https://doi.org/10.1175/BAMS-D-14-00272.1

Pan, L. L., Bowman, K. P., Shapiro, M., Randel, W. J., Gao, R. S., Campos, T., et al. (2007). Chemical behavior of the tropopause observed during the Stratosphere-Troposphere Analyses of Regional Transport experiment. *Journal of Geophysical Research*, *112*(D18). https://doi.org/10.1029/2007JD008645

Pan, L. L., Randel, W. J., Gary, B. L., Mahoney, M. J., and Hintsa, E. J. (2004). Definitions and sharpness of the extratropical tropopause: A trace gas perspective. *Journal of Geophysical Research: Atmospheres*, *109*(D23), 1–11. https://doi.org/10.1029/2004JD004982

Parrella, J. P., Chance, K., Salawitch, R. J., Canty, T., Dorf, M., and Pfeilsticker, K. (2013). New retrieval of BrO from SCIAMACHY limb: An estimate of the stratospheric bromine loading during April 2008. *Atmospheric Measurement Techniques*, *6*(10), 2549–2561. https://doi.org/10.5194/amt-6-2549-2013

Parrella, J. P., Jacob, D. J., Liang, Q., Zhang, Y., Mickley, L. J., Miller, B., et al. (2012). Tropospheric bromine chemistry: Implications for present and pre-industrial ozone and mercury. *Atmospheric Chemistry and Physics*, *12*(15), 6723–6740. https://doi.org/10.5194/acp-12-6723-2012

Pawson, S., Steinbrecht, W., Charlton-Perez, A. J., Fujiwara, M., Karpechko, A. Y., Petropavlovskikh, I., et al. (2014). Update on global ozone: Past, present, and future, Chapter 2. In *Scientific Assessment of Ozone Depletion: 2014*. Geneva, Switzerland: World Meteorological Organization.

Peterson, P. K., Simpson, W. R., Pratt, K. A., Shepson, P. B., Frieß, U., Zielcke, J., et al. (2015). Dependence of the vertical distribution of bromine monoxide in the lower troposphere on meteorological factors such as wind speed and stability. *Atmospheric Chemistry and Physics*, *15*(4), 2119–2137. https://doi.org/10.5194/acp-15-2119-2015

Pfeilsticker, K., Sturges, W. T., Bösch, H., Camy-Peyret, C., Chipperfield, M. P., Engel, A., et al. (2000). Lower stratospheric organic and inorganic bromine

budget for the Arctic winter 1998/99. *Geophysical Research Letters*, *27*(20), 3305–3308. https://doi.org/10.1029/2000GL011650
Pitari, G., Aquila, V., Kravitz, B., Robock, A., Watanabe, S., Cionni, I., et al. (2014). Stratospheric ozone response to sulfate geoengineering: Results from the Geoengineering Model Intercomparison Project (GeoMIP). *Journal of Geophysical Research: Atmospheres*, *119*(5), 2629–2653. https://doi.org/10.1002/2013JD020566
Platt, U., and Stutz, J. (2008). *Differential Optical Absorption Spectroscopy*.
Plumb, I. C., Vohralik, P. F., and Ryan, K. R. (1999). Normalization of correlations for atmospheric species with chemical loss. *Journal of Geophysical Research: Atmospheres*, *104*(D9), 11723–11732. https://doi.org/10.1029/1999JD900014
Plumb, R. A., and Ko, M. K. W. (1992). Interrelationships between mixing ratios of long-lived stratospheric constituents. *Journal of Geophysical Research: Atmospheres*, *97*(D9), 10145–10156. https://doi.org/10.1029/92JD00450
Poulet, G., Pirre, M., Maguin, F., Ramaroson, R., and Le Bras, G. (1992). Role of the BrO + HO2 reaction in the stratospheric chemistry of bromine. *Geophysical Research Letters*, *19*(23), 2305–2308. https://doi.org/10.1029/92GL00781
Pratt, K. A., Custard, K. D., Shepson, P. B., Douglas, T. A., Pöhler, D., General, S., et al. (2013). Photochemical production of molecular bromine in Arctic surface snowpacks. *Nature Geoscience*, *6*(5), 351–356. https://doi.org/10.1038/ngeo1779
Prinn, R. G., Weiss, R. F., Fraser, P. J., Simmonds, P. G., Cunnold, D. M., Alyea, F. N., et al. (2000). A history of chemically and radiatively important gases in air deduced from ALE/GAGE/AGAGE. *Journal of Geophysical Research: Atmospheres*, *105*(D14), 17751–17792. https://doi.org/10.1029/2000JD900141
Pyle, J. A., Ashfold, M. J., Harris, N. R. P., Robinson, A. D., Warwick, N. J., Carver, G. D., et al. (2011). Bromoform in the tropical boundary layer of the Maritime Continent during OP3. *Atmospheric Chemistry and Physics*, *11*(2), 529–542. https://doi.org/10.5194/acp-11-529-2011
Quack, B., and Wallace, D. W. R. (2003). Air-sea flux of bromoform: Controls, rates, and implications. *Global Biogeochemical Cycles*, *17*(1). https://doi.org/10.1029/2002GB001890
Randeniya, L. K., Vohralik, P. F., and Plumb, I. C. (2002). Stratospheric ozone depletion at northern mid latitudes in the 21 st century: The importance of future concentrations of greenhouse gases nitrous oxide and methane. *Geophysical Research Letters*, *29*(4), 1051. https://doi.org/10.1029/2001GL014295
Ravishankara, A. R., Daniel, J. S., and Portmann, R. W. (2009). Nitrous Oxide (N2O): The Dominant Ozone-Depleting Substance Emitted in the 21st Century. *Science*, *326*(5949), 123–125. https://doi.org/10.1126/science.1176985
Revell, L. E., Bodeker, G. E., Huck, P. E., Williamson, B. E., and Rozanov, E. (2012). The sensitivity of stratospheric ozone changes through the 21st century to N_2O and CH_4. *Atmospheric Chemistry and Physics*, *12*(23), 11309–11317. https://doi.org/10.5194/acp-12-11309-2012
Revell, L. E., Tummon, F., Salawitch, R. J., Stenke, A., and Peter, T. (2015). The changing ozone depletion potential of N2O in a future climate. *Geophysical Research Letters*, *42*(22), 10,047-10,055.

https://doi.org/10.1002/2015GL065702
Rex, M., Wohltmann, I., Ridder, T., Lehmann, R., Rosenlof, K., Wennberg, P., et al. (2014). A tropical West Pacific OH minimum and implications for stratospheric composition. *Atmospheric Chemistry and Physics*, *14*(9), 4827–4841. https://doi.org/10.5194/acp-14-4827-2014
Richter, A., Wittrock, F., Eisinger, M., and Burrows, J. P. (1998). GOME observations of tropospheric BrO in northern hemispheric spring and summer 1997. *Geophysical Research Letters*, *25*(14), 2683–2686. https://doi.org/10.1029/98GL52016
Ridley, B. A., and Grahek, F. E. (1990). A small, low flow, high sensitivity reaction vessel for NO chemiluminescence detectors. *Journal of Atmospheric and Oceanic Technology*, *7*(2), 307–311. https://doi.org/10.1175/1520-0426(1990)007<0307:ASLFHS>2.0.CO;2
Rienecker, M. M., Suarez, M. J., Gelaro, R., Todling, R., Bacmeister, J., Liu, E., et al. (2011). MERRA: NASA's Modern-Era Retrospective Analysis for Research and Applications. *Journal of Climate*, *24*(14), 3624–3648. https://doi.org/10.1175/JCLI-D-11-00015.1
Rinsland, C. P., Mahieu, E., Zander, R., Jones, N. B., Chipperfield, M. P., Goldman, A., et al. (2003). Long-term trends of inorganic chlorine from ground-based infrared solar spectra: Past increases and evidence for stabilization. *Journal of Geophysical Research*, *108*(D8), 4252. https://doi.org/10.1029/2002JD003001
Robinson, A. D., Harris, N. R. P., Ashfold, M. J., Gostlow, B., Warwick, N. J., O'Brien, L. M., et al. (2014). Long-term halocarbon observations from a coastal and an inland site in Sabah, Malaysian Borneo. *Atmospheric Chemistry and Physics*, *14*(16), 8369–8388. https://doi.org/10.5194/acp-14-8369-2014
Rosenfield, J. E., and Douglass, A. R. (1998). Doubled CO_2 effects on NO_y in a coupled 2D model. *Geophysical Research Letters*, *25*(23), 4381–4384. https://doi.org/10.1029/1998GL900147
Russell, J. M., Gordley, L. L., Deaver, L. E., Thompson, R. E., and Park, J. H. (1994). An overview of the halogen occultation experiment (HALOE) and preliminary results. *Advances in Space Research*, *14*(9), 13–20. https://doi.org/10.1016/0273-1177(94)90110-4
Saiz-Lopez, A., Fernandez, R. P., Ordóñez, C., Kinnison, D. E., Martín, J. C. G., Lamarque, J. F., and Tilmes, S. (2014). Iodine chemistry in the troposphere and its effect on ozone. *Atmospheric Chemistry and Physics*, *14*(23), 13119–13143. https://doi.org/10.5194/acp-14-13119-2014
Saiz-Lopez, A., Lamarque, J. F., Kinnison, D. E., Tilmes, S., Ordóñez, C., Orlando, J. J., et al. (2012). Estimating the climate significance of halogen-driven ozone loss in the tropical marine troposphere. *Atmospheric Chemistry and Physics*, *12*(9), 3939–3949. https://doi.org/10.5194/acp-12-3939-2012
Saiz-Lopez, A., and von Glasow, R. (2012). Reactive halogen chemistry in the troposphere. *Chemical Society Reviews*, *41*(19), 6448. https://doi.org/10.1039/c2cs35208g
Sala, S., Bönisch, H., Keber, T., Oram, D. E., Mills, G., and Engel, A. (2014). Deriving an atmospheric budget of total organic bromine using airborne in situ measurements from the western Pacific area during SHIVA. *Atmospheric*

Chemistry and Physics, *14*(13), 6903–6923. https://doi.org/10.5194/acp-14-6903-2014

Salawitch, R. J., Canty, T., Kurosu, T., Chance, K., Liang, Q., Da Silva, A., et al. (2010). A new interpretation of total column BrO during Arctic spring. *Geophysical Research Letters*, *37*(21), 1–9. https://doi.org/10.1029/2010GL043798

Salawitch, R. J., Weisenstein, D. K., Kovalenko, L. J., Sioris, C. E., Wennberg, P. O., Chance, K., et al. (2005). Sensitivity of ozone to bromine in the lower stratosphere. *Geophysical Research Letters*, *32*(5), 1–5. https://doi.org/10.1029/2004GL021504

Sander, S. P., Friedl, R. R., Golden, D. M., Kurylo, M. J., Moortgat, G. K., Wine, P. H., et al. (2011). *Chemical Kinetics and Photochemical Data for Use in Atmospheric Studies, Evaluation No. 17," JPL Publication 10-6, Jet Propulsion Laboratory, Pasadena*. *JPL Publication 10-6*. https://doi.org/10.1002/kin.550171010

Sander, S. P., Ray, G. W., and Watson, R. T. (1981). Kinetics Study of the Pressure Dependence of the BrO + NO_2 Reaction at 298 K. *J. Phys. Chem*, *85*(2), 199–210.

Santee, M. L., Lambert, A., Read, W. G., Livesey, N. J., Manney, G. L., Cofield, R. E., et al. (2008). Validation of the Aura Microwave Limb Sounder ClO measurements. *Journal of Geophysical Research*, *113*(D15), D15S22. https://doi.org/10.1029/2007JD008762

Schauffler, S. M., Atlas, E. L., Blake, D. R., Flocke, F., Lueb, R. A., Lee-Taylor, J. M., et al. (1999). Distributions of brominated organic compounds in the troposphere and lower stratosphere. *Journal of Geophysical Research: Atmospheres*, *104*(D17), 21513–21535. https://doi.org/10.1029/1999JD900197

Schauffler, S. M., Atlas, E. L., Donnelly, S. G., Andrews, A., Montzka, S. A., Elkins, J. W., et al. (2003). Chlorine budget and partitioning during the Stratospheric Aerosol and Gas Experiment (SAGE) III Ozone Loss and Validation Experiment (SOLVE). *Journal of Geophysical Research*, *108*(D5), 4173. https://doi.org/10.1029/2001JD002040

Schmidt, J. A., Jacob, D. J., Horowitz, H. M., Hu, L., Sherwen, T., Evans, M. J., et al. (2016). Modeling the observed tropospheric BrO background: Importance of multiphase chemistry and implications for ozone, OH, and mercury. *Journal of Geophysical Research: Atmospheres*, *121*(19), 11,819-11,835. https://doi.org/10.1002/2015JD024229

Schofield, R., Fueglistaler, S., Wohltmann, I., and Rex, M. (2011). Sensitivity of stratospheric Br_y to uncertainties in very short lived substance emissions and atmospheric transport. *Atmospheric Chemistry and Physics*, *11*(4), 1379–1392. https://doi.org/10.5194/acp-11-1379-2011

Schofield, R., Johnston, P. V., Thomas, A., Kreher, K., Connor, B. J., Wood, S., et al. (2006). Tropospheric and stratospheric BrO columns over Arrival Heights, Antarctica, 2002. *Journal of Geophysical Research*, *111*(D22), D22310. https://doi.org/10.1029/2005JD007022

Schofield, R., Kreher, K., Conner, B. J., Johnston, P. V., Thomas, A., Shooter, D., et al. (2004). Retrieved tropospheric and stratospheric BrO columns over Lauder,

New Zealand. *Journal of Geophysical Research*, *109*(D14), D14304. https://doi.org/10.1029/2003JD004463

Scinocca, J. F., McFarlane, N. A., Lazare, M., Li, J., and Plummer, D. (2008). Technical Note: The CCCma third generation AGCM and its extension into the middle atmosphere. *Atmospheric Chemistry and Physics*, *8*(23), 7055–7074. https://doi.org/10.5194/acp-8-7055-2008

Shepherd, T. G. (2008). Dynamics, stratospheric ozone, and climate change. *Atmosphere-Ocean*, *46*(1), 117–138. https://doi.org/10.3137/ao.460106

Shetter, R. E., and Müller, M. (1999). Photolysis frequency measurements using actinic flux spectroradiometry during the PEM-Tropics mission: Instrumentation description and some results. *Journal of Geophysical Research: Atmospheres*, *104*(D5), 5647–5661. https://doi.org/10.1029/98JD01381

Shindell, D. T., Rind, D., and Lonergan, P. (1998). Increased polar stratospheric ozone losses and delayed eventual recovery owing to increasing greenhouse-gas concentrations. *Nature*, *392*(6676), 589–592. https://doi.org/10.1038/33385

Simpson, W. R., Brown, S. S., Saiz-Lopez, A., Thornton, J. A., and Von Glasow, R. (2015). Tropospheric Halogen Chemistry: Sources, Cycling, and Impacts. *Chemical Reviews*, *115*(10), 4035–4062. https://doi.org/10.1021/cr5006638

Simpson, W. R., Carlson, D., Hönninger, G., Douglas, T. A., Sturm, M., Perovich, D., and Platt, U. (2007a). First-year sea-ice contact predicts bromine monoxide (BrO) levels at Barrow, Alaska better than potential frost flower contact. *Atmospheric Chemistry and Physics*, *7*(3), 621–627. https://doi.org/10.5194/acp-7-621-2007

Simpson, W. R., Peterson, P. K., Frieß, U., Sihler, H., Lampel, J., Platt, U., et al. (2017). Horizontal and vertical structure of reactive bromine events probed by bromine monoxide MAX-DOAS. *Atmospheric Chemistry and Physics*, *17*(15), 9291–9309. https://doi.org/10.5194/acp-17-9291-2017

Simpson, W. R., Von Glasow, R., Riedel, K., Anderson, P., Ariya, P., Bottenheim, J., et al. (2007b). Halogens and their role in polar boundary-layer ozone depletion. *Atmos. Chem. Phys.*, *7*, 4375–4418. https://doi.org/10.5194/acpd-7-4285-2007

Sinnhuber, B.-M., and Folkins, I. (2006). Estimating the contribution of bromoform to stratospheric bromine and its relation to dehydration in the tropical tropopause layer. *Atmospheric Chemistry and Physics*, *6*(12), 4755–4761. https://doi.org/10.5194/acp-6-4755-2006

Sinnhuber, B.-M., Rozanov, A., Sheode, N., Afe, O. T., Richter, A., Sinnhuber, M., et al. (2005). Global observations of stratospheric bromine monoxide from SCIAMACHY. *Geophysical Research Letters*, *32*(20), L20810. https://doi.org/10.1029/2005GL023839

Sinnhuber, B.-M., Sheode, N., Sinnhuber, M., Chipperfield, M. P., and Feng, W. (2009). The contribution of anthropogenic bromine emissions to past stratospheric ozone trends: a modelling study. *Atmos. Chem. Phys.*, *9*, 2863–2871. https://doi.org/www.atmos-chem-phys.net/9/2863/2009/

Sinnhuber, B. M., and Meul, S. (2015). Simulating the impact of emissions of brominated very short lived substances on past stratospheric ozone trends. *Geophysical Research Letters*, *42*(7), 2449–2456. https://doi.org/10.1002/2014GL062975

Sioris, C. E., Kovalenko, L. J., McLinden, C. A., Salawitch, R. J., Van Roozendael, M., Goutail, F., et al. (2006). Latitudinal and vertical distribution of bromine monoxide in the lower stratosphere from Scanning Imaging Absorption Spectrometer for Atmospheric Chartography limb scattering measurements. *Journal of Geophysical Research*, *111*(D14), D14301. https://doi.org/10.1029/2005JD006479

Solomon, S., Ivy, D. J., Kinnison, D., Mills, M. J., Iii, R. R. N., and Schmidt, A. (2016). Emergence of healing in the Antarctic ozone layer. *Science*, *353*(6296), 269–274. https://doi.org/10.1126/science.aae0061

Solomon, S., Kinnison, D., Bandoro, J., and Garcia, R. (2015). Simulation of polar ozone depletion: An update. *Journal of Geophysical Research: Atmospheres*, *120*(15), 7958–7974. https://doi.org/10.1002/2015JD023365

Solomon, S., Mills, M., Heidt, L. E., Pollock, W. H., and Tuck, A. F. (1992). On the evaluation of ozone depletion potentials. *Journal of Geophysical Research*, *97*(D1), 825. https://doi.org/10.1029/91JD02613

SPARC. (2010). *SPARC CCMVal Report on the Evaluation of Chemistry-Climate Models* (WCRP-132,). (D. W. W. V. Eyring, T. G. Shepherd, Ed.), *SPARC Report No. 5, WCRP-30/2010,WMO/TD-No.40*. Retrieved from http://www.atmosp.physics.utoronto.ca/SPARC/News15/15_Udelhofen.html

SPARC. (2013). *SPARC report on lifetimes of stratospheric ozone-depleting substances, their replacements, and related species*. (M. Ko, P. Newman, S. Reimann, & S. Strahan, Eds.), *SPARC Report No. 6, WCRP-15/2013*. Retrieved from http://www.sparc-climate.org/publications/sparc-reports/

Spencer, J. E., and Rowland, F. S. (1978). Bromine nitrate and its stratospheric significance. *The Journal of Physical Chemistry*, *82*(1), 7–10. https://doi.org/10.1021/j100490a002

Spinei, E., Carn, S. A., Krotkov, N. A., Mount, G. H., Yang, K., and Krueger, A. (2010). Validation of ozone monitoring instrument SO2 measurements in the Okmok volcanic cloud over Pullman, WA, July 2008. *Journal of Geophysical Research Atmospheres*, *115*(18), 1–14. https://doi.org/10.1029/2009JD013492

Spurr, R. J. D., Kurosu, T. P., and Chance, K. V. (2001). A linearized discrete ordinate radiative transfer model for atmospheric remote-sensing retrieval. *Journal of Quantitative Spectroscopy and Radiative Transfer*, *68*(6), 689–735. https://doi.org/10.1016/S0022-4073(00)00055-8

Stachnik, R. A., Millán, L., Jarnot, R., Monroe, R., McLinden, C., Kühl, S., et al. (2013). Stratospheric BrO abundance measured by a balloon-borne submillimeterwave radiometer. *Atmospheric Chemistry and Physics*, *13*(6), 3307–3319. https://doi.org/10.5194/acp-13-3307-2013

Stauffer, R. M., Morris, G. A., Thompson, A. M., Joseph, E., Coetzee, G. J. R., and Nalli, N. R. (2014). Propagation of radiosonde pressure sensor errors to ozonesonde measurements. *Atmospheric Measurement Techniques*, *7*(1), 65–79. https://doi.org/10.5194/amt-7-65-2014

Stenke, A., Schraner, M., Rozanov, E., Egorova, T., Luo, B., and Peter, T. (2013). The SOCOL version 3.0 chemistry-climate model: Description, evaluation, and implications from an advanced transport algorithm. *Geoscientific Model Development*, *6*(5), 1407–1427. https://doi.org/10.5194/gmd-6-1407-2013

Stone, K. A., Morgenstern, O., Karoly, D. J., Klekociuk, A. R., French, W. J., Abraham, N. L., and Schofield, R. (2016). Evaluation of the ACCESS - Chemistry-climate model for the Southern Hemisphere. *Atmospheric Chemistry and Physics*, *16*(4), 2401–2415. https://doi.org/10.5194/acp-16-2401-2016

Strahan, S. E., and Douglass, A. R. (2018). Decline in Antarctic Ozone Depletion and Lower Stratospheric Chlorine Determined From Aura Microwave Limb Sounder Observations. *Geophysical Research Letters*, 382–390. https://doi.org/10.1002/2017GL074830

Strahan, S. E., Duncan, B. N., and Hoor, P. (2007). Observationally derived transport diagnostics for the lowermost stratosphere and their application to the GMI chemistry and transport model. *Atmospheric Chemistry and Physics*, *7*, 2435–2445. https://doi.org/10.5194/acpd-7-1449-2007

Sturges, W. T., Cota, G. F., and Buckley, P. T. (1992). Bromoform emission from Arctic ice algae. *Nature*, *358*, 660–662.

Stutz, J., and Platt, U. (1996). Numerical analysis and estimation of the statistical error of differential optical absorption spectroscopy measurements with least-squares methods. *Applied Optics*, *35*(30), 6041–6053.

Stutz, J., Werner, B., Spolaor, M., Scalone, L., Festa, J., Tsai, C., et al. (2017). A new Differential Optical Absorption Spectroscopy instrument to study atmospheric chemistry from a high-altitude unmanned aircraft. *Atmospheric Measurement Techniques*, *10*(3), 1017–1042. https://doi.org/10.5194/amt-10-1017-2017

Suleiman, R. M., Chance, K., Liu, X., González Abad, G., Kurosu, T. P., Hendrick, F., and Theys, N. (2018). OMI total bromine monoxide (OMBRO) data product: Algorithm, retrieval and measurement comparisons. *Atmospheric Measurement Techniques Discussions*, *2*(January), 1–33. https://doi.org/10.5194/amt-2018-1

Tegtmeier, S., Krüger, K., Quack, B., Atlas, E. L., Pisso, I., Stohl, A., and Yang, X. (2012). Emission and transport of bromocarbons: From the West Pacific ocean into the stratosphere. *Atmospheric Chemistry and Physics*, *12*(22), 10633–10648. https://doi.org/10.5194/acp-12-10633-2012

Theys, N., Van Roozendael, M., Hendrick, F., Fayt, C., Hermans, C., Baray, J.-L., et al. (2007). Retrieval of stratospheric and tropospheric BrO columns from multi-axis DOAS measurements at Reunion Island (21° S, 56° E). *Atmospheric Chemistry and Physics*, *7*(18), 4733–4749. https://doi.org/10.5194/acp-7-4733-2007

Theys, N., Van Roozendael, M., Hendrick, F., Yang, X., De Smedt, I., Richter, A., et al. (2011). Global observations of tropospheric BrO columns using GOME-2 satellite data. *Atmospheric Chemistry and Physics*, *11*(4), 1791–1811. https://doi.org/10.5194/acp-11-1791-2011

Thorn, R. P., Daykin, E. P., and Wine, P. H. (1993). Kinetics of the BrO + NO_2 Association Reaction. Temperature and Pressure Dependence in the Falloff Regime. *International Journal of Chemical Kinetics*, *25*, 521–537.

Tian, W., and Chipperfield, M. P. (2005). A new coupled chemistry–climate model for the stratosphere: The importance of coupling for future O_3-climate predictions. *Quarterly Journal of the Royal Meteorological Society*, *131*(605), 281–303. https://doi.org/10.1256/qj.04.05

Tilmes, S., Kinnison, D. E., Garcia, R. R., Salawitch, R., Canty, T., Lee-Taylor, J., et

al. (2012). Impact of very short-lived halogens on stratospheric ozone abundance and UV radiation in a geo-engineered atmosphere. *Atmospheric Chemistry and Physics*, *12*, 10945–10955. https://doi.org/10.5194/acp-12-10945-2012

Tilmes, S., Lamarque, J.-F., Emmons, L. K., Kinnison, D. E., Ma, P.-L., Liu, X., et al. (2015). Description and evaluation of tropospheric chemistry and aerosols in the Community Earth System Model (CESM1.2). *Geoscientific Model Development*, *8*(5), 1395–1426. https://doi.org/10.5194/gmd-8-1395-2015

Tilmes, S., Lamarque, J. F., Emmons, L. K., Kinnison, D. E., Marsh, D., Garcia, R. R., et al. (2016). Representation of the Community Earth System Model (CESM1) CAM4-chem within the Chemistry-Climate Model Initiative (CCMI). *Geoscientific Model Development*, *9*(5), 1853–1890. https://doi.org/10.5194/gmd-9-1853-2016

Tilmes, S., Müller, R., and Salawitch, R. (2008). The sensitivity of polar ozone depletion to proposed geoengineering schemes. *Science*, *320*(5880), 1201–1204. https://doi.org/10.1126/science.1153966

Tokarczyk, R., and Moore, R. M. (1994). Production of volatile organohalogens by phytoplankton cultures. *Geophysical Research Letters*, *21*(4), 285–288. https://doi.org/10.1029/94GL00009

Toon, O. B., Starr, D. O., Jensen, E. J., Newman, P. A., Platnick, S., Schoeberl, M. R., et al. (2010). Planning, implementation, and first results of the Tropical Composition, Cloud and Climate Coupling Experiment (TC4). *Journal of Geophysical Research Atmospheres*, *115*(13), 1–33. https://doi.org/10.1029/2009JD013073

Tzortziou, M., Herman, J. R., Cede, A., and Abuhassan, N. (2012). High precision, absolute total column ozone measurements from the Pandora spectrometer system: Comparisons with data from a Brewer double monochromator and Aura OMI. *Journal of Geophysical Research Atmospheres*, *117*(16), 1–14. https://doi.org/10.1029/2012JD017814

Van Roozendael, M., Wagner, T., Richter, A., Pundt, I., Arlander, D. W., Burrows, J. P., et al. (2002). Intercomparison of BrO measurements from ERS-2 GOME, ground-based and balloon platforms. *Advances in Space Research*, *29*(11), 1661–1666. https://doi.org/10.1016/S0273-1177(02)00098-4

Veefkind, J. P., Aben, I., McMullan, K., Förster, H., de Vries, J., Otter, G., et al. (2012). TROPOMI on the ESA Sentinel-5 Precursor: A GMES mission for global observations of the atmospheric composition for climate, air quality and ozone layer applications. *Remote Sensing of Environment*, *120*(2012), 70–83. https://doi.org/10.1016/j.rse.2011.09.027

Veefkind, J. P., Bhartia, P. K., Gleason, J., de Haan, J. F., Wellemeyer, C., Qin, W., and Levelt, P. F. (2006). Total Ozone from the Ozone Monitoring Instrument (OMI) using TOMS and DOAS Methods. *IEEE TRANSACTIONS ON GEOSCIENCE AND REMOTE SENSING*, *44*(5), 8932.

Vogt, R., Paul J Crutzen, and Sander, R. (1996). A mechanism for halogen release from sea-salt aerosol in the remote marine boundary layer. *Nature*, *383*, 327–329.

Voldoire, A., Sanchez-Gomez, E., Salas y Mélia, D., Decharme, B., Cassou, C., Sénési, S., et al. (2012). The CNRM-CM5.1 global climate model: description

and basic evaluation. *Climate Dynamics*, *40*(9–10), 2091–2121. https://doi.org/10.1007/s00382-011-1259-y

Volk, C. M., Elkins, J. W., Fahey, D. W., Dutton, G. S., Gilligan, J. M., Loewenstein, M., et al. (1997). Evaluation of source gas lifetimes from stratospheric observations. *Journal of Geophysical Research*, *102*(D21), 25543. https://doi.org/10.1029/97JD02215

Volk, C. M., Elkins, J. W., Fahey, D. W., Salawitch, R. J., Dutton, G. S., Gilligan, J. M., et al. (1996). Quantifying transport between the tropical and mid-latitude lower stratosphere. *Science*, *272*(5269), 1763–1768. https://doi.org/10.1126/science.272.5269.1763

Volkamer, R., Baidar, S., Campos, T. L., Coburn, S., DiGangi, J. P., Dix, B., et al. (2015). Aircraft measurements of BrO, IO, glyoxal, NO2, H2O, O2–O2 and aerosol extinction profiles in the tropics: comparison with aircraft-/ship-based in situe and lidar measurements. *Atmospheric Measurement Techniques*, *8*(5), 2121–2148. https://doi.org/10.5194/amt-8-2121-2015

von Glasow, R., von Kuhlmann, R., Lawrence, M. G., Platt, U., and Crutzen, P. J. (2004). Impact of reactive bromine chemistry in the troposphere. *Atmospheric Chemistry and Physics Discussions*, *4*(4), 4877–4913. https://doi.org/10.5194/acpd-4-4877-2004

Wagner, T., Leue, C., Wenig, M., Pfeilsticker, K., and Platt, U. (2001). Spatial and temporal distribution of enhanced boundary layer BrO concentrations measured by the GOME instrumnet aboard ERS-2. *J. Geophys. Res.*, *106*, 24225–24235. https://doi.org/https://doi.org/10.1029/2000JD000201

Wagner, T., and Platt, U. (1998). Satellite mapping of enhanced BrO concentrations in the troposphere. *Nature*, *395*(6701), 486–490. https://doi.org/10.1038/26723

Wales, P. A., Salawitch, R. J., Nicely, J. M., Anderson, D. C., Canty, T. P., Baidar, S., et al. (2018). Stratospheric Injection of Brominated Very Short-Lived Substances: Aircraft Observations in the Western Pacific and Representation in Global Models. *Journal of Geophysical Research: Atmospheres*, *123*(10), 5690–5719. https://doi.org/10.1029/2017JD027978

Wamsley, P. R., Elkins, J. W., Fahey, D. W., Dutton, G. S., Volk, C. M., Myers, R. C., et al. (1998). Distribution of halon-1211 in the upper troposphere and lower stratosphere and the 1994 total bromine budget. *Journal of Geophysical Research: Atmospheres*, *103*(D1), 1513–1526. https://doi.org/10.1029/97JD02466

Wang, S., Schmidt, J. A., Baidar, S., Coburn, S., Dix, B., Koenig, T. K., et al. (2015). Active and widespread halogen chemistry in the tropical and subtropical free troposphere. *Proceedings of the National Academy of Sciences*, *112*(30), 9281–9286. https://doi.org/10.1073/pnas.1505142112

Warwick, N. J., Pyle, J. A., Carver, G. D., Yang, X., Savage, N. H., O'Connor, F. M., and Cox, R. A. (2006). Global modeling of biogenic bromocarbons. *Journal of Geophysical Research Atmospheres*, *111*(24), 1–12. https://doi.org/10.1029/2006JD007264

Watson, R., Machado, G., Fischer, S., and Davis, D. D. (1976). A temperature dependence kinetics study of the reactions of Cl ($^2P_{3/2}$) with O_3, CH_4, and H_2O_2. *The Journal of Chemical Physics*, *65*(6), 2126–2138.

https://doi.org/10.1063/1.433369
Waugh, D., and Hall, T. M. (2002). Age of stratospheric air: Theory, observations, and models. *Reviews of Geophysics*, *40*(4), 1010. https://doi.org/10.1029/2000RG000101
Waugh, D. W., Strahan, S. E., and Newman, P. A. (2007). Sensitivity of stratospheric inorganic chlorine to differences in transport. *Atmospheric Chemistry and Physics*, *7*(18), 4935–4941. https://doi.org/10.5194/acp-7-4935-2007
Wennberg, P. O., Brault, J. W., Hanisco, T. F., Salawitch, R. J., and Mount, G. H. (1997). The atmospheric column abundance of IO: Implications for stratospheric ozone. *Journal of Geophysical Research: Atmospheres*, *102*(D7), 8887–8898. https://doi.org/10.1029/96JD03712
Werner, B., Stutz, J., Spolaor, M., Scalone, L., Raecke, R., Festa, J., et al. (2017). Probing the subtropical lowermost stratosphere and the tropical upper troposphere and tropopause layer for inorganic bromine. *Atmospheric Chemistry and Physics*, *17*(2), 1161–1186. https://doi.org/10.5194/acp-17-1161-2017
Wetzel, G., Oelhaf, H., Höpfner, M., Friedl-Vallon, F., Ebersoldt, A., Gulde, T., et al. (2017). Diurnal variations of $BrONO_2$ observed by MIPAS-B at midlatitudes and in the Arctic. *Atmospheric Chemistry and Physics*, *17*(23), 14631–14643. https://doi.org/10.5194/acp-17-14631-2017
Wilmouth, D. M., Hanisco, T. F., Donahue, N. M., and Anderson, J. G. (1999). Fourier Transform Ultraviolet Spectroscopy of the A 2Π3/2 ← X 2Π3/2 Transition of BrO. *The Journal of Physical Chemistry A*, *103*(45), 8935–8945. https://doi.org/10.1021/jp991651o
Wisher, A., Oram, D. E., Laube, J. C., Mills, G. P., van Velthoven, P., Zahn, A., and Brenninkmeijer, C. A. M. (2014). Very short-lived bromomethanes measured by the CARIBIC observatory over the North Atlantic, Africa and Southeast Asia during 2009-2013. *Atmospheric Chemistry and Physics*, *14*(7), 3557–3570. https://doi.org/10.5194/acp-14-3557-2014
Wofsy, S. C., McElroy, M. B., and Yung, Y. L. (1975). The chemistry of atmospheric bromine. *Geophysical Research Letters*, *2*(6), 215–218. https://doi.org/10.1029/GL002i006p00215
World Meteorological Organization. (1957). Meteorology—A three-dimensional science: Second session of the Commission for Aerology. *WMO Bull.*
World Meteorological Organization. (2018). Executive Summary: Scientific Assessment of Ozone Depletion: 2018. In *Global Ozone Research and Monitoring Project – Report No. 58* (p. 67). Geneva, Switzerland: World Meteorological Organization.
Yang, E. S., Cunnold, D. M., Salawitch, R. J., McCormick, M. P., Russell, J., Zawodny, J. M., et al. (2006). Attribution of recovery in lower-stratospheric ozone. *Journal of Geophysical Research Atmospheres*, *111*(17), 1–21. https://doi.org/10.1029/2005JD006371
Yang, X., Cox, R. A., Warwick, N. J., Pyle, J. A., Carver, G. D., O'Connor, F. M., and Savage, N. H. (2005). Tropospheric bromine chemistry and its impacts on ozone: A model study. *Journal of Geophysical Research Atmospheres*, *110*(23), 1–18. https://doi.org/10.1029/2005JD006244
Yukimoto, S., Adachi, Y., Hosaka, M., Sakami, T., Yoshimura, H., Hirabara, M., et

al. (2012). A new global climate model of the Meteorological Research Institute: MRI-CGCM3: Model description and Basic Performance. *Journal of the Meteorological Society of Japan*, *90A*(0), 23–64. https://doi.org/10.2151/jmsj.2012-A02

Yung, Y. L., Pinto, J. P., Watson, R. T., and Sander, S. P. (1980). Atmospheric Bromine and Ozone Perturbations in the Lower Stratosphere. *Journal of the Atmospheric Sciences*, *37*(2), 339–353. https://doi.org/10.1175/1520-0469(1980)037<0339:ABAOPI>2.0.CO;2

Zahn, A., and Brenninkmeijer, C. A. M. (2003). New Directions: A Chemical Tropopause Defined. *Atmospheric Environment*, *37*, 439–440.

Zander, R., Mahieu, E., Demoulin, P., Duchatelet, P., Roland, G., Servais, C., et al. (2008). Our changing atmosphere: Evidence based on long-term infrared solar observations at the Jungfraujoch since 1950. *Science of the Total Environment*, *391*(2–3), 184–195. https://doi.org/10.1016/j.scitotenv.2007.10.018

Zander, R., Mahieu, E., Gunson, M. R., Abrams, M. C., Chang, A. Y., Abbas, M., et al. (1996). The 1994 northern midlatitude budget of stratospheric chlorine derived from ATMOS/ATLAS-3 observations. *Geophysical Research Letters*, *23*(17), 2357–2360. https://doi.org/10.1029/96GL01792

Ziska, F., Quack, B., Abrahamsson, K., Archer, S. D., Atlas, E., Bell, T., et al. (2013). Global sea-to-air flux climatology for bromoform, dibromomethane and methyl iodide. *Atmospheric Chemistry and Physics*, *13*(17), 8915–8934. https://doi.org/10.5194/acp-13-8915-2013

Ziska, F., Quack, B., Tegtmeier, S., Stemmler, I., and Krüger, K. (2017). Future emissions of marine halogenated very-short lived substances under climate change. *Journal of Atmospheric Chemistry*, *74*(2), 245–260. https://doi.org/10.1007/s10874-016-9355-3

Zondlo, M. A., Paige, M. E., Massick, S. M., and Silver, J. A. (2010). Vertical cavity laser hygrometer for the National Science Foundation Gulfstream-V aircraft. *Journal of Geophysical Research*, *115*(D20), D20309. https://doi.org/10.1029/2010JD014445

Zoogman, P., Liu, X., Suleiman, R. M., Pennington, W. F., Flittner, D. E., Al-Saadi, J., et al. (2017). Tropospheric emissions: Monitoring of pollution (TEMPO). *Journal of Quantitative Spectroscopy and Radiative Transfer*, *186*, 17–39. https://doi.org/10.1016/j.jqsrt.2016.05.008